



Design and Applications of Plasmonic Superlattice Nanomembrane

A Dissertation Submitted for the Degree of Doctor of Philosophy

By

Yi Chen

Department of Chemical Engineering

Faculty of Engineering

MONASH UNIVERSITY

December 2013

This thesis is dedicated to my parents

謹以此論文獻給我的父母親

COPYRIGHT NOTICES

Under the Copyright Act 1968, this thesis must be used only under the normal conditions of scholarly fair dealing. In particular no results or conclusions should be extracted from it, nor should it be copied or closely paraphrased in whole or in part without the written consent of the author. Proper written acknowledgement should be made for any assistance obtained from this thesis.

I certify that I have made all reasonable efforts to secure copyright permissions for third-party content included in this thesis and have not knowingly added copyright content to my work without the owner's permission.

Signed: _____



Date: 23/04/2014

This page is intentionally blank

TABLE OF CONTENTS

TABLE OF CONTENTS	i
ABSTRACT	v
DECLARATION	vii
LIST OF PUBLICATIONS	xi
LIST OF FIGURES	xv
LIST OF ABBREVIATIONS	xxix
LIST OF NOMENCLATURE	xxxii
Chapter 1 Introduction	34
Chapter 2 Literature Review	42
2.1 General design principles for nanoparticle superlattice	43
2.1.1 Nanoparticle interactions during assembly of ‘soft spheres’	44
2.1.2 Modeling ligand deformation in soft crystallization.....	46
2.1.3 Basic design rules for DNA-based crystallization.....	48
2.2 Molecule-based nanoparticle superlattice	49
2.2.1 Single-component nanoparticle superlattice.....	51
2.2.2 Multicomponent nanoparticle superlattice	58
2.3 DNA-based nanoparticle superlattice.....	61
2.3.1 DNA-programmed self-assembly	63
2.3.1.1 Nanoparticle superlattice derived from mono-DNA conjugates.....	63
2.3.1.2 Nanoparticle superlattice derived from site-specific DNA conjugates.....	65
2.3.1.3 Nanoparticle superlattice derived from multi-DNA conjugates	66
2.3.1.4 Nanoparticle superlattice from DNA polymerization	70
2.3.2 DNA-templated self-assembly.....	72
2.3.2.1 Simple dsDNA templates.....	72
2.3.2.2 Templates based on DNA tiles, DNA frames and DNA Origami.....	72
2.3.3 Unconventional DNA technologies and nanopatterning	76
2.3.3.1 As entropic ligands in drying-mediated self-assembly.....	76
2.3.3.2 In conjunction with top-down lithography.....	78
2.4 Polymer-based nanoparticle superlattice.....	80
2.4.1 Polymer-templated self-assembly.....	80
2.4.2 Polymer-assistant self-assembly	82
2.4.3 Polymer-mediated self-assembly.....	83

2.5 References.....	89
Chapter 3 Free-standing Superlattice Nanomembrane from Polymer-capped Gold Nanospheres	102
3.1 Experimental methods	104
3.1.1 Materials.....	104
3.1.2 Synthesis of AuNPs	104
3.1.3 Conjugation of AuNPs with PS-SH	105
3.1.4 Characterization	105
3.2 Results and discussion	106
3.2.1 Characterization of PS-capped gold nanoparticles.....	106
3.2.2 Fabrication and transfer of PS-capped AuNPs superlattice sheets.....	110
3.2.3 Characterization of PS-capped AuNPs superlattice sheets	112
3.2.4 Plasmonic property of PS-capped AuNPs superlattice sheets	116
3.3 Conclusion	117
3.4 References.....	117
Chapter 4 Giant Metal Superlattice Nanomembranes From Ultrathin Gold Nanowires	122
4.1 Experimental methods	124
4.1.1 Materials.....	124
4.1.2 Synthesis of ultrathin AuNWs	124
4.1.3 Fabrication and transfer of AuNWs superlattice nanomembrane	124
4.1.4 Characterization	125
4.2 Results and discussion	126
4.2.1 Fabrication of AuNWs superlattice nanomembrane	126
4.2.2 Transfer and manipulation of AuNWs superlattice nanomembrane	129
4.2.3 Morphological characterization of AuNWs superlattice nanomembrane	131
4.2.4 Mechanical properties of AuNWs superlattice nanomembrane.....	132
4.2.4.1 <i>Young's modulus of AuNWs superlattice nanomembrane</i>	133
4.2.4.2 <i>Mechanical strength of AuNWs superlattice nanomembrane</i>	135
4.2.5 Optical property of AuNWs superlattice nanomembrane	136
4.2.6 Electrical conductivity of AuNWs superlattice nanomembrane	138
4.2.7 Nanomembrane-based supercapacitor and electrocatalytic electrode.....	142
4.3 Conclusion	145
4.4 References.....	146
Chapter 5 Giant Plasmonic Superlattice Sheet From Polymer-capped Bimetallic Nanocrystals.....	152
5.1 Experimental methods	153
5.1.1 Materials.....	153

5.1.2 Synthesis of CTAB-capped gold nanorods.....	154
5.1.3 Synthesis of CTAC-capped Au@Ag NBs.....	154
5.1.4 Synthesis of Polystyrene-capped Au@Ag NBs.....	155
5.1.5 Fabrication of giant NB superlattice sheet.....	155
5.1.6 Characterization.....	155
5.1.7 Numerical method for simulation.....	156
5.2 Results and discussion.....	157
5.2.1 Synthesis of monodisperse NBs	157
5.2.2 Plasmon modes of NBs.....	158
5.2.3 Synthesis of polystyrene-capped Au@Ag NBs by ligand exchange.....	159
5.2.4 Fabrication of NB superlattice sheets	160
5.2.5 Morphological characterization of NB superlattice sheets	160
5.2.5.1 <i>Giant superlattice sheets at different magnifications</i>	160
5.2.5.2 <i>Ordering parameter of NB superlattice sheet</i>	161
5.2.5.3 <i>Parameters in affecting growth of giant superlattice sheets</i>	163
5.2.5.4 <i>Transferability and 2D patterning of giant superlattice sheets</i>	164
5.2.6 Mechanical properties of giant superlattice sheets	166
5.2.7 Customizing plasmonics of superlattice sheet and theoretical modeling	167
5.2.7.1 <i>Dimensions of three different plasmonic building blocks</i>	167
5.2.7.2 <i>Measurement of interparticle spacing of three NB superlattice sheets</i>	168
5.2.7.3 <i>Extinction spectra of three NB superlattice sheets</i>	170
5.2.7.4 <i>SERS efficiency and near-field distribution for NB superlattice sheets</i>	171
5.2.8 Giant superlattice sheets as universal and unique SERS substrates	173
5.2.8.1 <i>SERS spectra from patterned square sheets</i>	173
5.2.8.2 <i>Liquid and vapor detection using free-standing superlattice sheets</i>	175
5.3 Conclusion.....	177
5.4 References	177
Chapter 6 Conclusions and Outlook	182
Appendix: First-Authored Papers Relevant to This Thesis	187

This page is intentionally blank

ABSTRACT

Building plasmonic superlattice nanomembrane enables new class of two-dimensional (2D) optical metamaterials, which are free-standing, one-particle-thick, supracrystalline structures constituted by metallic nanocrystals. The past two decades have witnessed the wet chemical synthesis of plasmon-active nanocrystals, allowing them to serve as “meta-atoms” from the “plasmonic periodic table”. The following challenge lies on rationally group those artificial atoms into 2D plasmonic superlattices. In theory, it is possible to virtually design nanostructures with desired plasmonic properties by selecting nanocrystal types, adjusting soft ligand length, and controlling lattice structures. In practice, however, it has been notoriously challenging to manipulate at will for large-scale, ordered assembly of these meta-atoms. This thesis addresses the existing challenges, specifically, focuses on high-quality synthesis of plasmonic nanocrystal building blocks including gold nanospheres (AuNPs), ultrathin gold nanowires (AuNWs), bimetallic core-shell Au@Ag nanobricks (NBs), following by their programmed assembly with a general polymer-ligand-based approach in conjunction with drying-mediated self-assembly at air-water interface. Three types of novel plasmonic superlattice nanomembranes are prepared, which represent the thinnest possible metallic membrane known to date, including free-standing AuNPs superlattice nanomembrane, giant AuNWs superlattice nanomembranes with mechanical strength, optical transparency and electrical conductivity, and giant superlattice membranes with customizable hybridized plasmon modes and near-field distributions.

This thesis begins with a literature review of initial success in growing 1D~3D nanoparticle superlattices by soft ligands. The dominant nanoscale interactions and theoretical model that involved in superlattice construction are firstly outlined. From the view of methodological perspective, pioneering and ongoing research on nanoparticle superlattices are categorized in three types, namely, molecule-based, DNA-based, and polymer-based nanoparticle superlattices.

Based on those previously reported design rules, Chapter 3 presents a novel and general method to construct free-standing nanoparticle superlattice nanomembranes using

polymers as ligands. The long-range ordered superlattice nanomembranes could be transferred onto arbitrary substrates, and both structural features (interparticle spacing) and functional properties (plasmonic coupling) can be precisely adjusted by tailoring the sizes of the constituent nanoparticles.

To further tackle the challenge in fabricating defect-free superlattice membranes at large area, Langmuir-Blodgett techniques is employed to assemble ultraflexible AuNWs into giant mettalic superlattice membrane. Chapter 4 presents the thinnest possible version of metallic membranes known to date, which is about 2.5 nm thick but with macroscopic lateral dimensions. Such giant metallic nanomembranes are transparent, conductive and mechanically strong, with an optical transmittance of 90-97%, an electrical resistance of $\sim 1142 \text{ k}\Omega \text{ sq}^{-1}$, and a breaking strength of $\sim 14 \text{ N m}^{-1}$ with a typical atomic force microscope probe. Beside the structural and mechanical features, this nanomembrane exhibits multi-angular potential applications, such as in lightweight foldable supercapacitor and electrocatalysis.

Beyond structural and functional programmability, Chapter 5 extends the fabrication technique to more complex bimetallic nanobricks. Both experimental evaluation and theoretical simulation demonstrated the customizable plasmon modes and near-field distributions of giant superlattice nanomembrane. Consequently, Raman hot spots could be generated at specific excitation wavelength in a highly predictable way. The NB superlattice membranes are homogeneous in structure, vapor-permeable and mechanically flexible. It can be used as universal and unique SERS substrates with highly uniform Raman hotspot distributions across large area, for rapid and sensitive multi-phase detection of chemical species in air and liquid.

Finally, conclusions arising from this thesis have been summarized in Chapter 6, as well as opportunities and perspectives for future focus of this field.

DECLARATION

I hereby declare that this thesis contains no material which has been accepted for the award of any other degree or diploma at any university or equivalent institution and that, to the best of my knowledge and belief, this thesis contains no material previously published or written by another person, except where due reference is made in the text of the thesis.

Signed: _____



Date: 23/04/2014

This page is intentionally blank

ACKNOWLEDGEMENTS

I would like to express my deepest gratitude to my supervisor, *Assoc. Prof.* Wenlong Cheng, for his excellent guidance throughout this research journey, as well as interdisciplinary and nurturing environment he has created in our group.

As his first PhD candidate, he guides me to this exciting field and inspires me with great ideas across nanotechnology. I still remember the first day I entered the lab, he taught me from the basic synthesis technique. During last three years, he provided me with freedom in choosing research topics and respected my choice in all time. His unreserved support, enthusiasm in research, multi-task working habits did and will print in my mind permanently.

I would like to thank my collaborators during this research: *Prof.* Min Gu, *Prof.* Malin Premaratne, *Dr.* Zi Ouyang, *Dr.* Christina Cortez-Jugo, *Dr.* Fatima Eftekhari, *Dr.* Jing Fu, *Dr.* Junfei Tian, *Dr.* Ivan D. Rukhlenko, *Dr.* Qiaoliang Bao, *Dr.* Bin Su, *Dr.* Xiaowei Yang, *Ms.* Shouyi Xie, *Mr.* Finlay Shanks. Their technical assistance and scientific suggestions are really helpful and greatly appreciated. In particular, my sincere thanks goes to my friend and good collaborator, *Mr.* Debabrata Sikdar, for his diligent work and patience during theoretical simulation.

I gratefully acknowledge all the examiners during my candidature confirmation, mid-candidature review, and pre-submission seminar – *Prof.* Huanting Wang, *Prof.* George Simon, *Prof.* Wei Shen, and *Prof.* Dan Li, for their insightful comments and helpful suggestions.

I would like to acknowledge the use of facilities at Melbourne Centre for Nanofabrication, Monash Centre for Electron Microscopy, Monash Micro Imaging and Department of Chemical Engineering. Also, I would like to thank all the administrative and technical staffs in above organizations, including: *Prof.* Joanne Etheridge, *Dr.* Xiya Fang, *Dr.* Flame Burgmann, *Dr.* Matthew Weyland, Ellen Lavoie, Paul Spizzirri, John

Zhu, Lilyanne Price, Jill Crisfield, Kim Phu, Ron Graham, Gamini Ganegoda, for their support and assistance during my PhD.

Moreover, many thanks goes to all my fellow labmates at CHENG NanoBionics Group and friends at Monash: Yue Tang, Khee Chaw Ng, Kae Jye Si, Romiza Mazid, Wei Xiong, Shu Gong, Lim Wei Yap, Pengzhen Guo, Wenjuan Yang, Yongwei Wang, Dong Hou, Upulie Divisekera, Naveen Jason, Ramya Chandrasekaran, Yuzhou Wu, Kun Wang, Yong Peng, Ling Qiu, Yao Zeng, Yuan Li, Yufei Wang, Ruohui Lin, Jiahua Chew, Kathryn Waldron, Dominic Agyei, Charlotte Wong, Jiayao Li, Xing Zhang. I will always cherish those moments of stimulating discussions, sleepless working nights, and all the fun we had during last three years.

I also would like to acknowledge Monash University and the Department of Chemical Engineering, for postgraduate scholarships (MGS & IPRS) during my PhD. Special acknowledgement also goes to my country for the award and great care when studying overseas.

Special thanks to my parents and fiancée, for their endless love and support.

LIST OF PUBLICATIONS

Peer-Reviewed Journal Papers

1. **Chen, Y.**; Ouyang, Z.; Gu, M.; Cheng, W. L., Mechanically Strong, Optically Transparent, Giant Metal Superlattice Nanomembranes From Ultrathin Gold Nanowires. *Adv. Mater.* 2013, 25, 80-85.
2. **Chen, Y.**; Cheng, W. L., DNA-based plasmonic nanoarchitectures: from structural design to emerging applications. *WIREs Nanomed. Nanobiotechnol.* 2012, 4, 587-604.
3. **Chen, Y.**; Fu, J.; Ng, K. C.; Tang, Y.; Cheng, W. L., Free-Standing Polymer-Nanoparticle Superlattice Sheets Self-Assembled at the Air Liquid Interface. *Cryst. Growth Des.* 2011, 11, 4742-4746.
4. **Chen, Y.**; Ng, K. C.; Yan, W.; Tang, Y.; Cheng, W. L., Ultraflexible plasmonic nanocomposite aerogel. *RSC Adv.* 2011, 1, 1265-1270.
5. Su, B.; Wu, Y.; Tang, Y.; **Chen, Y.**; Cheng, W.; Jiang, L., Free-Standing 1D Assemblies of Plasmonic Nanoparticles. *Adv. Mater.* 2013, 25, 3968-3972.
6. Tang, Y.; Yeo, K. L.; **Chen, Y.**; Yap, L. W.; Xiong, W.; Cheng, W. L., Ultralow-density copper nanowire aerogel monoliths with tunable mechanical and electrical properties. *J. Mater. Chem. A* 2013, 1, 6723-6726.
7. Tang, Y.; Ng, K. C.; **Chen, Y.**; Cheng, W. L., Lightweight, flexible, nanorod electrode with high electrocatalytic activity. *Electrochem. Commun.* 2013, 27, 120-123.
8. Xiong, W.; Sikdar, D.; Walsh, M.; Si, K. J.; Tang, Y.; **Chen, Y.**; Mazid, R.; Weyland, M.; Rukhlenko, I. D.; Etheridge, J.; Premaratne, M.; Li, Y. X.; Cheng, W. L., Single-crystal caged gold nanorods with tunable broadband plasmon resonances.

Chem. Commun. 2013, 49, 9630-9632.

9. Ng, K. C.; Udagedara, I. B.; Rukhlenko, I. D.; **Chen, Y.**; Tang, Y.; Premaratne, M.; Cheng, W. L., Free-Standing Plasmonic-Nanorod Superlattice Sheets. *ACS Nano* 2011, 6, 925-934.
10. Campolongo, M. J.; Tan, S. J.; Smilgies, D.-M.; Zhao, M.; **Chen, Y.**; Xhangolli, I.; Cheng, W. L.; Luo, D., Crystalline Gibbs Monolayers of DNA-Capped Nanoparticles at the Air–Liquid Interface. *ACS Nano* 2011, 5, 7978-7985.
11. Gong, S.; Schwalb, W; Wang, Y.W.; **Chen, Y.**; Tang, Y.; Si, J.; Shirinzadeh, B.; Cheng, W. L., A Wearable and Highly Sensitive Pressure Sensor With Ultrathin Gold Nanowires. *Nature Commun.* 2014, 5, 3132.

Manuscripts in Preparation

1. **Chen, Y.**; Si, K. J.; Sikdar, D.; Eftekhari, F.; Bao, Q.; Rukhlenko, I. D.; Tang, Y.; Xiong, W.; Premaratne, M.; Cheng, W. L., Giant Plasmene Nanosheets with Customizable Properties.
2. Si, K. J.; **Chen, Y.**; Cheng, W. L., Engineering Nanoparticle Superlattices with Soft Ligands. Invited review from *Nano Today*, submitted and under review.

Book Chapter

1. Yang, W. J.; **Chen, Y.**; Cheng, W. L., Properties of DNA-Capped Nanoparticles, in "*Handbook of Nanomaterials Properties*", Bhushan, B.; Luo, D.; Schrickler, S.R.; Sigmund, W.; Zauscher, S. (Eds.), ISBN 978-3-642-31107-9, (Springer, 2014)

Conferences

1. **Chen, Y.**, Cheng, W. L., "Giant Metal Nanowire Superlattice Nanomembranes by

Self-Assembly”, (*Oral presentation*) International Conference on Nanoscience & Technology (ChinaNANO 2013), Beijing, China, 4-7 Sep. 2013

2. **Chen, Y.**, Cheng, W. L., “Polymer-Based Plasmonic Superlattice Nanosheets”, (*Oral presentation*) 12th International Conference on the Science and Application of Nanotubes, Brisbane, Australia, 24-29 Jun. 2012

This page is intentionally blank

LIST OF FIGURES

Chapter 2

Scheme 2.1 | Schematic summary of various nanoparticle superlattices assembled from libraries of soft-ligand capped nanocrystals using molecule-based, DNA-based and polymer-based methodologies. Figure reproduced with permission from Ref. [1, 2, 5, 8, 12-14, 17, 20, 22, 24, 49-55]. © (1998, 2001, 2006, 2007, 2009, 2010, 2012, 2013) NPG. (2006, 2009) AAAS. (2010, 2013) Wiley-VCH. (2008, 2011) ACS.44

Figure 2.1 | Interparticle potential derived from vdW attraction potential (U_{vdW}) and steric repulsion potential (U_{steric}). The profile is outlined based on two oleic acid-capped Co nanoparticles with a diameter of 3.3 nm. Figure reproduced with permission from Ref.[60]. © (2010) Beilstein-Institut. 45

Figure 2.2 | (a) Scheme for the deformation of soft-corona nanoparticles in soft-crystallization. (b) Probing soft crystallization using in situ SAXS demonstrates the continuous deformation of corona. (c) Scheme of DNA-capped hydrodynamic nanoparticle in complementary contact model. The spherical cap represent overlapped portion of corona with adjacent nanoparticle. (d) Illustration of design rule (3) that nanoparticles with same hydrodynamic size form similar superlattice structure. (e) Phase diagram shows predictable superlattice structure by controlling core size and DNA ligand ratio. Each colored domain denotes the specific superlattice structure. The dots represent the superlattice obtain in experimental. Figures reproduced with permission from Ref. [23, 45]. (a, b) © (2010) Wiley-VCH. (c-e) © (2011) AAAS. 47

Figure 2.3 | TEM image and photograph (inset) of superlattice using dodecanethiol-capped AuNPs. Reproduced with permission from Ref. [21]. © (1996) Wiley-VCH. 50

Figure 2.4 | Effect of chain length of surfactant ligand on superlattice structure. TEM images show 3D to 2D superlattices (left to right) using surfactants with increasing length by applying the ‘digestive ripening’ method. Reproduced with permission from Ref. [74]. © (2002) ACS. 52

Figure 2.5 | TEM image and inset model shows free-floating superlattices constructed by DMAET-stabilized CdTe quantum dots. Reproduced with permission from Ref. [20]. © (2006) AAAS. 53

Figure 2.6 | 2D superlattice shows long-range order of AuNPs kinetically self-assembled at air/water interface using drop-drying method. Reproduced with permission from Ref. [14]. © (2006) NPG. 55

Figure 2.7 | Mechanically robust free-standing superlattice membrane constructed by surfactant-capped nanoparticles. TEM images of 2D superlattice membrane assembled by (a) dodecanethiol-capped AuNPs, (b) oleylamine-capped Fe/Fe₃O₄ and (c) oleic acid-capped CoO nanoparticles. (d) Histograms of Young's modulus indicates median value of 6 Gpa, 1 Gpa and 14 Gpa for those nanomembranes, respectively. Reproduced with permission from Ref.[5, 87] © (2007) NPG and (2010) Wiley-VCH. 56

Figure 2.8 | Free-standing 1D & 2D nanoparticle superlattices. (a) Optical micrograph and (b) TEM image of zigzag-type 1D assemblies formed between neighboring superhydrophobic micropillars. (c) magnified TEM images show tunable width of linear assembly by changing GNP/calcein ratio. (d) Scheme shows nitrogen-assistant method for transferring 2D free-standing superlattice membrane from copper grid (inset image) onto (e) SiO₂/Si substrate. (f) magnified TEM image of red area in (e). Reproduced with permission from Ref. [90] [11] © (2013&2011) Wiley-VCH. 58

Figure 2.9 | TEM images of binary superlattice membrane composed by different-sized nanoparticles. (a) Ordered binary array with $R_B/R_A \approx 0.58$. (b) size-segregated array with $R_B/R_A \approx 0.47$. (c) Random distributed array with $R_B/R_A > 0.85$. TEM images of superlattice co-assembled by AuNPs/AuNRs with anisotropic gold nanowires. SEM and TEM images of (e) AuNPs and (f) AuNRs embedded in AuNWs. (g, h) Scheme and TEM image of AIB2-type BNSL membrane constructed by 15nm Fe₃O₄ and 6nm FePt nanoparticles. (i) TEM image of quasicrystalline superlattice assembled by 13.4nm Fe₂O₃ and 5nm AuNPs. Figure reproduced with permission from Ref.[2, 17, 49] © (1998&2010) NPG, (2010) Wiley-VCH. 59

Figure 2.10 | Plasmonic nanostructures derived from mono-DNA and site-specific DNA conjugates. (a) Schematic and TEM images for 10 nm AuNPs homodimer and 5/10/10 nm AuNPs heterotrimer constructed from mono-DNA conjugates. (b) Chiral nanostructures built by using DNA-AuNPs monoconjugates with four different sizes at DNA pyramids tips. (c) Dendrimer-like nanostructures formed by asymmetric functionalized AuNPs. (d) End, side, and satellite nanostructures formed by AuNPs and Au nanorods after selective modification using DNA. (e) Stepwise surface modification of AuNPs and formation of two-faced cluster with anisotropic nanostructures..... 65

Figure 2.11 | (a) DNA-functionalized AuNPs can be assembled into different crystallographic lattice structures programmed by the sequence of the DNA linkers. (b) Schematic of hexagonal superlattice of standing AuNRs with corresponding TEM images. (c) Scheme illustration of using 3D hollow DNA spacers in AuNP crystallization. TEM images of a bcc lattice (left) formed from AuNPs (20 nm) and DNA spacer (10 nm), and 'Lattice X' (right) structure formed from AuNPs (10 nm) and DNA spacer (20 nm). (d) Controllable switching of

interparticle distances by using a reconfigurable DNA device (l_d) that acts as an interparticle linkage. After addition of set DNA strands (s_1, s_2), l_d structure can be reversibly transformed from a flexible C configuration to stem loop R_S and linear R_L morphologies..... 67

Figure 2.12 | (a) Slow-cooling method shows crystallization of DNA-AuNPs. (b-c) SEM images of rhombic dodecahedron microcrystal. Scale bars are 2 μm and 1 μm . (d) Design of DNA linkers for AuNPs-AgNPs binary superlattice. (e-f) STEM images and EDX elemental maps of AB- and AB₂-type lattices. (g) DNA-functionalized nanoparticles/nanoshells into heteropentamer clusters (pentamers), which consist of a smaller gold nanosphere (74 nm) surrounded by a ring of four larger nanoshells ($[r_1, r_2] = [62.5, 92.5]$ nm). (h) Schematic illustration of RCA on DNA-AuNPs that served as a scaffold for the formation of satellite 3D nanostructures. AFM image (right) showed superstructures constructed from 5 nm and 15 nm AuNPs (large bright spots)..... 71

Figure 2.13 | DNA-templated self-assembly constructed by using DNA tiles and DNA origami. (a) DNA-functionalized AuNPs were organized into closely packed rows with precisely defined regular inter-row spacings templated by the DNA scaffolding. (b) 3D plasmonic tubular spirals of AuNPs using DNA tile-mediated self-assembly. (c) Encapsulated ‘nanopeapod’ AuNPs 1D chains using triangular DNA nanotubes with longitudinal variation as host. TEM image (right side) shows that encapsulated AuNPs could be spontaneously released from the nanotubes by simple addition of specific DNA strands. (d) Six-nanoparticle self-similar chain nanostructures using triangular DNA-origami templates. (e) DNA origami-templated AuNRs dimer that forming with various predetermined inter-rod angles. 73

Figure 2.14 | DNA as entropic ligands in drying-mediated self-assembly. (a) Free-standing monolayered DNA-AuNPs superlattice sheets. 3D STEM tomography reconstruction of a folded sheet (left) and TEM image (right) showing hexagonal ordering. (b) drying-mediated deformation of DNA corona in 3D supercrystals.. 76

Figure 2.15 | Top-down lithography integrates with bottom-up DNA-programmed self-assembly. (a) Cross-sectional scheme of a microdroplet confined in a micromould showing centre dewetting. Localized assembly of the AuNPs microdiscs was then achieved by DNA-programmed crystallization. (b) SEM image of nanoparticle disks pattern with highly ordered internal structures. (c) Large-area patterning of AuNPs (5 nm) onto spatially ordered, 2D arrays through the site-selective deposition of triangular DNA origami onto lithographically patterned substrates. 78

Figure 2.16 | (a) Vertically aligned CdSe nanorods in PMMA matrix under the combined guidance of external electric field. (b) Formation of nanoparticle chains in PS-*b*-PMMA copolymer domains. (c) Ordered lamellar structure formed by AuNPs at the interfaces of PS-*b*-P2VP block copolymer. (d~f) Lamellar and

cylindrical nanostructures of ordered CdSe nanorods formed in PS-*b*-P4VP domains. Figure reproduced with permission from Ref.[54, 149-151] © (2006) ACS, (2001) NPG,(2007) ACS, and (2011) ACS..... 81

Figure 2.17 | (a) Aggregation induced dimers of AuNPs and simultaneously encapsulated by PS₁₅₄-*b*-PAA₆₀. (b) Etching agent induced dimerization with the assistance of PVP. Ag nanocubes were acting as precursor and etched into Ag nanospheres. Reproduced with permission from Ref.[155, 157] © (2008) ACS, (2010) Wiley-VCH. 83

Figure 2.18 | (a) Schematic illustration of the synthesis of PEG/PMMA-capped AuNPs. It was achieved by sequentially combined “grafting to” (conjugation of PEG and ATRP initiator to particle surface) and “grafting from” (surface-initiated polymerization). Monolayer was formed at oil/water interface. (b) Free-standing superlattice membrane with area of 1 cm². TEM image shows ordered array of AuNPs. Reproduced with permission from Ref. [12, 160] © (2008&2010) ACS. 85

Figure 2.19 | (a) Schematic illustration of Langmuir-Blodgett trough. (b-d) SEM images and inset optical images show tunable interparticle distances and plasmon responses of superlattice membrane formed by Ag cuboctahedra. Reproduced with permission from Ref. [13, 161]. © (2008) ACS and (2007) NPG..... 86

Figure 2.20 | (a) Optical image of sedimentation-driven assembly of Ag octahedron into 3D supercrystals at bottom of cuvette. Reflectance spectra collected at different height indicated structure difference. (b) Scheme shows the supercrystal formation. (c) SEM images and corresponding scheme of densest lattice packing of Ag cubes, truncated cubes and cuboctahedra. Reproduced with permission from Ref.[24, 162]. © (2008) ACS and (2011) NPG. 87

Figure 2.21 | (a-e) Nanostructures self-assembled by AuNRs with end-capped polystyrene and side-capped CTAB. SEM images show the structures of (a) rings, (b) chains, (c) bundled chains, (d) side-to-side bundles, (e) microspheres. (f) SEM image of AuNRs superlattice membrane. (g) High magnification images show vertically aligned monolayer (V-sheets) and horizontally aligned monolayer (H-sheets). Reproduced with permission from Ref.[8, 55]. © (2007) NPG, (2011) ACS..... 88

Chapter 3

Figure 3.1 | Histogram on diameter distribution of “bare” gold nanoparticles as determined by TEM. Curves in both plots represent Gaussian fits. 107

Figure 3.2 | UV-vis spectra of (a) 13 nm citrate-capped/ PS-capped AuNPs, and (b) 26 nm citrate-capped/ PS-capped AuNPs dispersed in THF. Insets are photographs of corresponding AuNPs. (c) Phase transfer process indicates successful ligand exchange from citrate into PS. 107

Figure 3.3 FT-IR spectra of 26 nm citrate-capped AuNPs, PS-capped AuNPs and thiolated-PS in two magnified spectral regions.	108
Figure 3.4 TGA curves of (a) 13nm PS-capped AuNPs and (b) 26nm PS-capped AuNPs. The weight ratio of Au/PS and corresponding calculation results have been summarized in Table 3.1.	109
Figure 3.5 Low-magnification images of free-standing superlattice sheets formed using 26.0 nm PS-capped AuNPs in 50×50 μm grids, which were acquired under (a) transmission and (b) reflection mode by microscope. (c) TEM image of a monolayer sheet self-assembled from 26.0 nm PS-capped AuNPs with a diameter of ~15 μm, crumpled area indicates the flexibility of the sheet, (d) Higher-magnification TEM image of (c) shows that nanoparticles are hexagonally-packed yet well spaced.	110
Figure 3.6 TEM characterization of free-standing nanoparticle superlattice sheets formed using (a~d) 26 nm and (e, f) 13 nm PS-capped AuNPs on a random hollow lacey-carbon grid. In (e, f), the lacey carbon substrate resulted in the crumpled area on the membrane, the membrane still maintained its shape and demonstrates the flexibility of the sheets.	111
Figure 3.7 SEM characterization of nanoparticle superlattice sheets formed using 26 nm PS-capped AuNPs transferred onto a silicon nitrate wafer. (d) One sheet was cut by using a focused ion beam, which demonstrated a facile way to pattern the monolayer arrays into desired shapes.	112
Figure 3.8 TEM characterization of different superlattice sheets formed using (a) 13.1 nm and (b) 26.0 nm PS-capped AuNPs, (c) and (d) are corresponding histograms of interparticle distance analyzed from TEM images. Curves in both plots represent Gaussian fits.	113
Figure 3.9 Representative AFM height image and the corresponding cross section profile for monolayer superlattice sheets constructed from 26 nm PS-capped AuNPs. The measurements were repeated ten times, and the average height is 32.1 ± 2.3 nm.	114
Figure 3.10 The integrated and extracted structure factors $S(q)$ from SAXS patterns (insets) of drop-casted films constructed by PS-capped AuNPs. Dashed line at bottom suggests the theoretical peak positions for f.c.c. arrangement.	115
Figure 3.11 UV-vis spectra of AuNPs dispersed in water and superlattice sheets constructed from (a) 13.1 nm PS-capped AuNPs and (b) 26.0 nm PS-capped AuNPs.	116

Chapter 4

Figure 4.1 | Large-scale synthesis of ultrathin single crystalline AuNWs with high-aspect ratio. (a) and (b) Photographs of the synthesis of ultrathin AuNWs at the initial and final state of reaction. (c) Schematic illustration for the oleylamine-capped AuNWs. (d) High resolution TEM image of an individual single crystalline ultrathin AuNW shows [111] lattice planes. (e) TEM image of aligned AuNWs assemblies. (f) TEM image of AuNWs bundles. (g) SEM image of AuNWs bundles. 126

Figure 4.2 | TGA curve of OA-capped AuNWs. The calculated weight ratio of OA/AuNWs is 18%/ 82%. The turning point at 348 °C is corresponding to the boiling point of oleylamine. 127

Figure 4.3 | Typical π -A isotherm of the AuNWs superlattice nanomembrane during LB compression obtained at the air/liquid interface at 25 °C. The AuNWs superlattice nanomembrane undergoes four transition stages as surface pressure is increased, indicated by a change in the isotherm slope. 128

Figure 4.4 | Fabrication of monolayered AuNWs superlattice nanomembrane. (a) Photograph of a homogeneous nanomembrane with an area of 35 cm² on the LB trough. (b) Photograph of a membrane transferred onto a glass slide. (c) Photographs of sessile water droplets on glass and on membrane. (d) AFM height image of the superlattice nanomembrane transferred onto silicon wafer. (e) AFM cross-sectional height plot corresponding to the dashed line in (d). (f) and (g) TEM images of monolayer superlattice nanomembranes collected at surface pressure of 20 mN m⁻¹ and 30 mN m⁻¹, respectively. 129

Figure 4.5 | (a) Photograph shows that monolayer AuNWs superlattice nanomembrane was entirely transferred onto PDMS (3cm×3cm). The printed words are clearly visible, indicating the high optical transparency of monolayer nanomembrane. (b) The nanomembrane could withstand repeated bending without deterioration or rupturing. 130

Figure 4.6 | Process of substrate-to-substrate transfer process from PDMS to PET surface. Note that the transfer is 100% fidelity. 130

Figure 4.7 | (a) and (b) TEM images of AuNWs superlattice nanomembrane after transferred to holey carbon film at high surface pressure of 40 mN m⁻¹, which exhibited tight packed arrays with periodic wrinkling folds in the membrane. Panel (b) shows the magnified parts of the membrane (red dash) in panel (a). (c) is the magnified TEM image of yellow dashed part in (b), indicating the arc structure of monolayer and reflects the flexibility of ultrathin AuNWs. (d) TEM image shows a nanomesh-like morphology of two layers of AuNWs superlattice nanomembrane. This is formed by first transferring one layer of membrane onto carbon film, followed by transferring the second layer after turning 90° of carbon film during deposition. 131

- Figure 4.8 | TEM images of the free-standing AuNWs superlattice nanomembrane formed by transferring onto a holey silicon nitride substrate with 2 μ m-diameter holes. (a) The monolayer superlattice nanomembranes were stretched themselves across over the substrate with the holes without deterioration. (b) Magnified TEM image of an intact monolayered superlattice nanomembrane in (a), indicating an ordered array of AuNWs. These free-standing AuNWs membranes were further indented by AFM for characterization of mechanical properties..... 132
- Figure 4.9 | Mechanical properties of monolayered superlattice nanomembranes. (a) Force-displacement curves from AFM indentation (circle) and from theoretical fitting (line). Fracture load is indicated by a \times mark. (b) Histogram of 2D elastic modulus, E^{2D} . (c) Histogram of membrane pretention, σ^{2D} . d) AFM height image of superlattice nanomembrane cover over a 2- μ m-diameter microhole in the silicon nitride substrate before indentation. (e) AFM height image of a ruptured nanomembrane. (f) corresponding TEM image of the same ruptured nanomembrane in (e). Note that triangle hole in (e) becomes v-shaped hole in (f), which indicates that the “triangular tongue-like membrane” yielded in AFM imaging but recovered back in TEM imaging. This result echoes the strong mechanical properties as revealed in (a)..... 133
- Figure 4.10 | (a) AFM height image of AuNWs superlattice nanomembrane after two times indentation and allowed for multiple ruptures within the same membrane. (b) Corresponding TEM image of double poking. The degradation of AuNWs was observed in TEM image in (b) upon long exposure to the high-energy electron beam..... 134
- Figure 4.11 | (a) Typical force-displacement curve of AuNWs superlattice nanomembrane in Fig. 3a. Black represents the indent cycle and red represents the retract cycle. The tip experienced a strong attractive force that caused a jump into contact with sample surface. On the retract cycle the tip jumps out of contact just as the retraction force overcomes adhesion and then pulled off. (b) Statistical distribution of force-displacement curves of ten indents from different membranes in Fig. 4.8. 135
- Figure 4.12 | High optical transparency of monolayered AuNWs superlattice nanomembrane. (a) photograph of a PET plastic sheet partially covered with superlattice nanomembrane. (b) a paper sheet coated with nanomembrane on both sides. (c) experimental (black) and theoretical (red) transmittance spectra of monolayered superlattice nanomembrane on a glass slide. Approximate agreement in experiment and theoretical calculation proves that nanomembranes are composed of predominantly a single nanowire layer..... 137
- Figure 4.13 | Theoretical calculation on transmittance spectra of monolayer superlattice nanomembranes composed by AuNWs with different diameters..... 138

Figure 4.14 | (a) Optical transmittance spectra of monolayer and multilayer AuNWs superlattice nanomembranes. Insets show images of different layers of AuNWs nanomembranes transferred onto the PDMS substrate, and the words printed on bottom paper help visualize the transparency. (b) Transmittance ($\lambda = 800$ nm) as a function of sheet resistance. Data of both nanomembranes (experimental, blue squares) and perfect grating (modeled, red triangle) are shown. Solid and dashed curves predict the transmittance-sheet resistance relationship of nanomembranes and gratings (shown in inset scheme), respectively. 140

Figure 4.15 | Sheet resistance as a function of bending cycles for one- and eight-layer of AuNWs nanomembranes. 141

Figure 4.16 | (a), Schematic illustration of nanomembrane-based supercapacitor device. (b) Cyclic voltammograms of supercapacitor in Li_2SO_4 at different scan rates. (c) Charge-discharge curves at various current density. (d) Nyquist plot (a plot of the imaginary component, Z' , versus the real component, Z'' of the impedance) for the supercapacitor. (e) Electrocatalysis of AuNWs superlattice nanomembrane towards oxygen reduction reaction in 0.1 M PBS (pH = 7.2) solution at room temperature (sweep rate 50 mV s^{-1}). 142

Figure 4.17 | Specific capacitance (C_s) *versus* discharge current density plots..... 143

Chapter 5

Figure 5.1 | Synthesis and characterization of monodisperse Au@Ag NBs with finely-tunable thickness. (a) Schematic illustration of growth process from Au nanorods to Au@Ag NBs. (b) TEM images of Au nanorods, and Au@Ag NBs with increasing Ag thickness. The inset shows the photographs of solution products with distinct colors. (c) Extinction spectral development of Au@Ag NBs as Ag shell thickness increased. 157

Figure 5.2 | (a) Calculated extinction spectrum of Au@Ag NB. (b) Calculation of near-field intensity distribution to evaluate electric field distribution of a single NB, when incident light is polarized along the transverse edge (TE) and longitudinal edge (LE) (as shown in inset schemes). The peaks I, II, III are excited under the TE polarization, and the peak IV is excited along the LE polarization. E-field distribution contours of Au@Ag NBs show the origin of the four plasmon resonance peaks. Moreover, the intensity of electric field in each case also predicts the relative strengths of the peaks in the extinction spectrum. 158

Figure 5.3 | (a, b) Schematic of fabrication process of PS-capped NB by ligand exchange (c) The experimental extinction spectra of CTAC-capped NBs in water and PS-capped NBs in chloroform; (d) Calculated extinction spectra of NBs dispersed in water ($n=1.33$) and chloroform ($n=1.45$) using DDA method; All the

calculated spectra are normalized by their peak values. The capping ligands were not included in the simulation model since they had negligible influences on the overall extinction spectra. 159

Figure 5.4 | Fabrication of giant NB superlattice sheet. (a-c), Schematic of fabrication process in conjunction with drying-mediated self-assembly. (d-f), Characterization of giant NB superlattice sheet at the macro-, micro- and nano-scale by optical microscope, SEM and TEM, respectively..... 161

Figure 5.5 | SEM and TEM images of a typical millimeter-scale giant superlattice sheet at various magnifications. (a) SEM image showed the giant superlattice sheet covering almost the entire copper grid. The red arrows indicate the crumpled sheet with ridge-like morphology, demonstrating the high flexibility and robustness. (b) Higher-magnification SEM image of the region in (a). (c), (d) TEM images of the NB superlattice sheet show the high homogeneity in surface structures and ordered packing..... 162

Figure 5.6 | (a) TEM image of NB superlattice sheet. (b) 2D orientational-order parameter S_{2D} plotted as a function of the radius (r) of the analyzed region, which is marked as yellow dashed circles in panels (a). The representative three circles have a radius of 1,200 nm which were selected for calculating the S_{2D} 162

Figure 5.7 | TEM images of self-assembled Au@Ag NBs with long and short PS ligands. (a) TEM images show that the superlattice sheet is continuous in structures with uniform interparticle separations by using long PS ligand ($M_n = 50,000 \text{ g mol}^{-1}$). (b) Disordered, multi-stacked and closely-packed assembly structures by using shorter PS ligand ($M_n = 12,000 \text{ g mol}^{-1}$). 163

Figure 5.8 | TEM images of the giant NB superlattice sheet formed on (a) copper grid with square holes ($7 \mu\text{m} \times 7 \mu\text{m}$) and (b) holey silicon nitride substrate with $2 \mu\text{m}$ -diameter holes. In both cases, the superlattice sheets were stretched themselves across over the substrate with the holes without deterioration. The sheet in (b) was further indented by AFM for characterization of mechanical properties..... 164

Figure 5.9 | (a) Schematic illustration of PDMS-assisted transfer process. The back side of a holey copper grid with a giant superlattice sheet on the front side was brought into contact with a PDMS elastomer with a moderate pressure applied to ensure the intimate contact (step 1). After peeling off the copper grid, the superlattice sheets were transferred onto PDMS with square-shaped patterns (step 2). The square superlattice sheets could be further stamped onto other substrates such as silicon (step 3). (b) AFM height image of NB superlattice sheets transferred to Si wafer. (c) AFM cross-sectional height plot corresponding to the dashed line in (b), showing an average thickness of $56 \pm 2 \text{ nm}$ 165

Figure 5.11 | (a) A typical force-displacement curve from AFM indentation (black) and from theoretical fitting (red) for NB superlattice sheet. (b) TEM image of

superlattice sheet cover over a 2- μm -diameter microhole in the silicon nitride substrate after indentation. The inset arrows show the local rips of ruptured sheets.

..... 167

Figure 5.12 | Schematic illustration of three building blocks. 167

Figure 5.13 | Statistical analysis showing distribution of side-by-side (l_{ss}) and end-to-end (l_{ee}) spacing in NB superlattice sheets measured from TEM images. Red curves represent the Gaussian fits to the distributions. 169

Figure 5.14 | Superlattice sheets from three different building blocks. (a-c), Experimental and simulated extinction spectra of NB-superlattice sheets. Insets are the optical microscope images and TEM images of individual sheets. Scale bar is 100 nm for all TEM images. 170

Figure 5.15 | SERS enhancement factors obtained on NB-superlattice sheets under various excitation wavelengths. 171

Figure 5.16 | Extinction spectra of NB superlattice sheets simulated based on DDA method. The spectra were calculated using mean values of the interparticle spacing parameters (l_{ee} and l_{ss}) shows in Fig. 5.13. The dashed vertical lines show the wavelengths of excitation laser used in Raman spectroscopy, *i.e.*, 514, 633, and 782 nm. 172

Figure 5.17 | Calculated near-field distributions on m-NB-superlattice sheet ($l_{ee} = 3$ nm, $l_{ss} = 4$ nm) under three excitation wavelengths of 514 nm, 633 nm, and 782 nm. The distribution was calculated across the plane passing through nanoparticle centres. 172

Figure 5.18 | (a) SERS spectra for NB superlattice sheet with incident laser wavelength of 633 nm. (b) Simulated E-field intensity distribution on for s-NB, m-NB, l-NB superlattice sheets at 633 nm. The simulated E-field distribution in (b) show relevant intensities of hotspots generated in NB superlattice sheets, which is consistent with the Raman scattering intensities shown in (a). 173

Figure 5.19 | (a) Schematic illustration of transferring superlattice sheets onto Si wafer, which can be readily used as SERS substrate. (b) Scheme shows the setup of Raman spectrometer. 174

Figure 5.20 | (a) Superimposed SERS spectra obtained from 20 different spots on NB-superlattice sheets under the laser excitation wavelength of 633 nm. (b) Histogram of SERS enhancement factors on NB-superlattice sheets. 175

Figure 5.21 | NB superlattice sheets as universal SERS substrates for chemical identification of analytes in liquid, in air. (a) SERS spectra acquired from 4-ATP ethanol solutions. (b) SERS spectra from airborne 4-ATP at different exposure times. Inset illustrates permeation of 4-ATP molecules through and their binding onto suspended superlattice sheets. 176

Figure 5.22 | (a) Raman spectra for airborne detection of 4-ATP at various exposure times. (b) The peak intensity at 1078 cm^{-1} of vibrational band was plotted as a function of exposure time of free-standing superlattice sheets to the 4-ATP vapor.
..... 177

This page is intentionally blank

LIST OF TABLES

Chapter 2

Table 2.1 | Summary on methodologies for constructing DNA-based nanostructures.. 62

Chapter 3

Table 3.1 | Analytical characteristics of PS-capped AuNPs and superlattice sheets ... 109

Chapter 5

Table 5.1 | Dimension of synthesized Au@Ag NBs..... 168

Table 5.2 | Raman spectral peak assignment for 4-ATP adsorbed on superlattice sheet
..... 174

This page is intentionally blank

LIST OF ABBREVIATIONS

1D	One-dimensional
2D	Two-dimensional
3D	Three-dimensional
4-ATP	4-aminothiophenol
AFM	Atomic force microscope
AgNPs	Silver nanoparticles
Au@Ag	Gold core-silver shell
AuNPs	Gold nanoparticles
AuNRs	Gold nanorods
AuNWs	Gold nanowires
bcc	body-centered cubic
BNSL	Binary nanoparticle superlattice
CTAB	Cetyltrimethylammonium bromide
CTAC	Cetyltrimethylammonium chloride
CV	Cyclic voltammogram
DDA	Discrete dipole approximation
DEG	Diethylene glycol
DMAET	2-(Dimethylamino) ethanethiol
DNA	Deoxyribonucleic acid
EDX	Energy-dispersive X-ray spectroscopy
EF	Enhancement factor
fcc	face-centered cubic
FIB	Focused ion beam
FT-IR	Fourier transform infrared
hcp	Hexagonal close-packed
HPLC	high-performance liquid chromatography
LB	Langmuir-Blodgett

l-NB	large-nanobrick
LSPR	Localized surface plasmon resonance
m-NB	medium-nanobrick
NB	Nanobrick
NC	Nanocube
OA	Oleylamine
PAA	Poly(acrylic acid)
PBS	Phosphate buffered saline
PCR	Polymerase chain reaction
PDMS	Polydimethylsiloxane
PEG	Polyethylene glycol
PET	Polyethylene terephthalate
PMMA	Poly(methyl methacrylate)
PS	Polystyrene
PS-SH	Thiolated-polystyrene
PVP	Polyvinylpyrrolidone
RCA	Rolling circle amplification
SAXS	Small-angle X-ray scattering
SEM	Scanning electron microscope
SERS	Surface-enhanced Raman spectroscopy
s-NB	small-nanobrick
ss/ds-DNA	Single strand/double strand-DNA
STEM	Scanning transmission electron microscope
TEM	Transmission electron microscope
TGA	Thermogravimetric analysis
THF	Tetrahydrofuran
TUC	Target unit cell
UV-vis	Ultraviolet–visible
vdW	Van der Waals

LIST OF NOMENCLATURE

cm	centimeter
°C	degree Celsius
μL	microlitre
μm	micrometer
μM	micromolar
A	ampere
A_{laser}	area of the focal laser spot
A_{N}	nanoparticle surface area
C	capacitance
C_{s}	specific capacitance
E	Young's modulus
F	farad
g	gravitational constant
h	thickness of membrane
I	current
I_{BULK}	peak intensity of bulk material
I_{SERS}	peak intensity for SERS
kg	kilogram
kW	kilowatt
l_{e}	end thickness
l_{ee}	end-to-end distance
l_{s}	side thickness
l_{ss}	side-by-side distance
M	molar
mg	milligram
mL	millilitre
mm	millimeter
mM	millimolar

M_n	number average molecular weight
mN	millinewton
M_w	molecular weight
N_d	number density of particles per unit area
nm	nanometer
P	power density
Pa	pascal

Chapter 1

Introduction

This page is intentionally blank

Plasmonic superlattice nanomembrane is a conceptually new class of two-dimensional thinnest possible metamaterials [1-14]. It consists of self-assembled metallic nanocrystals with highly ordered nanoscopic structures and programmable multifunctionality. Remarkably, such nanomembranes integrate both striking mechanical robustness and tailorable plasmonics into one customizable system. Unlike conventional biomimetic or polymeric membranes, their functionality can be precisely programmed by adjusting the morphology and composition of constituent nanoparticles, varying types or lengths of soft ligands, and engineering packing order of lattice structures. Hence, the ability to build plasmonic superlattice nanomembrane of macroscopic surfaces but nanoscale thicknesses is crucial for understanding the unparalleled optical signature of 2D plasmonics,[3, 8, 13, 15] and is of great practical significance for bottom-up plasmonic devices and circuits with implications in many important research disciplines[16].

As the basic constituent elements for the superlattice nanomembrane, metallic nanocrystals possess of unparalleled optical signature originating from composition, specific size and morphology [17, 18]. To date, a wide range of plasmon-active nanocrystals have been synthesized by well-developed procedures, allowing them to serve as “meta-atoms” from the “plasmonic periodic table”[14]. The following challenge, then, lies on rationally group these artificial atoms into well-defined plasmonic superlattices with unique optical property.

Theoretically, plasmon hybridization theory predicts the possibility to virtually design such 2D superlattice nanomembranes with any desired plasmonic properties by adjusting sizes, shapes and lattice structures of constituent nanoparticles[19, 20]. In practice, nevertheless, it has been notoriously challenging to manipulate at will large-scale, ordered assembly of these “meta-atoms”, despite initial success in growing nanoparticle superlattices[1-3, 5, 7, 13, 15, 21-31]. Substantial efforts have been made in precisely regulating the distinct pairwise interactions during the nanoparticle self-assembly by soft ligands such as short-chain molecules, DNA, and polymer (as reviewed in Chapter 2). However, their practical applications are often hampered by the

difficulty in fabricating defect-free superlattice membranes with nanometers thickness but with macroscopic lateral dimensions, which are apparently conflicting characteristics difficult to achieve simultaneously.

To essentially tackle those challenges, the following design principles and assembly rules have mapped out the research focus and requirements: (1) high monodispersity of constituent nanoparticles with strong surface plasmon resonance properties; (2) effective soft ligand capping to precisely control over complex interactions/forces at different spatial and temporal scales; (3) strict 1D physical confinement for 2D growth of superlattices; (4) free-standing, isolated forms in their final stage of growth for facile transfer and post-manipulation. Unless those requirements have been simultaneously realized, well-defined plasmonic superlattice nanomembrane with arbitrary design will not be realized.

With those in mind, this thesis addresses those challenges, particularly, presenting the following original concepts and efficient methods: (1) successful synthesis of high-quality monodispersed plasmonic nanocrystals with precisely designed SPR signatures, including gold nanospheres, ultrathin single-crystalline gold nanowires (AuNWs), bimetallic Au@Ag core-shell nanobricks (NB); (2) a general methodology to use polymer-capped nanocrystals with densely capping density for drying-mediated self-assembly at the air-liquid interface; (3) simple yet efficient method to fabricate giant superlattice nanomembranes of nanometer-scale thickness but macroscopic lateral dimensions, which representing the thinnest version of metallic membranes; (4) facile PDMS-assisted technique to transfer free-standing superlattice membranes onto arbitrary substrates for device construction; (5) multifunctional superlattice nanomembranes with customizable plasmonic responses (Chapter 3), conductivity and mechanically strong (Chapter 4), programmable near-field confinement and hotspots distribution (Chapter 5).

In the subsequent Chapter 2, an elaborate literature review has been presented to outline the building of nanoparticle superlattice using soft ligands. Based on

perspective of materials design, various pioneering and ongoing research on nanoparticle superlattice are included, including molecule-based, DNA-based, and polymer-based superlattices. Under the inspiration of those pioneering research, Chapter 3 describes a generic polymer-ligand-based approach to fabricate free-standing, monolayered nanoparticle superlattice sheets. In the following Chapter 4, building block has been extended to anisotropic ultrathin AuNWs, and presents giant AuNWs superlattice nanomembrane with high transparency, mechanical strength and conductivity. Remarkably, Chapter 5 further extended the polymer-based assembly technique, and shows giant superlattice membrane with customizable hybridized plasmon modes and near-field distributions. Coupled with accurate discrete-dipole-approximation (DDA) simulations, the plasmonic property can be predicted a priori. Beyond structural and functional programmability, the giant NB superlattice sheet is homogeneous in structure, vapor-permeable and mechanically flexible, enabling their uses as universal and unique SERS substrates with highly uniform Raman hotspot distributions across large area, for rapid and sensitive detection of chemical species in both air and liquid.

Finally, this thesis envisions the future work and challenges for engineering superlattice nanomembrane, including large-scale growth combined with post-manipulation, multi-component superlattice membrane, *etc.* The ease of self-assembly manufacture, highly customizable plasmonics and superior SERS enhancements, as well as the potential integration with other nanomaterials, makes superlattice nanomembrane a unique material base for the next-generation of nanophotonic devices and smart sensors.

References

1. Whetten, R.L., Khoury, J.T., Alvarez, M.M., Murthy, S., Vezmar, I. *et al.* Nanocrystal gold molecules. *Adv. Mater.* **8**, 428-433 (1996).
2. Collier, C.P., Saykally, R.J., Shiang, J.J., Henrichs, S.E. and Heath, J.R. Reversible tuning of silver quantum dot monolayers through the metal-insulator transition. *Science* **277**, 1978-1981 (1997).
3. Cheng, W.L., Campolongo, M.J., Cha, J.J., Tan, S.J., Umbach, C.C., Muller, D.A. and Luo, D. Free-standing nanoparticle superlattice sheets controlled by DNA. *Nature Mater.* **8**, 519-525 (2009).

4. Cheng, W.L., Campolongo, M.J., Tan, S.J. and Luo, D. Freestanding ultrathin nano-membranes via self-assembly. *Nano Today* **4**, 482-493 (2009).
5. Dong, A.G., Chen, J., Vora, P.M., Kikkawa, J.M. and Murray, C.B. Binary nanocrystal superlattice membranes self-assembled at the liquid-air interface. *Nature* **466**, 474-477 (2010).
6. Dong, A.G., Ye, X.C., Chen, J. and Murray, C.B. Two-Dimensional Binary and Ternary Nanocrystal Superlattices: The Case of Monolayers and Bilayers. *Nano Lett.* **11**, 1804-1809 (2011).
7. Mueggenburg, K.E., Lin, X.M., Goldsmith, R.H. and Jaeger, H.M. Elastic membranes of close-packed nanoparticle arrays. *Nature Mater.* **6**, 656-660 (2007).
8. Ng, K.C., Udagedara, I.B., Rukhlenko, I.D., Chen, Y., Tang, Y., Premaratne, M. and Cheng, W.L. Free-Standing Plasmonic-Nanorod Superlattice Sheets. *ACS Nano* **6**, 925-934 (2011).
9. Bigioni, T.P., Lin, X.M., Nguyen, T.T., Corwin, E.I., Witten, T.A. and Jaeger, H.M. Kinetically driven self assembly of highly ordered nanoparticle monolayers. *Nature Mater.* **5**, 265-270 (2006).
10. He, J., Lin, X.-M., Chan, H., Vuković, L., Král, P. and Jaeger, H.M. Diffusion and Filtration Properties of Self-Assembled Gold Nanocrystal Membranes. *Nano Lett.* **11**, 2430-2435 (2011).
11. Liao, J.H., Zhou, Y.Z., Huang, C.L., Wang, Y. and Peng, L.M. Fabrication, Transfer, and Transport Properties of Monolayered Freestanding Nanoparticle Sheets. *Small* **7**, 583-587 (2011).
12. Pang, J., Xiong, S., Jaeckel, F., Sun, Z., Dunphy, D. and Brinker, C.J. Free-Standing, Patternable Nanoparticle/Polymer Monolayer Arrays Formed by Evaporation Induced Self-Assembly at a Fluid Interface. *J. Am. Chem. Soc* **130**, 3284-3285 (2008).
13. Tao, A., Sinsermsuksakul, P. and Yang, P. Tunable plasmonic lattices of silver nanocrystals. *Nature Nanotech.* **2**, 435-440 (2007).
14. Tan, S.J., Campolongo, M.J., Luo, D. and Cheng, W.L. Building plasmonic nanostructures with DNA. *Nature Nanotech.* **6**, 268-276 (2011).
15. Tang, Z., Zhang, Z., Wang, Y., Glotzer, S.C. and Kotov, N.A. Self-Assembly of CdTe Nanocrystals into Free-Floating Sheets. *Science* **314**, 274-278 (2006).
16. Talapin, D.V., Lee, J.-S., Kovalenko, M.V. and Shevchenko, E.V. Prospects of Colloidal Nanocrystals for Electronic and Optoelectronic Applications. *Chem. Rev.* **110**, 389-458 (2009).
17. Grzelczak, M., Perez-Juste, J., Mulvaney, P. and Liz-Marzan, L.M. Shape control in gold nanoparticle synthesis. *Chem. Soc. Rev.* **37**, 1783-1791 (2008).
18. Xia, Y., Xiong, Y., Lim, B. and Skrabalak, S.E. Shape-Controlled Synthesis of Metal Nanocrystals: Simple Chemistry Meets Complex Physics? *Angew. Chem. Int. Ed.* **48**, 60-103 (2009).
19. Halas, N.J., Lal, S., Chang, W.-S., Link, S. and Nordlander, P. Plasmons in Strongly Coupled Metallic Nanostructures. *Chem. Rev.* **111**, 3913-3961 (2011).
20. Prodan, E., Radloff, C., Halas, N.J. and Nordlander, P. A Hybridization Model for the Plasmon Response of Complex Nanostructures. *Science* **302**, 419-422 (2003).
21. Xiong, W., Sikdar, D., Walsh, M., Si, K.J., Tang, Y. *et al.* Single-crystal caged gold nanorods with tunable broadband plasmon resonances. *Chem. Commun.* **49**, 9630-9632 (2013).

22. Redl, F.X., Cho, K.S., Murray, C.B. and O'Brien, S. Three-dimensional binary superlattices of magnetic nanocrystals and semiconductor quantum dots. *Nature* **423**, 968-971 (2003).
23. Talapin, D.V., Shevchenko, E.V., Bodnarchuk, M.I., Ye, X., Chen, J. and Murray, C.B. Quasicrystalline order in self-assembled binary nanoparticle superlattices. *Nature* **461**, 964-967 (2009).
24. Kiely, C.J., Fink, J., Brust, M., Bethell, D. and Schiffrin, D.J. Spontaneous ordering of bimodal ensembles of nanoscopic gold clusters. *Nature* **396**, 444-446 (1998).
25. Courty, A., Mermet, A., Albouy, P.A., Duval, E. and Pileni, M.P. Vibrational coherence of self-organized silver nanocrystals in f.c.c. supra-crystals. *Nature Mater.* **4**, 395-398 (2005).
26. Henzie, J., Grünwald, M., Widmer-Cooper, A., Geissler, P.L. and Yang, P. Self-assembly of uniform polyhedral silver nanocrystals into densest packings and exotic superlattices. *Nature Mater.* **11**, 131-137 (2012).
27. Cheng, W.L., Hartman, M.R., Smilgies, D.-M., Long, R., Campolongo, M.J., Li, R., Sekar, K., Hui, C.-Y. and Luo, D. Probing in Real Time the Soft Crystallization of DNA-Capped Nanoparticles. *Angew. Chem. Int. Ed.* **49**, 380-384 (2010).
28. Park, S.Y., Lytton-Jean, A.K.R., Lee, B., Weigand, S., Schatz, G.C. and Mirkin, C.A. DNA-programmable nanoparticle crystallization. *Nature* **451**, 553-556 (2008).
29. Nykypanchuk, D., Maye, M.M., van der Lelie, D. and Gang, O. DNA-guided crystallization of colloidal nanoparticles. *Nature* **451**, 549-552 (2008).
30. Korgel, B.A. Nanocrystal Superlattices Assembly at Liquid Interfaces. *Nature Mater.* **9**, 701-703 (2010).
31. Auyeung, E., Cutler, J.I., Macfarlane, R.J., Jones, M.R., Wu, J., Liu, G., Zhang, K., Osberg, K.D. and Mirkin, C.A. Synthetically programmable nanoparticle superlattices using a hollow three-dimensional spacer approach. *Nature Nanotech.* **7**, 24-28 (2012).

This page is intentionally blank

Chapter 2

Literature Review

This page is intentionally blank

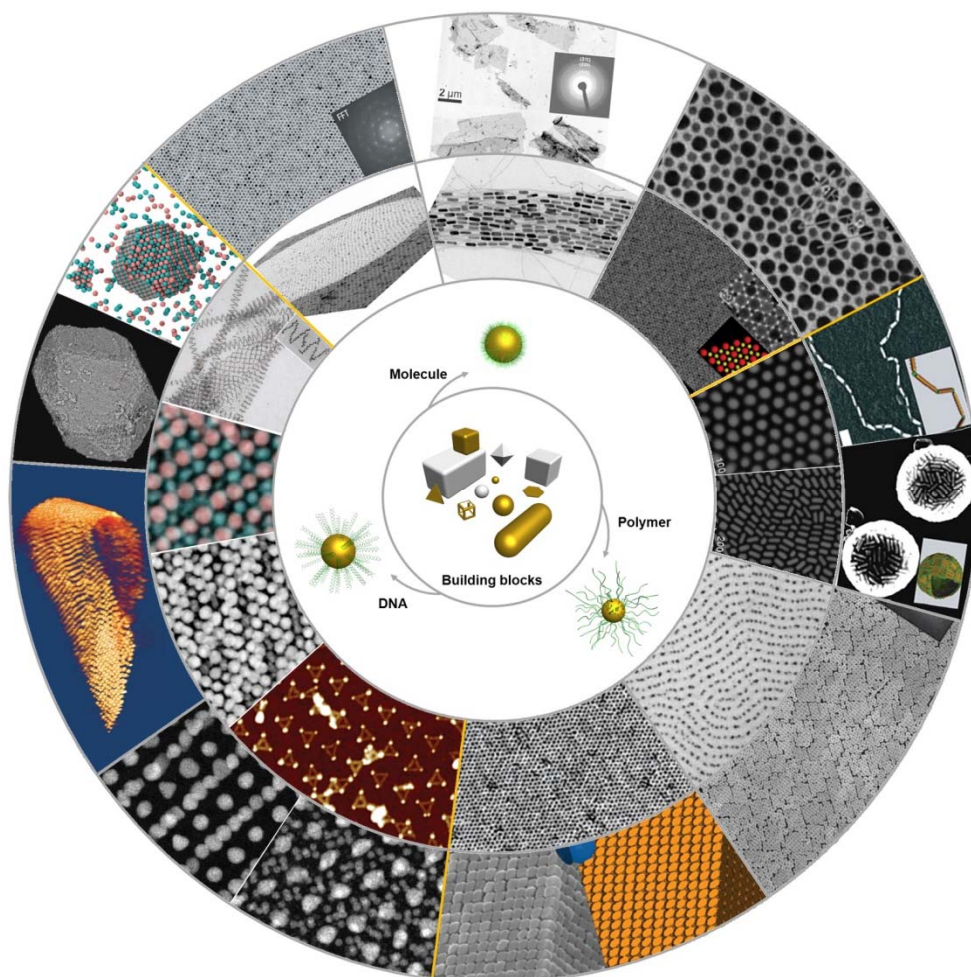
Nanoparticle superlattice refers to ordered array of elementary nanocrystals. It is an essential task in modern nanoscience and nanotechnology to rationally design and build such highly ordered structures with programmable multifunctions.[1-31] Substantial efforts have been made in the last two decades in developing synthetic approaches with wet chemical techniques, enabling a wide range of nanoparticles with controllable composition, geometry, and properties[32-37] (including semiconductor, magnetic, and plasmonic nanoparticles). The following challenge is to efficiently group these “artificial atoms” [4] into well-defined nanoarchitectures including “artificial molecules and polymers” [38-41], two-dimensional superlattice membranes[1, 2, 5], and “supracrystals”[23, 42-46]. Nevertheless, it is non-trivial to rationally group nanoparticles together due to complex nanoscale forces at different spatial and temporal scales. Numerous attempts have been made by using physical methods (optical, electrical, magnetic, mechanical), chemical methods (short-chain molecule, polymer), and biological approaches (peptide, protein, DNA)[47].

In this chapter, the assembly of nanoparticle superlattice is highlighted from a materials design perspective, namely, by categorizing the methodologies with soft ligands. It begins with the outline of key interparticle forces and general design principles that involved in superlattice construction. Then, various pioneering and ongoing research on nanoparticle superlattice are reviewed, including molecule-based, DNA-based, and polymer-based superlattices (**Scheme 2.1**).

2.1 General design principles for nanoparticle superlattice

Building nanoparticle superlattice with soft materials relies crucially on rational control over interparticle interactions at various magnitudes and length scales.[48] To unravel the nanoscale-characteristic interactions, it is required to understand and subsequently manipulate various nanoscale forces among building blocks, such as van der Waals attraction, magnetic/electrostatic interaction, steric repulsion, short-rang ligand interactions. Comprehensive consideration of those specific forces is needed for engineering nanoparticle assemblies into desired stable architectures with minimum thermodynamic potentials (Gibbs or Helmholtz free energies). In this section, the dominant nanoparticle interactions are summarized based on the view of ‘soft spheres’,

and then reviewed recent theoretical advances in modeling ligand deformation in soft crystallization and design rules for DNA-based superlattice.



Scheme 2.1 | Schematic summary of various nanoparticle superlattices assembled from libraries of soft-ligand capped nanocrystals using molecule-based, DNA-based and polymer-based methodologies. Figure reproduced with permission from Ref. [1, 2, 5, 8, 12-14, 17, 20, 22, 24, 49-55]. © (1998, 2001, 2006, 2007, 2009, 2010, 2012, 2013) NPG. (2006, 2009) AAAS. (2010, 2013) Wiley-VCH. (2008, 2011) ACS.

2.1.1 Nanoparticle interactions during assembly of ‘soft spheres’

Pioneering simulations have treated sterically stabilized nanoparticles as hard spheres that exhibiting an infinite repulsive force upon contact.[56, 57] The basic prerequisite from hard sphere model is that the free energy for phase transition depends on the entropy. However, the interaction potential in reality is actually contributed from the combination of vdW attractive forces between nanoparticle cores and steric repulsion of soft ligands.[58] Based on this perspective, ligand-capped nanoparticles behave more like ‘soft spheres’ during self-assembly,[59] in which the nanophysics for

interaction potential can be estimated as the combined contributions from vdW attraction potential (U_{vdW}) and steric repulsion potential (U_{steric}) (**Figure 2.1**),

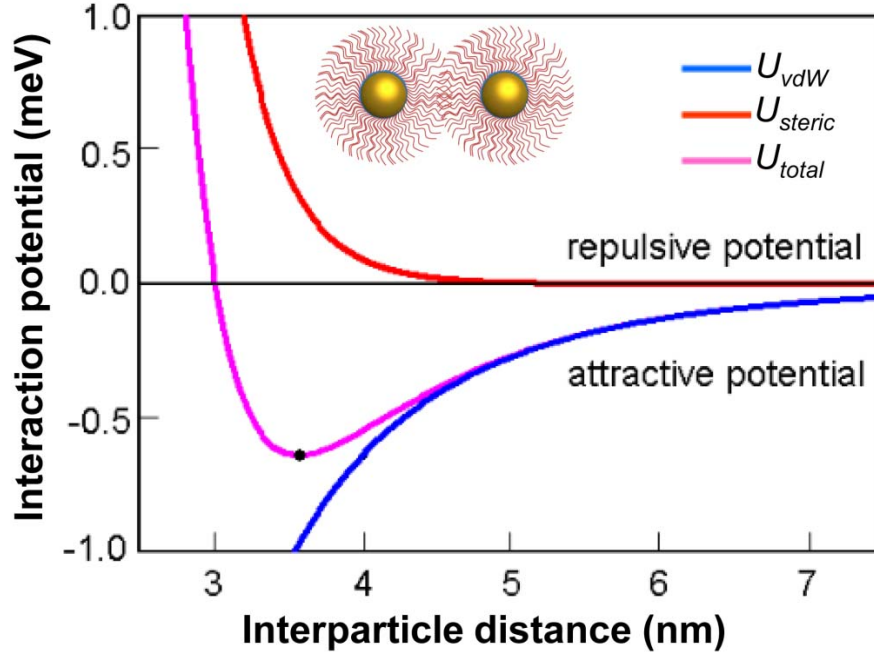


Figure 2.1 | Interparticle potential derived from vdW attraction potential (U_{vdW}) and steric repulsion potential (U_{steric}). The profile is outlined based on two oleic acid-capped Co nanoparticles with a diameter of 3.3 nm. Figure reproduced with permission from Ref.[60]. © (2010) Beilstein-Institut.

$$U_{total} = U_{vdW} + U_{steric} \quad \text{Equation (2.1)}$$

Using Hamaker's derivation,[61] the van der Waals interaction can be estimated between a pair of nanospheres with diameter (d_{core}) and nearest neighbor core-to-core distance (d_{NN}),

$$U_{vdW} = -\frac{A}{12} \left[\frac{d_{core}^2}{d_{NN}^2 - d_{core}^2} + \frac{d_{core}^2}{d_{NN}^2} + 2 \ln \left(\frac{d_{NN}^2 - d_{core}^2}{d_{NN}^2} \right) \right] \quad \text{Equation (2.2)}$$

where A is the Hamaker constant that depends on the polarizability of nanoparticle and surrounding medium. The steric repulsion derives from interactions of ligands with solvent as well as ligand-ligand interactions. In a good solvent, U_{steric} can be calculated by employing de Gennes' expression,[62]

$$U_{steric} = \frac{100Rh_0^2}{(d_{NN} - d_{core})\pi\sigma^3} k_B T \exp[-\pi(d_{NN} - d_{core})/h_0] \quad \text{Equation (2.3)}$$

where h_0 is the ligand brush thickness and σ is the diameter of the circular footprint occupied by a single ligand on the nanoparticle surface. Those theoretical equations indicate that the total interaction potential depends on the diameter and composition of nanoparticle, as well as the length and conformation of soft ligands. Besides the above ubiquitous forces, other interactions are also playing crucial roles in nanoparticle assembly and superlattice formation, such as electrostatic attraction/repulsion between surface-charged particles,[63, 64] permanent magnetic moments between semiconducting nanoparticles,[2, 65] Watson-Crick base-pairing interaction from DNA-capped nanoparticles,[4, 18, 27, 38, 66] *et al.* With those fundamental theories in mind, rational engineering of nanoparticle superlattice can be achieved by incorporating those nanoscopic forces in a predictable envision.

2.1.2 Modeling ligand deformation in soft crystallization

Unlike the conventional crystallization of hard spheres, the self-assembly of nanoparticle superlattice is a soft process, in which the organic corona will deform dynamically with transitionally scalable crystalline states. This dynamic soft crystallization has been demonstrated by using single strand (ss) DNA capped AuNPs as model system (**Figure 2.2a**).[23] To quantify the soft-crystallization process, two dimensionless parameters have been defined to evaluate the softness (χ) and deformation degree (λ) of ligand corona,

$$\chi = 2h_0/d_{core} \quad \text{Equation (2.4)}$$

$$\lambda = \frac{2h_0 - (d_{NN} - d_{core})}{2h_0 + d_{core}} \quad \text{Equation (2.5)}$$

Based on this definition, the typical softness of alkyl-capped nanoparticles is at the range of 0.3-0.8, whereas ssDNA-capped AuNPs indicates a softness of 0.6-5.1. By using polymer as soft ligands, much wider range of softness can be achieved. For example, polystyrene-capped AuNPs exhibit a larger softness ($\chi = 1.6-2.5$) compared with the traditional short-length ligands.[6] This will lead to a smooth and uniform

deformation of polymer-capped AuNPs during the soft-crystallization process and afford a large-scale self-assembly superlattice compared with short chain stabilized nanoparticles.

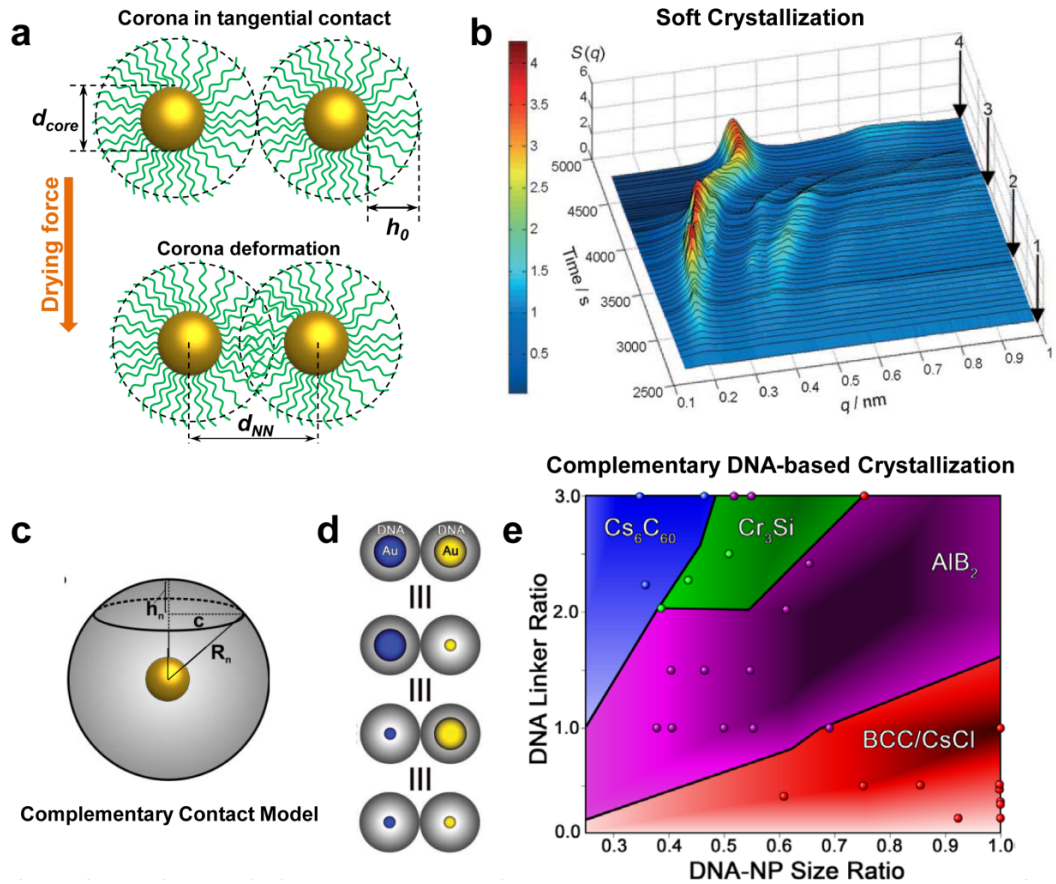


Figure 2.2 | (a) Scheme for the deformation of soft-corona nanoparticles in soft-crystallization. (b) Probing soft crystallization using in situ SAXS demonstrates the continuous deformation of corona. (c) Scheme of DNA-capped hydrodynamic nanoparticle in complementary contact model. The spherical cap represent overlapped portion of corona with adjacent nanoparticle. (d) Illustration of design rule (3) that nanoparticles with same hydrodynamic size form similar superlattice structure. (e) Phase diagram shows predictable superlattice structure by controlling core size and DNA ligand ratio. Each colored domain denotes the specific superlattice structure. The dots represent the superlattice obtain in experimental. Figures reproduced with permission from Ref. [23, 45]. (a, b) © (2010) Wiley-VCH. (c-e) © (2011) AAAS.

During the drying-mediated self-assembly process, the extended chains behave as molecular spring in accordance with an entropic spring model (ESM), which is derived based on the ideal polymer chains[67] and brush polymer theory.

$$\lambda = \frac{2fb^{4/3}}{3k_B T(\gamma\sigma)^{1/3}} \frac{\chi}{1+\chi}$$

Equation (2.6)

where b is the Kuhn length, k_B is the Boltzmann constant, T is temperature, γ is scaling constant (including excluded volume effects) and σ is the grafting density of ligand. Real time SAXS characterization reveals that the deformation parameter (λ) is solely dependent on the softness (χ) of building blocks under the same driving force (f), which matches well with the entropic spring model (**Figure 2.2b**). This model can be used as a generic expression to interpret soft corona deformation at the nanoscale, and as a guideline for conjugating various soft materials in superlattice formation. The soft-crystallization will definitely induce pathways to control interparticle interactions for applications in adaptive nanodevices.

2.1.3 Basic design rules for DNA-based crystallization

Predictable superlattice control has been established in crystallization of DNA-capped nanoparticles by using programmable DNA hybridization as the driving force.[44] By means of independently design nanoparticle size and DNA interconnect length, superlattices with different length scale and crystallographic symmetries can be intentionally achieved.[45] During the assembly of DNA-nanoparticles with complementary sticky ends, multiple interaction types are existed in the system, such as van der Waals, Watson-Crick base pairing forces, electrostatic repulsive forces from negatively charged DNA, *et al.* But in the real crystallization, the vdW and negative repulsion are negligible due to large distances between adjacent nanoparticles and high local salt concentration.[68] Hence, the DNA duplex formation can be taken into account as the dominant force for crystal stabilization. Based on this, a simplified complementary contact model (CCM) can be used to evaluate relative superlattice stabilities for DNA-based system.[45] In this model, complementary DNA sticky ends are assumed to physically contact with each other, and any contacted sticky ends will eventually form a DNA duplex. Also, DNA-nanoparticles are treated as ‘fuzzy spheres’ where the sticky ends are confined in a predictable region surrounding the nanoparticles (**Figure 2.2c**). The maximum radius (R_n) of DNA-nanoparticle in superlattice can be calculated as:

$$R_n = r_n + 0.34 \cdot x + 0.4 \quad \text{Equation (2.7)}$$

where r_n is the radius of nanoparticle n , x is number of DNA bases. If the overlapped portion of DNA corona with neighbor nanoparticles is considered as spherical caps, then the surface area (S_n) of adjacent fuzzy spheres is:

$$S_n = \pi(c^2 + h_n^2) \quad \text{Equation (2.8)}$$

where c and h_n represent the radius and height of the overlapped spherical cap. Then the number ($N_{duplex,n}$) of hybridized DNA strands on nanoparticle n can be calculated as:

$$N_{duplex,n} = S_n N_{neighbor,n} N_{DNA,n} N_{particle,n} / 4\pi R_n^2 \quad \text{Equation (2.9)}$$

where $N_{neighbor,n}$, $N_{DNA,n}$, $N_{particle,n}$ represent the number of neighboring particles, DNA capped to particle n , and n -type nanoparticles for a unit cell, respectively. By applying this model, a phase diagram has been simulated for predicting crystallographic structures as a function of nanoparticle size ratio and DNA ligand ratio (**Figure 2.2d and e**), which is demonstrated to be consistent with experimental lattices. Based on both theoretical modeling and through SAXS characterization, basic qualitative design principles have been outlined for rational engineering of DNA-nanoparticle based superlattices[44, 45]: (1) DNA-NPs (with equal R_n) will maximize the number of closest neighbors with which it can be hybridized; (2) slowing down the rate of DNA linker releasing and rehybridization would facilitate lattice growth and stabilize kinetic products; (3) the hydrodynamic size, instead of core size or DNA length, mainly determines the superlattice structure; (4) for binary components, the stabilized superlattice is mainly determined by the hydrodynamic size ratio and DNA ligand ratio between two building blocks; (5) by co-modification with different DNA complementary sequences, a nanoparticle with different linkers that contain different base sequences, multiple DNA interactions can create sophisticated and complex superlattices.

2.2 Molecule-based nanoparticle superlattice

Within this section, the review is mainly focused on the viable assembly approaches for fabrication of superlattices that formed by molecule-capped nanoparticles from the

view of methodological perspective. Here, the molecule refers to short-chain ligands that capped around nanoparticles, such as surfactants, alkylthiols. By utilising its conventional function, surfactant itself can be used to form dried foam films that assembled by two reversed Gibbs monolayers of surfactants.[69] This free-standing bilayer film that constructed by surfactants was used as sacrificial template for deposition of inorganic materials, and finally guided fabrication of inorganic nanomembranes with thickness of a few to a hundred nanometres. Different from the traditional membrane formation techniques, surfactant provided a flexible way to form free-standing inorganic multilayered membranes. Apart from its conventional functions, surfactants are acting as the most widely used stabilizing ligands for nanoengineering of nanoparticles with precise periodicity and complexity. The specific functionalized terminating groups of various surfactants facilitate the conjugation with surface of bare nanoparticles. Such organic-inorganic soft-hard conjugates perform as a useful vehicle during drying-mediated entropy-driven self-assembly at interfaces, external field-activated assembly, and template-directed assembly.[70-72] Such promising nanoarchitectures will enable diverse assortment of superlattice structures with appealing optoelectronic properties and mechanical robustness.[19]

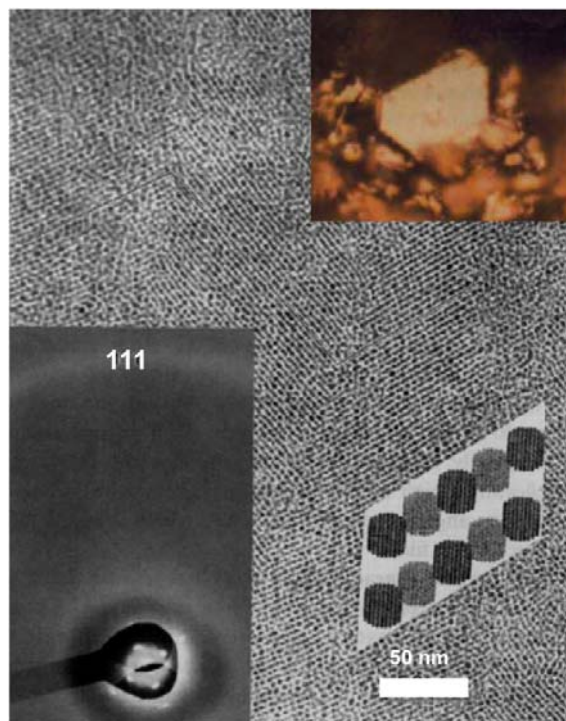


Figure 2.3 | TEM image and photograph (inset) of superlattice using dodecanethiol-capped AuNPs. Reproduced with permission from Ref. [21]. © (1996) Wiley-VCH.

2.2.1 Single-component nanoparticle superlattice

Pioneering strategies were introduced by using alkyl-functionalized gold nanoparticles ($n\text{-C}_{12}\text{H}_{25}$) with selectively separated sizes, and formed nanocrystal superlattices characterized by both translational and orientational orders.[21] Small fraction of 2D monolayers can be observed after spreading toluene solution of precisely determined nanoparticles on carbon substrates (**Figure 2.3**). Slow drying led to ordered fractions of 2D monolayers with small surface areas (~ 200 nanoparticles from fraction domain).

By controlling the surfactant length and external parameters during superlattice formation, the interparticle distances can be easily tuned, enabling customizable optical property and predictable transitions. In one report, alkylthiol-capped Ag nanoparticles (AgNPs) were used to form quasi-ordered Langmuir monolayers on water surface.[15] Three different surfactants (i.e., propanethiol, hexanethiol and decanethiol) were combined with two sized AgNPs. The compressing of Langmuir-Blodgett (LB) trough changed the surface pressure, lead to controllable interparticle distances. When the distances decreased from 1.2 to 0.5 nm, both quantum and classical effects can be observed from the optical responses. However, keep decreasing the distances will result in an insulator-to-metal transition. At this reversible transition point, the nonlinear optical response of superlattice membrane would decrease to constant value, while the linear reflectance also decrease and finally close to the property of a thin metallic film. This method suggested a tailorable way to adjust coupling property and electronic wave function overlap within adjacent nanoparticles.

To form close-packed nanoparticles superlattice, it needs small size dispersity of nanoparticles that consistently capped by soft ligands. Broad deviations of capping ligands would prevent disorder-order phase transition and lead to structure with low ordering. One fundamental research reveals that dodecanethiol-capped nanoparticles behave similarly to soft spheres consisting of metallic hard core and organic soft corona.[59] Different from the assembly of hard particles, the effects of capping ligand, facet and morphology of nanoparticle, and interparticle forces all contribute to the superlattice formation and ordering. For the same type of chain structure, the functional group of ligands also influences superlattice ordering. One systematic research has pointed out that alkanethiol-capped nanoparticles formed better superlattices compared

with amine-capped nanoparticles.[73] This may be due to the weaker binding between amine and particle surface that leads to disorder of the exterior alkane chain.

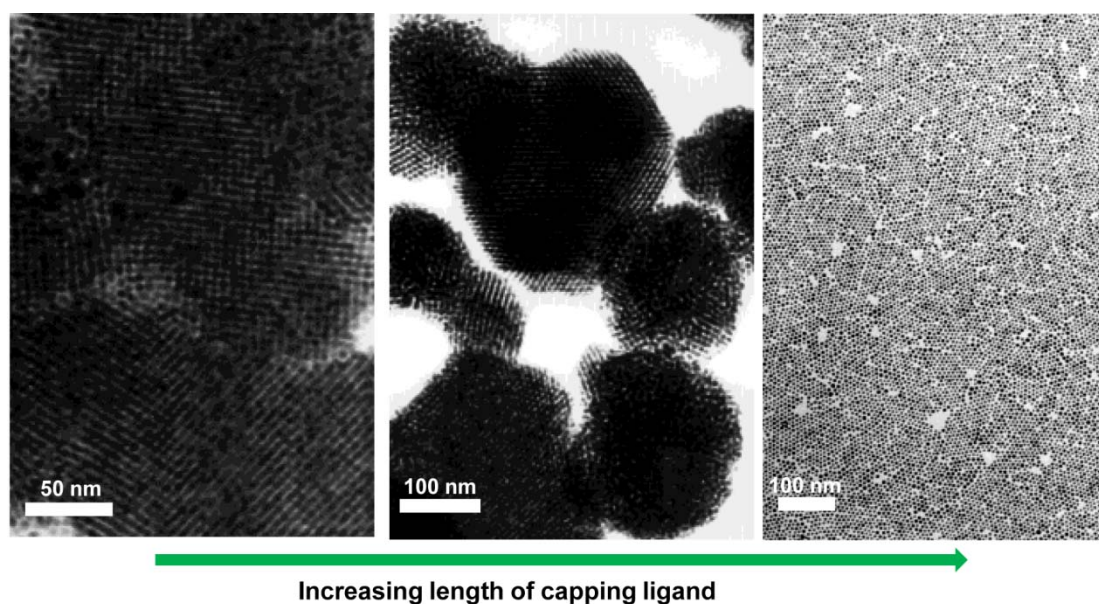


Figure 2.4 | Effect of chain length of surfactant ligand on superlattice structure. TEM images show 3D to 2D superlattices (left to right) using surfactants with increasing length by applying the ‘digestive ripening’ method. Reproduced with permission from Ref. [74]. © (2002) ACS.

Besides from capping groups, the chain length greatly influences the structure and property of assembled superlattice.[75, 76] By applying the digestive ripening, a detailed study reported the effect of chain length on the superlattice.[74] Four different surfactants (i.e., octanethiol, decanethiol, dodecanethiol, and hexadecanethiol) were used as the capping ligand for comparison of assembled superlattices (**Figure 2.4**). For short ligand such as octanethiol, 3D assemblies or aggregation were observed due to large attracting forces between particles. With the increase of chain length, the balanced interaction among particles leads to self-correction and organization, finally forming small fractions of 2D hcp assemblies and 3D structures. While the ligand length further increased to C₁₆, 2D arrangements of nanoparticles were mostly formed with well-ordered structures. This fact indicates that the interparticle interactions can be well-controlled by using surfactants with different lengths, finally leading to tunable superlattice structures. In addition, the density, volume fraction, along with chemical characteristics of ligand/nanoparticle interface, may influence the thermal conductivities of assemblies.[77]

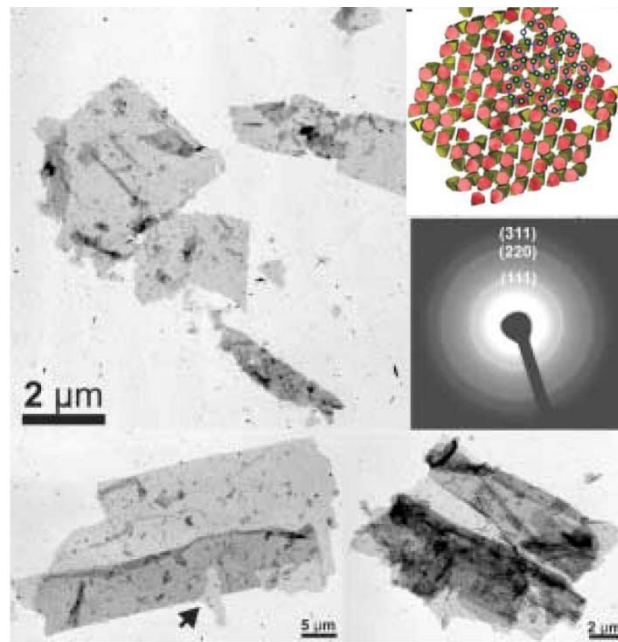


Figure 2.5 | TEM image and inset model shows free-floating superlattices constructed by DMAET-stabilized CdTe quantum dots. Reproduced with permission from Ref. [20]. © (2006) AAAS.

The soft surfactant can also provide multiple driving forces as balance parameter to govern the self-assembly of nanoparticles. As an example for assembly of quantum dots, 2-(Dimethylamino) ethanethiol (DMAET) capped CdTe nanoparticle was able to spontaneously assemble into free-floating monolayer in solution (**Figure 2.5**).[20] Both experimental results and multiple simulations demonstrated that the driving force is originated from anisotropic electrostatic interactions and directional hydrophobic attractions. The DMAET contributed positive charge to the CdTe particles and hydrophobicity that originating from methyl groups. Similar to the function of surfactant, chiral ionic liquids can also acting as capping ligand around nanoparticles and guiding the assembly. The molecular structures of different ligands determine the hydrophilicity and steric hindrance during superlattice formation, and largely affect the nanoparticle patterns during the surfactant-enhanced Marangoni-Benard convection. [78]

The nanoparticles capped by heterogeneous ligands would trigger the site-specific interactions and self-assembly. The physical or chemical interactions between soft ligands, such as hydrogen bonding, electrostatic and hydrophobic forces, are able to induce asymmetrical assembly of nanocrystals.[79, 80] CTAB (Cetyltrimethylammonium bromide) is a common ionic surfactant for control over

shapes of gold nanorods and stabilization during seed mediated synthesis. When CATB-capped AuNRs were partly exchanged by polystyrene at the two arrowheads, they can self-assemble into 1D regularly spaced chains that mediated by adding mixed solvent into the well-dispersed system, which is due soluble differences between side-capped CTAB and end-capped PS ligands.[41] The AuNRs act as multifunctional monomer units and organize themselves into macromolecule-like assemblies during the chain-like structure formation, which is a process that analogous to step-growth polymerization. By selectively control the property and ratio of mixed solvent, various nanostructures can be formed.[55] This method established an approach to the quantitative prediction of the structural characteristics and LSPR properties of linear, branched, ring/bundle-shaped ensembles of AuNRs. [81]

The use of appropriate surfactant is able to maintain the separation between nanoparticles, which enables 2D monolayers by either LB techniques or droplet evaporation. To unravel the structure evolution of superlattice membrane as a function of surface pressure during LB process, in situ optical microscope and X-ray scattering can be used to probe the formation process. The concentration of surfactant ligand, other than the surface pressure, is crucial for controlling the interparticle spacing.[82] Also, under high surface pressure, the reversibility of crumpled multilayer also largely depends on the surfactants. Besides the LB techniques, 2D superlattice membrane with long-range ordering can be prepared by drop-drying method. By utilizing air/liquid interface as natural platform, such method is truly scalable, enabling monolayer superlattice membranes with controllable long-range ordering (**Figure 2.6**).[14, 83] By using dodecanethiol-capped AuNPs (6 nm) as model building block, concentrated AuNPs in toluene was carefully spread on a water droplet. The rapid evaporation dynamically leads to 2D confinement of AuNPs at the air/water interface. After the evaporation of water droplet, the small islands of 2D assemblies would nucleate and grow into large membrane with considerate ordering. It proves that high concentration of particle along with the small fraction of excess surfactant in the system may promote monolayer formation. In the earlier report, it has been demonstrated that the excess nonvolatile dodecanethiol ligand may provide a lasting wetting layer that giving nanoparticles a high surface mobility.[83] During this interfacial assembly regime, the evaporation kinetics and attractive interaction between the particles and interface determined the quality of 2D membrane.[14] Two parameters are essentially important

in this assembly kinetics: flux of particles into the interface (f) and interfacial diffusion length (δ). A sufficiently higher f that determined by both evaporation rate and nanoparticle concentration, along with larger δ resulting from considerable nanoparticle-interface interaction, are necessary for 2D membranes. Small value of these two parameters will contribute to ‘stain-’ or ‘belt-’ like fractions that prevent large-scale membrane during late-stage drying. Based on this mechanism, highly ordered superlattice membrane with giant surface areas can be realized by carefully choosing different capping ligands to control the interaction forces between particles and interface.

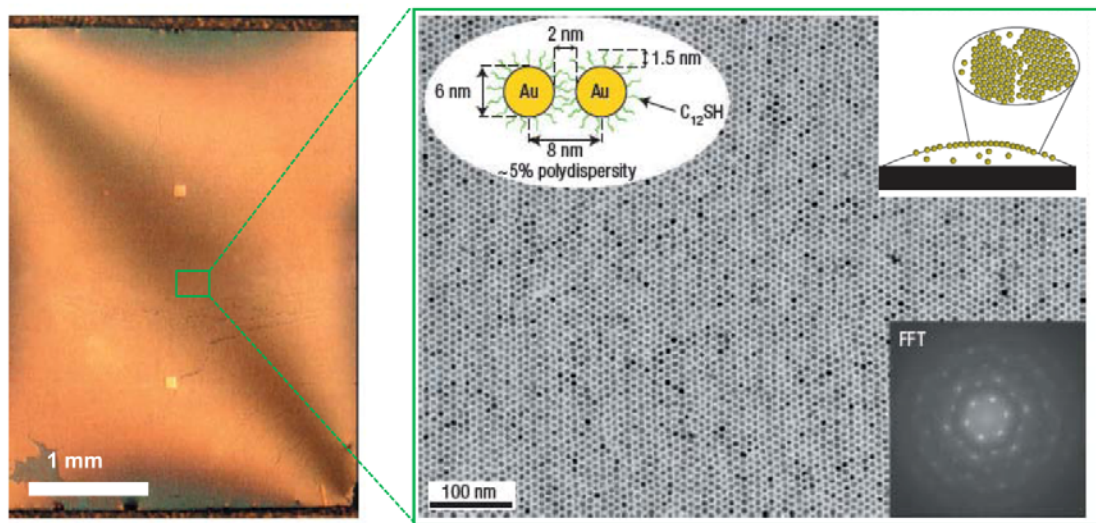


Figure 2.6 | 2D superlattice shows long-range order of AuNPs kinetically self-assembled at air/water interface using drop-drying method. Reproduced with permission from Ref. [14]. © (2006) NPG.

Hierarchical self-assembly of more elaborate nanoparticles is a challenging task compared with spherical or simple anisotropic nanoparticles.[84] A sequential assembly scheme has been achieved by using monodispersed octapod-shaped nanoparticles (CdSe/CdS) that capped by hydrophobic surfactants. They can assembly into chain-like structures when dissolved in toluene.[85] Further addition of acetonitrile would trigger the aggregation of octapod chains into 3D superlattices with high porosity. The interlocked configuration of such porous superlattice would lead to fast cation exchange and offer application potential in photovoltaic and sensors.[86]

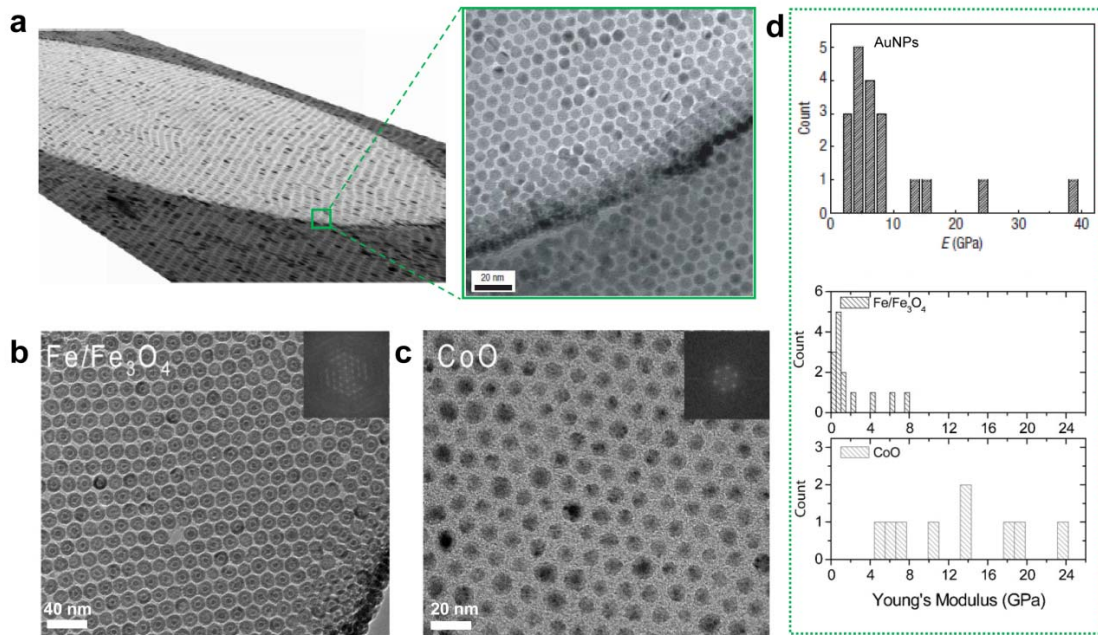


Figure 2.7 | Mechanically robust free-standing superlattice membrane constructed by surfactant-capped nanoparticles. TEM images of 2D superlattice membrane assembled by (a) dodecanethiol-capped AuNPs, (b) oleylamine-capped Fe/Fe₃O₄ and (c) oleic acid-capped CoO nanoparticles. (d) Histograms of Young's modulus indicates median value of 6 GPa, 1 GPa and 14 GPa for those nanomembranes, respectively. Reproduced with permission from Ref.[5, 87] © (2007) NPG and (2010) Wiley-VCH.

Surfactant-capped nanoparticles are able to form close-packed 2D superlattice membranes showing electronic transport properties,[88] and more strikingly, with remarkable mechanical strength and robustness. The first reported free-standing nanoparticle membrane was assembled by hydrophobic dodecanethiol-capped AuNPs as basic building blocks. 2D monolayered superlattices were formed by spreading AuNPs dispersed toluene solution across water droplet resting on a silicon nitride substrate. Then the following self-assembly process would occur at the air-water interface[5]. The resulting monolayered membranes were highly ordered close-packed arrays that spanned across micrometer-sized holes, yielding freestanding structures (**Figure 2.7a**). Mechanical studies revealed a surprisingly large Young's modulus in the range of 3~39 GPa by analyzing from elasticity theory.[89] The short dodecanethiol ligands may overlapped from neighboring nanoparticles and interdigitate with each other. The extracted Young's modulus of ligand ($E_{\text{thiol}} \sim 4$ GPa) in the membrane is larger than most common polymers, which could be attributed to the confinement of ligands on the nanoparticle surfaces and interstices between the nanoparticles. Based on this fundamental result, the surfactant ligands have not only effectively balanced the

interparticle attraction, but also offered intrinsic tensile strength of superlattice membrane in forms of ligand-ligand interactions. Followed systematic study was conducted on large-area free-standing superlattice sheets of various building blocks (*i.e.*, Au, Fe/Fe₃O₄, and CoO) and capping ligands (*i.e.*, dodecanethiol, oleylamine, and oleic acid, respectively) (**Figure 2.7b, c**)[87]. In the fabrication method, drying-mediated assembly technique was used for different nanoparticle systems to create close-packed monolayer membranes that span holes of tens of micrometers in diameter. Particularly, CoO membrane was able to span over 70- μ m-wide square holes with huge amount of freely suspending particles. Detailed mechanical study reveals that the Young's moduli is constant value and irrelevant to the surface area of membrane (**Figure 2.7d**). Importantly, the size of building blocks, ligand-core and ligand-ligand interactions mainly determined the mechanical strength. The stronger binding and interdigitated ligands contributes to larger mechanical robustness and stiffness. Also, the larger particle size may increase the fracture strength of membrane, but multilayer may decrease the fracture strength owing to differences in residual strain during deposition.

Pathway to the device applications always relies on the free-standing form of assembly and stratagem for transferring such nanostructure onto various substrates.[3] Free-standing 1D plasmonic chain can be generated under the mechanism of superhydrophobicity-directed fluid drying. By combination of top-down and bottom-up strategy, citrate-capped AuNPs (45nm)/calcein composites formed 1D nanowires that free-standing on the superhydrophobic toothing-pillar-pair-structured silicon substrate (**Figure 2.8a~c**).[90] During the evaporation of droplet, microscale liquid bridges between neighboring micropillars guided the assembly direction, enabling 1D AuNPs nanowires as long as 30 μ m with controllable width. The superhydrophobic pillars and ration of AuNPs/calcein are two key parameters that determined chain formation. Strikingly, such 1D nanowires with single particle width can free-suspended with one end connected to the micropillars, indicating remarkable mechanical robustness. In addition, the nanowires show plasmonic waveguiding property with a propagation length of \sim 2.1 μ m, indicating a potential application for nanophotonic circuits.

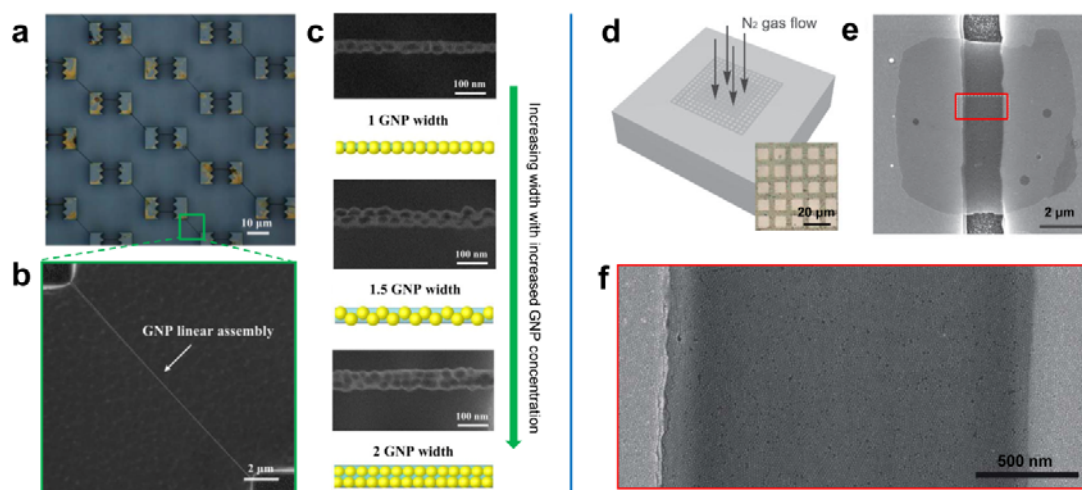


Figure 2.8 | Free-standing 1D & 2D nanoparticle superlattices. (a) Optical micrograph and (b) TEM image of zigzag-type 1D assemblies formed between neighboring superhydrophobic micropillars. (c) magnified TEM images show tunable width of linear assembly by changing GNP/calcein ratio. (d) Scheme shows nitrogen-assisted method for transferring 2D free-standing superlattice membrane from copper grid (inset image) onto (e) SiO₂/Si substrate. (f) magnified TEM image of red area in (e). Reproduced with permission from Ref. [90] [11] © (2013&2011) Wiley-VCH.

Notably, a feasible transfer method and detailed electrical measurements of monolayered free-standing superlattice sheets has been presented[11]. In the first step, a TEM grid was sandwiched between Teflon with a cone-shaped cave and aluminum foil with a centered hole. Dodecanethiol-capped AuNPs (13.6 nm) were then self-assembled into 2D superlattice membranes at the air/water interface. After evaporation of water, the membrane gradually deposited onto the TEM grid and formed the free-standing membrane under the shape confinement and surface compression of cone-shaped cave. Then, a nitrogen gas flow forces the membranes to leave the TEM grid and deposit onto hard substrate (**Figure 2.8d**). During this gas-forced transfer process, most free-standing membranes preserved the original shapes and without deterioration (**Figure 2.8e, f**). Moreover, the order of the local structure is also similar to that over the holes of the TEM grid, which proved that this method can be used to transfer nanomembranes onto arbitrary substrates while maintaining the local packing order, the global shape, and the relative positions.

2.2.2 Multicomponent nanoparticle superlattice

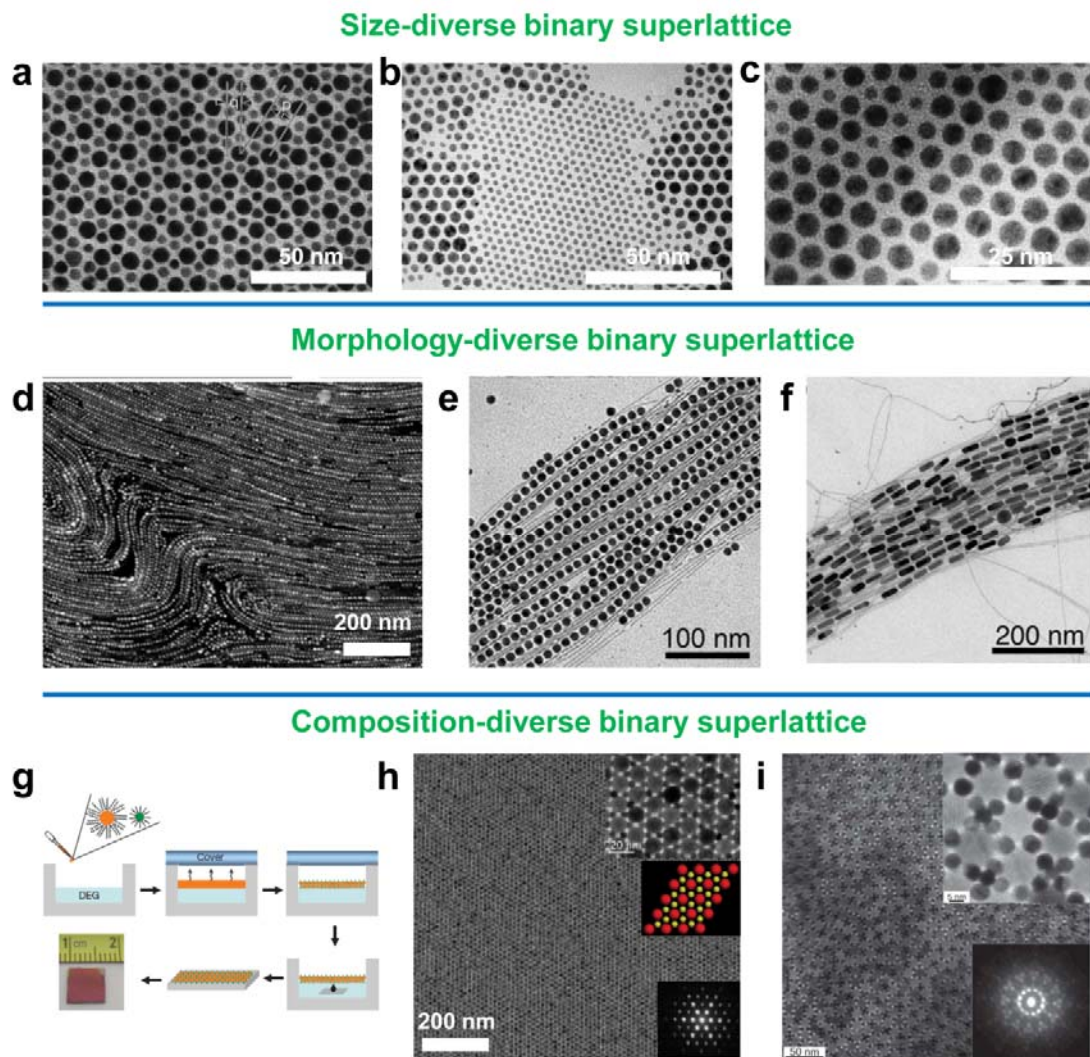


Figure 2.9 | TEM images of binary superlattice membrane composed by different-sized nanoparticles. (a) Ordered binary array with $R_B/R_A \approx 0.58$. (b) size-segregated array with $R_B/R_A \approx 0.47$. (c) Random distributed array with $R_B/R_A > 0.85$. TEM images of superlattice co-assembled by AuNPs/AuNRs with anisotropic gold nanowires. SEM and TEM images of (e) AuNPs and (f) AuNRs embedded in AuNWs. (g, h) Scheme and TEM image of AIB2-type BNSL membrane constructed by 15 nm Fe_3O_4 and 6 nm FePt nanoparticles. (i) TEM image of quasicrystalline superlattice assembled by 13.4 nm Fe_2O_3 and 5 nm AuNPs. Figure reproduced with permission from Ref.[2, 17, 49] © (1998&2010) NPG, (2010) Wiley-VCH.

Soft ligands also guide co-assembly of multicomponent building blocks (with various size, morphology, or composition) in one system, creates binary/ternary superlattice with distinct multifunctional properties. By precisely controlling the type and size ratios of constituent nanocrystals, it is possible to manipulate the structure and composition of superlattice.[28] One early example is the bimodal superlattice structures constructed by alkanethiol-capped AuNPs with two different sizes.[17] Simply by evaporation of toluene, three types of bimodal structure were observed that

closely related to the size ratios of coexisted AuNPs: (1) intimately organized bimodal array with AB_2 stoichiometry, which is particularly favored when radius ratio of particles R_B/R_A within the range of 0.482 to 0.624 (**Figure 2.9a**); (2) phase-segregated domains with two different particles when R_B/R_A is in the range of 0.458 to 0.482 (**Figure 2.9b**); (3) randomly distributed particles with small R_B/R_A (**Figure 2.9c**).

Binary structures with geometrical diversity have been generated by co-assembling of AuNPs/AuNRs with anisotropic gold nanowires (AuNWs, with diameter of 1.6 nm and length larger than 5mm) (**Figure 2.9d-f**).^[49] Compared with drop-casting assembly at solid substrate, the controllable assembly at air/liquid interface shows extended monolayer area and tunable structures. In this report, oleyamine was acting as the capping ligand and balancing the interactions between different building blocks. Also, excess oleyamine in solution facilitate diffusion of nanoparticles along the AuNWs and led to highly ordered structure. The AuNWs would form bundles that guided the orientation of AuNRs with end-to-end alignments. The interparticle distances can be programmed through changing the ratio of nanoparticle and AuNWs in solution, enabling variable SPR responses of binary assembly.

Binary nanocrystal superlattices (BNSLs) have also been demonstrated recently and enriched design of novel metamaterials^[2]. A general method has been created for preparation of centimeter-scale BNSLs that can readily be transferred to arbitrary substrates. By spreading a drop of hexane solution containing Fe_3O_4 and FePt nanocrystals with selected sizes and concentrations over the surface ($\sim 1.5\text{ cm} \times 1.5\text{ cm}$) of diethylene glycol (DEG), liquid-air interfacial assembly of multicomponent nanocrystals allowed rapidly growing of large-scale monolayers with long-range ordered BNSLs (**Figure 2.9g, h**). This method has provided a facile and robust way to grow membranes of quasicrystalline BNSLs (**Figure 2.9i**) and ternary nanocrystal superlattices. Various superlattice structures (*e.g.*, isostructural with NaCl, CuAu, AlB_2 , $MgZn_2$, $MgNi_2$, Cu_3Au , Fe_4C , $CaCu_5$, CaB_6 , $NaZn_{13}$, and *cub*- AB_{13} compounds, and dodecagonal quasicrystalline superlattice *et al.*) and can be formed by using combinations of semiconducting, plasmonic and magnetic nanocrystals.^[29, 91] The electrical charges, together with entropic, van der Waals, steric and dipolar interactions, determined the BNSL stoichiometry.^[63] For example, by altering the charges on PbSe nanoparticles through adding extra surfactant molecules (oleic acid or tri-*n*-

alkylphosphine oxides), self-assembly of different superlattice structure can be directed. Those superlattice structures allow in depth analysis of crystallography including structure defects,[92] offering unique ordering parameter and mechanisms in assembly of various nanoparticles.[93] BNSLs shows unique plasmonic properties contributed from the different composition and near-field coupling between adjacent nanoparticles. As an example, the BNSLs constructed by AuNPs, and non-plasmonic particles (Fe_3O_4 , PbS, PbTe) shows a tunable SPR coupling ranging from 551 nm to 640 nm.[31] It can be systematically controlled by tuning the lattice structure, nanoparticle size/shapes/compositons, enabling a programmable spectral property across broad range.

Different from continuously self-assembly, non-uniform inorganic nanoparticles can spontaneously assemble into large core-shell supraparticles.[94] Such self-limiting process is mediated by the balanced van der Waals attraction and electrostatic repulsion among the constituent nanoparticles, creating inorganic nanostructures with complexity that mimicking the biological assemblies. For example, citrate-capped CdSe particles (2.9 ± 0.7 nm) can assemble into supraparticles with a median diameter range from 22 ± 2.4 nm to 49 ± 4.1 nm with the increasing growth time. Also, hybrid core-shell metal-semiconductor supraparticles can be formed by introducing Au nanoparticles into the system, enabling distinct hierarchical assemblies.[95]

2.3 DNA-based nanoparticle superlattice

Compared with the short-chain molecules, DNA turns out to be the most promising candidate to manipulate nanoparticles at will due to its many inherent advantages, such as (a) the unique Watson-Crick base-pairing forces between complementary strands that allow for adjusting interparticle potentials with high accuracy; (b) DNA length that is finely and widely tunable from nanoscale to microscale with available chemical and biological toolkits; (c) emerging structural DNA nanotechnologies that allow for facile control over topology and mechanics of DNA motifs, enabling superior accuracy in templated assembly of nanoparticles. These unique characteristics enable DNA to be engineered either into various topological structures (*structural engineering*) or with desired sequences to optimize hybridization forces (*sequence engineering*), allowing

for facile programmed, templated or ligand-based assembly of nanoparticles into well-defined nanoarchitectures.

In this section, various viable approaches for building structurally-well-defined nanoarchitectures have been reviewed, along with discussion on their pros and cons. We thoroughly summarize viable strategies developed for building DNA-based nanostructures (**Table 2.1**). These methods and techniques can be categorized in three types, namely DNA-programmed self-assembly, DNA-templated self-assembly, and unconventional DNA technologies and nanopatterning.

Table 2.1 | Summary on methodologies for constructing DNA-based nanostructures

Methodologies	Category of Architectures	Building Blocks	Conjugation Method	Specific Structures	References
DNA-Programmed Self-Assembly	“Plasmonic Molecules”	AuNPs (5/10nm)	Mono-DNA Conjugation	Dimer/Trimer	[38, 96]
		AuNPs (5-20nm)	Mono-DNA Conjugation	Pyramids	[97]
		AuNPs (13/30/60 nm)	Site-Specific DNA Conjugation	Cat Paw/Satellite /Dendrimer	[98]
		Au/Ag core-shell (20nm)	Site-Specific DNA Conjugation	Nanodumbbells	[99]
		AuNP/AgNP & nanoshell (11-75nm)	Site-Specific DNA Conjugation	Heteropentamer/ Janus Nanoclusters	[39, 100, 101]
		Au Nanorods and Spheres	Site-Specific DNA Conjugation	Heteromers	[102]
		AuNPs (5-18 nm)	PCR/RCA	Dimer to multimer	[103-105]
	“Plasmonic Polymers”	AuNP (4.4 nm)	Non-specific Electrostatic forces	Linear Chains	[106]
	“Plasmonic Crystals”	AuNP (11-15nm)	Multi-DNA conjugation	BCC/FCC superlattices	[18, 23, 27, 39, 66]
		Anisotropic NPs (14-140nm)	Multi-DNA conjugation	superlattices	[43]
		AuNPs (5-20nm)	Multi-DNA conjugation	Multiple Lattice Structures	[22, 45]

DNA-templated Self-Assembly	“Plasmonic Molecules”	AuNPs (5/15nm)	Cyclic DNA frames	Triangles/squares	[107]
		Au/AgNPs (5-20nm)	DNA Origami	Dimers/Trimers	[108, 109]
		AuNPs & AuNRs	DNA Origami	Heter-dimers	[110]
	“Plasmonic Polymers”	AuNPs (10/15nm)	DNA Nanotube	Nanopeapod	[111]
		AuNPs (5-15nm)	DNA tile/origami	Stacked Rings/Spirals	[52, 112, 113]
	“Plasmonic Sheets”	AuNPs (6.2nm)	DNA tiles	2D superlattices	[114-116]
Unconventional DNA Technologies and Nanopatterning	“Plasmonic molecules”	AuNPs (5nm)	Origami/lithography	2D arrays	[51]
	“Plasmonic Polymers”	AuNPs (40nm)	Printing	Plasmonic Chains	[117]
	“Plasmonic Sheets”	AuNPs (13nm)	Dry-ligand combined with top-down	Large-area free-standing superlattices	[3, 118]
	“Plasmonic polymers/sheets/ Crystals”	AuNPs (13nm)	Dry-ligand /lithography	Chains/corrals/ sheets/crystals	[119]

(AuNPs: Au nanoparticles; AuNRs: Au nanorods; ss/ds-DNA: single strand/double strand-DNA; BCC, body-centered cubic; FCC: face-centered cubic; PCR, polymerase chain reaction; RCA, rolling circle amplification)

2.3.1 DNA-programmed self-assembly

One of the unique features of DNA molecules is the specific Watson-Crick base pairing interactions between complementary sequences. These forces can be used to regulate interparticle potentials (enthalpic interactions) between adjacent nanoparticles and, therefore, program assembly of pre-synthesized nanoparticles. In two seminal papers, Alivisatos and Mirkin reported their initial results in 1996: the former focused on grouping finite-number nanoparticles together[38], whereas, the later focused on constructing three-dimensional arrays[66]. The initial reports outlined the concepts of DNA-programmed materials synthesis in which multicomponent assemblies could be arranged in space on the basis of rational design of DNA linkers and conjugates. Numerous techniques and methods, inspired by these pioneering approaches, have since been developed.

2.3.1.1 Nanoparticle superlattice derived from mono-DNA conjugates

To precisely define the spatial positions of nanoparticles, it is often necessary to obtain high-purity mono-DNA conjugates (*i.e.* one oligonucleotide per particle)[38]. In the initial paper, mono-DNA conjugates led to the assembly of homodimeric and homotrimeric nanostructures, which are not attainable with multi-DNA conjugates (*i.e.* multiple oligonucleotides per particle). However, this strategy has been limited to small nanoparticles (< 10 nm) and typically leads to mixtures that need separation by electrophoretic methods. In a subsequent work, hetero-dimeric/trimeric plasmonic nanostructures were obtained [96] (**Figure 2.10a**). Briefly, AuNPs with two different diameters (5 and 10 nm) were used as building blocks and three different strategies were tested. The first involved the use of two complementary strands; the second involved the use of three DNA strands in which one of them act as a linker; the third involved multiple DNA strands and post-hybridization attachment of nanoparticles. All the desired products were purified by gel electrophoresis on 3-4% agarose gel. Dimer and trimer plasmonic molecules were formed by all three strategies as confirmed by TEM. However, the resulting assemblies were not structurally rigid, with deviations in the interparticle spacings and orientations because of the flexibility of DNA molecules. This flexibility resulted in different spatial arrangements of the AuNPs ranging from collinear to triangular distributions. The relative spatial distances between AuNPs was controllable by adjusting the lengths of double-stranded DNA, and the interparticle spacings of 1.2 nm, 1.5 nm and 5.8 nm were reported for the sequences with 18, 28, and 38 base pairs, respectively. The yields of designed plasmonic nanostructures are highly dependent on the quality of plasmonic nanoparticle mono-DNA conjugates which requires purification by gel electrophoresis and anion-exchange high-performance liquid chromatography (HPLC) purification methods[120, 121].

Vectorial control over nanoparticle placement by DNA programming is possible. In one excellent demonstration, nanoparticles could be grouped with high spatial control, leading to the formation of plasmonic tetrahedral molecules[97]. In this work, dsDNA was used as a scaffold to control the placement of 5-nm-diameter AuNPs. Four different types of AuNPs could be precisely positioned to each tip of the DNA tetrahedron. Gel electrophoresis was used to purify the tetrahedral assemblies which were further confirmed by both TEM and small-angle X-ray scattering (SAXS) characterization. Remarkably, this method could be used to produce chiral plasmonic structures with two different configurations of the constituent particles (**Figure 2.10b**).

The authors argued that their system could potentially act as a more sensitive plasmon ruler than simple dimeric structures because the conformation changes in such a multiparticle assembly could create a symmetry breaking that is apparent in the optical spectral measurements.

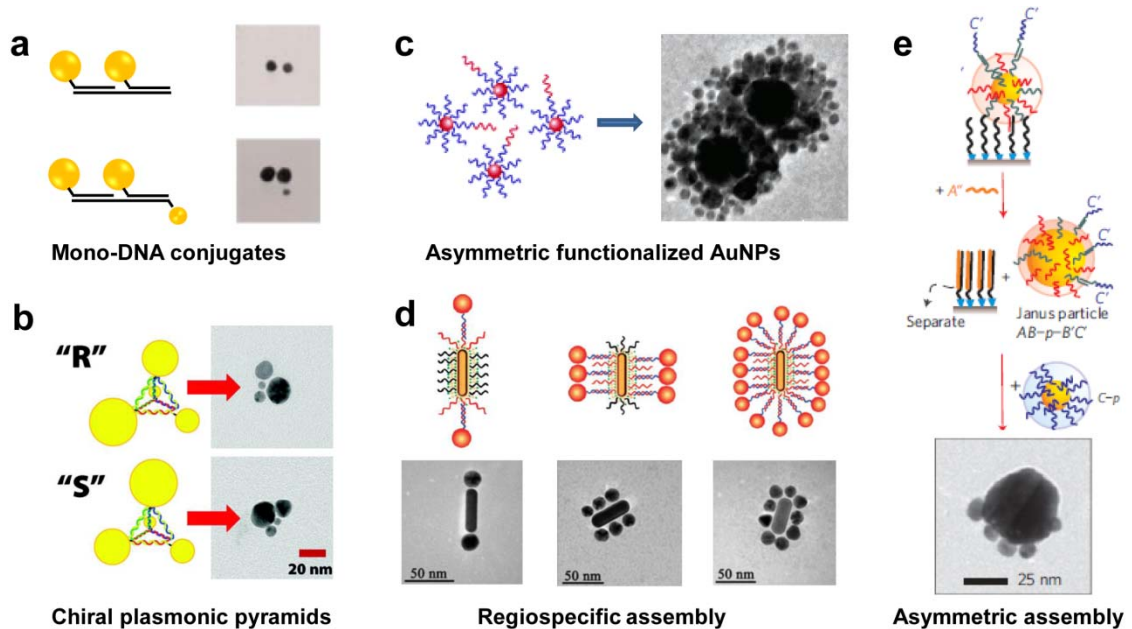


Figure 2.10 | Plasmonic nanostructures derived from mono-DNA and site-specific DNA conjugates. (a) Schematic and TEM images for 10 nm AuNPs homodimer and 5/10/10 nm AuNPs heterotrimer constructed from mono-DNA conjugates. (b) Chiral nanostructures built by using DNA-AuNPs monoconjugates with four different sizes at DNA pyramids tips. (c) Dendrimer-like nanostructures formed by asymmetric functionalized AuNPs. (d) End, side, and satellite nanostructures formed by AuNPs and Au nanorods after selective modification using DNA. (e) Stepwise surface modification of AuNPs and formation of two-faced cluster with anisotropic nanostructures.

2.3.1.2 Nanoparticle superlattice derived from site-specific DNA conjugates

Site-specific DNA conjugates refer to DNA-nanoparticle conjugates with multiple DNA strands attached to only specific sites on nanoparticle surfaces. Such conjugates can lead to the formation of anisotropic plasmonic assemblies. The asymmetric DNA-functionalization of AuNPs could be achieved by using magnetic microparticles as geometric restriction templates[98]. With this strategy, AuNPs could be anisotropically functionalized with two different oligonucleotide sequences. This offers the divalent linking capability of the resulting AuNPs, allowing for the design and programmable assembly of discrete nanoparticle heterostructures, such as satellite, cat paw, and dendrimer-like assemblies (**Figure 2.10c**). Nam *et al.* used the similar method to synthesize SERS-active Au-Ag core-shell nanodumbbells[99]. By virtue of magnetic

particle-assisted separation, a high yield of anisotropically-functionalized nanoparticle conjugate was achieved, consequently, led to large quantities of dimeric AuNPs upon DNA hybridization. Furthermore, silver shells could be specifically deposited onto AuNP cores, forming Au-Ag core-shell nanodumbbells. The interparticle spacing could be controlled by adjusting Ag shell thickness. By fine-tuning this spacing, a detection limit of single molecule could be achieved.

In a different approach, Kotov *et al.* reported complex assemblies from nanoparticles and nanorods based on selective modification of gold nanorods (AuNRs) with DNA. Three types of regiospecific assemblies denoted as *End*, *Side*, and *Satellite* isomers were achieved with a yield of exceeding 85% (**Figure 2.10d**)[102]. All three types of nanostructures had an AuNR in the center and AuNPs sentinels at different positions that were controlled by regiospecific modification of AuNRs. Multiple experimental techniques were used to verify the various structural features, uniformity, and stability of the designed plasmonic assemblies. These plasmonic structures could serve as label-free intracellular probes to acquire local organelle environment information within live cells.

Alternatively, Gang *et al.* reported a stepwise assembly approach to synthesize AuNP dimers from anisotropically-functionalized AuNPs [101]. In this approach, DNA-encoded nanoparticles were assembled onto a solid support in a stepwise manner. The steps of repeated assembly and disassembly at a surface imparted AuNPs with anisotropy, consequently generating remarkably high yields of well-defined dimer clusters and Janus (two-faced) nanoparticles (**Figure 2.10e**). The authors claimed that the stepwise approach could give higher yield of dimers than the conventional solution-based strategies.

2.3.1.3 Nanoparticle superlattice derived from multi-DNA conjugates

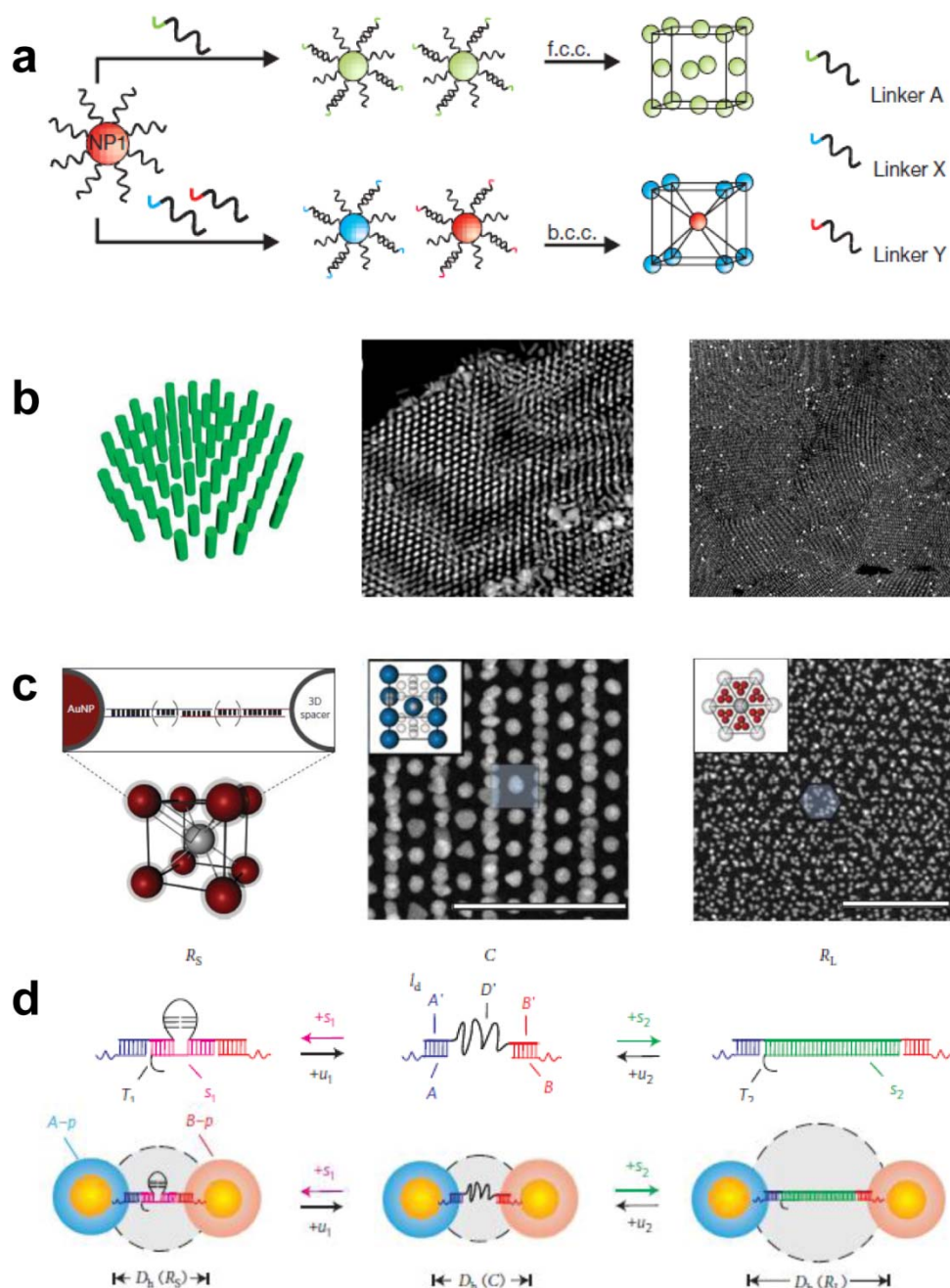


Figure 2.11 | (a) DNA-functionalized AuNPs can be assembled into different crystallographic lattice structures programmed by the sequence of the DNA linkers. (b) Schematic of hexagonal superlattice of standing AuNRs with corresponding TEM images. (c) Scheme illustration of using 3D hollow DNA spacers in AuNP crystallization. TEM images of a bcc lattice (left) formed from AuNPs (20 nm) and DNA spacer (10 nm), and ‘Lattice X’ (right) structure formed from AuNPs (10 nm) and DNA spacer (20 nm). (d) Controllable switching of interparticle distances by using a reconfigurable DNA device (l_d) that acts as an interparticle linkage. After addition of set DNA strands (s_1 , s_2), l_d structure can be reversibly transformed from a flexible C configuration to stem loop R_S and linear R_L morphologies.

Multi-DNA conjugates refer to DNA-nanoparticle conjugates with multiple DNA strands associated with one particle. The conjugation was mostly achieved by thiolated-

DNA capped at the nanoparticle surface through Au-S covalent bond. Recently, an efficient and novel method has demonstrated to use poly adenine (polyA) as anchoring block that conjugated with nanoparticle surface[122]. Programming self-assembly of multi-DNA conjugates often leads to three-dimensional assemblies, which, however, requires careful control over DNA sequences, number density, ionic strength and hybridization temperatures. Initial attempts only led to aggregates with limited order [66], with observable red-blue color changes due to plasmonic coupling. Interestingly, the formation of particles aggregates were reversible, which could be controlled by DNA sequence and length, solvent, and temperature along with supporting electrolyte concentration. This finding was rapidly developed into a powerful diagnostic tool for detections of DNA, RNA and protein. Furthermore, the success in single-component systems could be extended to binary nanoparticle systems[123].

Remarkably, the quality of 3D crystals from multi-DNA conjugates was significantly improved. In the same issue of Nature journal, two independent groups led by Mirkin[18] and Gang [27] reported their 3D nanoparticle crystals from multi-DNA conjugates by programmed temperature control. Both groups characterized the formation of nanoparticle crystals by synchrotron-based small-angle X-ray scattering (SAXS) and revealed the crystallization mechanism during each heating and cooling cycle. The results show that it is possible to achieve two distinct crystalline states (i.e. face-centered-cubic (FCC) or body-centered-cubic lattices (BCC)) by choosing different DNA sequences even with the same type of nanoparticle (**Figure 2.11a**)[18]. Nanoparticles could be assembled through a single DNA linker that gave rise to equal binding affinities between particles, resulting in a close-packed FCC structure; alternatively, nanoparticles could be assembled through two different DNA linkers, leading to a binary system which favored the less close-packed BCC structure. These results demonstrated the power of DNA in regulating lattice structures of nanoparticle crystals.

The concept of optimizing crystallization of multi-DNA conjugates by precise temperature control could also be extended to anisotropic building blocks such as gold nanorods, rhombic dodecahedra and octahedral nanoparticles. It was found that particle shape had a strong influence on the superlattice dimensionality, crystallographic symmetry and phase of DNA-functionalized nanoparticles[43]. Mirkin *et al.* observed

that one-, two- and three-dimensional structures from anisotropic particles and the similar structures could not be made through the assembly of spherical particles. For example, AuNRs formed predominantly into 2D sheets with hexagonal symmetry in most samples investigated (**Figure 2.11b**). They argued that this was due to the preferred base-pairing interactions perpendicular to their long axis to maximize the hybridization events.

Furthermore, a diverse array of 3D nanoparticle superlattices were thoroughly investigated from different DNA linkers and particles with various sizes[45]. Six basic design rules were formulated for regulating crystal structures, including crystallographic symmetry, and interparticle distances. In a recent work, the library of achievable DNA-programmed 3D superlattices was extended to new lattice structures by using hollow DNA nanostructures as 3D spacers [22] (**Figure 2.11c**). The unique hollow DNA structures served as voids that could be selectively placed into a lattice structure of AuNPs, leading to several distinct lattice structures that were difficult to obtain by conventional strategies (e.g., AB₂ type, simple hexagonal, graphite type, AB₆ type, ‘lattice X’). This hollow DNA spacer-based method opens a new route to design crystals with novel lattice structures that are not naturally occurring.

The structural flexibility of DNA and the reversibility of DNA hybridization events make it possible to obtain dynamic, reconfigurable and responsive nanostructures [124, 125]. In one example, 3D superlattices and dimer clusters could be constructed with controllable switching of interparticle distances (in the range of 15-25%) by using a reconfigurable DNA structure that acted as an interparticle linkage[39]. By adding the specific DNA strands, the interparticle distances in the superlattices and clusters can be modified even in their post-assembly states (**Figure 2.11d**). The transition states and local re-arrangements were probed by SAXS which revealed the structural integrity of the systems during the reconfiguration process.

Although crystallization of DNA-nanoparticles was typically achieved upon thermal annealing below its melting temperature, only polycrystalline micro-domains were obtained so far. By mimicking traditional crystallization techniques, slowing cooling of DNA-capped nanoparticles enables faceted rhombic dodecahedron microcrystals (**Figure 2.12a-c**), which further extended the DNA-programmable crystallization

method[50]. During the formation of such single-crystal, the crystal shape was demonstrated to be independent of nanoparticle sizes. Both experimental and theoretical calculation of surface energy values indicated that the rhombic dodecahedron is the thermodynamically most favorable crystal shape over a range of particle sizes. This method reveals that DNA-mediated self-assembly of nanoparticles can be rationally designed by controlling the surface energies of macroscopic nanoparticle crystals, which acting as a true analogue to atomic crystallizations.

The DNA-mediated assembly of 3D AgNPs superlattice was not developed until recently. With an extension to this superlattice, DNA-programmed assembly can be used to construct binary plasmonic superlattice with AgNPs and AuNPs as building blocks (**Figure 2.12d-f**)[53]. Four types of binary superlattices can be achieved by varying the nanoparticle ratios, combined with rational design of DNA linkers, including AB-type (CsCl), AB₂-type (AlB₂), AB₃-type (Cr₃Si) and AB₆-type (Cs₆C₆₀) superlattices. The extinction spectra of such Au-Ag binary superlattice exhibited a Fano-like interference, resulting in an observable dampening of SPR responses.

DNA-programmed pathways could be combined with other methods, such capillary force-assisted self-assembly. In one example, AuNPs and nanoshells could grouped into structurally well-defined heteropentamer clusters (pentamers), which consist of a 74nm-diameter AuNP surrounded by four nanoshells[100]. To obtain this structure, the pentamers were first synthesized by DNA hybridization but the structures were “loose” due to the soft nature of DNA. In a following step, the “loose” pentamers in solution could be “compressed” into a 2D plane by capillary forces during drying process (**Figure 2.12g**). To optimize the pentamer formation, a 75 bases ds-DNA spacer was used. Interestingly, this heteropentamer nanostructure showed specific magnetic and Fano-like resonances characterized by a broad electric dipole resonance spanning the entire range of the spectra.

2.3.1.4 Nanoparticle superlattice from DNA polymerization

DNA-programmed materials synthesis can be combined with polymerase chain reaction (PCR) or rolling circle amplification (RCA) to form various superstructures. Kotov *et al.* attached DNA primers onto nanoparticle surfaces and then carried out PCR reactions[103]. By changing the density of the primer on the surface of AuNPs and

controlling the number of PCR cycles, a number of plasmonic nanostructures were generated ranging from a mixture of dimers, trimers, tetramers, to chiral spatial organizations of AuNPs. The improvement of this method would rely on the development of separation methods for different oligomers. High yield of different generations of products will also be highly desirable for systematic studies of their chiral properties.

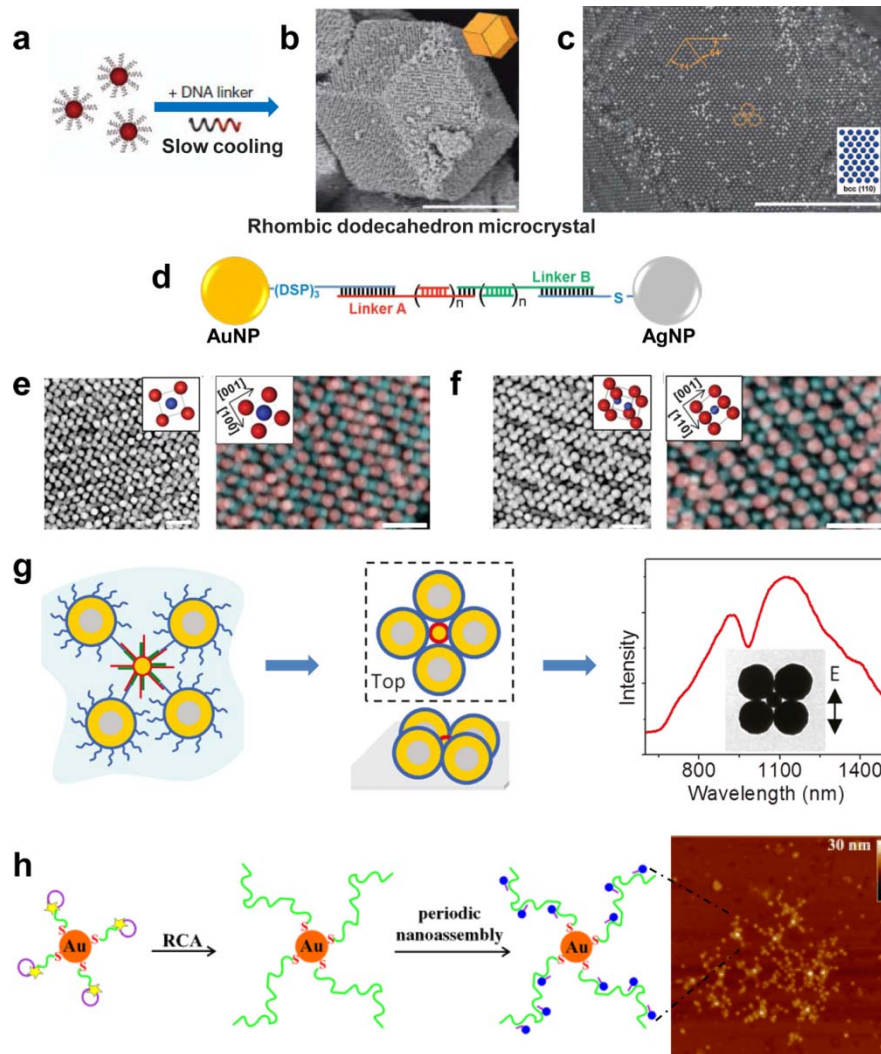


Figure 2.12 | (a) Slow-cooling method shows crystallization of DNA-AuNPs. (b-c) SEM images of rhombic dodecahedron microcrystal. Scale bars are 2 μm and 1 μm. (d) Design of DNA linkers for AuNPs-AgNPs binary superlattice. (e-f) STEM images and EDX elemental maps of AB- and AB₂-type lattices. (g) DNA-functionalized nanoparticles/nanoshells into heteropentamer clusters (pentamers), which consist of a smaller gold nanosphere (74 nm) surrounded by a ring of four larger nanoshells ($[r_1, r_2] = [62.5, 92.5]$ nm). (h) Schematic illustration of RCA on DNA-AuNPs that served as a scaffold for the formation of satellite 3D nanostructures. AFM image (right) showed superstructures constructed from 5 nm and 15 nm AuNPs (large bright spots).

Another DNA polymerization-based method to fabricate plasmonic nanostructures is by RCA which can produce long and linear single DNA strands from a short (<100 bases), circular DNA template. The first RCA-based method to plasmonic structures was reported by Mao *et al.* They first synthesized monofunctionalized DNA-AuNPs (5 nm) and then mixed them with RCA products (namely, long DNA strands with repeating sequences complementary to DNA sequence on AuNPs). This process led to the formation of micrometer-long 1D chains of AuNPs[104]. In a different approach, Li *et al.* fabricate satellite-like plasmonic nanostructures by RCA[105]. In this report, DNA oligonucleotides were tethered to AuNPs as the primer and a single-stranded circular DNA was used as a template. In the presence of ϕ 29 DNA polymerase, RCA reactions led to extension of nanoparticle-tethered DNA with repeats complementary to circular DNA templates (**Figure 2.12h**). Furthermore, AuNPs were attached to these repeats, forming satellite 3D nanoassemblies.

2.3.2 DNA-templated self-assembly

2.3.2.1 Simple dsDNA templates

Murray *et al.* described the assembly of 1D linear chains of AuNPs (4.4 nm) coated by cationic trimethyl (mercaptoundecyl) ammonium (TMA) monolayers[106, 126]. The DNA acted as a template for cationic AuNPs by electrostatic interactions. The morphology of nanostructures varied from chains to complex bundles, which was controlled by controlling relative ratios of nanoparticles versus DNA base pairs. The edge-to-edge distance was estimated to 2.9 ± 0.9 nm, consistent with the predicted thickness corresponding to twice the TMA monolayer thickness. However, some precipitation would occur if the ratio of DNA to monolayer-protected cluster increased. This was likely due to the large binding constant provided by individual cation-anion electrostatic interactions.

2.3.2.2 Templates based on DNA tiles, DNA frames and DNA Origami

Both DNA-programmed and dsDNA-templated nanostructures suffer from weak mechanical strength. Dehydration often leads to the structural collapse or shrinkage. Recently developed structural DNA nanotechnology can overcome this challenge by sophisticated design of rigid DNA tiles, frames and origami.

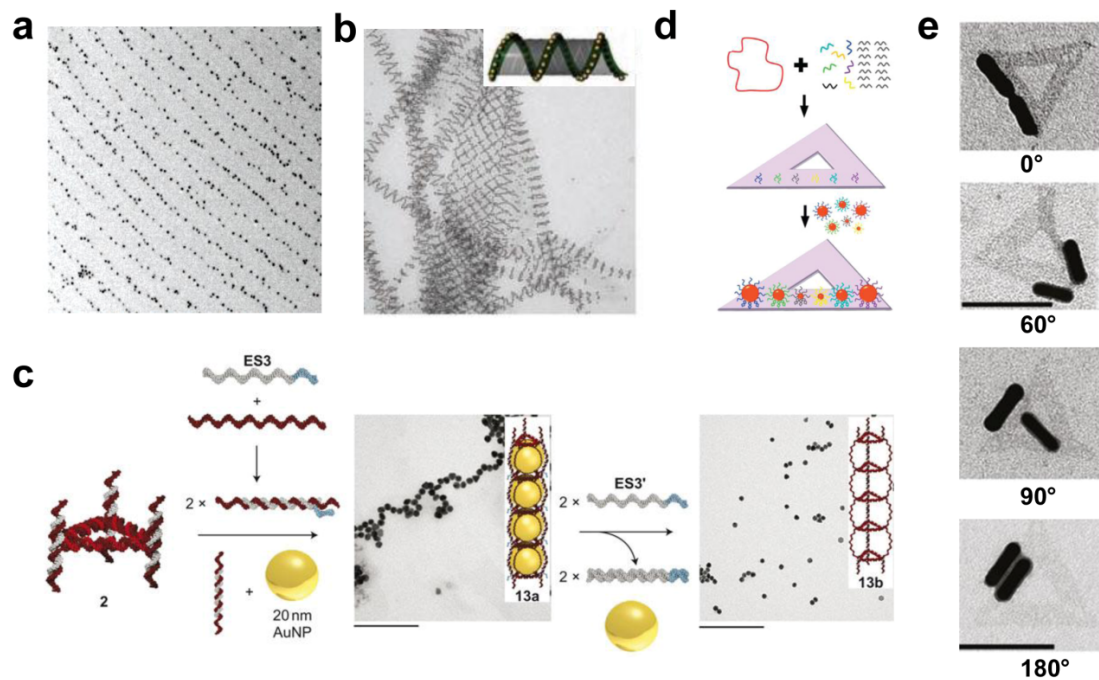


Figure 2.13 | DNA-templated self-assembly constructed by using DNA tiles and DNA origami. (a) DNA-functionalized AuNPs were organized into closely packed rows with precisely defined regular inter-row spacings templated by the DNA scaffolding. (b) 3D plasmonic tubular spirals of AuNPs using DNA tile-mediated self-assembly. (c) Encapsulated ‘nanopeapod’ AuNPs 1D chains using triangular DNA nanotubes with longitudinal variation as host. TEM image (right side) shows that encapsulated AuNPs could be spontaneously released from the nanotubes by simple addition of specific DNA strands. (d) Six-nanoparticle self-similar chain nanostructures using triangular DNA-origami templates. (e) DNA origami-templated AuNRs dimer that forming with various predetermined inter-rod angles.

DNA can be interweaved to form rigid double-crossover (DX) tiles which can be further interlinked to form 2D DNA grids. Kiehl *et al.* utilized four different DX tiles to assemble 2D DNA grids on a solid substrate[116, 127]. Then DNA-modified AuNPs were positioned onto the grids with precisely defined regular inter-row spacing, via Watson-Crick base-pairing forces (**Figure 2.13a**). Seeman *et al.* used a similar method but with different DNA scaffolds and reported the formation of two-component (5 and 10 nm AuNPs) 2D periodic patterns[114]. By using 3D DX triangles, a rhombic lattice arrangement tailed with different sticky ends enabled the formation of the two-component template which then guided formation of 2D nanoparticle assemblies.

DNA-tile-based method can also lead to 3D plasmonic nanostructures. Yan *et al.* reported the formation of 3D plasmonic tubular nanostructures (stacked rings, single spirals, double spirals, and nested spiral tubes) of AuNPs by using DNA tile-mediated

self-assembly (**Figure 2.13b**)[52]. The different conformations of tubular structure and chiralities could be controlled by size-dependent steric repulsions among AuNPs. With two different AuNPs (5 nm and 10 nm), complex 3D patterns, such as double helix and quadruplex structures, were obtained. These AuNPs were wrapped parallel to the DNA tubular axis. By further engineering the DX-DNA tiles structures, it should be possible to place AuNPs of different sizes in or outside of the DNA tubes. This work extended DNA-templated nanostructures to 3D complex architectures similar to some naturally existing patterns.

With the aid of synthetic chemistry techniques, Sleiman *et al.* developed a different route to fabricate rigid DNA frames. They reported the creation of dynamic DNA templates which were fully functional in their single-stranded and cyclic forms. This template guided the selective attachment of AuNPs with different diameters on the complementary arms. Different nanostructures have been established by using the same square DNA template, such as square, trapezoidal, and rectangular clusters. Interestingly, post-assembly ‘write/erase’ methods were demonstrated by selectively removing one particle from triangles of three AuNPs, followed by positioning another AuNP onto the specific site[107].

Linear chain structures of AuNPs could also be produced from rigid DNA frames. In particular, AuNPs could be positioned inside DNA nanotubes fabricated from rigid DNA triangles to form ‘nanopeapod’ (**Figure 2.13c**)[111]. The advantages of using the DNA nanotubes are that conjugation with AuNPs (10 and 15 nm) was size-specific, and the core-to-core distances of AuNPs could be precisely controlled. Notably, the encapsulated AuNPs could be spontaneously released from the nanotubes by simply adding specific DNA replacement strands. The external strands could selectively open the DNA nanotube structure and break the chain-like structures, which could be potentially be applied in gene-triggered delivery of drugs and cell-specific therapies.

Structurally more complex plasmonic nanoarchitectures could be produced from DNA origami templates. DNA origami has attracted much attention to the field of DNA nanotechnology since the landmark work established by Rothemund[128]. In contrast to the conventional crossover strategy that uses single building block to construct larger structures in a ‘two-step’ process, DNA origami provides a versatile and simple ‘one-

pot' method to create addressable DNA nanopatterns by using various short staple DNA strands to fold genomic DNA into geometrically desired nanopatterns[108, 129, 130].

Liu *et al.* reported a bottom-up assembly method to synthesize monomeric, dimeric and trimeric AgNPs (20 nm) cluster, and AgNP-AuNP heterodimer nanostructures templated by triangular-shaped DNA origami with a side length of 114 ± 2 nm [108]. The synthesis involved two steps: (1) preparation of triangular-shaped DNA origami with high quality and desired capture strands at predetermined locations on the structure; (2) hybridization of phosphorothioated chimeric DNA conjugated AgNPs on the DNA origami template. They demonstrated that the core-to-core distance between each AgNPs can be precisely controlled from 29 to 94 nm. The yield of dimer could reach 81%, and the yield of trimer could reach 62.5%.

In addition, Bokor *et al.* developed the six-nanoparticle self-similar chain structures by using DNA origami templates[109]. The long scaffold strand hybridized with designed staple strands, forming the triangular DNA origami with specific binding sites on one side of the origami surface (**Figure 2.13d**). These binding sites guided the different AuNPs (5, 10, 15 nm) to the desired locations through complementary base-pairing forces. A plasmonic resonance band shift from 521 to 526 nm was observed, indicating strong local electromagnetic field enhancements in the interstices between nanoparticles.

The anisotropic building blocks could also be assembled into nanoarchitectures by DNA-origami templates. AuNRs have been successfully assembled into discrete, well-ordered AuNR and AuNR-AuNP hybrid nanoarchitectures[110]. The DNA origami-templated AuNRs dimer could form various predetermined inter-rod angles (0° , 60° , 90° , 180°) (**Figure 2.13e**). This opens a new route to coordinate the spatial orientations of anisotropic nanoparticle building blocks.

With DNA origami methods, it is possible to design more complex plasmonic nanostructures [131] [132] for various applications in nanodevices[133]. For example, Ding *et al.* reported the construction of 3D AuNP helices by rolling and stapling 2D rectangular DNA origami[112]. The geometric dimension of stapling positions on DNA

origami could be rationally controlled, tailoring the structural parameters of AuNPs helices. Similar nanohelices with left- and right-handed morphologies were reported by Kuzyk *et al.* using a different DNA origami-template method[113]. For each plasmonic helix, nine AuNPs were specifically conjugated to the site of DNA origami 24-helix bundles consisting of complementary staple DNA extensions. The nanohelices exhibited both circular dichroism and optical rotatory dispersion effects due to plasmonic coupling in chiral structures. These plasmonic helices resembled natural chiral molecules, opening a new route to manipulate light by programming chirality.

2.3.3 Unconventional DNA technologies and nanopatterning

2.3.3.1 As entropic ligands in drying-mediated self-assembly

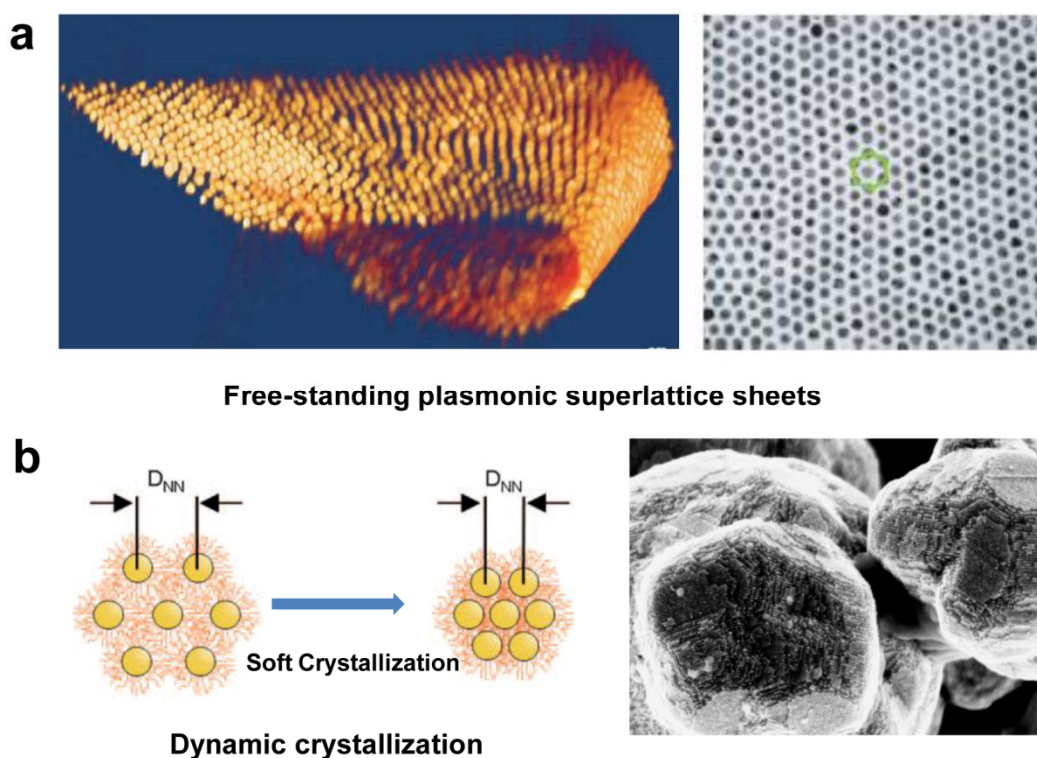


Figure 2.14 | DNA as entropic ligands in drying-mediated self-assembly. (a) Free-standing monolayered DNA-AuNPs superlattice sheets. 3D STEM tomography reconstruction of a folded sheet (left) and TEM image (right) showing hexagonal ordering. (b) drying-mediated deformation of DNA corona in 3D supercrystals.

The programmed pathway and template strategies have led to a diverse range of plasmonic nanostructures. In a different route, Cheng *et al.* successfully put DNA to an unconventional use as an entropic “dry ligand” in a drying-mediated self-assembly process[134]. Under low ionic strength, this method led to large-area highly-ordered

nanoparticle superlattices without, in some circumstances, the requirement of specific Watson-Crick base-pairing (**Figure 2.14a**). Cheng *et al.* systematically investigated the mechanism of dry-DNA-ligand-mediated self-assembly on solid support, holey substrate, and at the air/water interface. In particular, drying-mediated self-assembly of DNA-capped nanoparticles has been systematically investigated by synchrotron-based small-angle X-ray scattering (SAXS)[23]. This represented a hybrid strategy of drying-mediated self-assembly and programmable crystal formation, and the studies on such dynamic crystallization demonstrated that DNA-mediated nanoparticle crystals were soft with continuously scalable lattice constants (**Figure 2.14b**). Furthermore, this result showed that crystallization time in the soft-crystallization process can be tuned by programming base-pairing forces. It also revealed that DNA behaved as a molecular spring in the drying-mediated self-assembly process, from which a simple entropic spring argument could be applied to generic soft-corona hard-sphere interactions at the nanoscale (such as alkyl-molecule-mediated self-assembly of nanoparticles).

Furthermore, DNA-mediated self-assembly of AuNPs has been investigated at the air/water interface by Synchrotron-based Grazing-incidence Small-Angle X-ray Scattering (GISAXS). Specifically, an X-ray beam was positioned parallel to a silicon support, raster-scanning a droplet containing DNA-capped nanoparticles. This allows for mapping spatial crystallization events across the entire droplet [118]. The experimental results showed that DNA could direct self-assembly of the nanoparticles into Gibbs monolayers at the air/water interface., and that the spacing within the monolayer was highly dependent on ionic strength. These synchrotron-based studies on DNA-ligand-mediated self-assembly showed that DNA can manipulate nanoparticle crystallization both temporally and spatially. This may substantially extend the scope of application of DNA in materials and interfaces.

DNA ligands offer superior advantages to alkyl molecule ligands. The highly controllable molecular lengths of DNA ligands enable tailoring of both structural (inter-particle spacings) and functional properties (plasmonic and mechanical) over a wide window. In particular, the edge-to-edge inter-particle spacing in DNA-based nanoparticle superlattices can be adjusted up to 20 nm in dehydrated state [3], which is a significantly wider range than that has been achieved with alkyl molecular ligands. Such control allows for tuning plasmonic colors without changing chemical

compositions and shows potential applications in future plasmonic circuits. Compared to DNA-programmed and DNA-templated strategies, DNA-ligand-based method provides a simple yet efficient route to fabricate large-area nanoparticle superlattices stable in dehydrated state with low cost. However, the drawback of ligand-based approach is to lose the specificity in constructing more complex lattice structures other than face-centered-cubic or hexagonally-close-packed packing geometries.

2.3.3.2 In conjunction with top-down lithography

DNA-based bottom-up self-assembly can be combined with top-down lithography. In particular, DNA-dry-ligand-based strategy exhibited excellent compatibility with top-down lithography. This combination may be a critical step for future integration of DNA-derived plasmonic nanostructures into nanophotonic circuits.

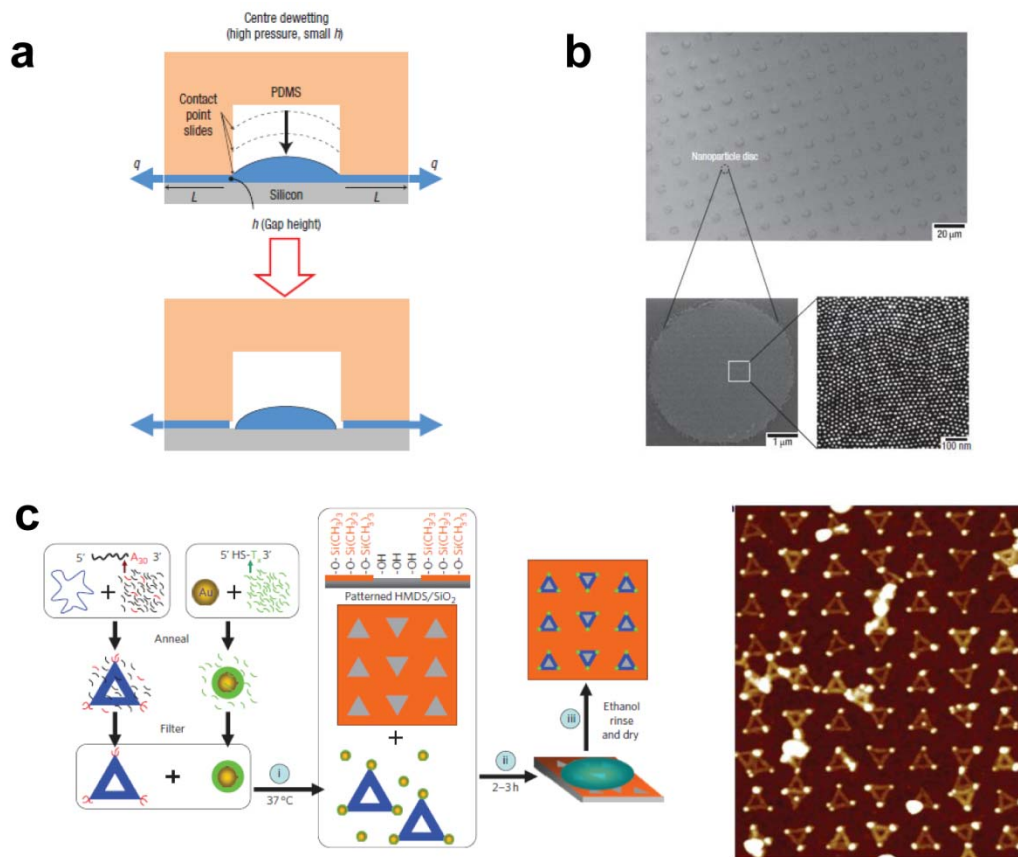


Figure 2.15 | Top-down lithography integrates with bottom-up DNA-programmed self-assembly. (a) Cross-sectional scheme of a microdroplet confined in a micromould showing centre dewetting. Localized assembly of the AuNPs microdiscs was then achieved by DNA-programmed crystallization. (b) SEM image of nanoparticle disks pattern with highly ordered internal structures. (c) Large-area patterning of AuNPs (5 nm) onto spatially ordered, 2D arrays through the site-selective deposition of triangular DNA origami onto lithographically patterned substrates.

By virtue of lithographically-fabricated micromoulds, DNA-mediated nanoparticle crystallization events could be localized, leading to patterned superlattices. This strategy was able to rationally control the local crystallization events of the nanoparticles superlattices, which resulted in versatile structures with high degrees of internal order, such as single particle-width corrals, single particle-thickness microdiscs and submicrometre-sized ‘supercrystals’ (**Figure 2.15a and b**)[119]. These nanoscale features were produced from micrometer-sized moulds, corresponding to a few hundred times of size reduction. Notably, these patterned superlattices could be addressed by micropatterned electrode arrays, suggesting compatibility with current solid-state devices.

Furthermore, by virtue of lithographically-fabricated microholes, the crystallization of DNA-capped nanoparticles can be confined to 2D planes. This process led to free-standing monolayered DNA-nanoparticle superlattice membranes (**Figure 2.15a**)[3]. Both internal and overall structures of sheets could be controlled. For examples, circular and square sheets were obtained conforming to the hole geometries defined by top-down lithography; the edge-to-edge interparticle spacing could be precisely tuned from ~1 nm to ~20 nm. The spacing control influenced the plasmonic coupling, leading to plasmonic nanosheets with different colors. This method opens a simple yet efficient avenue towards the assembly of plasmonic nanoparticle solids in their ultimate thickness limit – a promising step that may enable their integration into solid-state nanodevices.

DNA origami-templated plasmonic nanostructures could also be combined with top-down lithography. Cha *et al.* reported the repeated patterning of large-area arrays of 10nm ssDNA-functionalized AuNPs by a soft-lithographic subtraction printing process[135]. In this method, ssDNA were first adsorbed on PDMS substrates, followed by subtraction printing using a lithographically templated silicon master. The patterned ssDNA domains were then transferred to silicon substrates. Furthermore, DNA hybridization was applied to induce assembly of ssDNA-functionalized AuNPs. Finally, patterned and crossed lines were achieved. Furthermore, Cha *et al.* also reported the large-area patterning of AuNPs (5 nm) into spatially ordered, 2D arrays through the site-selective deposition of triangular DNA origami onto lithographically patterned substrates (**Figure 2.15c**)[51]. Precise binding of AuNPs to each DNA

structure was achieved and formed macroscopic arrays with characteristic length scales ranging from a few to several hundreds of nanometers. Different patterns, such as multiple triangles with alternating left and right orientations, were also formed, providing a new way to rationally generate complex patterned networks[136].

In addition, there were reports of using printing methods with photolithographically-fabricated stamps to pattern DNA-capped nanoparticles. Stellacci *et al.* reported the applicability of supramolecular nanostamping for replicating DNA arrays by using 9 nm AuNPs with high fidelity[137]. Udo *et al.* also reported a Gutenberg-type method with electron beam-fabricated stamps to replicate lithographically defined nanostructures[138]. Dense nanoparticle loading and high transfer yields were achieved over three consecutive printing cycles.

2.4 Polymer-based nanoparticle superlattice

The facile functionalization and unique topological features of polymer allow it to template and guide the assembly of nanoparticle building blocks into well-defined architectures. Such self-assembly process is similar to the case of surfactant-capped nanoparticles, but polymer ligands shows unprecedented advantages to widely tune interparticle spacing especially for large nanoparticles, which are essential for vast assortment of plasmonic applications. Previously, polymer has been successfully used as ligands to stabilize nanoparticles either by direct synthesis [139, 140] or ligand-exchange procedure[141]. Such success has led to ordered nanoparticle arrays self-assembled at solid substrates[140, 142] and as free-standing state.[6, 8, 12] In addition, polymer has also been used to template the assembly of nanoparticles into various structures [54, 143-146]. In this section, we review the established pathways in polymer-based construction of nanoparticle architectures.

2.4.1 Polymer-templated self-assembly

By appropriate conjugation with homopolymer and block copolymer, nanoparticles can be assembled into multiple nanostructures with distinct ordering.[147, 148] In this method, the nanoparticles are embedded with the polymer matrix, which acting as a soft template for guiding the assembly process. [143] In one example, alkane-capped CdSe nanorods can densely packed into vertical arrays in the PMMA matrix under the

combined forces of external electric field and interfacial energy.[149] The CdSe nanorods were aligned along the direction of applied field, and the ‘self-corralling’ process facilitated the formation of side-by-side packed arrays owing to nonfavorable interactions between ligands and polymer matrix (**Figure 2.16a**). Without the polymer matrix or changed into PMMA-miscible ligands, the phase separation would not happen, resulted in a randomly distributed nanoparticles.

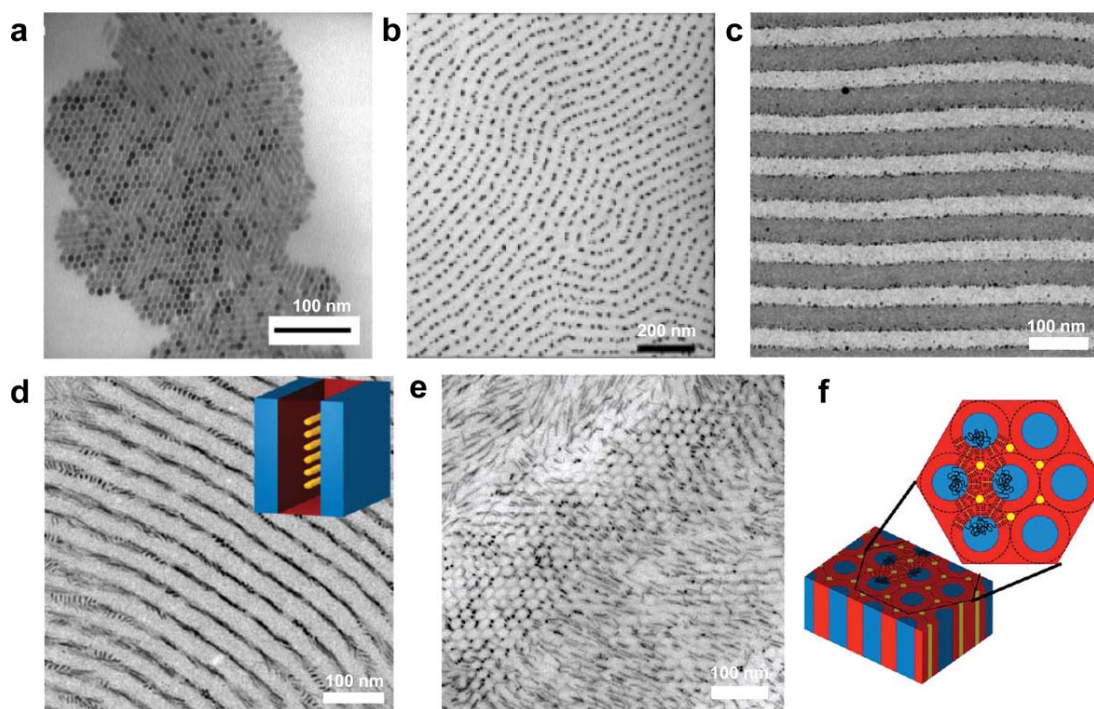


Figure 2.16 | (a) Vertically aligned CdSe nanorods in PMMA matrix under the combined guidance of external electric field. (b) Formation of nanoparticle chains in PS-*b*-PMMA copolymer domains. (c) Ordered lamellar structure formed by AuNPs at the interfaces of PS-*b*-P2VP block copolymer. (d~f) Lamellar and cylindrical nanostructures of ordered CdSe nanorods formed in PS-*b*-P4VP domains. Figure reproduced with permission from Ref.[54, 149-151] © (2006) ACS, (2001) NPG,(2007) ACS, and (2011) ACS.

Specifically, the microphase separation of block polymer can guide the assembly of nanoparticles,[152] which can be tailored by both enthalpic (tuning particle ligands) and entropic effects (particle diameters relative to gyration radius of polymer). Hierarchical self-assembly of Au and Ag nanoparticles were achieved using polystyrene-block-poly(methylmethacrylate) (PS-*b*-PMMA) copolymer as template.[54] The copolymer film was first formed on SiN₄ substrate by spin-cast and induced regular stripe-like domains. Then the metallic nanoparticle was deposited on the film and diffused selectively along the domains, leading to ordered nanochains and continuous wires (**Figure 2.16b**). In addition, by verifying volume fractions of

nanoparticles, stable bicontinuous microstructures with small dimensions (100 nm) can be created.[151] The AuNPs specifically bind to interfaces without causing macrophase separation of symmetric AB diblock copolymers polystyrene-block-poly(2-vinylpyridine) (PS-*b*-P2VP) (**Figure 2.16c**).

Copolymer-based supramolecules can also template the assembly of anisotropic CdS nanorods with controllable nanostructures. Morphological control in nanorods assembly was achieved by varying supramolecular microdomains (i.e., spherical, lamellar, and cylindrical morphology) of PS-*b*-P4VP, enabling cylindrical alignment of nanorods parallel to copolymer, continuous networks, and nanorod clusters.[150] (**Figure 2.16d-f**) Furthermore, quantitative analysis indicates that the interaction of nanorod and polymer ligand ($\Delta H_{\text{rod-polymer}}$), the entropy relevant to polymer chain deformation, ($\Delta S_{\text{polymer}}$), and the energy of nanorods interactions ($\Delta G_{\text{rod-rod}}$) are essential parameters for controlling nanorod assemblies. Further hierarchical ordered patterns has been created for ternary system which contains two kinds of nanoparticles (gold and silica) conjugated with poly(styrene-*b*-ethylene propylene) copolymer.[153] This copolymer-templated assembly provides multiple perspectives toward construction of high-performance nanocomposite with characteristic nanoscale orderings.

Growth of nanoparticles can also be induced within polymer micelles and microdomains, enabling ordered nanostructure in polymer matrix.[154] Such ‘microreactor’ confined the size, and reacting environment can be modified by adding additional interactions (e.g., hydrogen bond, coordinative, acid-base) that attributed by functional groups in polymer matrix. One example is the growth of AuNPs (1 nm) within the PVP micelle of PS-*b*-PVP block copolymer by utilizing a nucleation rate that is much larger than the diffusion rate. This method can be used to create nanocomposites for catalyst recycling in catalytic reactions.

2.4.2 Polymer-assistant self-assembly

“Artificial molecules” such as nanoparticle dimers and trimers are achieved based on control over the aggregation kinetics of nanoparticles by fine tuning of the electrostatic interactions under polymer encapsulation. Firstly, AuNPs capped by hydrophobic ligands[155, 156] can self-aggregated into randomly distributed nanoparticle clusters by inducing aggregation with HCl. The assemblies were then encapsulated by

amphiphilic diblock copolymers polystyrene-*b*-poly(acrylic acid) (PS154-*b*-PAA60) in a DMF/H₂O mixture, resulted in a yield of 61% for dimers and 15% for trimers[155] (**Figure 2.17a**). The encapsulated polymer shells efficiently stabilized the nanostructure and prevented disintegration during subsequent purification and enrichment processes. However, isolation techniques are needed to get high-purity nanostructures with high yield. An efficient sedimentation method has been developed by exploiting CsCl solutions with high density. [156] The enhanced relative difference in sedimentation velocity enhanced separation purity with yields of dimers as high as 95%[156]. Subsequently, a different method was developed to prepare Ag NP dimers by introducing etching agent to Ag nanocubes with the assistance of poly(vinyl pyrrolidone) (PVP).[157] The Fe(NO₃)₃ efficiently etched the cubes into spheres and induced the dimerizing of AgNPs with yield of 66% (**Figure 2.17b**). The hotspots generated at nanogaps (~1nm) between the dimers triggered intense SERS signal on the order of ~10⁸.

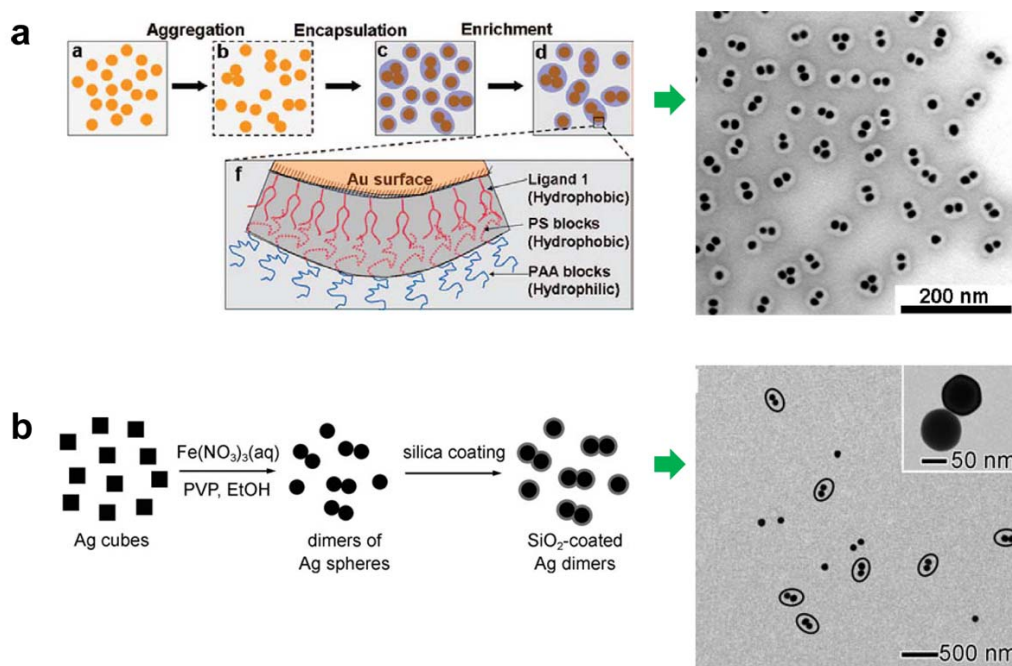


Figure 2.17 | (a) Aggregation induced dimers of AuNPs and simultaneously encapsulated by PS₁₅₄-*b*-PAA₆₀. (b) Etching agent induced dimerization with the assistance of PVP. Ag nanocubes were acting as precursor and etched into Ag nanospheres. Reproduced with permission from Ref.[155, 157] © (2008) ACS, (2010) Wiley-VCH.

2.4.3 Polymer-mediated self-assembly

Basically, two methods are developed for synthesis polymer-capped nanoparticles, namely, ‘grafting-from’ and ‘grafting-to’ approaches. For the ‘grafting-from’ method, the initiator was conjugated with particle surface and then polymer chain grows after applying polymerization.[158] However, the stability of initiator-particle bond has destroyed under high temperature, which limited this process only success under low temperature. Only mild polymerization process (e.g., ring-opening or controlled free-radical polymerization) can lead to well-dispersed polymer-capped nanoparticles.[159] Differently, the ‘grafting-to’ method was performed by reducing particle precursor under the existence of thiolated-polymers, enabling densely capping of polymer after particle formation.[140] But the presence of polymer in the reacting system may result in low uniformity of particle size and shapes. The exchange of the conventional alkane-based ligand with polymer needs fine-tuning the chemical nature of both ligands.

Based on those pioneering work, a more efficient ‘two-step grafting-to’ method was introduced for fabrication of polystyrene-capped AuNPs. Those PS-capped AuNPs can spontaneously assemble into short-range-ordered monolayers when cast onto solid substrates[142]. By independently modify the particle size or chain length of PS ligand (M_n from 3,770~66,000), the interparticle distances can be changed, enabling a tunable LSPR property that relevant to interparticular dipolar coupling. However, it is hard to arbitrarily transfer such monolayers onto other substrates, and the inevitable structure defects make it difficult to integrate membranes on a desired substrate for device applications. In this report, the conformation, capping density, thiol-footprint and hydrodynamic diameter of PS are thoroughly studied and concluded several basic rules for this system: (1) The capping density would decrease with increasing of PS chain length; (2) the average area occupied per PS ligand increases with larger PS molecular weight; (3) the PS ligand showed a brush conformation and can be treated as constrained stiff chains with a cylindrical-to-conical geometry (de Gennes’ equations).

With integration of “grafting to” and “grafting from” method, AuNPs and AuNRs capped by amphiphilic binary polymer brushes were synthesized by sequential ligand exchange and surface initiated atom transfer radical polymerization (ATRP).[160] The hybrid polymer capped AuNPs/AuNRs can self-assembly into ordered monolayers at oil/water interfaces (**Figure 2.18a**). Due to different property of polymer chains, it exhibited unique features such as stimuli-responsive assembly and disassembly with

fast kinetics and controlled interparticle distribution. With carefully controlling over solvent quality (chloroform/water/hexane percentage), PEG/PMMA-capped nanoparticle assemblies show tunable SPR responses. Owing to pH responsive property of PDEA, PEG/PDEA-capped nanoparticle formed variable structures at different pH. Such sequential surface modification technique give rise to hybrid polymer induced interfacial assembly. By changing polymer property, pH-variation and solvent quality controllable assembly can be achieved, enabling new ways for programmable plasmonic properties of superlattice.

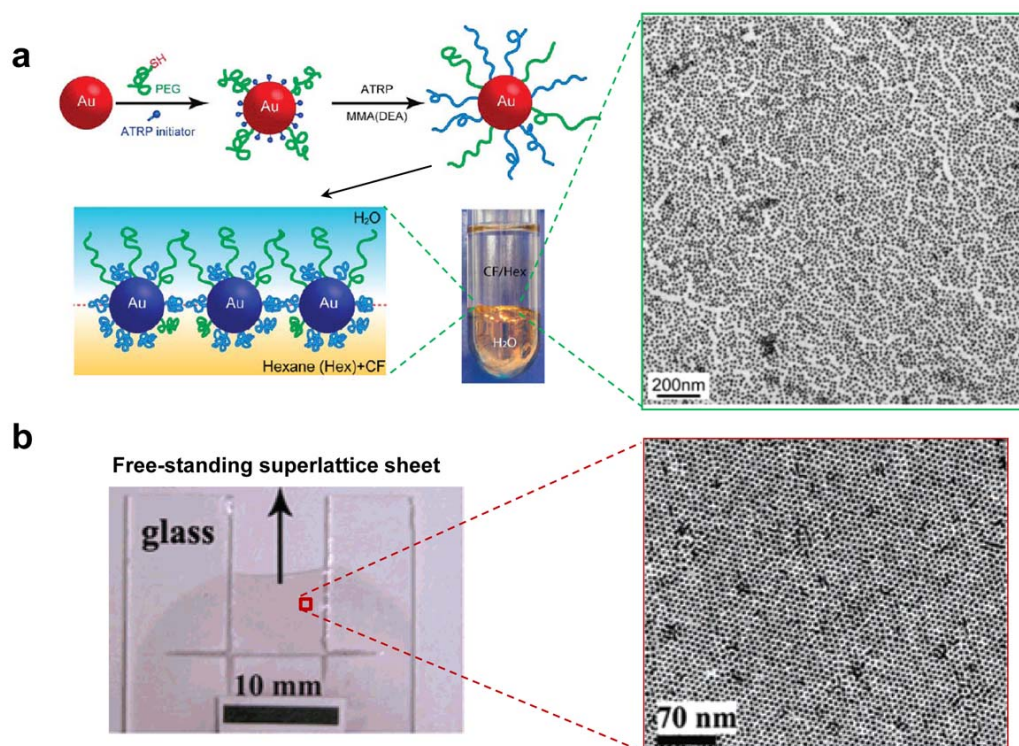


Figure 2.18 | (a) Schematic illustration of the synthesis of PEG/PMMA-capped AuNPs. It was achieved by sequentially combined “grafting to” (conjugation of PEG and ATRP initiator to particle surface) and “grafting from” (surface-initiated polymerization). Monolayer was formed at oil/water interface. (b) Free-standing superlattice membrane with area of 1 cm². TEM image shows ordered array of AuNPs. Reproduced with permission from Ref. [12, 160] © (2008&2010) ACS.

A myriad of design strategies have been sought for utilizing polymer-capped nanoparticle to construct 2D superlattice membrane, including evaporation-mediated assembly, LB technique, and interfacial self-assembly. It allows the growth of large area monolayers with highly ordered structure that combine the desirable properties of nanoparticles and polymers[143]. As an example, polymethylmethacrylate (PMMA) capped AuNPs (5.5 nm) can assembly into free-standing membrane under the evaporation-driven polymer solidification at air/water interface (**Figure 2.18b**).[12] In

this case the ordered AuNPs/PMMA nanocomposite monolayer can reach a physical dimension of 10 cm². This AuNPs/PMMA monolayer is transferable to arbitrary substrates and remains stable as a free-standing membrane suspended over centimeter-sized holes. Moreover, the PMMA serves as a photoresist enabling two modes of electron beam patterning, and the e-beam exposed area can be preserved after treatment of hexane and toluene.

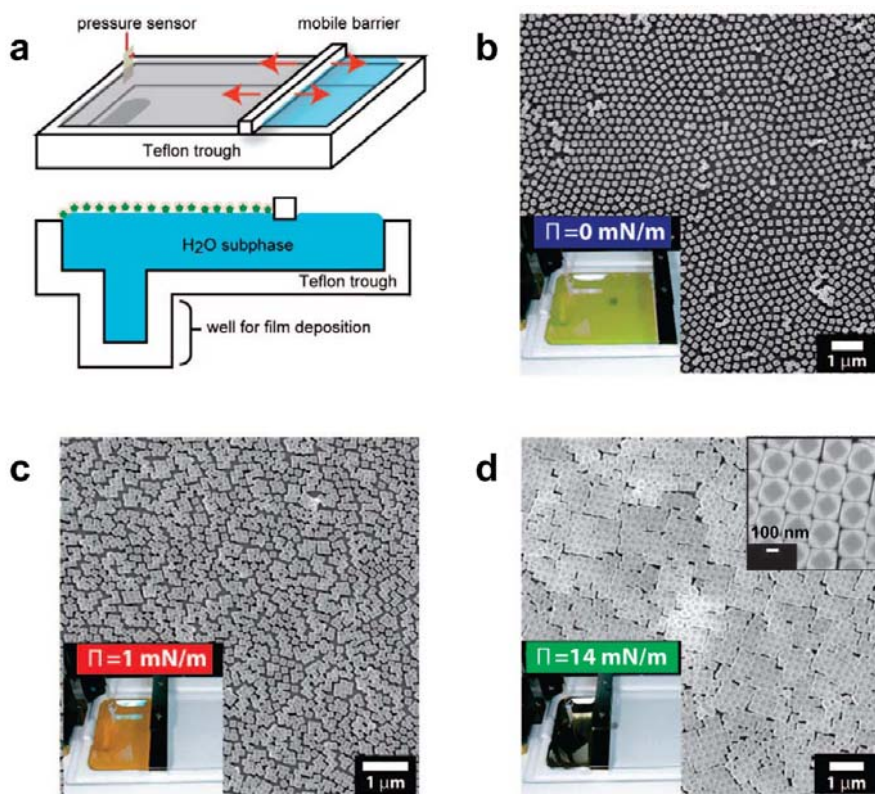


Figure 2.19 | (a) Schematic illustration of Langmuir-Blodgett trough. (b-d) SEM images and inset optical images show tunable interparticle distances and plasmon responses of superlattice membrane formed by Ag cuboctahedra. Reproduced with permission from Ref. [13, 161]. © (2008) ACS and (2007) NPG.

Combined with Langmuir-Blodgett (LB) techniques, polymer-based nanoparticles can assemble into various superlattices with high ordering at the air-water interface.[161] In this way, nanoscale assembly can be tuned upon controlling of macroscopic parameters such as surface pressure, and compressing speed. In one report, PVP capped Ag nanocrystals (including truncated cubes, cuboctahedra, and octahedra) were organized into densely packed 2D superlattices with tunable plasmonic properties (**Figure 2.19**).[13] For example, the cuboctahedra superlattice shows different SPR bands at various surface pressures. At low pressure and loose packing, single SPR band ascribed to quadrupolar mode coupling dominated the spectrum, and blue-shifted with

increasing surface pressure, indicating strong near-field interactions. With further compressing, higher-order mode coupling induced SPR bands at low wavelength, and new broad band associated with plasmon delocalization would appear at ~ 600 nm.

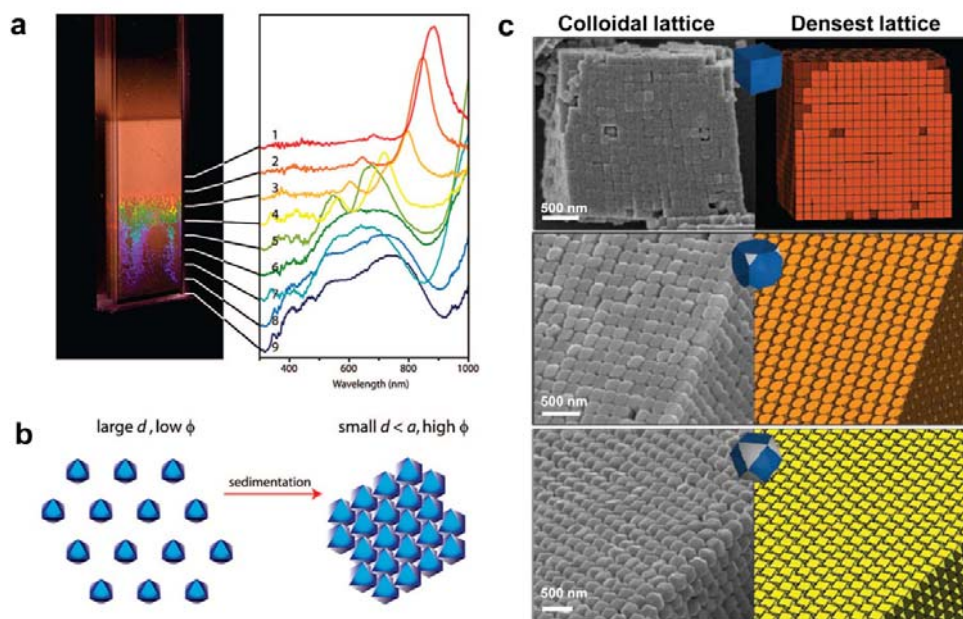


Figure 2.20 | (a) Optical image of sedimentation-driven assembly of Ag octahedron into 3D supercrystals at bottom of cuvette. Reflectance spectra collected at different height indicated structure difference. (b) Scheme shows the supercrystal formation. (c) SEM images and corresponding scheme of densest lattice packing of Ag cubes, truncated cubes and cuboctahedra. Reproduced with permission from Ref.[24, 162]. © (2008) ACS and (2011) NPG.

Compared with linear polymer ligand, amphiphilic branch copolymer may facilitate monolayer formation through vertical segregation of different polymer arms. In one example, V-shaped polybutadiene-poly(ethylene glycol) (PB-PEG) was capped on AuNPs (2 nm) and formed ordered monolayer using LB technique. But the pancake shaped nanostructure only reaches a maximum lateral dimension of $10 \mu\text{m}$. [145] A more concentrated nanoparticle solution should be used to spread on air/water interface to get large-scale monolayer. By using ‘grafting-from’ method, PMMA-capped AuNPs were synthesized by the surface-initiated living radical polymerization, and formed monolayer superlattice on air/water interface after LB compressing. [158] The controlled growth of chain length decided the interparticle distances in superlattice. The analysis on interparticle distances and PMMA grafting lengths reveals that the PMMA was fully stretched during assembly, arising from high-density capping and brush conformation. This flexible pathway enables control over optical response of polymer-

capped nanoparticles, and facilitates the transfer and manipulate of metallic nanostructure arrays into highly integrated and hierarchically organized nanodevices.

To avoid non-uniform fluctuations and severe salvation forces in drying-mediated assembly, sedimentation-driven assembly is proved to be a facile way to fabricate large-scale supercrystals of polyhedral nanoparticles with conjectured densest packings.[24, 162] In this assembly scheme, PVP stabilized Ag nanocrystals (cubes, truncated cubes, cuboctahedra, truncated octahedra and octahedral) were loaded in a designed PDMS reservoir and formed dense supercrystals by gravitational sedimentation (**Figure 2.20**). The assembly indicates that nanoparticles are more like entirely hard and non-attractive polyhedral. This can be explained by the repulsion induced from the PVP layers. The strong entropic repulsion balanced with vdW attraction of particle cores. Acting as depleting agents, free polymer chains in solution mediate substantial attractions between polymer-capped nanoparticles.

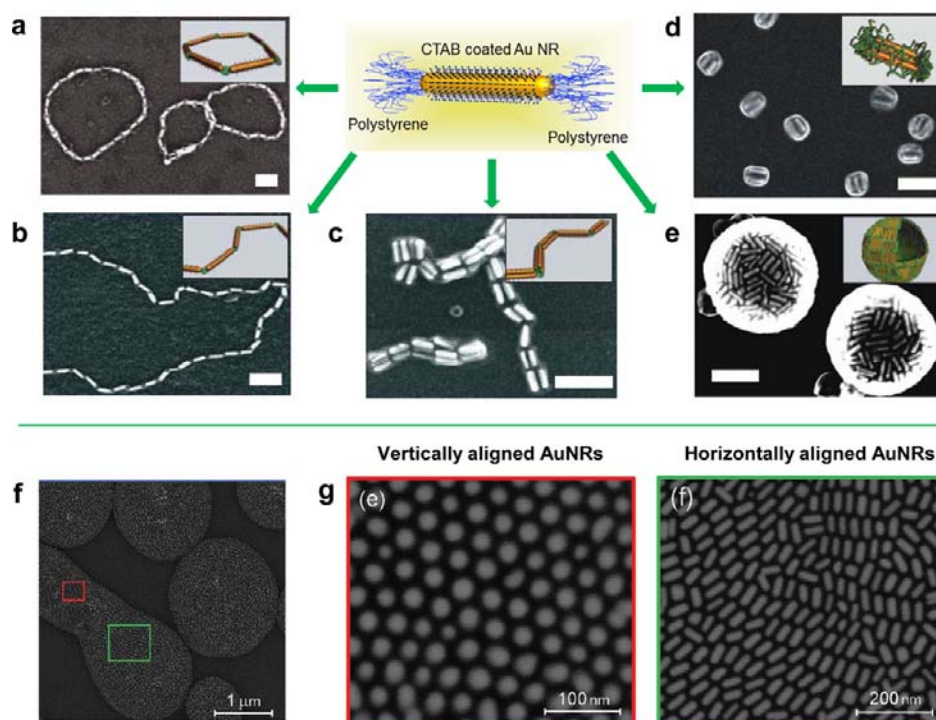


Figure 2.21 | (a-e) Nanostructures self-assembled by AuNRs with end-capped polystyrene and side-capped CTAB. SEM images show the structures of (a) rings, (b) chains, (c) bundled chains, (d) side-to-side bundles, (e) microspheres. (f) SEM image of AuNRs superlattice membrane. (g) High magnification images show vertically aligned monolayer (V-sheets) and horizontally aligned monolayer (H-sheets). Reproduced with permission from Ref.[8, 55]. © (2007) NPG, (2011) ACS.

Site-specific asymmetric functionalization of nanoparticle by using polymer lead to self-assembly of varying geometries. As described in previous section, amphiphilic AuNRs with longitudinal side-capped CTAB and end-capped hydrophobic polystyrene can be used as general building blocks for construction of various nanostructures (**Figure 2.21a-e**). Self-assembly was simply triggered by adding water to organic solvent containing AuNRs. In the DMF/water mixture, AuNRs assembled into rings and chain-like nanostructure with end-to-end connection of PS ligand. Whereas in THF/water mixture, the AuNRs aligned side-by-side and formed bundled-chains, aggregated balls and microspheres.[55] The selective hydrophilic and hydrophobic property induced from CTAB and PS guided the geometry of nanostructures. This method established a straightforward approach to the quantitative prediction of the structural characteristics and LSPR properties of linear, branched, ring/bundle-shaped ensembles of AuNRs. [81]

In contrast to the significant progress achieved in the construction of superlattices from nanospheres, much less success has been reported for nonspherical building blocks. A simple yet robust polymer ligand-based approach has been reported to assemble plasmonic AuNRs into two types of ordered superlattice sheets, which aligned horizontally into superlattice monolayer sheets (H-sheets) or vertically into superlattice monolayer sheets (V-sheets) (**Figure 2.21f and g**)[8]. Both sheets can be controlled at the monolayer level (*i.e.*, 31.3 ± 0.3 and 63.6 ± 2.1 nm for H- and V-sheets, respectively), with lateral dimensions in the submillimeter scale. The nanosheets display distinct spectral features dependent on the nanorod orientations, spacing, and size. These features are explained by the difference in plasmon modes excited on the sheets, which are confirmed through discrete-dipole-approximation (DDA) calculations. This general and facile polymer-ligand-based strategy can be applied to other anisotropic building blocks, thus serving as a promising method to fabricate free-standing superlattice membranes for various applications in nanophotonic devices and sensors.

2.5 References

1. Cheng, W.L., Campolongo, M.J., Cha, J.J., Tan, S.J., Umbach, C.C., Muller, D.A. and Luo, D. Free-standing nanoparticle superlattice sheets controlled by DNA. *Nature Mater.* **8**, 519-525 (2009).

2. Dong, A.G., Chen, J., Vora, P.M., Kikkawa, J.M. and Murray, C.B. Binary nanocrystal superlattice membranes self-assembled at the liquid-air interface. *Nature* **466**, 474-477 (2010).
3. Cheng, W.L., Campolongo, M.J., Tan, S.J. and Luo, D. Freestanding ultrathin nano-membranes via self-assembly. *Nano Today* **4**, 482-493 (2009).
4. Tan, S.J., Campolongo, M.J., Luo, D. and Cheng, W.L. Building plasmonic nanostructures with DNA. *Nature Nanotech.* **6**, 268-276 (2011).
5. Mueggenburg, K.E., Lin, X.M., Goldsmith, R.H. and Jaeger, H.M. Elastic membranes of close-packed nanoparticle arrays. *Nature Mater.* **6**, 656-660 (2007).
6. Chen, Y., Fu, J., Ng, K.C., Tang, Y. and Cheng, W.L. Free-Standing Polymer-Nanoparticle Superlattice Sheets Self-Assembled at the Air Liquid Interface. *Crystal Growth & Design* **11**, 4742-4746 (2011).
7. Chen, Y., Ouyang, Z., Gu, M. and Cheng, W. Mechanically Strong, Optically Transparent, Giant Metal Superlattice Nanomembranes From Ultrathin Gold Nanowires. *Adv. Mater.* **25**, 80-85 (2013).
8. Ng, K.C., Udagedara, I.B., Rukhlenko, I.D., Chen, Y., Tang, Y., Premaratne, M. and Cheng, W.L. Free-Standing Plasmonic-Nanorod Superlattice Sheets. *ACS Nano* **6**, 925-934 (2011).
9. Dong, A.G., Ye, X.C., Chen, J. and Murray, C.B. Two-Dimensional Binary and Ternary Nanocrystal Superlattices: The Case of Monolayers and Bilayers. *Nano Lett.* **11**, 1804-1809 (2011).
10. He, J., Lin, X.-M., Chan, H., Vuković, L., Král, P. and Jaeger, H.M. Diffusion and Filtration Properties of Self-Assembled Gold Nanocrystal Membranes. *Nano Lett.* **11**, 2430-2435 (2011).
11. Liao, J., Zhou, Y., Huang, C., Wang, Y. and Peng, L. Fabrication, Transfer, and Transport Properties of Monolayered Freestanding Nanoparticle Sheets. *Small* **7**, 583-587 (2011).
12. Pang, J., Xiong, S., Jaeckel, F., Sun, Z., Dunphy, D. and Brinker, C.J. Free-Standing, Patternable Nanoparticle/Polymer Monolayer Arrays Formed by Evaporation Induced Self-Assembly at a Fluid Interface. *J. Am. Chem. Soc* **130**, 3284-3285 (2008).
13. Tao, A., Sinsersuksakul, P. and Yang, P. Tunable plasmonic lattices of silver nanocrystals. *Nature Nanotech.* **2**, 435-440 (2007).
14. Bigioni, T.P., Lin, X.M., Nguyen, T.T., Corwin, E.I., Witten, T.A. and Jaeger, H.M. Kinetically driven self assembly of highly ordered nanoparticle monolayers. *Nature Mater.* **5**, 265-270 (2006).
15. Collier, C.P., Saykally, R.J., Shiang, J.J., Henrichs, S.E. and Heath, J.R. Reversible tuning of silver quantum dot monolayers through the metal-insulator transition. *Science* **277**, 1978-1981 (1997).
16. Courty, A., Mermet, A., Albouy, P.A., Duval, E. and Pileni, M.P. Vibrational coherence of self-organized silver nanocrystals in f.c.c. supra-crystals. *Nature Mater.* **4**, 395-398 (2005).
17. Kiely, C.J., Fink, J., Brust, M., Bethell, D. and Schiffrin, D.J. Spontaneous ordering of bimodal ensembles of nanoscopic gold clusters. *Nature* **396**, 444-446 (1998).
18. Park, S.Y., Lytton-Jean, A.K.R., Lee, B., Weigand, S., Schatz, G.C. and Mirkin, C.A. DNA-programmable nanoparticle crystallization. *Nature* **451**, 553-556 (2008).

19. Talapin, D.V., Lee, J.-S., Kovalenko, M.V. and Shevchenko, E.V. Prospects of Colloidal Nanocrystals for Electronic and Optoelectronic Applications. *Chem. Rev.* **110**, 389-458 (2009).
20. Tang, Z., Zhang, Z., Wang, Y., Glotzer, S.C. and Kotov, N.A. Self-Assembly of CdTe Nanocrystals into Free-Floating Sheets. *Science* **314**, 274-278 (2006).
21. Whetten, R.L., Houry, J.T., Alvarez, M.M., Murthy, S., Vezmar, I. *et al.* Nanocrystal gold molecules. *Adv. Mater.* **8**, 428-433 (1996).
22. Auyeung, E., Cutler, J.I., Macfarlane, R.J., Jones, M.R., Wu, J., Liu, G., Zhang, K., Osberg, K.D. and Mirkin, C.A. Synthetically programmable nanoparticle superlattices using a hollow three-dimensional spacer approach. *Nature Nanotech.* **7**, 24-28 (2012).
23. Cheng, W.L., Hartman, M.R., Smilgies, D.-M., Long, R., Campolongo, M.J., Li, R., Sekar, K., Hui, C.-Y. and Luo, D. Probing in Real Time the Soft Crystallization of DNA-Capped Nanoparticles. *Angew. Chem. Int. Ed.* **49**, 380-384 (2010).
24. Henzie, J., Grünwald, M., Widmer-Cooper, A., Geissler, P.L. and Yang, P. Self-assembly of uniform polyhedral silver nanocrystals into densest packings and exotic superlattices. *Nature Mater.* **11**, 131-137 (2012).
25. Korgel, B.A. Nanocrystal Superlattices Assembly at Liquid Interfaces. *Nature Mater.* **9**, 701-703 (2010).
26. Kostianen, M.A., Hiekkataipale, P., Laiho, A., Lemieux, V., Seitsonen, J., Ruokolainen, J. and Ceci, P. Electrostatic assembly of binary nanoparticle superlattices using protein cages. *Nature Nanotech.* **8**, 52-56 (2013).
27. Nykypanchuk, D., Maye, M.M., van der Lelie, D. and Gang, O. DNA-guided crystallization of colloidal nanoparticles. *Nature* **451**, 549-552 (2008).
28. Redl, F.X., Cho, K.S., Murray, C.B. and O'Brien, S. Three-dimensional binary superlattices of magnetic nanocrystals and semiconductor quantum dots. *Nature* **423**, 968-971 (2003).
29. Talapin, D.V., Shevchenko, E.V., Bodnarchuk, M.I., Ye, X., Chen, J. and Murray, C.B. Quasicrystalline order in self-assembled binary nanoparticle superlattices. *Nature* **461**, 964-967 (2009).
30. Chen, C.-F., Tzeng, S.-D., Chen, H.-Y., Lin, K.-J. and Gwo, S. Tunable Plasmonic Response from Alkanethiolate-Stabilized Gold Nanoparticle Superlattices: Evidence of Near-Field Coupling. *J. Am. Chem. Soc.* **130**, 824-826 (2007).
31. Ye, X., Chen, J., Diroll, B.T. and Murray, C.B. Tunable Plasmonic Coupling in Self-Assembled Binary Nanocrystal Superlattices Studied by Correlated Optical Microspectrophotometry and Electron Microscopy. *Nano Lett.* **13**, 1291-1297 (2013).
32. Frens, G. Controlled Nucleation for the Regulation of the Particle Size in Monodisperse Gold Suspensions. *Nature, Phys. Sci.* **241**, 20 (1973).
33. Jana, N.R., Gearheart, L. and Murphy, C.J. Seeding Growth for Size Control of 5–40 nm Diameter Gold Nanoparticles. *Langmuir* **17**, 6782-6786 (2001).
34. Millstone, J.E., Park, S., Shuford, K.L., Qin, L., Schatz, G.C. and Mirkin, C.A. Observation of a Quadrupole Plasmon Mode for a Colloidal Solution of Gold Nanoprisms. *J. Am. Chem. Soc.* **127**, 5312-5313 (2005).
35. Nikoobakht, B. and El-Sayed, M.A. Preparation and Growth Mechanism of Gold Nanorods (NRs) Using Seed-Mediated Growth Method. *Chem. Mater.* **15**, 1957-1962 (2003).

36. Perrault, S.D. and Chan, W.C.W. Synthesis and Surface Modification of Highly Monodispersed, Spherical Gold Nanoparticles of 50–200 nm. *J. Am. Chem. Soc.* **131**, 17042-17043 (2009).
37. Xia, Y., Xiong, Y., Lim, B. and Skrabalak, S.E. Shape-Controlled Synthesis of Metal Nanocrystals: Simple Chemistry Meets Complex Physics? *Angew. Chem. Int. Ed.* **48**, 60-103 (2009).
38. Alivisatos, A.P., Johnsson, K.P., Peng, X., Wilson, T.E., Loweth, C.J., Bruchez Jr, M.P. and Schultz, P.G. Organization of 'nanocrystal molecules' using DNA. *Nature* **382**, 609-611 (1996).
39. Maye, M.M., Kumara, M.T., Nykypanchuk, D., Sherman, W.B. and Gang, O. Switching binary states of nanoparticle superlattices and dimer clusters by DNA strands. *Nature Nanotechnol.* **5**, 116-120 (2010).
40. Chen, Y. and Cheng, W.L. DNA-based plasmonic nanoarchitectures: from structural design to emerging applications. *WIREs Nanomed. Nanobiotechnol.* **4**, 587-604 (2012).
41. Liu, K., Nie, Z., Zhao, N., Li, W., Rubinstein, M. and Kumacheva, E. Step-Growth Polymerization of Inorganic Nanoparticles. *Science* **329**, 197-200 (2010).
42. Heitsch, A.T., Patel, R.N., Goodfellow, B.W., Smilgies, D.-M. and Korgel, B.A. GISAXS characterization of order in hexagonal monolayers of FePt nanocrystals. *J. Phys. Chem. C* **114**, 14427-14432 (2010).
43. Jones, M.R., Macfarlane, R.J., Lee, B., Zhang, J., Young, K.L., Senesi, A.J. and Mirkin, C.A. DNA-nanoparticle superlattices formed from anisotropic building blocks. *Nature Mater.* **9**, 913-917 (2010).
44. Macfarlane, R.J., Jones, M.R., Senesi, A.J., Young, K.L., Lee, B., Wu, J. and Mirkin, C.A. Establishing the Design Rules for DNA-Mediated Programmable Colloidal Crystallization. *Angew. Chem. Int. Ed.* **49**, 4589-4592 (2010).
45. Macfarlane, R.J., Lee, B., Jones, M.R., Harris, N., Schatz, G.C. and Mirkin, C.A. Nanoparticle Superlattice Engineering with DNA. *Science* **334**, 204-208 (2011).
46. Pileni, M.-P. Self-assembly of inorganic nanocrystals: fabrication and collective intrinsic properties. *Acc. Chem. Res.* **40**, 685-693 (2007).
47. Jones, M.R., Osberg, K.D., Macfarlane, R.J., Langille, M.R. and Mirkin, C.A. Templated Techniques for the Synthesis and Assembly of Plasmonic Nanostructures. *Chem. Rev.* **111**, 3736-3827 (2011).
48. Bishop, K.J.M., Wilmer, C.E., Soh, S. and Grzybowski, B.A. Nanoscale Forces and Their Uses in Self-Assembly. *Small* **5**, 1600-1630 (2009).
49. Sánchez-Iglesias, A., Grzelczak, M., Pérez-Juste, J. and Liz-Marzán, L.M. Binary Self-Assembly of Gold Nanowires with Nanospheres and Nanorods. *Angew. Chem. Int. Ed.* **49**, 9985-9989 (2010).
50. Auyeung, E., Li, T.I.N.G., Senesi, A.J., Schmucker, A.L., Pals, B.C., de la Cruz, M.O. and Mirkin, C.A. DNA-mediated nanoparticle crystallization into Wulff polyhedra. *Nature in press*, 10.1038/nature12739 (2013).
51. Hung, A.M., Micheel, C.M., Bozano, L.D., Osterbur, L.W., Wallraff, G.M. and Cha, J.N. Large-area spatially ordered arrays of gold nanoparticles directed by lithographically confined DNA origami. *Nature Nanotech.* **5**, 121-126 (2010).
52. Sharma, J., Chhabra, R., Cheng, A., Brownell, J., Liu, Y. and Yan, H. Control of Self-Assembly of DNA Tubules Through Integration of Gold Nanoparticles. *Science* **323**, 112-116 (2009).

53. Young, K.L., Ross, M.B., Blaber, M.G., Rycenga, M., Jones, M.R. *et al.* Using DNA to Design Plasmonic Metamaterials with Tunable Optical Properties. *Adv. Mater.*, in press (2013).
54. Lopes, W.A. and Jaeger, H.M. Hierarchical self-assembly of metal nanostructures on diblock copolymer scaffolds. *Nature* **414**, 735-738 (2001).
55. Nie, Z., Fava, D., Kumacheva, E., Zou, S., Walker, G.C. and Rubinstein, M. Self-assembly of metal-polymer analogues of amphiphilic triblock copolymers. *Nature Mater.* **6**, 609-614 (2007).
56. Alder, B.J. and Wainwright, T.E. Phase Transition for a Hard Sphere System. *J. Chem. Phys.* **27**, 1208-1209 (1957).
57. Pusey, P.N. and van Megen, W. Phase behaviour of concentrated suspensions of nearly hard colloidal spheres. *Nature* **320**, 340-342 (1986).
58. Korgel, B.A. and Fitzmaurice, D. Condensation of Ordered Nanocrystal Thin Films. *Phys. Rev. Lett.* **80**, 3531-3534 (1998).
59. Korgel, B.A., Fullam, S., Connolly, S. and Fitzmaurice, D. Assembly and Self-Organization of Silver Nanocrystal Superlattices: Ordered “Soft Spheres”. *J. Phys. Chem. B* **102**, 8379-8388 (1998).
60. Weddemann, A., Ennen, I., Regtmeier, A., Albon, C., Wolff, A. *et al.* Review and outlook: from single nanoparticles to self-assembled monolayers and granular GMR sensors. *Beilstein J. Nanotechnol.* **1**, 75-93 (2010).
61. Hamaker, H.C. The London—van der Waals attraction between spherical particles. *Physica* **4**, 1058-1072 (1937).
62. de Gennes, P.G. Polymers at an interface; a simplified view. *Adv. Colloid Interface Sci.* **27**, 189-209 (1987).
63. Shevchenko, E.V., Talapin, D.V., Kotov, N.A., O'Brien, S. and Murray, C.B. Structural diversity in binary nanoparticle superlattices. *Nature* **439**, 55-59 (2006).
64. Sun, Z., Luo, Z. and Fang, J. Assembling Nonspherical 2D Binary Nanoparticle Superlattices by Opposite Electrical Charges: The Role of Coulomb Forces. *ACS Nano* **4**, 1821-1828 (2010).
65. Talapin, D.V., Shevchenko, E.V., Murray, C.B., Titov, A.V. and Král, P. Dipole–Dipole Interactions in Nanoparticle Superlattices. *Nano Lett.* **7**, 1213-1219 (2007).
66. Mirkin, C.A., Letsinger, R.L., Mucic, R.C. and Storhoff, J.J. A DNA-based method for rationally assembling nanoparticles into macroscopic materials. *Nature* **382**, 607-609 (1996).
67. de Gennes, P.G. Conformations of Polymers Attached to an Interface. *Macromolecules* **13**, 1069-1075 (1980).
68. Jin, R., Wu, G., Li, Z., Mirkin, C.A. and Schatz, G.C. What Controls the Melting Properties of DNA-Linked Gold Nanoparticle Assemblies? *J. Am. Chem. Soc.* **125**, 1643-1654 (2003).
69. Jin, J., Wakayama, Y., Peng, X. and Ichinose, I. Surfactant-assisted fabrication of free-standing inorganic sheets covering an array of micrometre-sized holes. *Nature Mater.* **6**, 686-691 (2007).
70. Xu, L., Ma, W., Wang, L., Xu, C., Kuang, H. and Kotov, N.A. Nanoparticle assemblies: dimensional transformation of nanomaterials and scalability. *Chem. Soc. Rev.* **42**, 3114-3126 (2013).
71. Nie, Z., Petukhova, A. and Kumacheva, E. Properties and emerging applications of self-assembled structures made from inorganic nanoparticles. *Nature Nanotech.* **5**, 15-25 (2010).

72. Gong, J., Li, G. and Tang, Z. Self-assembly of noble metal nanocrystals: Fabrication, optical property, and application. *Nano Today* **7**, 564-585 (2012).
73. Prasad, B.L.V., Stoeva, S.I., Sorensen, C.M. and Klabunde, K.J. Digestive-Ripening Agents for Gold Nanoparticles: Alternatives to Thiols. *Chem. Mater.* **15**, 935-942 (2003).
74. Prasad, B.L.V., Stoeva, S.I., Sorensen, C.M. and Klabunde, K.J. Digestive Ripening of Thiolated Gold Nanoparticles: The Effect of Alkyl Chain Length. *Langmuir* **18**, 7515-7520 (2002).
75. Fink, J., Kiely, C.J., Bethell, D. and Schiffrin, D.J. Self-Organization of Nanosized Gold Particles. *Chem. Mater.* **10**, 922-926 (1998).
76. Martin, J.E., Wilcoxon, J.P., Odinek, J. and Provencio, P. Control of the Interparticle Spacing in Gold Nanoparticle Superlattices. *J. Phys. Chem. B* **104**, 9475-9486 (2000).
77. Ong, W.-L., Rupich, S.M., Talapin, D.V., McGaughey, A.J.H. and Malen, J.A. Surface chemistry mediates thermal transport in three-dimensional nanocrystal arrays. *Nature Mater.* **12**, 410-415 (2013).
78. Bai, X., Ma, H., Li, X., Dong, B. and Zheng, L. Patterns of Gold Nanoparticles Formed at the Air/Water Interface: Effects of Capping Agents. *Langmuir* **26**, 14970-14974 (2010).
79. Rycenga, M., McLellan, J.M. and Xia, Y. Controlling the Assembly of Silver Nanocubes through Selective Functionalization of Their Faces. *Adv. Mater.* **20**, 2416-2420 (2008).
80. Liu, K., Zhao, N. and Kumacheva, E. Self-assembly of inorganic nanorods. *Chem. Soc. Rev.* **40**, 656-671 (2011).
81. Liu, K., Ahmed, A., Chung, S., Sugikawa, K., Wu, G., Nie, Z., Gordon, R. and Kumacheva, E. In Situ Plasmonic Counter for Polymerization of Chains of Gold Nanorods in Solution. *ACS Nano* **7**, 5901-5910 (2013).
82. Schultz, D.G., Lin, X.-M., Li, D., Gebhardt, J., Meron, M., Viccaro, J. and Lin, B. Structure, Wrinkling, and Reversibility of Langmuir Monolayers of Gold Nanoparticles. *J. Phys. Chem. B* **110**, 24522-24529 (2006).
83. Lin, X.M., Jaeger, H.M., Sorensen, C.M. and Klabunde, K.J. Formation of Long-Range-Ordered Nanocrystal Superlattices on Silicon Nitride Substrates. *J. Phys. Chem. B* **105**, 3353-3357 (2001).
84. Quan, Z. and Fang, J. Superlattices with non-spherical building blocks. *Nano Today* **5**, 390-411 (2010).
85. Miszta, K., de Graaf, J., Bertoni, G., Dorfs, D., Brescia, R. *et al.* Hierarchical self-assembly of suspended branched colloidal nanocrystals into superlattice structures. *Nature Mater.* **10**, 872-876 (2011).
86. Rupich, S.M. and Talapin, D.V. Colloidal self-assembly: Interlocked octapods. *Nature Mater.* **10**, 815-816 (2011).
87. He, J., Kanjanaboos, P., Frazer, N.L., Weis, A., Lin, X.-M. and Jaeger, H.M. Fabrication and Mechanical Properties of Large-Scale Freestanding Nanoparticle Membranes. *Small* **6**, 1449-1456 (2010).
88. Tran, T.B., Beloborodov, I.S., Hu, J., Lin, X.M., Rosenbaum, T.F. and Jaeger, H.M. Sequential tunneling and inelastic cotunneling in nanoparticle arrays. *Phys. Rev. B* **78**, 075437 (2008).
89. Lin, Y., Skaff, H., Böker, A., Dinsmore, A.D., Emrick, T. and Russell, T.P. Ultrathin Cross-Linked Nanoparticle Membranes. *J. Am. Chem. Soc* **125**, 12690-12691 (2003).

90. Su, B., Wu, Y., Tang, Y., Chen, Y., Cheng, W. and Jiang, L. Free-Standing 1D Assemblies of Plasmonic Nanoparticles. *Adv. Mater.*, n/a-n/a (2013).
91. Shevchenko, E.V., Talapin, D.V., Murray, C.B. and O'Brien, S. Structural Characterization of Self-Assembled Multifunctional Binary Nanoparticle Superlattices. *J. Am. Chem. Soc* **128**, 3620-3637 (2006).
92. Bodnarchuk, M.I., Shevchenko, E.V. and Talapin, D.V. Structural Defects in Periodic and Quasicrystalline Binary Nanocrystal Superlattices. *J. Am. Chem. Soc* **133**, 20837-20849 (2011).
93. Pichler, S., Bodnarchuk, M.I., Kovalenko, M.V., Yarema, M., Springholz, G., Talapin, D.V. and Heiss, W. Evaluation of Ordering in Single-Component and Binary Nanocrystal Superlattices by Analysis of Their Autocorrelation Functions. *ACS Nano* **5**, 1703-1712 (2011).
94. Wang, L., Xu, L., Kuang, H., Xu, C. and Kotov, N.A. Dynamic Nanoparticle Assemblies. *Acc. Chem. Res.* **45**, 1916-1926 (2012).
95. Xia, Y., Nguyen, T.D., Yang, M., Lee, B., Santos, A., Podsiadlo, P., Tang, Z., Glotzer, S.C. and Kotov, N.A. Self-assembly of self-limiting monodisperse supraparticles from polydisperse nanoparticles. *Nature Nanotech.* **6**, 580-587 (2011).
96. Loweth, C.J., Caldwell, W.B., Peng, X., Alivisatos, A.P. and Schultz, P.G. DNA-Based Assembly of Gold Nanocrystals. *Angew. Chem. Int. Ed.* **38**, 1808-1812 (1999).
97. Mastroianni, A.J., Claridge, S.A. and Alivisatos, A.P. Pyramidal and Chiral Groupings of Gold Nanocrystals Assembled Using DNA Scaffolds. *J. Am. Chem. Soc* **131**, 8455-8459 (2009).
98. Xu, X., Rosi, N.L., Wang, Y., Huo, F. and Mirkin, C.A. Asymmetric Functionalization of Gold Nanoparticles with Oligonucleotides. *J. Am. Chem. Soc* **128**, 9286-9287 (2006).
99. Lim, D.-K., Jeon, K.-S., Kim, H.M., Nam, J.-M. and Suh, Y.D. Nanogap-engineerable Raman-active nanodumbbells for single-molecule detection. *Nature Mater.* **9**, 60-67 (2010).
100. Fan, J.A., He, Y., Bao, K., Wu, C., Bao, J. *et al.* DNA-Enabled Self-Assembly of Plasmonic Nanoclusters. *Nano Lett.* **11**, 4859-4864 (2011).
101. Maye, M.M., Nykypanchuk, D., Cuisinier, M., van der Lelie, D. and Gang, O. Stepwise surface encoding for high-throughput assembly of nanoclusters. *Nature Mater.* **8**, 388-391 (2009).
102. Xu, L., Kuang, H., Xu, C., Ma, W., Wang, L. and Kotov, N.A. Regiospecific Plasmonic Assemblies for in Situ Raman Spectroscopy in Live Cells. *J. Am. Chem. Soc* **134**, 1699-1709 (2011).
103. Chen, W., Bian, A., Agarwal, A., Liu, L., Shen, H., Wang, L., Xu, C. and Kotov, N.A. Nanoparticle Superstructures Made by Polymerase Chain Reaction: Collective Interactions of Nanoparticles and a New Principle for Chiral Materials. *Nano Lett.* **9**, 2153-2159 (2009).
104. Deng, Z., Tian, Y., Lee, S.-H., Ribbe, A.E. and Mao, C. DNA-Encoded Self-Assembly of Gold Nanoparticles into One-Dimensional Arrays. *Angew. Chem. Int. Ed.* **44**, 3582-3585 (2005).
105. Zhao, W., Gao, Y., Kandadai, S.A., Brook, M.A. and Li, Y. DNA Polymerization on Gold Nanoparticles through Rolling Circle Amplification: Towards Novel Scaffolds for Three-Dimensional Periodic Nanoassemblies. *Angew. Chem. Int. Ed.* **45**, 2409-2413 (2006).

106. Wang, G. and Murray, R.W. Controlled Assembly of Monolayer-Protected Gold Clusters by Dissolved DNA. *Nano Lett.* **4**, 95-101 (2003).
107. Aldaye, F.A. and Sleiman, H.F. Dynamic DNA Templates for Discrete Gold Nanoparticle Assemblies: Control of Geometry, Modularity, Write/Erase and Structural Switching. *J. Am. Chem. Soc.* **129**, 4130-4131 (2007).
108. Pal, S., Deng, Z., Ding, B., Yan, H. and Liu, Y. DNA-Origami-Directed Self-Assembly of Discrete Silver-Nanoparticle Architectures. *Angew. Chem. Int. Ed.* **49**, 2700-2704 (2010).
109. Ding, B., Deng, Z., Yan, H., Cabrini, S., Zuckermann, R.N. and Bokor, J. Gold Nanoparticle Self-Similar Chain Structure Organized by DNA Origami. *J. Am. Chem. Soc.* **132**, 3248-3249 (2010).
110. Pal, S., Deng, Z., Wang, H., Zou, S., Liu, Y. and Yan, H. DNA Directed Self-Assembly of Anisotropic Plasmonic Nanostructures. *J. Am. Chem. Soc.* **133**, 17606-17609 (2011).
111. Lo, P.K., Karam, P., Aldaye, F.A., McLaughlin, C.K., Hamblin, G.D., Cosa, G. and Sleiman, H.F. Loading and selective release of cargo in DNA nanotubes with longitudinal variation. *Nat Chem* **2**, 319-328 (2010).
112. Shen, X., Song, C., Wang, J., Shi, D., Wang, Z., Liu, N. and Ding, B. Rolling Up Gold Nanoparticle-Dressed DNA Origami into Three-Dimensional Plasmonic Chiral Nanostructures. *J. Am. Chem. Soc.* **134**, 146-149 (2011).
113. Kuzyk, A., Schreiber, R., Fan, Z., Pardatscher, G., Roller, E.-M., Hogele, A., Simmel, F.C., Govorov, A.O. and Liedl, T. DNA-based self-assembly of chiral plasmonic nanostructures with tailored optical response. *Nature* **483**, 311-314 (2012).
114. Zheng, J., Constantinou, P.E., Micheel, C., Alivisatos, A.P., Kiehl, R.A. and Seeman, N.C. Two-Dimensional Nanoparticle Arrays Show the Organizational Power of Robust DNA Motifs. *Nano Lett.* **6**, 1502-1504 (2006).
115. Michelotti, N., Johnson-Buck, A., Mazon, A.J. and Walter, N.G. Beyond DNA origami: the unfolding prospects of nucleic acid nanotechnology. *WIREs Nanomed. Nanobiotechnol.* **4**, 139-152 (2012).
116. Le, J.D., Pinto, Y., Seeman, N.C., Musier-Forsyth, K., Taton, T.A. and Kiehl, R.A. DNA-Templated Self-Assembly of Metallic Nanocomponent Arrays on a Surface. *Nano Lett.* **4**, 2343-2347 (2004).
117. Cederquist, K.B., Dean, S.L. and Keating, C.D. Encoded anisotropic particles for multiplexed bioanalysis. *Wiley Interdiscip Rev Nanomed Nanobiotechnol* **2**, 578-600 (2010).
118. Campolongo, M.J., Tan, S.J., Smilgies, D.-M., Zhao, M., Chen, Y., Xhangolli, I., Cheng, W. and Luo, D. Crystalline Gibbs Monolayers of DNA-Capped Nanoparticles at the Air-Liquid Interface. *ACS Nano* **5**, 7978-7985 (2011).
119. Cheng, W.L., Park, N., Walter, M.T., Hartman, M.R. and Luo, D. Nanopatterning self-assembled nanoparticle superlattices by moulding microdroplets. *Nature Nanotech.* **3**, 682-690 (2008).
120. Zanchet, D., Micheel, C.M., Parak, W.J., Gerion, D., Williams, S.C. and Alivisatos, A.P. Electrophoretic and Structural Studies of DNA-Directed Au Nanoparticle Groupings. *J. Phys. Chem. B* **106**, 11758-11763 (2002).
121. Claridge, S.A., Liang, H.W., Basu, S.R., Fréchet, J.M.J. and Alivisatos, A.P. Isolation of Discrete Nanoparticle-DNA Conjugates for Plasmonic Applications. *Nano Lett.* **8**, 1202-1206 (2008).
122. Pei, H., Li, F., Wan, Y., Wei, M., Liu, H., Su, Y., Chen, N., Huang, Q. and Fan, C. Designed Diblock Oligonucleotide for the Synthesis of Spatially Isolated and

- Highly Hybridizable Functionalization of DNA–Gold Nanoparticle Nanoconjugates. *J. Am. Chem. Soc* **134**, 11876-11879 (2012).
123. Mucic, R.C., Storhoff, J.J., Mirkin, C.A. and Letsinger, R.L. DNA-Directed Synthesis of Binary Nanoparticle Network Materials. *J. Am. Chem. Soc* **120**, 12674-12675 (1998).
 124. Sebba, D., LaBean, T. and Lazarides, A. Plasmon coupling in binary metal core–satellite assemblies. *Appl. Phys. B* **93**, 69-78 (2008).
 125. Sonnichsen, C., Reinhard, B.M., Liphardt, J. and Alivisatos, A.P. A molecular ruler based on plasmon coupling of single gold and silver nanoparticles. *Nat Biotech* **23**, 741-745 (2005).
 126. Wolfe, R.L., Balasubramanian, R., Tracy, J.B. and Murray, R.W. Fully Ferrocenated Hexanethiolate Monolayer-Protected Gold Clusters. *Langmuir* **23**, 2247-2254 (2006).
 127. Pinto, Y.Y., Le, J.D., Seeman, N.C., Musier-Forsyth, K., Taton, T.A. and Kiehl, R.A. Sequence-Encoded Self-Assembly of Multiple-Nanocomponent Arrays by 2D DNA Scaffolding. *Nano Lett.* **5**, 2399-2402 (2005).
 128. Rothemund, P.W.K. Folding DNA to create nanoscale shapes and patterns. *Nature* **440**, 297-302 (2006).
 129. Fu, Y., Zeng, D., Chao, J., Jin, Y., Zhang, Z. *et al.* Single-Step Rapid Assembly of DNA Origami Nanostructures for Addressable Nanoscale Bioreactors. *J. Am. Chem. Soc* **135**, 696-702 (2012).
 130. Wu, N., Czajkowsky, D.M., Zhang, J., Qu, J., Ye, M. *et al.* Molecular Threading and Tunable Molecular Recognition on DNA Origami Nanostructures. *J. Am. Chem. Soc* **135**, 12172-12175 (2013).
 131. Han, D., Pal, S., Nangreave, J., Deng, Z., Liu, Y. and Yan, H. DNA Origami with Complex Curvatures in Three-Dimensional Space. *Science* **332**, 342-346 (2011).
 132. Pinheiro, A.V., Han, D., Shih, W.M. and Yan, H. Challenges and opportunities for structural DNA nanotechnology. *Nature Nanotech.* **6**, 763-772 (2011).
 133. Endo, M., Yang, Y., Emura, T., Hidaka, K. and Sugiyama, H. Programmed placement of gold nanoparticles onto a slit-type DNA origami scaffold. *Chem. Commun.* **47** (2011).
 134. Unconventional DNA-based route to self-assembled superlattices. *Nano Today* **4**, 287 (2009).
 135. Noh, H., Hung, A.M., Choi, C., Lee, J.H., Kim, J.-Y., Jin, S. and Cha, J.N. 50 nm DNA Nanoarrays Generated from Uniform Oligonucleotide Films. *ACS Nano* **3**, 2376-2382 (2009).
 136. Kershner, R.J., Bozano, L.D., Micheel, C.M., Hung, A.M., Fornof, A.R. *et al.* Placement and orientation of individual DNA shapes on lithographically patterned surfaces. *Nature Nanotech.* **4**, 557-561 (2009).
 137. Akbulut, O., Jung, J.-M., Bennett, R.D., Hu, Y., Jung, H.-T., Cohen, R.E., Mayes, A.M. and Stellacci, F. Application of Supramolecular Nanostamping to the Replication of DNA Nanoarrays. *Nano Lett.* **7**, 3493-3498 (2007).
 138. Zheng, Y., Lalander, C.H., Thai, T., Dhuey, S., Cabrini, S. and Bach, U. Gutenberg-Style Printing of Self-Assembled Nanoparticle Arrays: Electrostatic Nanoparticle Immobilization and DNA-Mediated Transfer. *Angew. Chem. Int. Ed.* **50**, 4398-4402 (2011).
 139. Corbierre, M.K., Cameron, N.S., Sutton, M., Mochrie, S.G., Lurio, L.B., Rühm, A. and Lennox, R.B. Polymer-stabilized gold nanoparticles and their

- incorporation into polymer matrices. *J. Am. Chem. Soc* **123**, 10411-10412 (2001).
140. Corbierre, M.K., Cameron, N.S. and Lennox, R.B. Polymer-stabilized gold nanoparticles with high grafting densities. *Langmuir* **20**, 2867-2873 (2004).
 141. Rucareanu, S., Maccarini, M., Shepherd, J.L. and Lennox, R.B. Polymer-capped gold nanoparticles by ligand-exchange reactions. *J. Mater. Chem.* **18**, 5830-5834 (2008).
 142. Yockell-Lelièvre, H., Desbiens, J. and Ritcey, A.M. Two-Dimensional Self-Organization of Polystyrene-Capped Gold Nanoparticles. *Langmuir* **23**, 2843-2850 (2007).
 143. Balazs, A.C., Emrick, T. and Russell, T.P. Nanoparticle Polymer Composites: Where Two Small Worlds Meet. *Science* **314**, 1107-1110 (2006).
 144. Boker, A., He, J., Emrick, T. and Russell, T.P. Self-assembly of nanoparticles at interfaces. *Soft Matter* **3**, 1231-1248 (2007).
 145. Genson, K.L., Holzmueller, J., Jiang, C., Xu, J., Gibson, J.D., Zubarev, E.R. and Tsukruk, V.V. Langmuir–Blodgett Monolayers of Gold Nanoparticles with Amphiphilic Shells from V-Shaped Binary Polymer Arms. *Langmuir* **22**, 7011-7015 (2006).
 146. Jiang, C., Markutsya, S., Pikus, Y. and Tsukruk, V.V. Freely suspended nanocomposite membranes as highly sensitive sensors. *Nature Mater.* **3**, 721-728 (2004).
 147. Shenhar, R., Norsten, T.B. and Rotello, V.M. Polymer-Mediated Nanoparticle Assembly: Structural Control and Applications. *Adv. Mater.* **17**, 657-669 (2005).
 148. Förster, S. and Antonietti, M. Amphiphilic Block Copolymers in Structure-Controlled Nanomaterial Hybrids. *Adv. Mater.* **10**, 195-217 (1998).
 149. Gupta, S., Zhang, Q., Emrick, T. and Russell, T.P. “Self-Corralling” Nanorods under an Applied Electric Field. *Nano Lett.* **6**, 2066-2069 (2006).
 150. Thorkelsson, K., Mastroianni, A.J., Ercius, P. and Xu, T. Direct Nanorod Assembly Using Block Copolymer-Based Supramolecules. *Nano Lett.* **12**, 498-504 (2011).
 151. Kim, B.J., Fredrickson, G.H., Hawker, C.J. and Kramer, E.J. Nanoparticle Surfactants as a Route to Bicontinuous Block Copolymer Morphologies. *Langmuir* **23**, 7804-7809 (2007).
 152. Stratford, K., Adhikari, R., Pagonabarraga, I., Desplat, J.-C. and Cates, M.E. Colloidal Jamming at Interfaces: A Route to Fluid-Bicontinuous Gels. *Science* **309**, 2198-2201 (2005).
 153. Bockstaller, M.R., Lapetnikov, Y., Margel, S. and Thomas, E.L. Size-Selective Organization of Enthalpic Compatibilized Nanocrystals in Ternary Block Copolymer/Particle Mixtures. *J. Am. Chem. Soc* **125**, 5276-5277 (2003).
 154. Mehdizadeh Taheri, S., Fischer, S. and Förster, S. Routes to Nanoparticle-Polymer Superlattices. *Polymers* **3**, 662-673 (2011).
 155. Wang, X., Li, G., Chen, T., Yang, M., Zhang, Z., Wu, T. and Chen, H. Polymer-Encapsulated Gold-Nanoparticle Dimers: Facile Preparation and Catalytical Application in Guided Growth of Dimeric ZnO-Nanowires. *Nano Lett.* **8**, 2643-2647 (2008).
 156. Chen, G., Wang, Y., Tan, L.H., Yang, M., Tan, L.S., Chen, Y. and Chen, H. High-Purity Separation of Gold Nanoparticle Dimers and Trimers. *J. Am. Chem. Soc* **131**, 4218-4219 (2009).

157. Li, W., Camargo, P.H.C., Au, L., Zhang, Q., Rycenga, M. and Xia, Y. Etching and Dimerization: A Simple and Versatile Route to Dimers of Silver Nanospheres with a Range of Sizes. *Angew. Chem. Int. Ed.* **49**, 164-168 (2010).
158. Ohno, K., Koh, K., Tsujii, Y. and Fukuda, T. Fabrication of Ordered Arrays of Gold Nanoparticles Coated with High-Density Polymer Brushes. *Angew. Chem. Int. Ed.* **42**, 2751-2754 (2003).
159. Watson, K.J., Zhu, J., Nguyen, S.T. and Mirkin, C.A. Hybrid Nanoparticles with Block Copolymer Shell Structures. *J. Am. Chem. Soc.* **121**, 462-463 (1998).
160. Cheng, L., Liu, A., Peng, S. and Duan, H. Responsive Plasmonic Assemblies of Amphiphilic Nanocrystals at Oil–Water Interfaces. *ACS Nano* **4**, 6098-6104 (2010).
161. Tao, A.R., Huang, J. and Yang, P. Langmuir–Blodgett of Nanocrystals and Nanowires. *Acc. Chem. Res.* **41**, 1662-1673 (2008).
162. Tao, A.R., Ceperley, D.P., Sinsersuksakul, P., Neureuther, A.R. and Yang, P. Self-Organized Silver Nanoparticles for Three-Dimensional Plasmonic Crystals. *Nano Lett.* **8**, 4033-4038 (2008).

This page is intentionally blank

Chapter 3

Free-standing Superlattice Nanomembrane from Polymer-capped Gold Nanospheres

This page is intentionally blank

The modular self-assembly of plasmonic superlattice sheets enables new two-dimensional metamaterials with programmable properties. Such sheets integrate unique properties of optoelectronic nanomaterials with striking mechanical robustness and tailorable plasmonics into one multifunctional system. It allows programming their properties by modifying the morphology and composition of constituent nanoparticles and engineering packing order of lattice structures. Recently, there has been emerging interest in building the free-standing superlattice sheets for a plethora of potential applications, including ultrafiltration[1] and optoelectronic devices[2-4].

As reviewed in previous chapter, representative success in constructing such superlattice nanosheets has been realized *via* the alkyl molecular ligands [2, 3, 5-9]. The drying-mediated, entropy-driven self-assembly at air-liquid interfaces has been demonstrated to be a general approach to fabricate defect-free superlattice sheets with superior mechanical strength[8]. Nevertheless, a potential drawback in alkyl-nanoparticle superlattice membranes is the limited molecular length that restricts the range for tailoring interparticle electromagnetic coupling. Recently, DNA has been successfully utilized as a ‘dry ligand’ under unusually low ionic strength and successfully obtained free-standing, monolayered DNA-nanoparticle superlattice sheets in a microhole-confined self-assembly process [10-12]. The highly controllable molecular lengths of DNA ligands enable tailoring of both structural (interparticle spacings) and functional properties (plasmonic and mechanical) over a wide window. In particular, the edge-to-edge interparticle spacing for DNA-based monolayer superlattice sheets can be adjusted up to 20 nm – a greater size range than has been achieved with alkyl molecular ligands[13].

In this chapter, a generic approach has been presented to use polymers as ligands to fabricate the free-standing, monolayered nanoparticle superlattice sheets based on drying-mediated, entropy-driven self-assembly at the air-liquid interface. In this approach, polystyrene (PS) capped nanoparticle was used as a model system. The self-assembly process is similar to the case of alkyl-capped nanoparticles, but longer polymer ligands enable wider tuning of interparticle spacing especially for large

nanoparticles which are important for plasmonic applications. As outlined in Section 2.4, polymers have been successfully used as ligands to stabilize nanoparticles either by direct synthesis [14, 15] or ligand-exchange procedure[16]. Such successes have led to ordered nanoparticle arrays self-assembled at solid substrates[15, 17]. However, to the best of our knowledge the use of generic polymers as ligands in drying-mediated assembly at the air-liquid interface has not been reported.

With this approach, it is possible to fabricate superlattice nanosheets as large as ~15 micrometers in lateral dimensions with a thickness of ~13 nm, corresponding to an aspect ratio (lateral size/thickness) of more than 1000. Both internal structures (particle size and interparticle spacing) and collective properties (plasmonic coupling) are tunable. The monolayered polymer-nanoparticle sheets are highly stable under various conditions, transferable to any arbitrary substrates, and can be manufactured with focused ion beams. This demonstrates the potential to integrate the superlattice nanosheets into miniaturized optical and electronic devices.

3.1 Experimental methods

3.1.1 Materials

Gold (III) chloride trihydrate ($\text{HAuCl}_4 \cdot 3\text{H}_2\text{O}$, $\geq 99.9\%$) and trisodium citrate dihydrate were obtained from Sigma Aldrich. Hexane, THF, and chloroform were obtained from Merck KGaA. Thiol-functionalized polystyrene ($M_n = 12$ kDa, $M_w/M_n = 1.09$) was purchased from Polymer Source Inc. All chemicals were used as received unless otherwise indicated. All aqueous solutions were made using demineralized water, which was further purified with a Milli-Q system (Millipore). All glassware used in the following procedures was cleaned in a bath of freshly prepared aqua regia and rinsed thoroughly in H_2O prior to use.

3.1.2 Synthesis of AuNPs

Gold nanoparticles with diameters of 13 nm and 26 nm were synthesized according to the literature.[18] A representative procedure for the preparation of 13nm AuNPs is as

follows: 2 mL HAuCl₄ solution (25 mM) was diluted by 170 mL Milli-Q water and heat to 100°C until boiling. Next, 6 mL sodium citrate solution (34 mM) was added into the above auric solution. After heating for 3 min, the clear solution changed to a wine-red color, which indicated the formation of Au nanoparticles. After further boiling for 10 minutes, the heat source was removed and the dispersion was cooled down to room temperature. Reducing the volume of sodium citrate solution to 3 mL led to 26 nm Au nanoparticles.

3.1.3 Conjugation of AuNPs with PS-SH

PS-capping of the citrate-reduced AuNPs was achieved by following to the reported “Grafting to” method.[15, 17] In a typical experiment, 5 mL as prepared AuNPs (13nm, 3.7 nM) was spun down and concentrated into 0.2 mL, followed by dropwise addition of above concentrated AuNPs to an excess solution of PS-SH in THF (1.5 mg mL⁻¹) under vigorous stirring. After aging for 24 hours at room temperature, the supernatant was discarded and the samples were purified by repeated centrifugation-resuspension cycles with chloroform until the supernatant showed no presence of residual PS-SH upon the addition of methanol. The PS-capped AuNPs with different sizes were well-dispersed in organic solution and no changes in properties were noted with time.

3.1.4 Characterization

The free-standing PS-capped AuNPs superlattice sheets were simply transferred from the air-liquid interface to 300 mesh lacey-carbon grids as mentioned in main text, and characterized by TEM using a Philips CM20 at a 200 kV accelerating voltage.

UV-vis spectra of superlattice sheets were recorded at room temperature using a J&M MSP210 Microscope Spectrometry System over a tiny area while the film was illuminated by a high-intensity fiber light source under a 40× objective, and the transparent/reflection images were recorded by a CCD camera on the microscope. In addition, the monolayer sheets were also transferred onto a silicon nitrate wafer and easily cut to different shapes by using focused ion beam-SEM (FEI Quanta 3D FEG). The monolayer sheet can be cut into different shapes with designed patterns in FIB-SEM.

Synchrotron-based SAXS was performed at the Australian Synchrotron. 2D diffraction patterns were recorded on a Dectris-Pilatus 1 M detector of 10 modules at sample-to-detector distances of 3388 mm, as calibrated using a silver behenate standard. The effective beam size was approximately 100 μm x 200 μm , and the exposure time was 1 second. Exposures were taken at 25°C at a wavelength of 1.24 Å.

Thermogravimetric analysis (TGA) was carried out using a Mettler Toledo TGA-SDTA851 analyser in the temperature range from 25 to 700 °C at a heating rate of 10°C/min. The runs were performed under N₂ gas, and the gas was switched to air for 10 min at the end of the run at 700°C to ensure complete combustion of the organic material. N₂ and air gases were used at a rate of 50 mL/min.

AFM experiments were performed with a Dimension Icon Scanning Probe Microscope at 25°C. Data visualization and analysis was carried out by using Gwyddion software. Fourier transform infrared (FT-IR) spectra were recorded with KBr disks, using a GX spectrophotometer (Perkin-Elmer, Waltham, MA, USA). The PS-capped AuNPs and citrate-capped AuNPs were dispersed in chloroform and water respectively, and then evaporated onto the KBr disks.

3.2 Results and discussion

3.2.1 Characterization of PS-capped gold nanoparticles

High-quality polystyrene-capped gold nanoparticles (PS-capped AuNPs) with two distinct sizes were synthesized based on a modified grafting approach reported by others[17]. In a typical procedure, the “bare” aqueous gold nanoparticles (citrate-capped AuNPs) were firstly synthesized via Frens’ approach. Then excess amount of thiolated polystyrene with molecular weight of 12,000 in THF was brought in contact with nanoparticles solution with vigorous agitation to prevent aggregation and incomplete exchange arises from the poor surface coverage of nanoparticles. During the ligand exchange process, thiolated polystyrene acts as both a phase-transfer reagent

and capping agent *via* a robust covalent linkage between the polymer and the gold surface[15]. Based on the TEM images of synthesized PS-capped AuNPs, the diameters of different AuNPs are 13.1 ± 1.9 nm and 26.0 ± 4.5 nm, as indicated in **Figure 3.1**.

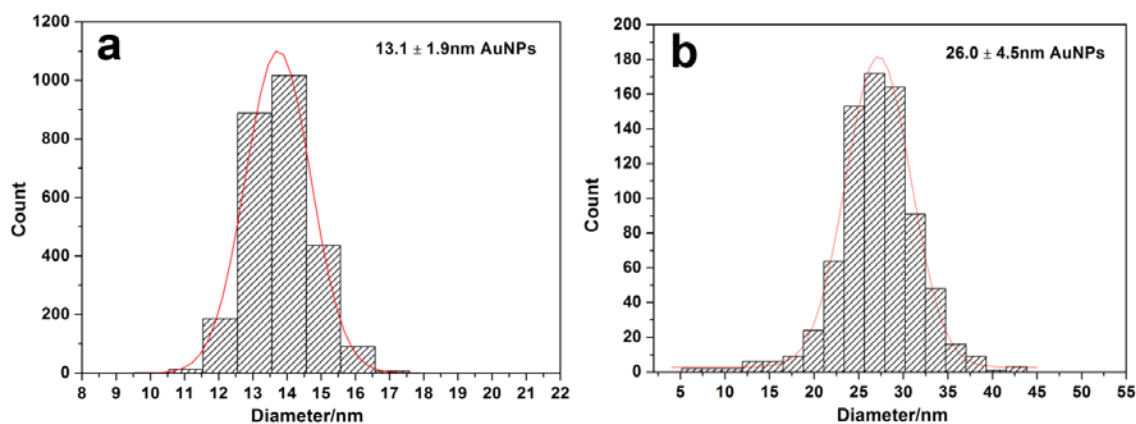


Figure 3.1 | Histogram on diameter distribution of “bare” gold nanoparticles as determined by TEM. Curves in both plots represent Gaussian fits.

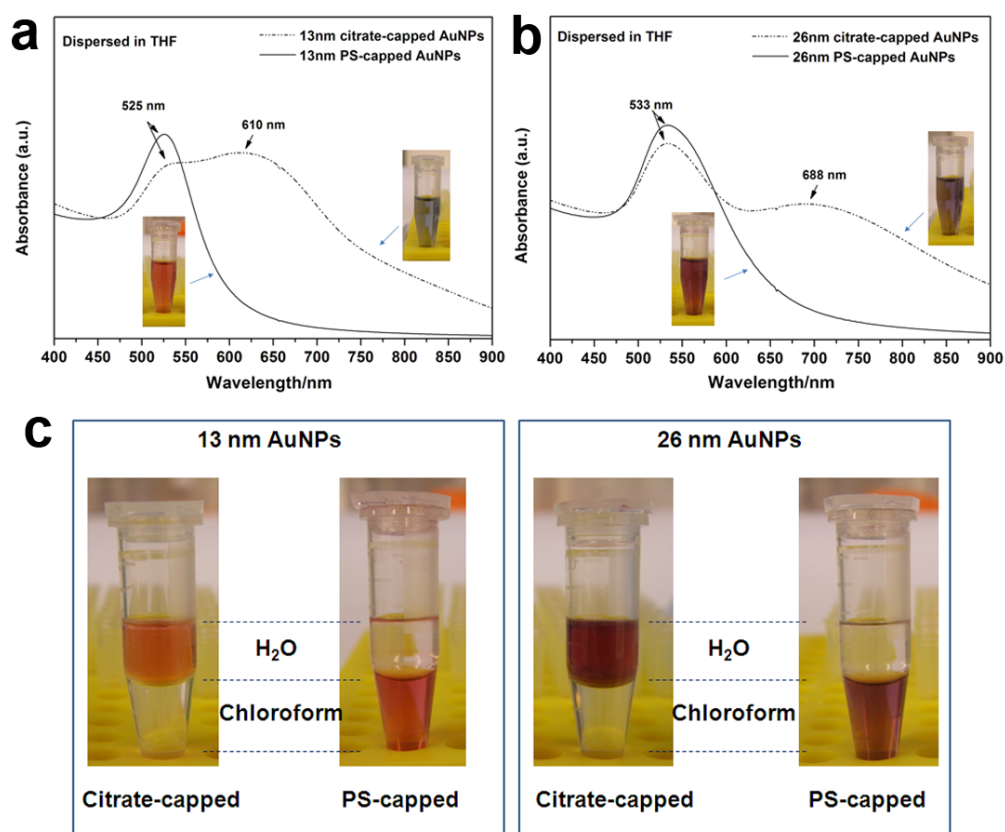


Figure 3.2 | UV-vis spectra of (a) 13 nm citrate-capped/ PS-capped AuNPs, and (b) 26 nm citrate-capped/ PS-capped AuNPs dispersed in THF. Insets are photographs of corresponding AuNPs. (c) Phase transfer process indicates successful ligand exchange from citrate into PS.

Stabilization of nanoparticles by thiolated polystyrene was confirmed by measurements of localized surface plasmon resonance (LSPR) and FT-IR. Originally, AuNPs generated by citrate reduction are well-dispersed in water due to citrate-based charge-charge repulsion[19]. This electrostatic interaction would be weakened and lead to partial flocculation if the citrate-capped AuNPs were transfer from water to THF, resulting in the sudden color change from ruby red to dark purple-blue. As shown in **Figure 3.2a and b**, the citrate-capped AuNPs give rise to a dramatic red-shifting and broadening of the surface plasmon resonance (SPR) band to 610 nm and 688 nm for 13 nm and 26 nm AuNPs. After surface functionalization of PS, the PS-capped AuNPs exhibits monodispersed SPR bands at 525 nm and 533 nm for both AuNPs, which clearly demonstrates the successful ligand exchange process. Specifically, the phase transfer phenomena further proved this conclusion[20] (**Figure 3.2c**). After ligand displacement of citrate into PS, the hydrophobic PS-stabilized AuNPs are well dispersing in bottom chloroform layer, while the citrate-capped AuNPs are only dispersing in upper water layer.

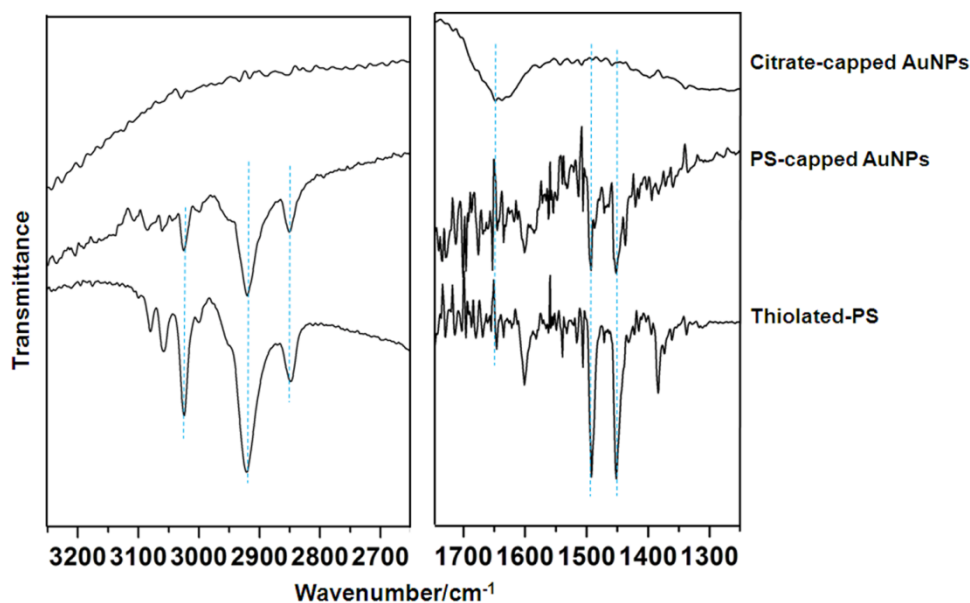


Figure 3.3 | FT-IR spectra of 26 nm citrate-capped AuNPs, PS-capped AuNPs and thiolated-PS in two magnified spectral regions.

Transmission FT-IR spectroscopy also demonstrated the surface functionalization of AuNPs by PS (**Figure 3.3**). The $C=O$ carbonyl group valence vibrational band of citrate at 1645 cm^{-1} disappeared after the PS capping. In addition, characteristic $C-C$ stretching vibrations bands (1492 cm^{-1} and 1452 cm^{-1}) and $C-H$ stretching vibrations

bands (2849 cm^{-1} , 2922 cm^{-1} , and 3025 cm^{-1}) were observed even after washing samples multiple times to completely remove non-bonded ligands. Thus, the above results demonstrate the effective stabilization of nanoparticles by thiolated PS.

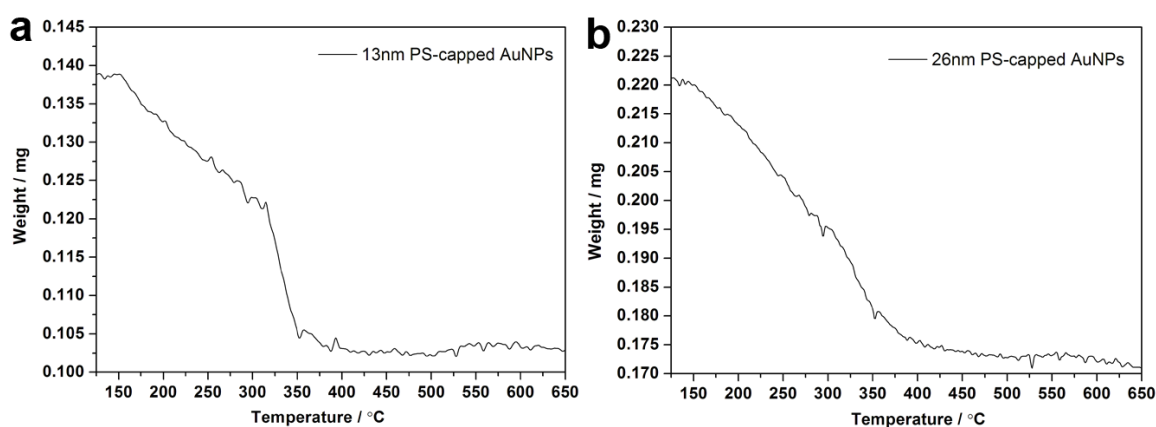


Figure 3.4 | TGA curves of (a) 13nm PS-capped AuNPs and (b) 26nm PS-capped AuNPs. The weight ratio of Au/PS and corresponding calculation results have been summarized in Table 3.1.

Table 3.1 | Analytical characteristics of PS-capped AuNPs and superlattice sheets

Entry ^a	PS-capped AuNPs					Superlattice sheets		
	d_{core}^b (nm)	PS/Au % (wt. %) ^c	Grafting density ^c (chains/nm ²)	Diameter of PS footprint ^c (nm)	Calculated corona height ^d (nm)	Softness ^e (χ)	Edge-to- edge spacing ^b (nm)	Deformation parameter ^e (λ)
13nm PS- AuNPs	13.1 ± 1.9	26.6/73.4	0.77	1.29	18.4	2.8	2.5	0.7
26nm PS- AuNPs	26.0 ± 4.5	19.8/80.2	1.03	1.11	20.4	1.6	2.1	0.6

a: The ligands for all the nanoparticles were thiol-functionalized polystyrene ($M_n=12,000$, $M_w/M_n = 1.09$, Degree of polymerization = 115); b: Determined by TEM and statistical analysis through ImageJ; c: Estimated from data of TEM and TGA; d: Calculated by using de Gennes's model that assumes a polymer brush constrained inside a cylindrical tube of diameter d (footprint of PS chain) reported in Ref.[21]; e: the dimensionless quantity χ and deformation parameter λ were calculated by applying the entropic spring model reported in Ref.[22].

The grafting densities of PS-capped AuNPs were calculated from the diameters of AuNPs cores as evaluated by TEM analysis and the weight ratio of PS/AuNPs as determined by TGA (**Figure 3.4**). The weight fraction analysis led to a high grafting density of approximately 1 ligand/nm² (Table 3.1), which is comparable with the grafting densities reported by A. M. Ritcey *et al*[17]. The calculated diameters of the

effective footprint of the grafted PS is much smaller than the reported theoretical Flory radius of a tethered PS chain (~ 6.6 nm) with the similar length[17], indicating that the PS chains extends significantly in solvent and adopt a brush conformation on the surface of the AuNPs.

3.2.2 Fabrication and transfer of PS-capped AuNPs superlattice sheets

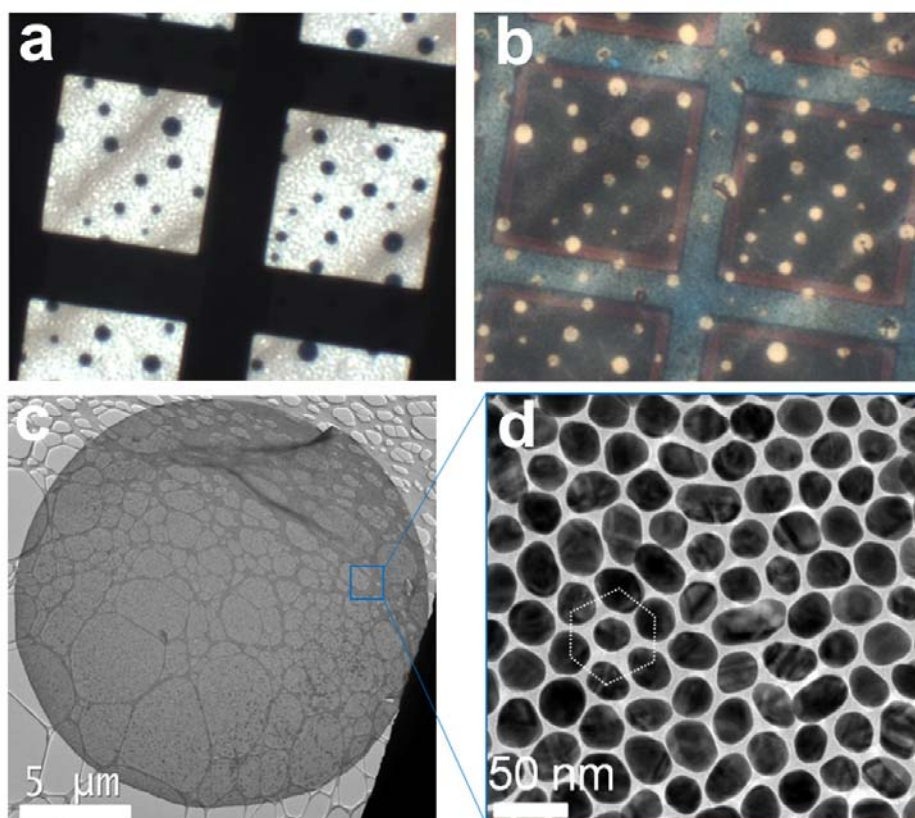


Figure 3.5 | Low-magnification images of free-standing superlattice sheets formed using 26.0 nm PS-capped AuNPs in 50×50 μm grids, which were acquired under (a) transmission and (b) reflection mode by microscope. (c) TEM image of a monolayer sheet self-assembled from 26.0 nm PS-capped AuNPs with a diameter of ~ 15 μm , crumpled area indicates the flexibility of the sheet, (d) Higher-magnification TEM image of (c) shows that nanoparticles are hexagonally-packed yet well spaced.

To fabricate free-standing monolayered superlattice nanosheets, PS-capped AuNPs with diameters of 26 nm were concentrated and finally dispersed in 0.5 mL chloroform (80 nM, 8.5 mg mL^{-1}), then one drop (~ 4 - 6 μL) of the solution was carefully spread onto the surface of Milli-Q water in a plastic petri dish. The droplet quickly spread over the water surface in less than 1s. The dish was then covered to prevent fluid flows and solvent fluctuations. The evaporation-mediated assembly of hydrophobic PS-capped

AuNPs led to the formation of thin particle sheets floating at the water surface. After 5 minutes, a gold-colored reflection was observed on the water surface, which indicated complete solidification. These sheets were circular-shaped, and readily observable under an optical microscope in both transmission and reflection modes (**Figure 3.5a and b**). Similar to the kinetically driven interfacial self-assembly of AuNPs reported earlier[5], we also observed polymer-AuNPs nanosheets were facilitated by the rapid evaporation, followed by nucleation and growth into 2D crystals at the monolayer level (**Figure 3.5c and d**).

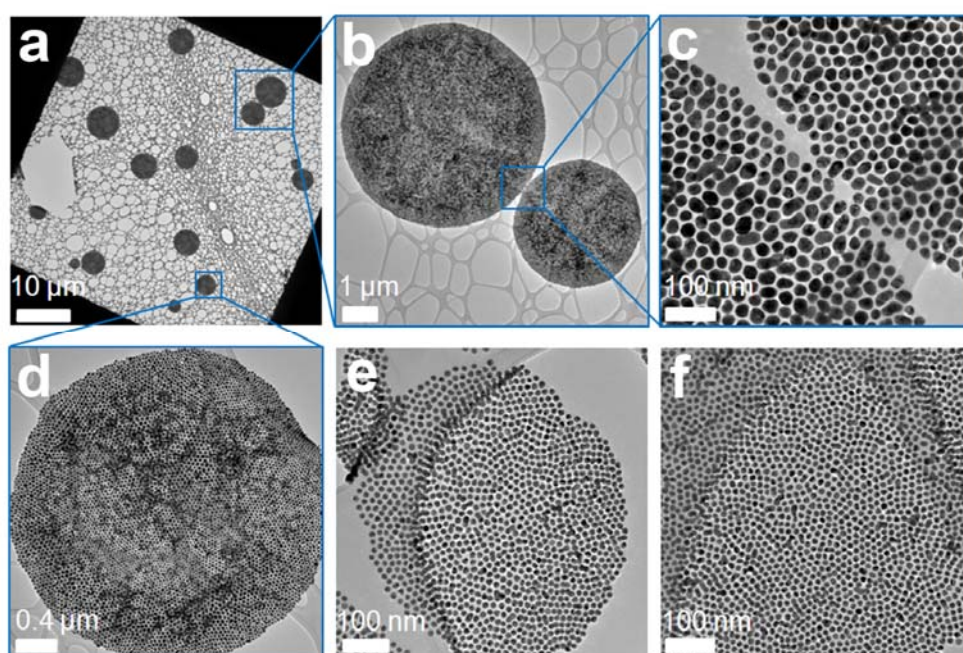


Figure 3.6 | TEM characterization of free-standing nanoparticle superlattice sheets formed using (a~d) 26 nm and (e, f) 13 nm PS-capped AuNPs on a random hollow lacey-carbon grid. In (e, f), the lacey carbon substrate resulted in the crumpled area on the membrane, the membrane still maintained its shape and demonstrates the flexibility of the sheets.

2D PS-capped AuNPs nanosheets are robust and flexible, and are transferable to a variety of substrates without deterioration. The transfer can typically be achieved by either Langmuir-Blodgett or Langmuir-Schaffer techniques. Notably, neither transfer process caused any rupturing or deterioration of the nanosheets (**Figure 3.5c and 3.6**). The PS-capped AuNP superlattice sheets are highly stable under electron irradiation and highly processable by focused-ion beam (FIB) lithography. Particularly, after being transferred onto silicon wafer, it can be cut into rectangular shapes (**Figure 3.7**), which

suggested a facile way to manufacture the superlattice sheets into arbitrary shapes for optoelectronic applications. In conjunction with programmable plasmonic coupling, this methodology is potentially enabling in the integration of free-standing, monolayered sheets into future optoelectronic devices.

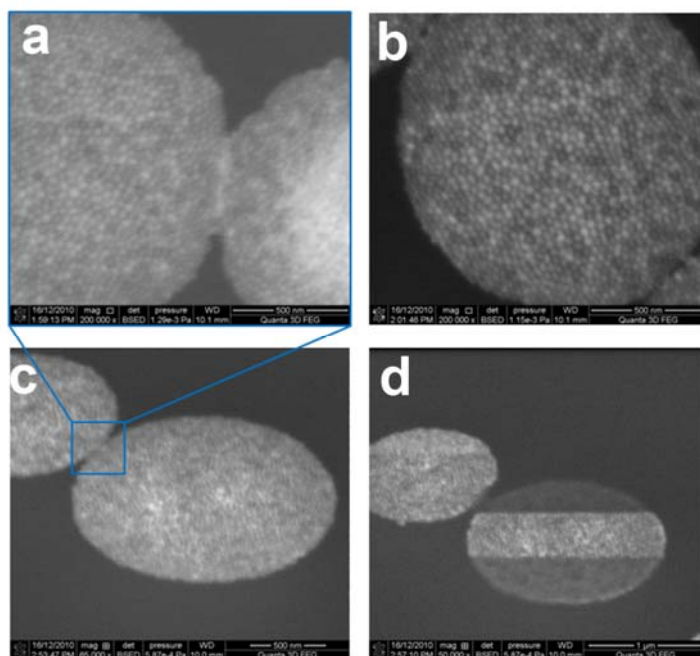


Figure 3.7 | SEM characterization of nanoparticle superlattice sheets formed using 26 nm PS-capped AuNPs transferred onto a silicon nitrate wafer. (d) One sheet was cut by using a focused ion beam, which demonstrated a facile way to pattern the monolayer arrays into desired shapes.

3.2.3 Characterization of PS-capped AuNPs superlattice sheets

High magnification TEM micrographs show that the superlattice sheets consisted of monolayered AuNPs with hexagonal packing symmetry (**Figure 3.5d**). Unlike most previously reported superlattices which usually formed from NPs with small diameters[13, 23-26], this technique achieved superlattice sheets with much larger particle size. Although polymer-stabilized AuNPs with comparable sizes have been previously used to form arrays on a solid support^{[15], [27-29]}, the success in forming large-scale, free-standing superlattice sheets has not yet been reported. By using polystyrene with higher molecular weight, it is possible to construct large particles into 2D superlattice membranes. **Figure 3.8** shows that superlattice sheets constructed by different sized nanoparticles. When particle sizes were changed, the structural features

including monolayer and hexagonally-ordered packing were maintained.

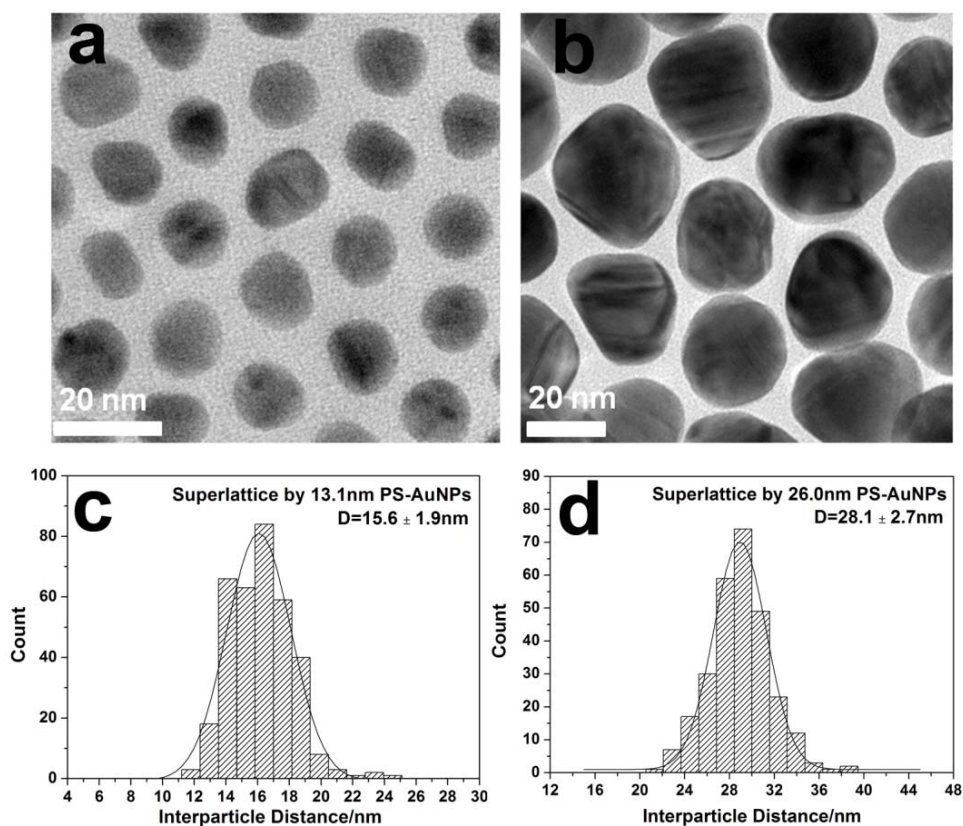


Figure 3.8 | TEM characterization of different superlattice sheets formed using (a) 13.1 nm and (b) 26.0 nm PS-capped AuNPs, (c) and (d) are corresponding histograms of interparticle distance analyzed from TEM images. Curves in both plots represent Gaussian fits.

The size of building blocks influences the PS ligand compression and conformation during the self-assembly process. With the same ligands capping two different particles (13 nm and 26 nm), two superlattice nanosheets were fabricated. The edge-to-edge interparticle spacing was measured (**Figure 3.8**). Based on analysis in Figure. 3.1 and 3.8, the corresponding core-to-core distance of self-assembled superlattice sheets are 15.6 ± 1.9 nm and 28.1 ± 2.7 nm. After subtracting the diameters, the former gave a edge-to-edge spacing of ~ 2.5 nm, whereas, the latter gave a spacing of ~ 2.1 nm. This indicates that the polystyrene ligands experienced larger compression in the lateral directions for larger nanoparticles. Notably, compared to those 2D particle arrays formed on a solid support[17], the spacing in this system is much smaller. This may be due to the absence of particle-substrate interactions at the air-water interface, whereas, the strong particle-substrate interaction in Ritcey's report may prevent lateral particle

collision. Similar small spacing was also found in the corresponding three-dimensional arrays[22]

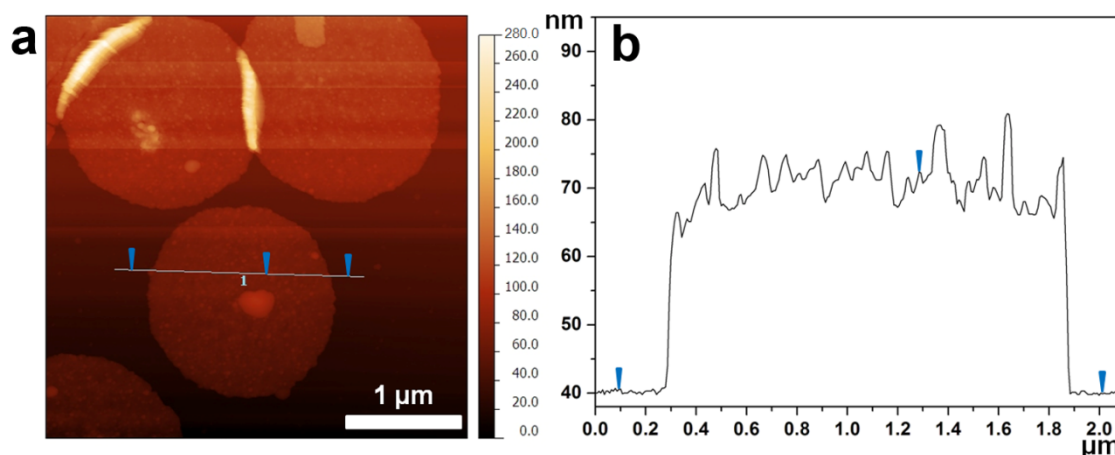


Figure 3.9 | Representative AFM height image and the corresponding cross section profile for monolayer superlattice sheets constructed from 26 nm PS-capped AuNPs. The measurements were repeated ten times, and the average height is 32.1 ± 2.3 nm.

The vertical compression was characterized by measuring the thickness of the superlattice nanosheets with atomic force microscope (AFM) after transferring the sheets onto a silicon wafer. A typical AFM image and the corresponding line scan are shown in **Figure 3.9**. Evidently, the monolayered structure is in agreement with the TEM imaging. After subtracting the nanoparticle diameters, the compressed polystyrene thickness in vertical directions can be estimated to be 3.5 nm and 3.1 nm for 13 nm and 26 nm AuNPs, respectively.

The interparticle spacing was further confirmed with the drop-casted particle films on a solid support. These drop-casted films are multi-layered particles and their crystalline structures were investigated by the synchrotron-based small-angle X-ray scattering (SAXS). 1D SAXS spectra were obtained by azimuthally integrating 2D SAXS patterns over a quadrant using the FIT2D program[22], and relative scattering intensities were plotted as a function of scattering vector q :

$$q = 4\pi \sin \theta / \lambda \quad \text{Equation (3.1)}$$

where θ is the scattering angle and λ is the wavelength of X-ray radiation. The structure factors, $S(q)$, from the SAXS patterns were obtained by dividing out the form factor, $F(q)$ (i.e. the predicted scattering pattern for particles that are completely dissociated).

$F(q)$ was measured by SAXS of low polystyrene-nanoparticles concentrations loaded in a capillary tube.

Interparticle spacing in the samples was determined using the following equations:[30]

$$d_{Au} = \left(\frac{2}{\sqrt{3}} \right) \left(\frac{2\pi}{q_0} \right) \quad \text{Equation (3.2)}$$

where d_{Au} is the distance between the centroid of two nearest neighbor particles and q_0 is the position of the first order scattering peak, which equal to 0.447 nm^{-1} for 13 nm PS-capped AuNPs arrays and 0.249 nm^{-1} for 26 nm PS-capped AuNPs arrays.

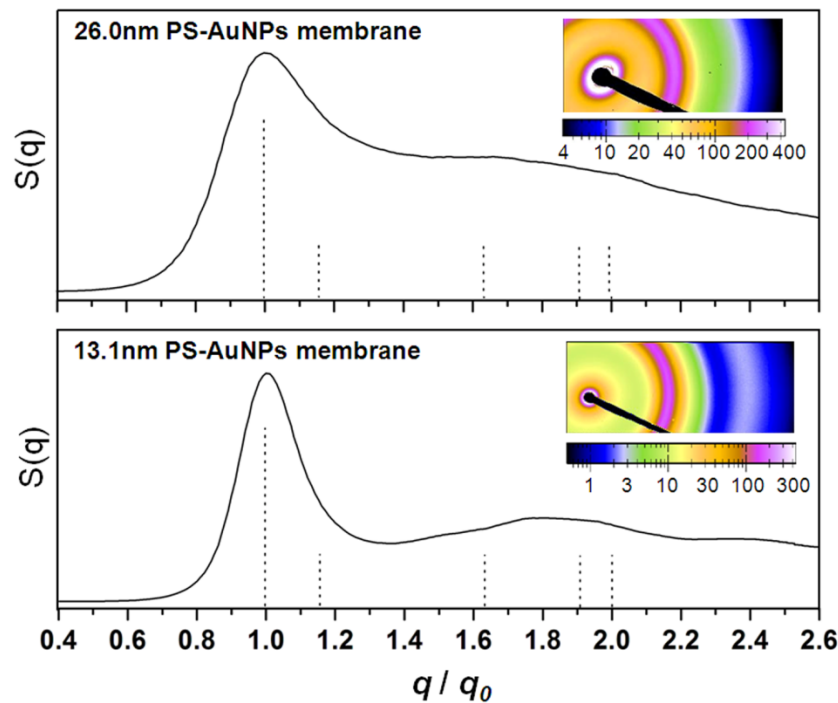


Figure 3.10 | The integrated and extracted structure factors $S(q)$ from SAXS patterns (insets) of drop-casted films constructed by PS-capped AuNPs. Dashed line at bottom suggests the theoretical peak positions for f.c.c. arrangement.

The representative 1D scattering data for the drop-casted films of 13 nm and 26 nm gold nanoparticles is shown in **Figure 3.10**. The discrete Bragg peaks were not observed, but it appears to be indicative of a face-centered cubic arrangement. Thus, the interparticle spacings could be estimated to be 16.2 nm and 28.8 nm for 13 nm and 26 nm AuNPs, respectively. This corresponds to the edge-to-edge interparticle spacing

of 3.1 nm and 2.8 nm. These values were close to those for 2D monolayered superlattice nanosheets (**Table 3.1**).

The above the experiments show that the vertical polystyrene thickness in the superlattice sheet is about 3 fold greater than the lateral thickness. Two reasons could account for this: (1) nanoparticles are trapped at the air/water interface to form monolayers, the core-core van der Waals attraction in the late stage of solvent drying leads to the strong lateral compression[1]; (2) PS ligands may be pushed above and below the monolayers during the drying-mediated self-assembly.

3.2.4 Plasmonic property of PS-capped AuNPs superlattice sheets

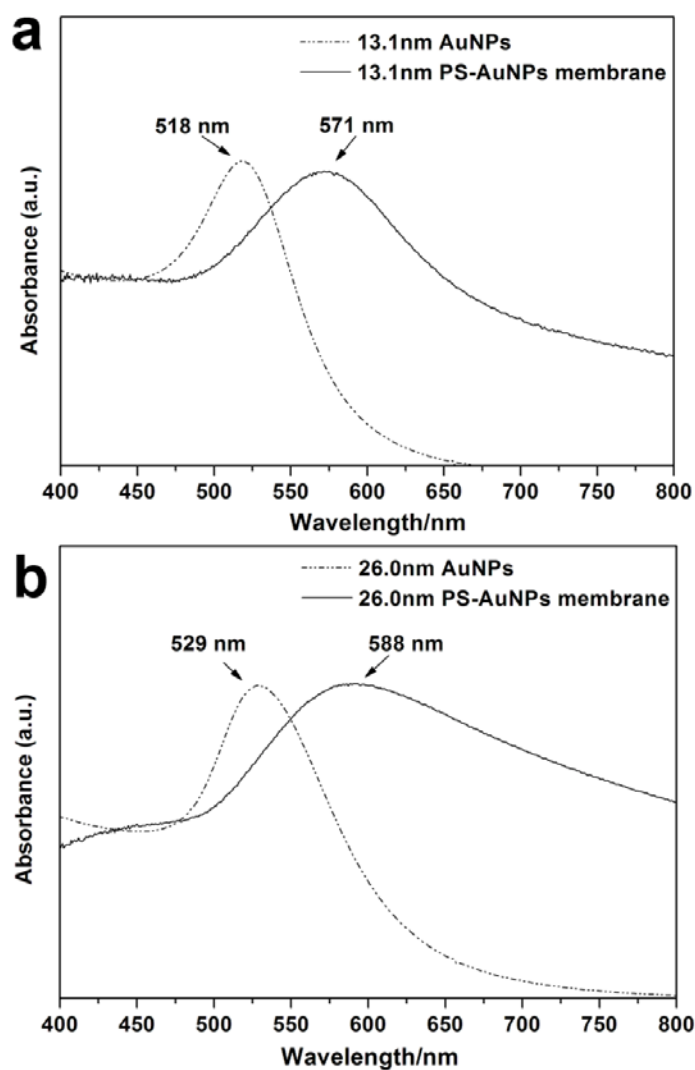


Figure 3.11 | UV-vis spectra of AuNPs dispersed in water and superlattice sheets constructed from (a) 13.1 nm PS-capped AuNPs and (b) 26.0 nm PS-capped AuNPs.

Plasmonic properties of PS-capped AuNPs superlattice nanosheets were investigated using a microscope UV-visible spectrometer in transmission mode (**Figure 3.11**). The superlattice sheets could be clearly observed under microscope with both transmission and reflection modes (**Figure 3.5a and b**), exhibiting blue and yellow colours, respectively. This is due to the unique absorption and scattering effects of the superlattice nanosheets due to the localized surface plasmon resonance (LSPR). Compared with the LSPR bands of dispersed AuNPs (**Figure 3.11**), the LSPR bands for the nanosheets shift significantly to red, suggesting strong interparticle coupling for both 13 nm and 26 nm AuNPs. The LSPR studies demonstrate that the plasmonic properties of superlattice nanosheets are customizable simply by adjusting particle size[31].

3.3 Conclusion

In this chapter, a general and facile method was developed to construct free-standing nanoparticle superlattice sheets using generic polymers as ligands through drying-mediated self-assembly at the air-liquid interface. The thicknesses of superlattice sheets are at monolayer level, yet they are mechanically robust and can be highly stable under various conditions, transferable to any arbitrary substrates, and processable with FIB milling. The superlattice sheets also exhibit strong plasmonic coupling resonances which are adjustable simply by varying particle sizes. This approach offers great modularity and versatility, and can potentially be extended to polymer-magnetic or quantum dot nanosheets. Thus, this methodology has great potential for applications in substrate-free optoelectronic devices, high-density data storage, new classes of biosensors and smart ultrafiltration membranes.

3.4 References

1. He, J., Lin, X.-M., Chan, H., Vuković, L., Král, P. and Jaeger, H.M. Diffusion and Filtration Properties of Self-Assembled Gold Nanocrystal Membranes. *Nano Lett.* **11**, 2430-2435 (2011).

2. Dong, A.G., Chen, J., Vora, P.M., Kikkawa, J.M. and Murray, C.B. Binary nanocrystal superlattice membranes self-assembled at the liquid-air interface. *Nature* **466**, 474-477 (2010).
3. Dong, A.G., Ye, X.C., Chen, J. and Murray, C.B. Two-Dimensional Binary and Ternary Nanocrystal Superlattices: The Case of Monolayers and Bilayers. *Nano Lett.* **11**, 1804-1809 (2011).
4. Liao, J., Zhou, Y., Huang, C., Wang, Y. and Peng, L. Fabrication, Transfer, and Transport Properties of Monolayered Freestanding Nanoparticle Sheets. *Small* **7**, 583-587 (2011).
5. Bigioni, T.P., Lin, X.M., Nguyen, T.T., Corwin, E.I., Witten, T.A. and Jaeger, H.M. Kinetically driven self assembly of highly ordered nanoparticle monolayers. *Nature Mater.* **5**, 265-270 (2006).
6. Cheng, W.L., Dong, S. and E., W. Synthesis and self-assembly of cetyltrimethylammonium bromide-capped gold nanoparticles. *Langmuir* **19**, 9434-9439 (2003).
7. Collier, C.P., Saykally, R.J., Shiang, J.J., Henrichs, S.E. and Heath, J.R. Reversible tuning of silver quantum dot monolayers through the metal-insulator transition. *Science* **277**, 1978-1981 (1997).
8. Mueggenburg, K.E., Lin, X.M., Goldsmith, R.H. and Jaeger, H.M. Elastic membranes of close-packed nanoparticle arrays. *Nature Mater.* **6**, 656-660 (2007).
9. Tan, S.J., Campolongo, M.J., Luo, D. and Cheng, W.L. Building plasmonic nanostructures with DNA. *Nature Nanotech.* **6**, 268-276 (2011).
10. Cheng, W.L., Campolongo, M.J., Cha, J.J., Tan, S.J., Umbach, C.C., Muller, D.A. and Luo, D. Free-standing nanoparticle superlattice sheets controlled by DNA. *Nature Mater.* **8**, 519-525 (2009).
11. Cheng, W.L., Campolongo, M.J., Tan, S.J. and Luo, D. Freestanding ultrathin nano-membranes via self-assembly. *Nano Today* **4**, 482-493 (2009).
12. Long, R., Hui, C.Y., Cheng, W.L., Campolongo, M.J. and Luo, D. Size Effect on Failure of Pre-stretched Free-Standing Nanomembranes. *Nanoscale Res. Lett.* **5**, 1236-1239 (2010).
13. Martin, J.E., Wilcoxon, J.P., Odinek, J. and Provencio, P. Control of the Interparticle Spacing in Gold Nanoparticle Superlattices. *J. Phys. Chem. B* **104**, 9475-9486 (2000).
14. Corbierre, M.K., Cameron, N.S., Sutton, M., Mochrie, S.G., Lurio, L.B., Rühm, A. and Lennox, R.B. Polymer-stabilized gold nanoparticles and their incorporation into polymer matrices. *J. Am. Chem. Soc* **123**, 10411-10412 (2001).
15. Corbierre, M.K., Cameron, N.S. and Lennox, R.B. Polymer-stabilized gold nanoparticles with high grafting densities. *Langmuir* **20**, 2867-2873 (2004).
16. Rucareanu, S., Maccarini, M., Shepherd, J.L. and Lennox, R.B. Polymer-capped gold nanoparticles by ligand-exchange reactions. *J. Mater. Chem.* **18**, 5830-5834 (2008).
17. Yockell-Lelièvre, H., Desbiens, J. and Ritcey, A.M. Two-Dimensional Self-Organization of Polystyrene-Capped Gold Nanoparticles. *Langmuir* **23**, 2843-2850 (2007).
18. Frens, G. Controlled Nucleation for the Regulation of the Particle Size in Monodisperse Gold Suspensions. *Nature, Phys. Sci.* **241**, 20 (1973).

19. Zhang, S., Leem, G., Srisombat, L.-o. and Lee, T.R. Rationally Designed Ligands that Inhibit the Aggregation of Large Gold Nanoparticles in Solution. *J. Am. Chem. Soc.* **130**, 113-120 (2007).
20. Tang, Q., Cheng, F., Lou, X.-L., Liu, H.-J. and Chen, Y. Comparative study of thiol-free amphiphilic hyperbranched and linear polymers for the stabilization of large gold nanoparticles in organic solvent. *J. Colloid Interface Sci.* **337**, 485-491 (2009).
21. Lopes, W.A. and Jaeger, H.M. Hierarchical self-assembly of metal nanostructures on diblock copolymer scaffolds. *Nature* **414**, 735-738 (2001).
22. Cheng, W.L., Hartman, M.R., Smilgies, D.-M., Long, R., Campolongo, M.J., Li, R., Sekar, K., Hui, C.-Y. and Luo, D. Probing in Real Time the Soft Crystallization of DNA-Capped Nanoparticles. *Angew. Chem. Int. Ed.* **49**, 380-384 (2010).
23. Balazs, A.C., Emrick, T. and Russell, T.P. Nanoparticle Polymer Composites: Where Two Small Worlds Meet. *Science* **314**, 1107-1110 (2006).
24. Böker, A., He, J., Emrick, T. and Russell, T.P. Self-assembly of nanoparticles at interfaces. *Soft Matter* **3**, 1231 (2007).
25. Genson, K.L., Holzmueller, J., Jiang, C., Xu, J., Gibson, J.D., Zubarev, E.R. and Tsukruk, V.V. Langmuir–Blodgett Monolayers of Gold Nanoparticles with Amphiphilic Shells from V-Shaped Binary Polymer Arms. *Langmuir* **22**, 7011-7015 (2006).
26. Jiang, C., Markutsya, S., Pikus, Y. and Tsukruk, V.V. Freely suspended nanocomposite membranes as highly sensitive sensors. *Nature Mater.* **3**, 721-728 (2004).
27. Gandubert, V.J. and Lennox, R.B. Assessment of 4-(Dimethylamino)pyridine as a Capping Agent for Gold Nanoparticles. *Langmuir* **21**, 6532-6539 (2005).
28. Dorris, A., Rucareanu, S., Reven, L., Barrett, C.J. and Lennox, R.B. Preparation and Characterization of Polyelectrolyte-Coated Gold Nanoparticles. *Langmuir* **24**, 2532-2538 (2008).
29. Millette, J., Toader, V., Reven, L. and Lennox, R.B. Tuning the miscibility of gold nanoparticles dispersed in liquid crystals via the thiol-for-DMAP reaction. *J. Mater. Chem.* **21**, 9043-9050 (2011).
30. Jones, M.R., Macfarlane, R.J., Lee, B., Zhang, J., Young, K.L., Senesi, A.J. and Mirkin, C.A. DNA-nanoparticle superlattices formed from anisotropic building blocks. *Nature Mater.* **9**, 913-917 (2010).
31. Yockell-Lelièvre, H.I.n., Gingras, D., Vallée, R.a. and Ritcey, A.M. Coupling of Localized Surface Plasmon Resonance in Self-Organized Polystyrene-Capped Gold Nanoparticle Films. *J. Phys. Chem. C* **113**, 21293-21302 (2009).

This page is intentionally blank

Chapter 4

Giant Metal Superlattice Nanomembranes From Ultrathin Gold Nanowires

This page is intentionally blank

Giant metal superlattice nanomembranes are two-dimensional, ordered metallic nanoparticle arrays forming ultrathin membrane of a few nanometers thick but with macroscopic lateral dimensions. Despite the exciting progress in the fabrication of free-standing metallic superlattice nanomembranes, their practical applications are often hampered by the difficulty in fabricating defect-free membranes at large area [1-13]. In particular, it is challenging to grow giant superlattice nanomembranes which feature the two apparently conflicting characteristics – nanoscale thickness and macroscopic lateral dimensions[2]. Previous attempts with sphere-like hard building blocks only led to superlattice membranes restricted to small lateral dimensions.[3, 5, 6, 9, 10] Metallic nanowires are of special interests among nonspherical building blocks[14, 15], since nanowires can not only be associated to provide a large diversity of molecular-scale interconnects[16-18], but also constitute an exciting route to form superlattice membranes with thinnest possible lateral thickness consisting of large quantities of closed-packed nanowires arrays with ordered spatial distribution[19].

In this chapter, giant superlattice nanomembranes were fabricated from soft one-dimensional building blocks – ultrathin single-crystalline gold nanowires (AuNWs) via Langmuir-Blodgett (LB) techniques. Although LB techniques have been widely used for the assembly of nanowires,[20-25] the ability to form mechanically-robust free-standing nanomembranes has not yet been reported, to the best of our knowledge. This could be due to the fact that gold nanowires are thinner and more flexible, contributing to maintaining the integrity of the nanomembranes at large area. Specifically, a single-layer AuNWs superlattice nanomembrane is transparent, conductive and mechanically robust, with an optical transmittance of 90-97% over a wide spectral window of 300-1100 nm, an electrical resistance of $\sim 1142 \text{ k}\Omega \text{ sq}^{-1}$, and a breaking strength of $\sim 14 \text{ N m}^{-1}$ with a typical atomic force microscope probe. Such single-layer nanowire membranes are transferable to any arbitrary substrates, facile to be integrated into lightweight, foldable optoelectronic devices with low consumption of materials and energy. This methodology may serve as a model system, extendable to superlattice nanomembranes from other materials for a myriad of applications in construction of new classes of two-dimensional metamaterials and devices.

4.1 Experimental methods

4.1.1 Materials

Gold (III) chloride trihydrate ($\text{HAuCl}_4 \cdot 3\text{H}_2\text{O}$, $\geq 99.9\%$), Triisopropylsilane (99%) and Oleylamine were purchased from Sigma Aldrich. Hexane and chloroform were obtained from Merck KGaA. All chemicals were used as received unless otherwise indicated. All aqueous solutions were made using demineralized water, which was further purified with a Milli-Q system (Millipore). All glassware used in the following procedures was cleaned in a bath of freshly prepared aqua regia and rinsed thoroughly in H_2O prior to use.

Holey Lacey Formvar/Carbon films (300 mesh and irregular pores with sizes varying from less than a quarter of $1 \mu\text{m}$ to more than $10 \mu\text{m}$) were purchased from Ted Pella. Quantifoil holey carbon films (2 μm -diameter hole, 2 μm in space) were purchased from Electron Microscopy Sciences. Holey silicon nitride support films (2- μm -diameter hole, 4 μm pitch) were purchased from SPI supplies.

4.1.2 Synthesis of ultrathin AuNWs

Large-scale synthesis of ultrathin AuNWs was performed according to the literature[26]. $\text{HAuCl}_4 \cdot 3\text{H}_2\text{O}$ (53 mg) and hexane (50 mL) were added into a 100mL Schott/Duran bottle, followed by addition of Oleylamine (OA, 1.8 mL) as both stabilizer and growth template. After completely dissolving of gold precursor, triisopropylsilane (TIPS, 2.5 mL) was added into above auric solution and allowed to stand for 2 days without disturbing at room temperature. Finally, the solution turned into dark-red, indicating the formation of AuNWs (0.58 mg mL^{-1}). The residue chemicals were removed by repeated centrifuging and thorough washing by ethanol/hexane (1/3, v/v) and finally concentrated into 5mL that dispersed in chloroform (5.82 mg mL^{-1}). Statistical evaluation from TEM images of as-prepared AuNWs shows an estimated yield of $\sim 90\%$. The surfaces of the as-made AuNWs were capped by oleylamine and indicated as hydrophobic property.

4.1.3 Fabrication and transfer of AuNWs superlattice nanomembrane

AuNWs superlattice membrane was prepared using a Langmuir-Blodgett trough (Nima Technology) at 25 °C. The Teflon-coated trough and barrier were wiped with CHCl_3 and then purged with ethanol to remove any dust or organic contaminants. In a typical experiment, 10 mL purified AuNWs (0.58 mg mL^{-1}) was centrifuged and redispersed in 1 mL CHCl_3 (5.82 mg mL^{-1}). Then the concentrated AuNWs solution was added dropwise to the air-water interface of the LB trough. The droplet quickly spread over the water surface in less than 1s and evaporated to leave an isotropically distributed AuNWs floating on the water surface. The trough was then covered to prevent fluid flows and solvent fluctuations, and allowed to equilibrate for 30 min. The AuNWs were then isothermally compressed by moving the two opposing barriers towards each other while the surface pressure was monitored with a Wilhelmy plate. At a target surface pressure (e.g. 20 mN m^{-1} for monolayered AuNWs superlattice membrane), the pressure was kept constant at least 1 h. After the equilibration, the AuNWs superlattice membrane was transferred onto hydrophilic substrates by slowly pulling the substrate out of the aqueous subphase with a vertical dipping speed of 5 mm min^{-1} , and transferred to hydrophobic substrates by horizontal deposition through Langmuir-Schaefer technique. Also, transfer of multilayer AuNWs nanomembrane could be realized by using layer-by-layer transfer method, which is discussed in details in Section 4.2.2.

4.1.4 Characterization

Morphology characterization was carried out using a Philips CM20 TEM at a 200 kV accelerating voltage, Hitachi H-7500 field emission TEM operating at 80kV, and JEOL JSM-7001F FEG SEM. High-resolution TEM images were performed on a JEOL JEM 2011 TEM operated at an acceleration voltage of 200 kV. Stepwise focusing with low beam currents helped to avoid distortion of AuNWs by the electron beam. The transmittance of superlattice nanomembrane is measured with Agilent 8453 UV-Vis spectrophotometer, and the transparent images were recorded by a CCD camera on the J&M MSP210 Microscope Spectrometry System, while the membrane was transferred onto glass slide and illuminated by a high-intensity fiber light source under a $40\times$ objective. Thermogravimetric analysis (TGA) was carried out using a Mettler Toledo TGA-SDTA851 analyzer in the temperature range from 25 to 700 °C at a heating rate

of 10°C/min. The runs were performed under N₂ gas, and the gas was switched to air for 10 min at the end of the run at 700°C to ensure complete combustion of the organic material. N₂ and air gases were used at a rate of 50 mL/min.

Force-displacement curves from nanoindentation and topography images were obtained with a Veeco Dimension Icon AFM in tapping mode using Bruker silicon probes (MPP-21100-10). The spring constant for cantilever was 3 N m⁻¹. The typical tip speed for the indentation was 500 nm s⁻¹. Each membrane was first imaged by AFM, then gradually increased the applied force and performed multiple indentations with the AuNWs superlattice membrane to collect the force-indentation curve, and finally imaged again to check for rupture of membrane.

4.2 Results and discussion

4.2.1 Fabrication of AuNWs superlattice nanomembrane

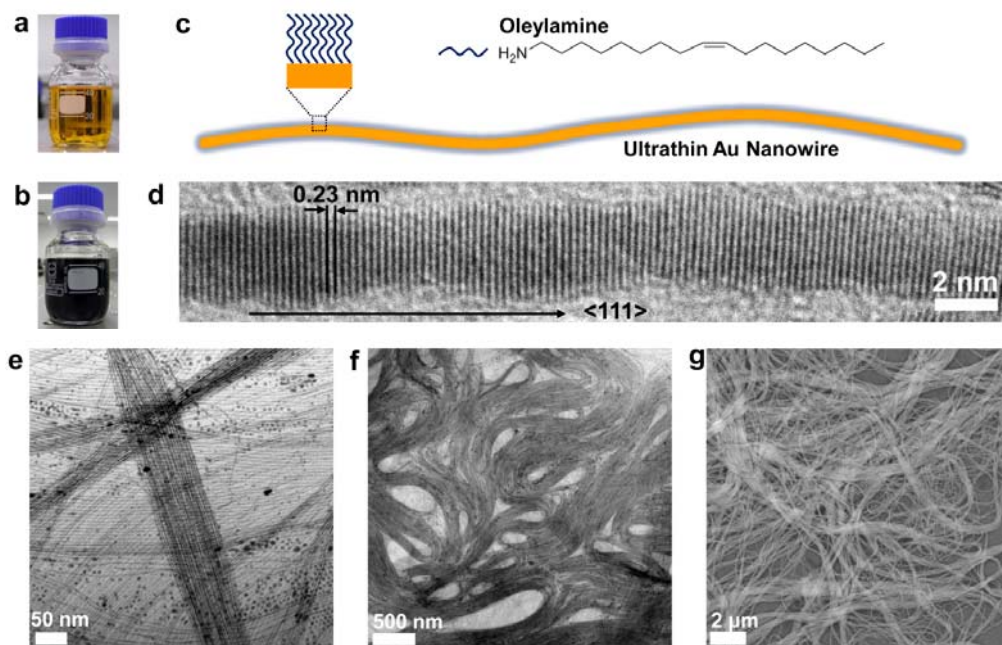


Figure 4.1 | Large-scale synthesis of ultrathin single crystalline AuNWs with high-aspect ratio. (a) and (b) Photographs of the synthesis of ultrathin AuNWs at the initial and final state of reaction. (c) Schematic illustration for the oleylamine-capped AuNWs. (d) High resolution TEM image of an individual single crystalline ultrathin AuNW shows [111] lattice planes. (e) TEM image of aligned AuNWs assemblies. (f) TEM image of AuNWs bundles. (g) SEM image of AuNWs bundles.

High-quality single crystalline ultrathin AuNWs were synthesized by adopting the

recently reported approaches.[26-28] In brief, gold precursor (HAuCl_4) was gradually reduced by triisopropylsilane (TIPS) in the presence of oleylamine (OA). After aging the solution at room temperature for 2 days, the solution turned from yellow to dark red (**Figure 4.1a and b**), indicating complete reduction of Au^+ -amine complex into OA-capped AuNWs dispersible in hexane[27] (**Figure 4.1c**). The nanowires were precipitated out by adding ethanol and centrifugation, and then washed twice with ethanol and re-dispersed in chloroform as concentrated stock solution for further use.

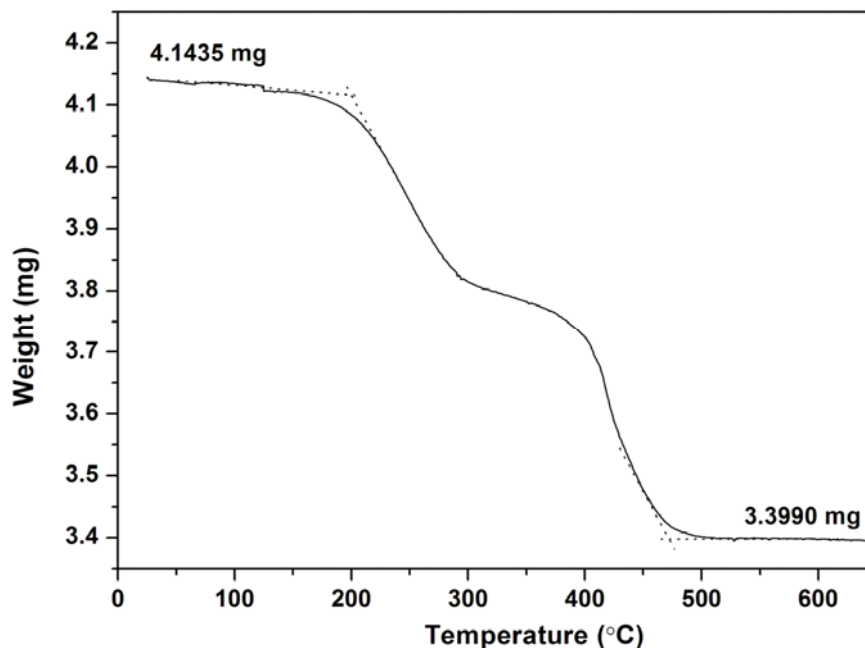


Figure 4.2 | TGA curve of OA-capped AuNWs. The calculated weight ratio of OA/AuNWs is 18%/ 82%. The turning point at 348 °C is corresponding to the boiling point of oleylamine.

In the purified nanowires, the OA molecules contribute to 18% of the total weight as demonstrated by thermogravimetric analysis (**Figure 4.2**). Thus, the OA capping effectively stabilizes nanowires and prevents them from deterioration in various characterization and processing in the fabrication of nanomembranes. Electron microscopy studies show each nanowire is single crystalline growing along the [111] direction (**Figure 4.1d**) with an interfringe distances of ~ 0.23 nm and ultrathin with a width of ~ 2.5 nm. The nanowires have enormous aspect ratios, extending to tens of micrometers in length. These structural characteristics give nanowires high mechanical robustness and flexibility, leading to hairy morphology (**Figure 4.1e**). Due to strong hydrophobic interactions between OA ligands, the nanowires tended to form parallel

bundle-like strands (**Figure 4.1f and g**).

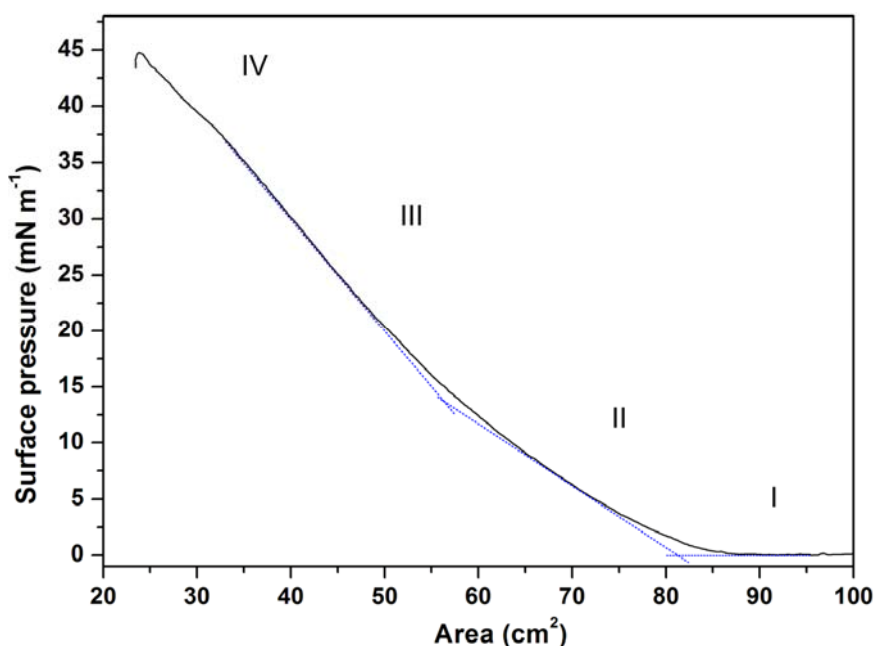


Figure 4.3 | Typical π -A isotherm of the AuNWs superlattice nanomembrane during LB compression obtained at the air/liquid interface at 25 °C. The AuNWs superlattice nanomembrane undergoes four transition stages as surface pressure is increased, indicated by a change in the isotherm slope.

The as-synthesized AuNWs were used to fabricate giant superlattice nanomembranes by LB techniques. Typically, one droplet (~ 4 -6 μ L) of nanowires dispersed chloroform solution was carefully spread onto the water surface in a LB trough. The droplet quickly spread and evaporated in less than 1s, distributing the nanowires uniformly on the water surface. By moving LB baffle, the free-floating nanowires were forced to approach each other with gradual phase transitions (**Figure 4.3**). In particular, a Mott-insulator-to-metal transition was noted at the surface pressure of ~ 13 mN m^{-1} . This transition was indicated by the appearance of red-colored metallic sheen, and further demonstrated by turning the slope in the typical π -A isotherm.[22] A further compression led to rapid pressure buildup from 13 mN m^{-1} to 38 mN m^{-1} until collapse, and in this process a condensed nanowire membrane formed on the water surface. **Figure 4.4a** shows a giant nanowire superlattice membrane covering an entire trough area of ~ 35 cm^2 . The membranes were mechanically strong yet flexible, transferable to a variety of substrates (including silicon, glass slides, paper, plastics, TEM copper grids, and PDMS, *etc*) without cracking or rupturing (**Figure 4.4b**). The coating could substantially alter the wetting properties. For example, the contact angle of a glass slide

increased from $\sim 26^\circ$ to $\sim 103^\circ$ after nanomembrane covering (**Figure 4.4c**).

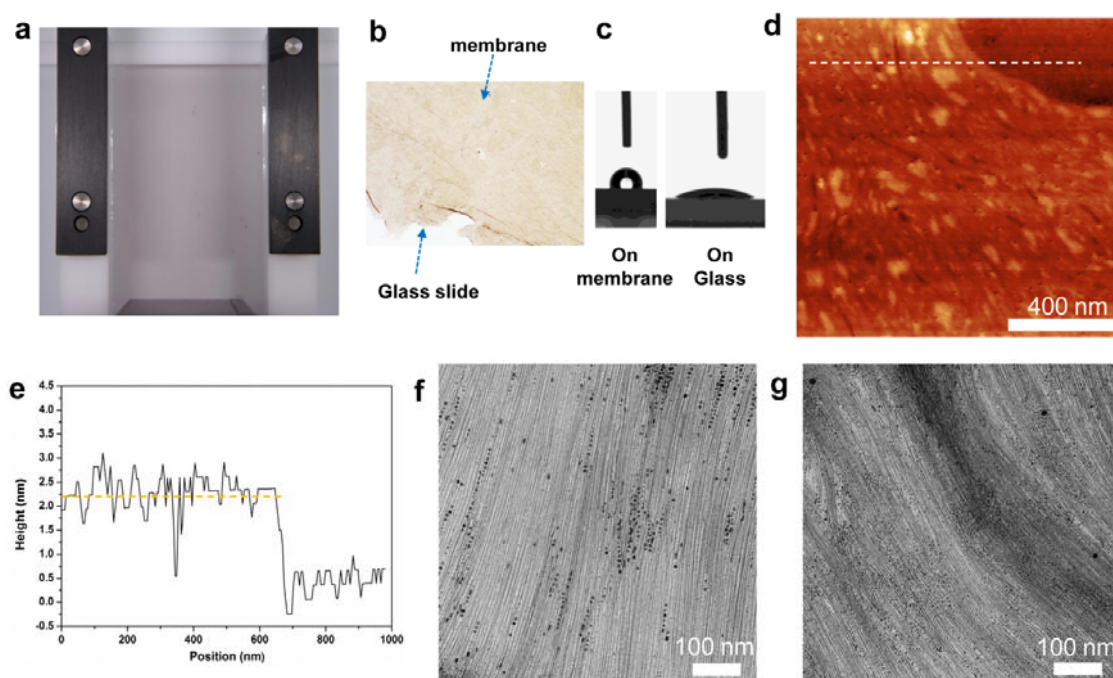


Figure 4.4 | Fabrication of monolayered AuNWs superlattice nanomembrane. (a) Photograph of a homogeneous nanomembrane with an area of 35 cm^2 on the LB trough. (b) Photograph of a membrane transferred onto a glass slide. (c) Photographs of sessile water droplets on glass and on membrane. (d) AFM height image of the superlattice nanomembrane transferred onto silicon wafer. (e) AFM cross-sectional height plot corresponding to the dashed line in (d). (f) and (g) TEM images of monolayer superlattice nanomembranes collected at surface pressure of 20 mN m^{-1} and 30 mN m^{-1} , respectively.

4.2.2 Transfer and manipulation of AuNWs superlattice nanomembrane

Facile and effective transfer could be achieved by both Langmuir-Blodgett vertical deposition[29] and Langmuir-Schaeffer techniques[18]. After the equilibration of nanomembrane at a target surface pressure, the AuNWs superlattice nanomembrane could be transferred onto hydrophilic substrates by slowly pulling the substrate out of the aqueous subphase with a steady dipping speed of 5 mm min^{-1} . Also, multilayer AuNWs nanomembranes can be obtained by repeating the LB deposition procedure through layer-by-layer method. For the hydrophobic substrates, horizontal deposition can be used through Langmuir-Schaeffer technique. **Figure 4.5** shows a direct transfer of AuNWs nanomembrane with a large area onto PDMS surface, and indicates flexibility without cracking after repeated bending cycles.

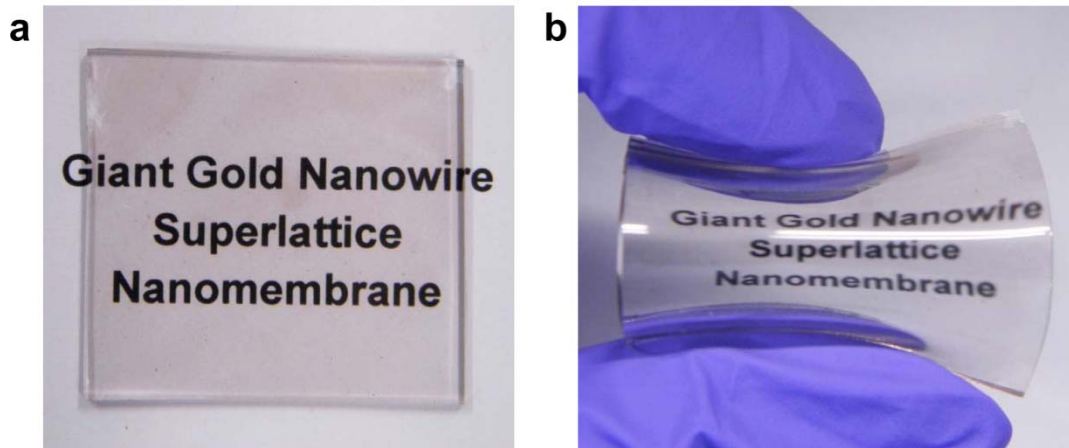


Figure 4.5 | (a) Photograph shows that monolayer AuNWs superlattice nanomembrane was entirely transferred onto PDMS (3cm×3cm). The printed words are clearly visible, indicating the high optical transparency of monolayer nanomembrane. (b) The nanomembrane could withstand repeated bending without deterioration or rupturing.

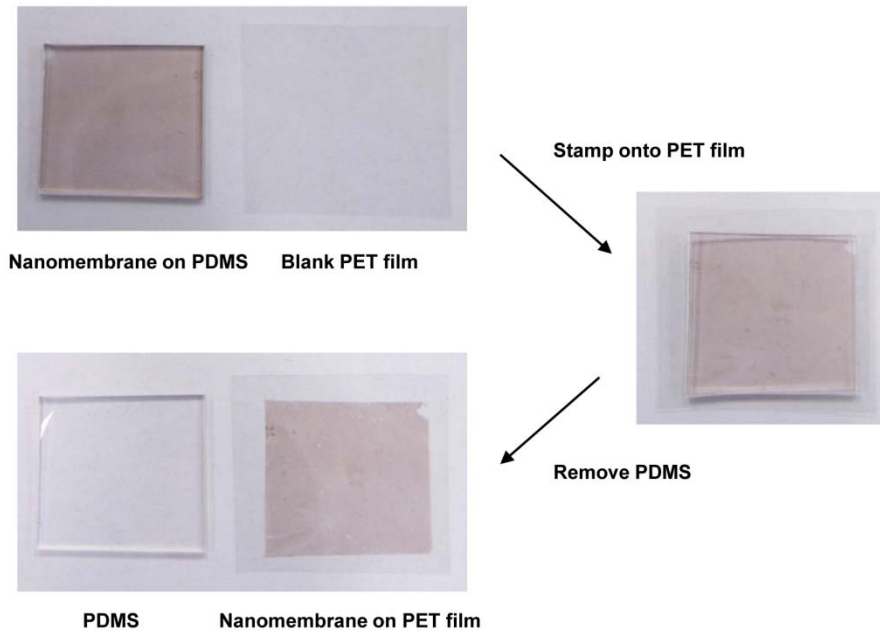


Figure 4.6 | Process of substrate-to-substrate transfer process from PDMS to PET surface. Note that the transfer is 100% fidelity.

Remarkably, AuNWs nanomembranes could also be transferred from one substrate to another. It could be firstly transferred onto a PDMS sheet, and then transferred to any other solid substrate. **Figure 4.6** shows the transferring process of nanomembranes from PDMS sheet to PET plastics. The AuNWs nanomembrane coated PDMS stamp was put onto PET film with a moderate pressure to ensure the intimate contact between two substrates. After slowly pulling away the PDMS stamp, the AuNWs

nanomembrane could be completely transferred onto PET surface. This facile transfer technique has suggested a prospective method to fabricate patterned AuNWs nanomembranes by integration with soft lithography[30].

4.2.3 Morphological characterization of AuNWs superlattice nanomembrane

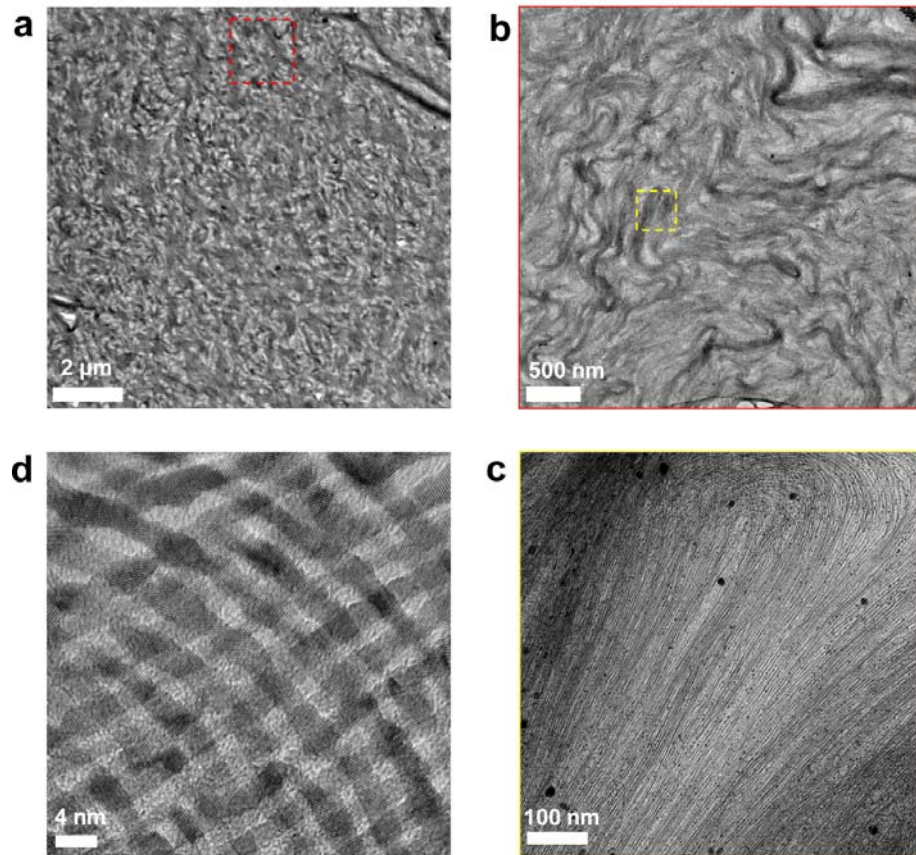


Figure 4.7 | (a) and (b) TEM images of AuNWs superlattice nanomembrane after transferred to holey carbon film at high surface pressure of 40 mN m^{-1} , which exhibited tight packed arrays with periodic wrinkling folds in the membrane. Panel (b) shows the magnified parts of the membrane (red dash) in panel (a). (c) is the magnified TEM image of yellow dashed part in (b), indicating the arc structure of monolayer and reflects the flexibility of ultrathin AuNWs. (d) TEM image shows a nanomesh-like morphology of two layers of AuNWs superlattice nanomembrane. This is formed by first transferring one layer of membrane onto carbon film, followed by transferring the second layer after turning 90° of carbon film during deposition.

Remarkably, the nanomembranes consisted of dominantly monolayered nanowires aligned in parallel. **Figure 4.4d** shows a typical atomic force microscopy (AFM) image of AuNWs nanomembranes transferred onto a silicon wafer. The membrane is uniformly continuous extending to centimeter-scale with little defects. Further AFM line scanning gave an average thickness of $2.2 \pm 0.1 \text{ nm}$ (**Figure 4.4e**). Monolayered

superlattice nanomembranes could withstand large lateral compression forces up to $\sim 38 \text{ mN m}^{-1}$. The membranes were then transferred to lacey/carbon copper grid at specific surface pressures of 20 mN m^{-1} and 30 mN m^{-1} , and their morphologies were characterized (**Figure 4.4f and g**). Both images indicated predominantly the monolayered AuNWs, in agreement with the above AFM characterizations. Nevertheless, under high compression forces, the membranes tended to be crumpled by piling (**Figure 4.4g**) or bending (**Figure 4.7**). Nevertheless, the membranes remain intact without any cracking or rupturing during the LB compression process.

4.2.4 Mechanical properties of AuNWs superlattice nanomembrane

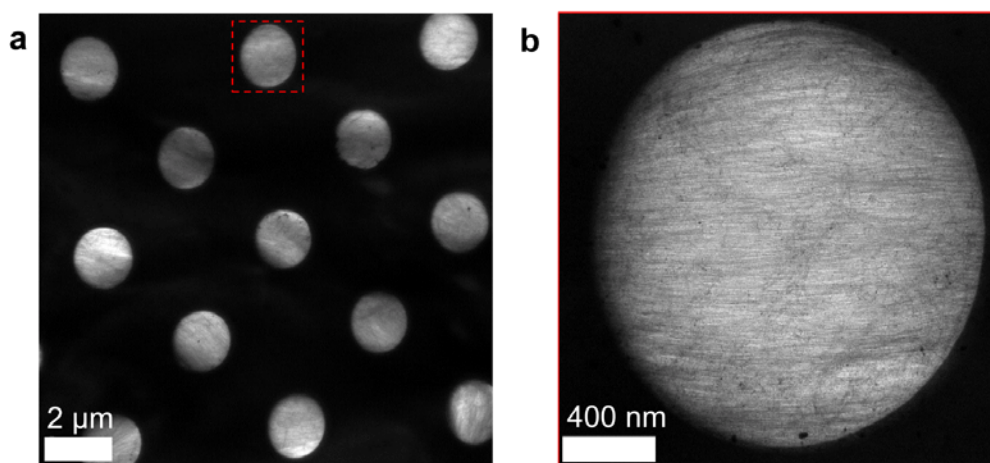


Figure 4.8 | TEM images of the free-standing AuNWs superlattice nanomembrane formed by transferring onto a holey silicon nitride substrate with $2\mu\text{m}$ -diameter holes. (a) The monolayer superlattice nanomembranes were stretched themselves across over the substrate with the holes without deterioration. (b) Magnified TEM image of an intact monolayered superlattice nanomembrane in (a), indicating an ordered array of AuNWs. These free-standing AuNWs membranes were further indented by AFM for characterization of mechanical properties.

To quantitatively determine the mechanical property of free-standing superlattice nanomembranes, AFM nanoindentation experiments were performed. Firstly, the superlattice membranes were transferred onto holey silicon nitride substrate patterned with periodic $2\mu\text{m}$ -diameter holes. The superlattice membranes could span over the holes. Majority of membranes ($\sim 80\%$) remained intact after transfer and survived from vacuum drying (**Figure 4.8**). By high-resolution imaging, we located specific intact membranes (**Figure 4.8b**) and then indented at the center of microholes. Force-displacement curves were recorded with stepwise increase of force until rupturing the

membrane (**Figure 4.9a**). Notably, the ruptured holes were V-shaped memorizing the shapes of pyramid AFM probes (**Figure 4.9e and f**), and the adjacent holes didn't coalesce, indicating paper-like mechanical properties. Consistent force curves were obtained for both multiple indents within a specific holey region, as well as other holey areas.

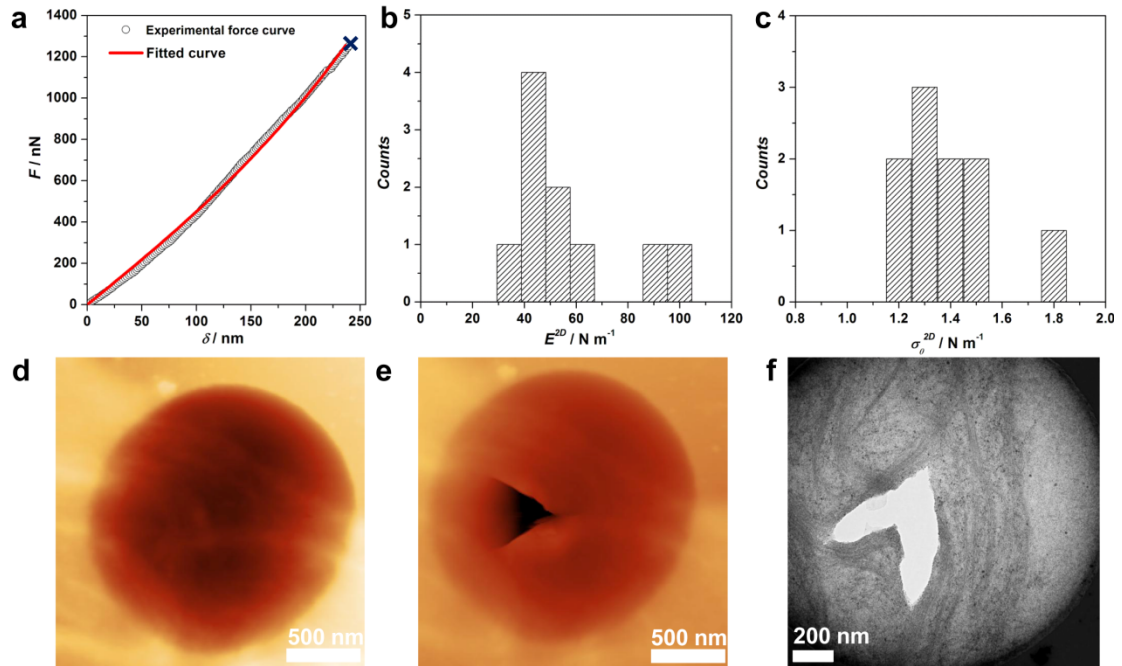


Figure 4.9 | Mechanical properties of monolayered superlattice nanomembranes. (a) Force-displacement curves from AFM indentation (circle) and from theoretical fitting (line). Fracture load is indicated by a \times mark. (b) Histogram of 2D elastic modulus, E^{2D} . (c) Histogram of membrane pretention, σ^{2D} . (d) AFM height image of superlattice nanomembrane cover over a 2- μm -diameter microhole in the silicon nitride substrate before indentation. (e) AFM height image of a ruptured nanomembrane. (f) corresponding TEM image of the same ruptured nanomembrane in (e). Note that triangle hole in (e) becomes v-shaped hole in (f), which indicates that the “triangular tongue-like membrane” yielded in AFM imaging but recovered back in TEM imaging. This result echoes the strong mechanical properties as revealed in (a).

4.2.4.1 Young's modulus of AuNWs superlattice nanomembrane

By fitting the force curves, Young's modulus can be derived using the similar model reported earlier[3] **Figure 4.9a** shows a typical trace of the force-displacement curves which plots the deflection of cantilever as it contacts and separates from the sample during the extension and retraction of the scanner. All curves are linear in small force and turn nonlinear at large displacement. Finally, the membrane will rupture at large force, resulting in the hysteresis of indenting and retracting traces. AuNWs superlattice

membranes allowed for multiple ruptures within the same membrane (**Figure 4.10**) and individual rip did not nucleate during repeated AFM imaging and TEM re-imaging. This characteristic suggests that superlattice nanomembrane behaves as if it was macroscopic paper or alumina foil, in agreement with the scaling law of elastic membranes[31].

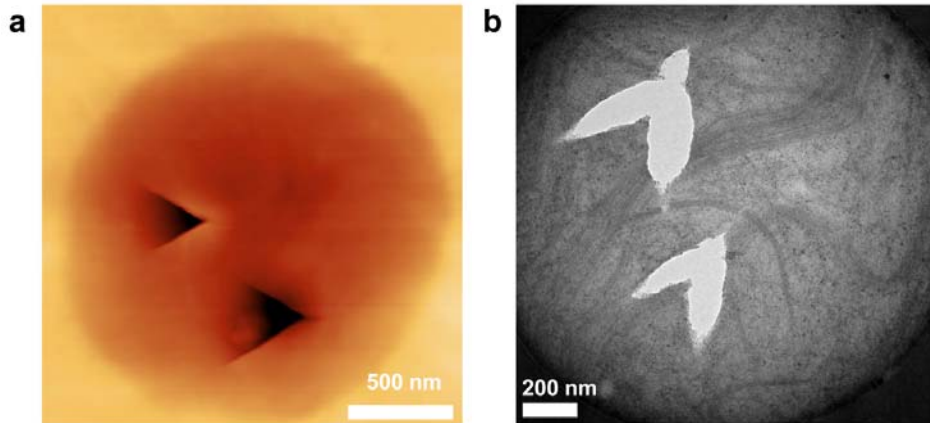


Figure 4.10 | (a) AFM height image of AuNWs superlattice nanomembrane after two times indentation and allowed for multiple ruptures within the same membrane. (b) Corresponding TEM image of double poking. The degradation of AuNWs was observed in TEM image in (b) upon long exposure to the high-energy electron beam.

To calculate the force applied to the membrane during indentation it is necessary to measure the cantilever sensitivity, which is the cantilever deflection signal *versus* the voltage applied to the Z piezo determined from the slope of the force plot during indentation on clean silicon surface immediately after indentation on membranes. Then nanoindentation was performed by using the same tip (cantilever spring constant is 3 N m^{-1}) without repositioning the tip or changing the laser alignment during the series of tests. Multiple indentations were performed by gradually increasing the forces not only on single AuNWs membrane, but also single indents on multiple membranes, without observing damage of our membrane prior to breakage at final high forces. The force brought to bear on the membrane was calculated from:

$$F = k \times \delta_{\text{deflection}} \quad \text{Equation (4.1)}$$

where k is the spring constant of cantilever and $\delta_{\text{deflection}}$ is the measured deflection .

Indentation depth (δ) in final force-displacement curves was calculated from:

$$\delta = Z_{\text{piezo}} - \delta_{\text{deflection}} \quad \text{Equation (4.2)}$$

where Z_{piezo} is the height of the cantilever. Force-displacement curves were obtained by plotting the applied force *versus* indentation depth, δ . The elastic behavior can be described by that of a clamped circular film indented at the center with an infinitely small point[3, 6]:

$$F = k\delta + \frac{\pi E h}{3R^2} \delta^3 \quad \text{Equation (4.3)}$$

where E is Young's modulus, h is the film thickness, and R is the film radius. This model is valid for the regime in which $\delta/h \gg 1$ and the tip diameter is small compared to the film radius. As long as the indentation depths reached distances much greater than the film thickness, a transition from linear to cubic term would appear[32]. Here Poisson's ratio was assumed to be 1/3. The spring constant of membrane (k) could be calculated from the linear regime of the curve, which was depending on the pre-strain of the film[6]. By using k as the fitting parameter, Young's modulus is able to be extracted through fitting of $F(\delta)$ to Equation (4.3). Finally, Young's modulus was calculated to be 5.2 ± 0.4 GPa for AuNWs superlattice membranes based on ten different measurements (**Figure 4.11**). This value is comparable to those for DNA-nanoparticle membrane[3] and alkyl-nanoparticle membrane.[6, 11]

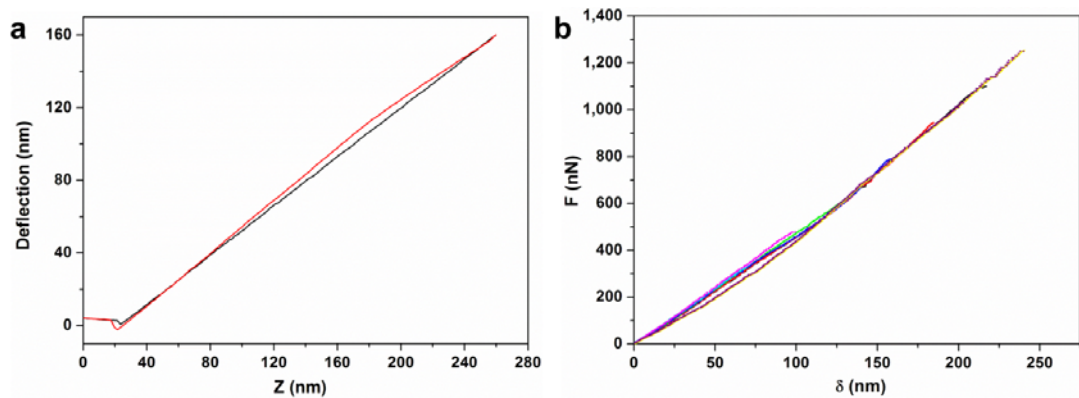


Figure 4.11 | (a) Typical force-displacement curve of AuNWs superlattice nanomembrane in Fig. 3a. Black represents the indent cycle and red represents the retract cycle. The tip experienced a strong attractive force that caused a jump into contact with sample surface. On the retract cycle the tip jumps out of contact just as the retraction force overcomes adhesion and then pulled off. (b) Statistical distribution of force-displacement curves of ten indents from different membranes in Fig. 4.8.

4.2.4.2 Mechanical strength of AuNWs superlattice nanomembrane

The breaking strength of AuNWs superlattice membrane was estimated by using a

typical AFM probe with a tip radius of 24 nm. Based on the models used for monolayer graphene,[32] it was assumed that nanowire superlattice nanomembrane as a true 2D material given the ultrathin nature and large aspect ratio of nanomembrane. Thus, the strain energy density can be normalized by the area rather than the volume of the nanomembrane. Hence, its mechanical behavior under AFM probe indentation is properly described by a 2D stress, σ^{2D} and 2D modulus, E^{2D} . Both have units of force/length rather than force/area for normal 3D material systems. The force-displacement behavior for a clamped circular membrane under central point loading can then be approximated as:

$$F = \sigma_0^{2D} (\pi R) \left(\frac{\delta}{R} \right) + E^{2D} (q^3 R) \left(\frac{\delta}{R} \right)^3 \quad \text{Equation (4.4)}$$

where F is the applied force, σ_0^{2D} is the pretension in the membrane, R is the radius of circular membrane, δ is the deflection at the center, E^{2D} is the 2D modulus, and q is a constant depending on poisson's ratio, ν , by the equation, $q = 1/(1.05-0.15\nu-0.16\nu^2)$. Numerical fitting of 10 sets of force curves from different locations under different loads gave σ^{2D} and E^{2D} of 1.4 ± 0.1 N/m and 52 ± 23 N/m, respectively (**Figure 4.9b and c**). With these values on the basis of the continuum model used for 2D material,[32] the breaking strength was calculated to be 14.3 ± 1.4 N/m. Following the identical treatment, the breaking strengths of previous reported DNA-based nanoparticle membranes were also calculated. By using DNA of 30 and 50 bases long, the breaking strength was estimated of 4.5 N/m and 1.8 N/m, respectively. Considering the fact that 100nm-radius probe was used in DNA-based nanomembranes, the above results show that the nanowire superlattice membrane is much stronger than DNA-nanoparticle membrane. This may originate from the 1D nanowire building blocks used in this study. It is harder to break gold nanowires than tangled DNA strands.

4.2.5 Optical property of AuNWs superlattice nanomembrane

The monolayer AuNWs nanomembrane exhibited exceptionally high optical transmittance of 90-97 % with an almost flat line over a fairly wide spectral range of 300~1100 nm (**Figure 4.12**). The observed high optical transparency is due to the ultrathin nature of our superlattice nanomembranes, which is in agreement with the

theoretical prediction.

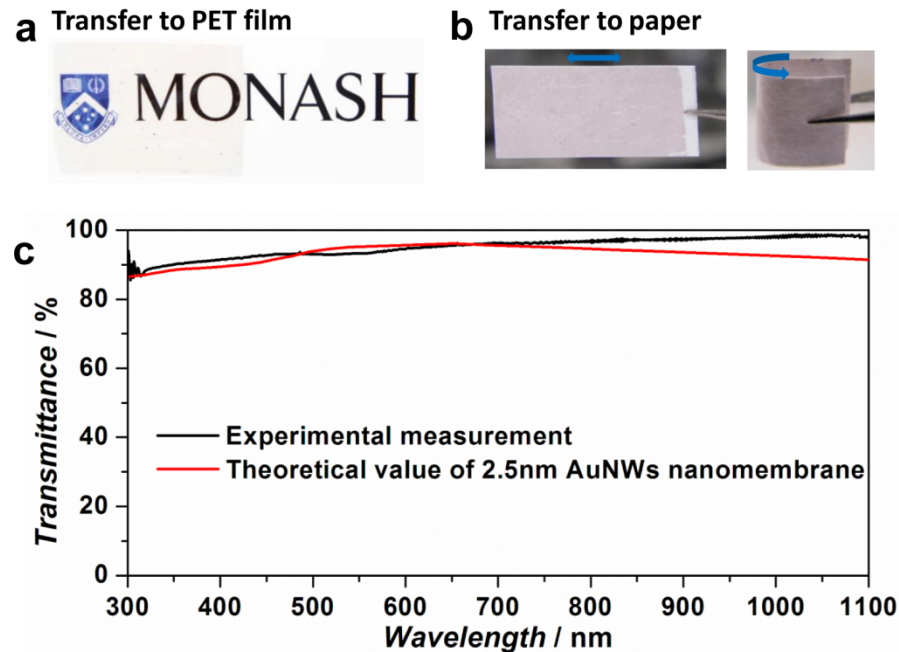


Figure 4.12 | High optical transparency of monolayered AuNWs superlattice nanomembrane. (a) photograph of a PET plastic sheet partially covered with superlattice nanomembrane. (b) a paper sheet coated with nanomembrane on both sides. (c) experimental (black) and theoretical (red) transmittance spectra of monolayered superlattice nanomembrane on a glass slide. Approximate agreement in experiment and theoretical calculation proves that nanomembranes are composed of predominantly a single nanowire layer.

The theoretical transmittances of nanomembranes with different AuNW diameters were determined by calculating the decay of an electromagnetic wave after propagating through a medium[33]. In this model, the incident light was vertical to the air/membrane/glass/air multi-layer 2-D cross-sectional structure. The structure was divided into rectangular unit cells (strips) with unified width and variable heights according with the surface topology of the AuNWs on the substrate. The calculation is then made separately in each cell, followed by an integration step over one lateral pattern period. The diameters of the AuNWs were set to be 1.9, 2.5, 10 and 15 nm as shown in **Figure. 4.13**. The surface coverage was fixed to 60% as calculated from the TEM images. The frequency-dependent refractive index and extinction coefficient values are obtained based on the reported reference[34]. The light polarization is not considered here, as the AuNWs are aligned in parallel in the scale of a few micrometers, much smaller than the beam size of the incident light for the transmittance measurements. Also, although transverse plasmonic modes are generated in a single

nanowire and between nanowires, this effect is not considered in this calculation, as the resonance wavelengths of AuNWs with diameters of a few nanometers should be beyond the lower end of the spectrum for the transmittance measurements.

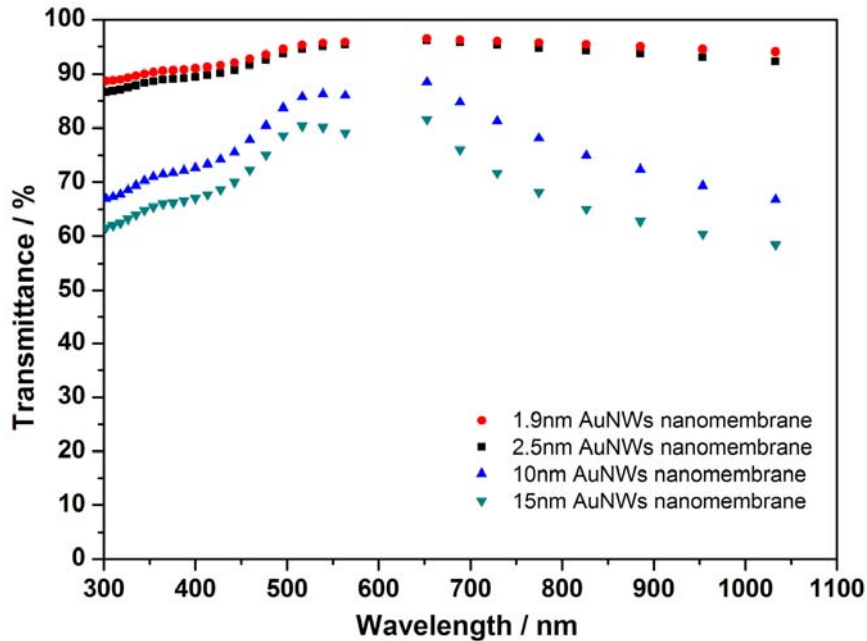


Figure 4.13 | Theoretical calculation on transmittance spectra of monolayer superlattice nanomembranes composed by AuNWs with different diameters.

As shown in **Figure 4.13**, the results showed an evident decreasing trend of the transmittance with increasing diameters. Note that the calculated theoretical transmittance of 2.5 nm AuNWs monolayer nanomembrane provides a reasonable fit of our measured profile, which further proved the monolayer structure of our nanomembrane. The slight decrease in the region of 500-550 nm is due to the surface plasmon resonance of spherical nanoparticles existing as impurity in the nanomembrane as seen in **Figure 4.1e** [35].

4.2.6 Electrical conductivity of AuNWs superlattice nanomembrane

For any optically transparent, electrically conductive thin films, there is a general trade-off between the transmittance and resistance, that is, the thicker films tend to be more conductive but less transparent, while the thinner films tend to be more transparent but less conductive. A proper transmittance-resistance combination is an important design factor for application of transparent, conductive thin films on real devices. For a better understanding of the AuNW superlattice nanomembranes, the optical-electrical

properties of multiple layers of nanomembranes were investigated by measuring transmittance (T) and four-point probe sheet resistance (R_{sh}). A single layer of nanomembrane gave T of 97% at 800 nm wavelength. The square resistances of a set of superlattice membranes from 15 batches of stock nanowire solutions were measured and giving a value of $1142 \pm 16 \text{ k}\Omega \text{ sq}^{-1}$. Both the T and R_{sh} decreased as increased coating layers, as shown in **Figure 4.14**. For 10-layer nanomembranes, T reduced to 37 % and R_{sh} reduced by one order of magnitude compared to those values for the monolayer.

Generally, the relationship between the transmittance and sheet resistance can be described as following[36, 37]:

$$T(\lambda) = \left(1 + \frac{188.5 \sigma_{op}(\lambda)}{R_{sh} \sigma_{dc}} \right)^{-2} \quad \text{Equation (4.5)}$$

where $\sigma_{op}(\lambda)$ is the optical conductivity for wavelength λ and σ_{dc} the DC conductivity. This expression was used to fit the experimental data (**Figure 4.14**). The λ was set to be 800 nm. The ratio σ_{dc}/σ_{op} can be considered as a figure of merit to represent the transparent conductive layer, e.g., higher σ_{dc}/σ_{op} means better DC conductance of membrane with the same transparency. The numerical fitting of experimental data gave, $\sigma_{dc}/\sigma_{op} = 1.25$.

Improving σ_{dc}/σ_{op} requires better understanding of the mechanisms behind the resistance of AuNWs superlattice nanomembranes. In general, the total resistance is a superposition of resistance from the single AuNW and resistance from the formation of the membrane network. This is affected by the following five factors: (i) The resistivity of single AuNW, which is generally larger than that of bulk. The additional resistance is from electrons hitting at the nanowire wall. In a constrained geometry there is always a fraction of electrons scatter to the wall and their energy is partially dissipated. The fraction of electrons scattered to the wall and the corresponding energy loss become considerably large, when the cross-section of the wire is smaller than the mean-free pathlength of electrons in the metal[38]. The AuNWs with diameter of $\sim 3 \text{ nm}$ fall right in this category. (ii) The grain boundary of metal can also create resistance[39]. (iii) The contact resistance at the joint of two nanowires, which can be quite significant,

resulting large resistivity of nanowire network of large lateral scale[30]. (iv) Insufficient paths for electrons to transport laterally along the surface. This can be quite significant if the nanowire surface coverage is too low. (v) Random orientation of nanowires (disorder) over large lateral scale. This will increase the pathlength (and therefore resistance) for electron to transport from one position to another position in the network. In the worst case, which also commonly happens for any physical networking system, there forms some clusters in the network and these clusters are linked weakly or even completely isolated. Therefore, the electron transport between two adjacent clusters could be very difficult[40].

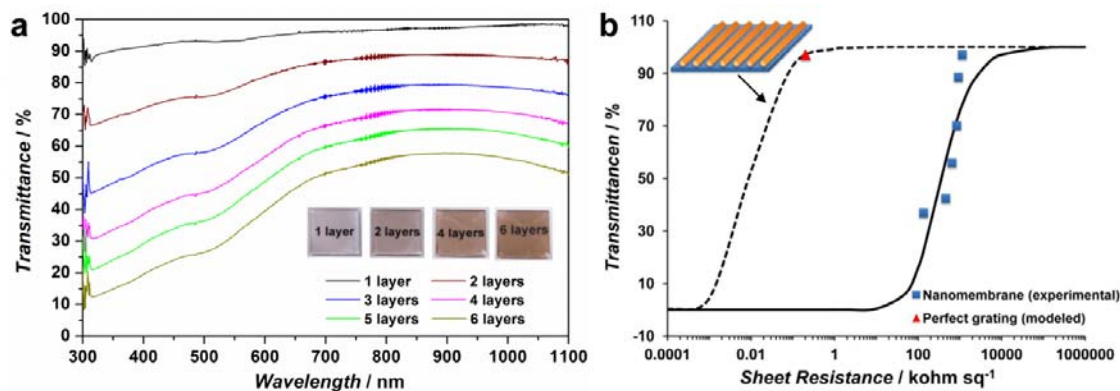


Figure 4.14 | (a) Optical transmittance spectra of monolayer and multilayer AuNWs superlattice nanomembranes. Insets show images of different layers of AuNWs nanomembranes transferred onto the PDMS substrate, and the words printed on bottom paper help visualize the transparency. (b) Transmittance ($\lambda = 800$ nm) as a function of sheet resistance. Data of both nanomembranes (experimental, blue squares) and perfect grating (modeled, red triangle) are shown. Solid and dashed curves predict the transmittance-sheet resistance relationship of nanomembranes and gratings (shown in inset scheme), respectively.

Firstly, the resistance due to the nanowire itself was considered, corresponding to factor (i) and (ii). The as-synthesized AuNWs is ultrathin, single-crystalline with ultra-long aspect ratios. According to the classic scattering model given by Sondheimer[38], the conductivity of a metal nanowire reduces almost proportionally when reducing its diameter. Assuming the bulk resistivity of Au is $22.2 \Omega \cdot \text{nm}$, the mean free pathlength of electrons in Au is 40 nm, and all the electrons scattered to the nanowire wall are absorbed with their energy dissipated, the calculated resistivity of a 3 nm-diameter AuNW is about $300 \Omega \cdot \text{nm}$. Most recent research has found that if the AuNWs are

highly crystalline and the surface is highly smooth, the energy can be mostly recovered from elastic scattering and the conductivity of the NWs can be close to its bulk condition[41]. Therefore, it is reasonable to assume a conductivity of $22.2 - 300 \text{ } \Omega \cdot \text{nm}$ for the AuNWs.

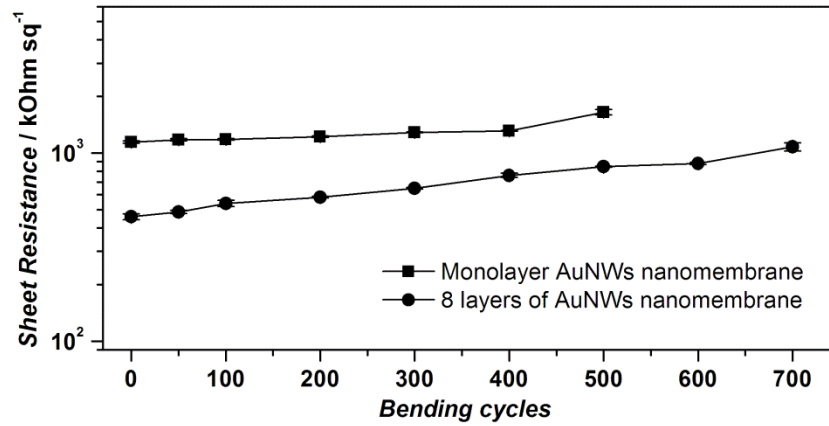


Figure 4.15 | Sheet resistance as a function of bending cycles for one- and eight-layer of AuNWs nanomembranes.

Then the resistance from superlattice membrane structures was considered. From structural characterization of nanomembranes by TEM, the nanowires reach a surface coverage of 60%. If it is assumed that the nanowires are infinitely long and ideally aligned at the device scale, then an estimated sheet resistance of $15 - 200 \text{ } \Omega/\text{sq}$ can be obtained for this perfect grating. The T of 97% and R_{sh} of $200 \text{ } \Omega/\text{sq}$ correspond to the red triangle showing in **Figure 4.14**. Using $\sigma_{dc}/\sigma_{op} = 50000$ to fit, the transmittance-resistance relationship of this perfect grating is also predicted in **Figure 4.14b**. Since the perfect grating ignores resistance factor (iii) to (v), the discrepancy may be due to the fact that AuNWs have finite length and the alignment is limited to micrometer-scale, and there may exist a large contact resistance at the joint of two nanowires.[30] To reduce the square resistance for multilayered nanomembranes, normal pressing forces were applied to the multilayered membranes and observed improvement in conductivity (15-19%), which may be due to the decrease of wire-to-wire spacing during mechanical compression.[42] Nevertheless, the conductivity remains far from theoretical prediction, indicating that the densely-packed capping oleylamine molecules surrounding AuNWs may substantially prevent electron-hopping from wire to wire. Despite high sheet

resistance, superlattice nanomembrane could withstand mechanical bending for hundreds of cycles. The monitored sheet resistance of superlattice nanomembranes was shown in **Figure 4.15**. In particular, the sheet resistance for monolayer nanomembrane only increased by about 14% after 400 bending cycles.

4.2.7 Nanomembrane-based supercapacitor and electrocatalytic electrode

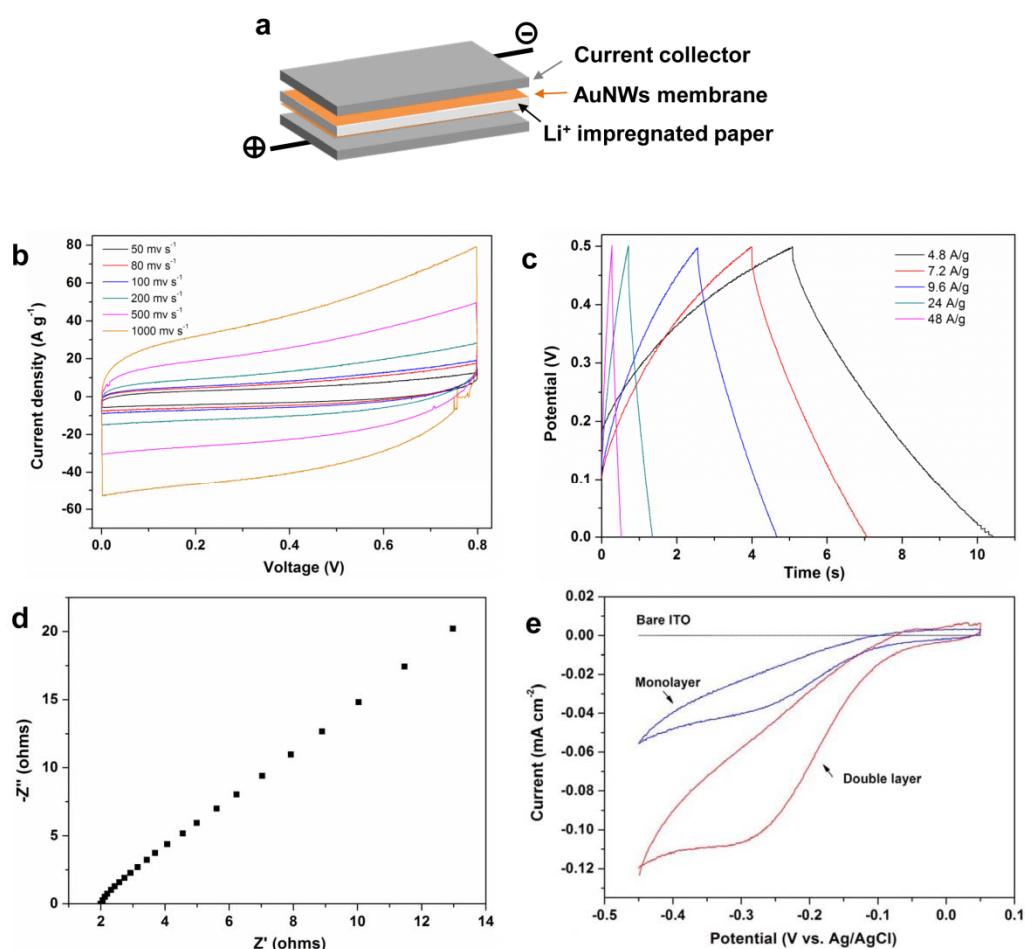


Figure 4.16 | (a), Schematic illustration of nanomembrane-based supercapacitor device. (b) Cyclic voltammograms of supercapacitor in Li₂SO₄ at different scan rates. (c) Charge-discharge curves at various current density. (d) Nyquist plot (a plot of the imaginary component, Z'' , versus the real component, Z' of the impedance) for the supercapacitor. (e) Electrocatalysis of AuNWs superlattice nanomembrane towards oxygen reduction reaction in 0.1 M PBS (pH = 7.2) solution at room temperature (sweep rate 50 mV s⁻¹).

Notably, both quantities of nanowires and the lateral dimensions of membranes are scalable, which allows fabrication of giant superlattice nanomembrane in large quantities promising for practical applications. In particular, nanomembranes could be easily integrated into a flexible supercapacitor device (**Figure 4.16a**). By Langmuir-

Shaeffer deposition, the superlattice membranes could be transferred onto both sides of paper (**Figure 4.12b**), and repeated bending didn't destroy membranes or influence conductivities. Then a two-electrode supercapacitor device could be constructed by impregnating the paper with the 2M Li_2SO_4 electrolyte and sandwiching the membrane/paper between two current collectors (**Figure 4.16a**).

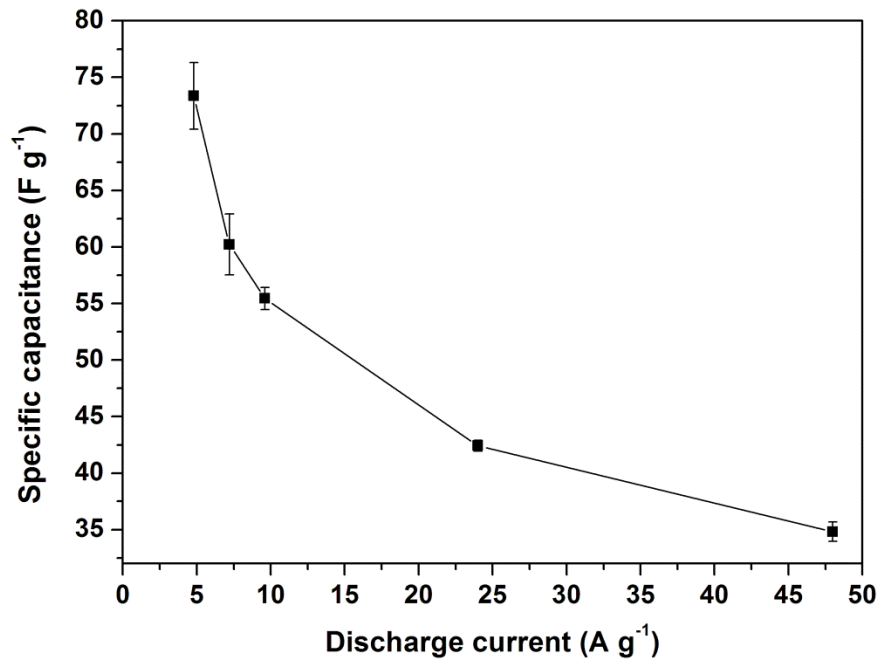


Figure 4.17 | Specific capacitance (C_s) versus discharge current density plots.

The device exhibited superior supercapacitive behavior. We first investigated the effect of scan rate on the electrochemical performances of nanowire membrane supercapacitors. **Figure 4.16b** shows the cyclic voltammogram (CV) over a broad scanning window from 10 to 1000 mV s^{-1} . Note that the current increases with scan rate and the CV curves were close to being rectangular in shape even at the scan rate of 1000 mV s^{-1} , suggesting a nearly ideal supercapacitive behavior[43]. Although the presence of OA capping layer on the surface of AuNWs membrane likely contributed to a small amount of pseudocapacitance, the linearity of the measured current indicates that this device is primarily nonfaradaic. Galvanostatic charge/discharge curve at various current density (4.8 - 48 A g^{-1}) displays a nearly linear response and thus excellent capacitive behavior (**Figure 4.16c**). Specific capacitance (C_s) is calculated from the discharge curves according to the following equation[44]:

$$C_s = i / [-(\Delta V / \Delta t)m] \quad \text{Equation (4.6)}$$

where i is the applied current, $\Delta V/\Delta t$ is the slope of the discharge curves after the voltage drop at the beginning of each discharge (iR drop), and m is the mass of AuNWs superlattice membrane on one electrode. Based on HR-TEM measurement, the total width of a single AuNW together with OA capped layer is estimated as 3.6 nm. Then the weight density of monolayer AuNWs superlattice membrane that covered on paper can be calculated and give a value of $3.5 \mu\text{g cm}^{-2}$. Based on the above calculations, the specific capacitance (C_s) as a function of the applied current densities were investigated (**Figure 4.17**), giving the highest specific capacitance as 73 F g^{-1} . From the charge/discharge curves, the energy density (E) and power density (P) could be calculated by using the total resistance calculated from internal resistance (IR) drop from the charge-discharge:

$$P = V^2 / 4Rm \quad \text{Equation (4.7)}$$

$$E = 0.5CV^2 / m \quad \text{Equation (4.8)}$$

where V is the cutoff voltage, C is the measured device capacitance, m is the total mass of the superlattice membrane on electrode. The internal resistance (R) was determined from the voltage drop at the beginning of each discharge:

$$R = \Delta V_{iR} / (2i) \quad \text{Equation (4.9)}$$

where ΔV_{iR} is the voltage drop between the first two points in the voltage drop at its top cutoff and i is the current applied. The maximum energy density of 2.5 Wh kg^{-1} and the highest power density of 107 kW kg^{-1} were achieved at an operation voltage of 0.5 V. This value is comparable to previously reported carbon-based electrode materials and exhibits substantially higher power density[45-47]. This high power density may be originated from the low equivalent series resistance (ESR) of giant superlattice nanomembrane-based device, which could be further evaluated by electrical impedance spectroscopy (EIS) in the frequency range of 0.05 Hz to 100 kHz (Fig. 5e). From the extrapolation of the vertical portion of the Nyquist plot to the real axis, the ESR was estimated to be 2.1Ω , which is contributed from both of the electrolyte resistance and electronic resistance of membrane[48]. This value is lower than that by other supercapacitors[45-47], which demonstrates the excellent electrical conductance

between the giant superlattice nanomembrans and the current collector, although the lateral in-plane conductance is low.

The nanowire superlattice membranes could behave as electrocatalysts towards cathodic oxygen reduction reaction (ORR). **Figure 4.16e** shows the ORR polarization curves for monolayer and bilayer nanomembranes covered on ITO electrode surfaces. For both giant superlattice nanomembrane modified ITO electrodes, the distinct reduction peak at -270 mV vs. Ag/AgCl/KCl (sat.) is attribute to the 2-electron reduction of O₂ to H₂O₂ (Equation 4.10)[49].



However, the further reduction of H₂O₂ to H₂O was not obvious and just showed as a shoulder at around -410 mV under the present experimental conditions. This is due to the H₂ evolution occurred predominantly during this reaction[49] and the preferential exposure of Au(111) active crystal facets for AuNWs, which is known to be mainly active toward two-electron reduction to hydrogen peroxide[50]. Interestingly, the electrocatalytic performances can be tailored. The bilayer nanomembranes displays more positive onset potential and greater catalytic current than the monolayer. This is arising from the higher interconnection of nanowires in the double layer that provided better electronic continuity.

4.3 Conclusion

In summary, this chapter presents a simple yet efficient method to fabricate giant metallic superlattice nanomembrane of about 2.5 nm thick but with macroscopic lateral dimensions from ultrathin flexible gold nanowires. Such superlattice nanomembrane represents the thinnest version of metallic membranes known to date.[3, 6, 11] Remarkably, the ultrathin superlattice nanomembranes are mechanically strong, optically transparent and electrically conductive. Notably, both synthesis of gold nanowires and fabrication process of superlattice nanomembranes are scalable, which render this methodology promising for practical applications in future lightweight foldable optoelectronics, such as touch-screen devices.[42, 51] Besides the excellent

structural and mechanical features, nanomembranes exhibited multi-angular applications, such as in lightweight foldable supercapacitor and electrocatalysis. This methodology can potentially be extended to fabricate nanomembranes from other types of nanowires or multiple components, therefore, it may become a general modular approach to integrate optoelectronic properties with mechanical robustness into a single lightweight, foldable 2D materials systems for promising applications in future foldable electronics.

4.4 References

1. Cheng, W.L., Campolongo, M.J., Tan, S.J. and Luo, D. Freestanding ultrathin nano-membranes via self-assembly. *Nano Today* **4**, 482-493 (2009).
2. Dong, A.G., Chen, J., Vora, P.M., Kikkawa, J.M. and Murray, C.B. Binary nanocrystal superlattice membranes self-assembled at the liquid-air interface. *Nature* **466**, 474-477 (2010).
3. Cheng, W.L., Campolongo, M.J., Cha, J.J., Tan, S.J., Umbach, C.C., Muller, D.A. and Luo, D. Free-standing nanoparticle superlattice sheets controlled by DNA. *Nature Mater.* **8**, 519-525 (2009).
4. Chen, Y., Fu, J., Ng, K.C., Tang, Y. and Cheng, W.L. Free-Standing Polymer-Nanoparticle Superlattice Sheets Self-Assembled at the Air Liquid Interface. *Crystal Growth & Design* **11**, 4742-4746 (2011).
5. Ng, K.C., Udagedara, I.B., Rukhlenko, I.D., Chen, Y., Tang, Y., Premaratne, M. and Cheng, W.L. Free-Standing Plasmonic-Nanorod Superlattice Sheets. *ACS Nano* **6**, 925-934 (2011).
6. Mueggenburg, K.E., Lin, X.M., Goldsmith, R.H. and Jaeger, H.M. Elastic membranes of close-packed nanoparticle arrays. *Nature Mater.* **6**, 656-660 (2007).
7. Vendamme, R., Onoue, S.-Y., Nakao, A. and Kunitake, T. Robust free-standing nanomembranes of organic/inorganic interpenetrating networks. *Nature Mater.* **5**, 494-501 (2006).
8. Tang, Z., Zhang, Z., Wang, Y., Glotzer, S.C. and Kotov, N.A. Self-Assembly of CdTe Nanocrystals into Free-Floating Sheets. *Science* **314**, 274-278 (2006).
9. Liao, J., Zhou, Y., Huang, C., Wang, Y. and Peng, L. Fabrication, Transfer, and Transport Properties of Monolayered Freestanding Nanoparticle Sheets. *Small* **7**, 583-587 (2011).
10. Pang, J., Xiong, S., Jaeckel, F., Sun, Z., Dunphy, D. and Brinker, C.J. Free-Standing, Patternable Nanoparticle/Polymer Monolayer Arrays Formed by Evaporation Induced Self-Assembly at a Fluid Interface. *J. Am. Chem. Soc* **130**, 3284-3285 (2008).
11. He, J., Kanjanaboos, P., Frazer, N.L., Weis, A., Lin, X.-M. and Jaeger, H.M. Fabrication and Mechanical Properties of Large-Scale Freestanding Nanoparticle Membranes. *Small* **6**, 1449-1456 (2010).

12. Lei, W., Qin, S., Liu, D., Portehault, D., Liu, Z. and Chen, Y. Large scale boron carbon nitride nanosheets with enhanced lithium storage capabilities. *Chem. Commun.* **49**, 352-354 (2013).
13. Lei, W., Portehault, D., Liu, D., Qin, S. and Chen, Y. Porous boron nitride nanosheets for effective water cleaning. *Nat Commun* **4**, 1777 (2013).
14. Glushenkov, A.M., Zhang, H.Z., Zou, J., Lu, G.Q. and Chen, Y. Efficient production of ZnO nanowires by a ball milling and annealing method. *Nanotechnology* **18**, 175604 (2007).
15. Chen, Y., Chi, B., Liu, Q., Mahon, D.C. and Chen, Y. Fluoride-assisted synthesis of mullite (Al_{15.65}Si_{0.35}O_{9.175}) nanowires. *Chem. Commun.*, 2780-2782 (2006).
16. Tian, B., Zheng, X., Kempa, T.J., Fang, Y., Yu, N., Yu, G., Huang, J. and Lieber, C.M. Coaxial silicon nanowires as solar cells and nanoelectronic power sources. *Nature* **449**, 885-889 (2007).
17. Patolsky, F., Timko, B.P., Yu, G., Fang, Y., Greytak, A.B., Zheng, G. and Lieber, C.M. Detection, Stimulation, and Inhibition of Neuronal Signals with High-Density Nanowire Transistor Arrays. *Science* **313**, 1100-1104 (2006).
18. Jin, S., Whang, D., McAlpine, M.C., Friedman, R.S., Wu, Y. and Lieber, C.M. Scalable Interconnection and Integration of Nanowire Devices without Registration. *Nano Lett.* **4**, 915-919 (2004).
19. Lu, W. and Lieber, C.M. Nanoelectronics from the bottom up. *Nature Mater.* **6**, 841-850 (2007).
20. Yang, P. and Kim, F. Langmuir–Blodgett Assembly of One-Dimensional Nanostructures. *ChemPhysChem* **3**, 503-506 (2002).
21. Tao, A.R., Huang, J. and Yang, P. Langmuir–Blodgett of Nanocrystals and Nanowires. *Acc. Chem. Res.* **41**, 1662-1673 (2008).
22. Tao, A., Kim, F., Hess, C., Goldberger, J., He, R., Sun, Y., Xia, Y. and Yang, P. Langmuir–Blodgett Silver Nanowire Monolayers for Molecular Sensing Using Surface-Enhanced Raman Spectroscopy. *Nano Lett.* **3**, 1229-1233 (2003).
23. Whang, D., Jin, S., Wu, Y. and Lieber, C.M. Large-Scale Hierarchical Organization of Nanowire Arrays for Integrated Nanosystems. *Nano Lett.* **3**, 1255-1259 (2003).
24. Mai, L., Gu, Y., Han, C., Hu, B., Chen, W., Zhang, P., Xu, L., Guo, W. and Dai, Y. Orientated Langmuir–Blodgett Assembly of VO₂ Nanowires. *Nano Lett.* **9**, 826-830 (2009).
25. Liu, J.-W., Zhu, J.-H., Zhang, C.-L., Liang, H.-W. and Yu, S.-H. Mesostructured Assemblies of Ultrathin Superlong Tellurium Nanowires and Their Photoconductivity. *J. Am. Chem. Soc* **132**, 8945-8952 (2010).
26. Feng, H., Yang, Y., You, Y., Li, G., Guo, J., Yu, T., Shen, Z., Wu, T. and Xing, B. Simple and rapid synthesis of ultrathin gold nanowires, their self-assembly and application in surface-enhanced Raman scattering. *Chem. Commun.*, 1984-1986 (2009).
27. Huo, Z., Tsung, C.-k., Huang, W., Zhang, X. and Yang, P. Sub-Two Nanometer Single Crystal Au Nanowires. *Nano Lett.* **8**, 2041-2044 (2008).
28. Lu, X., Yavuz, M.S., Tuan, H.-Y., Korgel, B.A. and Xia, Y. Ultrathin Gold Nanowires Can Be Obtained by Reducing Polymeric Strands of Oleylamine–AuCl Complexes Formed via Auophilic Interaction. *J. Am. Chem. Soc* **130**, 8900-8901 (2008).
29. Tao, A., Sinsermsuksakul, P. and Yang, P. Tunable plasmonic lattices of silver nanocrystals. *Nature Nanotech.* **2**, 435-440 (2007).

30. Hecht, D.S., Hu, L. and Irvin, G. Emerging Transparent Electrodes Based on Thin Films of Carbon Nanotubes, Graphene, and Metallic Nanostructures. *Adv. Mater.* **23**, 1482-1513 (2011).
31. Lobkovsky, A., Gentges, S., Li, H., Morse, D. and Witten, T.A. Scaling Properties of Stretching Ridges in a Crumpled Elastic Sheet. *Science* **270**, 1482-1485 (1995).
32. Lee, C., Wei, X., Kysar, J.W. and Hone, J. Measurement of the Elastic Properties and Intrinsic Strength of Monolayer Graphene. *Science* **321**, 385-388 (2008).
33. American Institute of Physics handbook, Edn. 3rd. (McGraw-Hill Book Company, New York; 1972).
34. Handbook of Optical Constants of Solids. (Academic Press, San Diego; 1985).
35. Pazos-Pérez, N.s., Baranov, D., Irsen, S., Hilgendorff, M., Liz-Marzán, L.M. and Giersig, M. Synthesis of Flexible, Ultrathin Gold Nanowires in Organic Media. *Langmuir* **24**, 9855-9860 (2008).
36. Dressel, M. and Grüner, G. Electrodynamics of Solids: Optical Properties of Electrons in Matter. (Cambridge University Press, Cambridge; 2002).
37. De, S., Higgins, T.M., Lyons, P.E., Doherty, E.M., Nirmalraj, P.N., Blau, W.J., Boland, J.J. and Coleman, J.N. Silver Nanowire Networks as Flexible, Transparent, Conducting Films: Extremely High DC to Optical Conductivity Ratios. *ACS Nano* **3**, 1767-1774 (2009).
38. Sondheimer, E.H. The mean free path of electrons in metals. *Advances in Physics* **1**, 1-42 (1952).
39. Bietsch, A. and Michel, B. Size and grain-boundary effects of a gold nanowire measured by conducting atomic force microscopy. *Appl. Phys. Lett.* **80**, 3346-3348 (2002).
40. Stauffer, D. and Aharony, A. Introduction To Percolation Theory. (Taylor & Francis, London; 1994).
41. Critchley, K., Khanal, B.P., Górzny, M.L., Vigderman, L., Evans, S.D., Zubarev, E.R. and Kotov, N.A. Near-Bulk Conductivity of Gold Nanowires as Nanoscale Interconnects and the Role of Atomically Smooth Interface. *Adv. Mater.* **22**, 2338-2342 (2010).
42. Maye, M.M., Kumara, M.T., Nykypanchuk, D., Sherman, W.B. and Gang, O. Switching binary states of nanoparticle superlattices and dimer clusters by DNA strands. *Nature Nanotechnol.* **5**, 116-120 (2010).
43. Simon, P. and Gogotsi, Y. Materials for electrochemical capacitors. *Nature Mater.* **7**, 845-854 (2008).
44. Lang, X., Hirata, A., Fujita, T. and Chen, M. Nanoporous metal/oxide hybrid electrodes for electrochemical supercapacitors. *Nature Nanotech.* **6**, 232-236 (2011).
45. Zhang, L.L. and Zhao, X.S. Carbon-based materials as supercapacitor electrodes. *Chem. Soc. Rev.* **38**, 2520-2531 (2009).
46. Cheng, Q., Tang, J., Ma, J., Zhang, H., Shinya, N. and Qin, L.-C. Graphene and nanostructured MnO₂ composite electrodes for supercapacitors. *Carbon* **49**, 2917-2925 (2011).
47. Kaempgen, M., Chan, C.K., Ma, J., Cui, Y. and Gruner, G. Printable Thin Film Supercapacitors Using Single-Walled Carbon Nanotubes. *Nano Lett.* **9**, 1872-1876 (2009).
48. Yu, G., Hu, L., Vosgueritchian, M., Wang, H., Xie, X., McDonough, J.R., Cui, X., Cui, Y. and Bao, Z. Solution-Processed Graphene/MnO₂ Nanostructured

- Textiles for High-Performance Electrochemical Capacitors. *Nano Lett.* **11**, 2905-2911 (2011).
49. El- Deab, M.S. and Ohsaka, T. An extraordinary electrocatalytic reduction of oxygen on gold nanoparticles-electrodeposited gold electrodes. *Electrochem. Commun.* **4**, 288-292 (2002).
50. Tian, Y., Liu, H., Zhao, G. and Tatsuma, T. Shape-Controlled Electrodeposition of Gold Nanostructures. *J. Phys. Chem. B* **110**, 23478-23481 (2006).
51. Rathmell, A.R. and Wiley, B.J. The Synthesis and Coating of Long, Thin Copper Nanowires to Make Flexible, Transparent Conducting Films on Plastic Substrates. *Adv. Mater.*, 4798-4803 (2011).

This page is intentionally blank

Chapter 5

Giant Plasmonic Superlattice Sheet From Polymer-capped Bimetallic Nanocrystals

This page is intentionally blank

The ability to build plasmonic superlattice sheets of macroscopic surfaces but nanoscale thicknesses using different nanocrystals from the “plasmonic periodic table”[1] is crucial for understanding the unparalleled optical signature of 2D nanoparticle superlattices,[2-14] and is of significance for bottom-up fabrication of plasmonic devices and circuits.[15] In chapter 3, polymer-ligand-based strategy has been proved as a robust avenue to fabricate superlattice sheets from nanospheres. This general strategy enables both structure regulation and spatial control of 2D superlattice. However, challenges are still ahead for large-scale ordered assembly of complex nanocrystals with desired plasmonic properties.

In this chapter, this challenge has been addressed by fabrication of giant-surface plasmonic superlattice sheets about 3-mm-wide and 40-nm-thick, corresponding to an aspect ratio of 75,000. It was achieved by using drying-mediated self-assembly of polystyrene-capped anisotropic Au@Ag core-shell nanobricks (NBs) at air/water interfaces. A unique feature of such superlattice sheets is their uniform optical response across the entire surface. It was achieved by synthesizing the sheets from large ensembles of highly monodispersed nanoparticles and capping the nanoparticles with soft ligands, which prevented their disordered aggregation at high concentrations. The connection between the nanoparticles provided by the ligands is strong enough to allow superlattice transfer among various substrates. This feature, along with the uniform distribution of hot spots across superlattice surface, makes possible high-sensitive detection of chemicals in different aggregate states using SERS. The ability of assembling different types of plasmonic nanoparticles using this polymer-ligand-based strategy opens up new avenues in designing novel two-dimensional metadevices and sensors.

5.1 Experimental methods

5.1.1 Materials

Gold (III) chloride trihydrate ($\text{HAuCl}_4 \cdot 3\text{H}_2\text{O}$, $\geq 99.9\%$), hexadecyltrimethylammonium bromide (CTAB), cetyltrimethylammonium chloride solution (CTAC, 25 wt. % in H_2O), silver nitrate (AgNO_3), sodium borohydride (NaBH_4), L-ascorbic acid, and 4-

aminothiophenol were purchased from Sigma Aldrich. Tetrahydrofuran (THF) and chloroform was obtained from Merck KGaA. Thiol-functionalized polystyrene ($M_n = 50,000$ g/mol, $M_w/M_n = 1.09$) was purchased from Polymer Source Inc. PDMS Sylgard (184) silicon elastomer, curing agent, and precursor were purchased from Dow Corning, USA. All chemicals were used as-received unless otherwise indicated. Deionized water was used in all aqueous solutions, which were further purified with a Milli-Q system (Millipore). All glasswares used in the following procedures were cleaned in a bath of freshly prepared aqua regia and were rinsed thoroughly in H₂O prior to use.

Gilder extra fine bar grids (2000 mesh with $7 \times 7 \mu\text{m}^2$ square holes) were purchased from Ted Pella. Holey silicon nitride support films (2- μm -diameter hole, 4 μm pitch) were purchased from SPI supplies.

5.1.2 Synthesis of CTAB-capped gold nanorods

Monodisperse CTAB-capped gold nanorods were prepared according to the well-established seed-mediated growth method in a two-step procedure[16-18]. First, a brownish seed solution was prepared by mixing 5.0 ml 0.2 M CTAB with 5.0 ml 0.5 mM HAuCl₄, followed by adding 0.6 ml 0.01 M ice-cold NaBH₄ under vigorous stirring. Then a growth solution was prepared by adding 5.0 ml 0.2 M CTAB solution into 0.2 ml 4 mM AgNO₃ solution, followed by addition of 5.0 ml 1.0 mM HAuCl₄ and 0.08 ml 0.08 M ascorbic acid. Finally, CTAB-capped gold nanorods were obtained by adding 12 μL seed solution into the above growth solution and aged for 2 hours at 30°C. The nanorod solutions were centrifuged at 7,000 rpm for 20 min and re-dispersed into 10 ml 80 mM CTAC solution. This step was repeated twice to ensure complete replacement of CTAB ligands by CTAC molecules.

5.1.3 Synthesis of CTAC-capped Au@Ag NBs

Highly monodisperse CTAC-capped Au@Ag NBs were synthesized by following the recently reported approaches[19] with slight modification To grow bimetallic Au@Ag NBs, a silver precursor solution was added into the as prepared Au nanorods to enable seed-mediated growth process. Typically, a mixture of 2*l* 0.01 M AgNO₃ and 1 0.1 M ascorbic acid (*l* = 0.1 ~ 1.0 ml) was mixed with 10 ml CTAC-capped nanorods and

aged for 30s before annealing at 60 °C for 4 h under stirring condition. The solution changed the color from dark blue to orange during the growth of the silver shells. Finally, the solution was purified by repeated centrifugation at 5000 rpm for 20 min and re-dispersed into 5 ml Milli-Q water. The silver coating thickness increased as the amount of AgNO₃ and ascorbic acid increased.

5.1.4 Synthesis of Polystyrene-capped Au@Ag NBs

Replacement of CTAC with thiolated PS was achieved by a two-step ligand exchange procedure[20, 21]. Typically, as-prepared CTAC-stabilized Au@Ag NBs (5 mL) were concentrated to 0.1 mL, and then added it dropwisely into thiol-functionalized polystyrene THF solution (2 mg mL⁻¹) under vigorous stirring. After aging for overnight at room temperature, the supernatant was discarded and samples were purified by repeated centrifugation–precipitation cycles and re-dispersed in chloroform as a stock solution.

5.1.5 Fabrication of giant NB superlattice sheet

Typically, one drop of chloroform solution of PS-capped Au@Ag NBs (~27 nM) was carefully spread onto the surface of convex-shape water droplet on a holey copper or silicon nitride grid. After quick chloroform evaporation, silver-colored reflective solid films formed on the water subphase. Subsequently, water slowly evaporated, leading to the formation of the giant superlattice sheets covered almost the whole grid.

5.1.6 Characterization

Electron imaging was carried out using a Philips CM20 TEM or FEI Tecnai G2 T20 TEM at an acceleration voltage of 200 kV, or Hitachi H-7500 field emission TEM operating at 80kV.

The optical extinction spectra of bulk solution samples were acquired by an Agilent 8453 UV-Vis spectrophotometer; whereas spectra of superlattice sheets were obtained using a J&M MSP210 microscope spectrometry system. Optical micrographs of the superlattice sheets were taken by a Nikon industrial bright field microscope (ECLIPSE LV 100D) under transmission and reflectance modes.

Force-displacement curves and topographical structures were obtained with a Veeco Dimension Icon AFM in tapping mode using Bruker silicon probes (MPP-11120-10). The spring constant for the cantilever was 40 N m^{-1} . The typical tip speed for the nanoindentation was 500 nm s^{-1} . The AFM data was characterized using Gwyddion software.

Raman spectra were recorded by using a Renishaw RM 2000 Confocal micro-Raman System with three different lasers: 514, 633, and 782 nm (laser spot size: $1 \mu\text{m}$). All Raman spectra were recorded by fine-focusing a $50\times$ microscope objective under data acquisition time of 10 s, and corrected by baseline subtraction to exclude the fluorescence contribution. The strong a_1 -type band at $\sim 1078 \text{ cm}^{-1}$ was used to calculate SERS enhancement factor (EF).

5.1.7 Numerical method for simulation

To compute the extinction spectra of NB giant superlattice sheet and to estimate the distribution of hot-spots in these sheets, an open-source numerical simulation tool — DDSCAT 7.2 was employed based on DDA method[22, 23] which has a faster computing efficiency as compared to other numerical tools[21, 23]. This method allowed to estimate the extinction of incident light by a 2D ensemble of nanoparticles, where each nanoparticle was represented as an array of polarizable point dipoles. NB was modeled as a silver nanocuboid with a capsule shaped gold nanorod at the center. The corners and edges of the NBs were smoothed as required to closely resemble the shapes obtained experimentally. The interaction of light with so designed nanoparticle (represented as an array of N dipoles) was then modeled by estimating the electric field \mathbf{E}_j of the j^{th} dipole ($j \in [1, N]$) as sum of incident field ($\mathbf{E}_{\text{inc},j}$) and contributions from other dipoles ($\mathbf{E}_{\text{other},j}$).

In case of a 2D periodic array of NBs in yz plane representing giant superlattice sheet, a set of linear coupled equations were solved in DDSCAT using periodic boundary conditions along both y and z directions, where light was assumed to propagate along x

direction and a target unit cell (TUC) was defined with the structural specifications of an NB. The whole target was considered as an ensemble of identical NBs (made of N dipoles, i.e. $j = 1, \dots, N$ in a TUC) arranged periodically in a 2D array (with indices m, n specifying periodic replicas of the TUC).

5.2 Results and discussion

5.2.1 Synthesis of monodisperse NBs

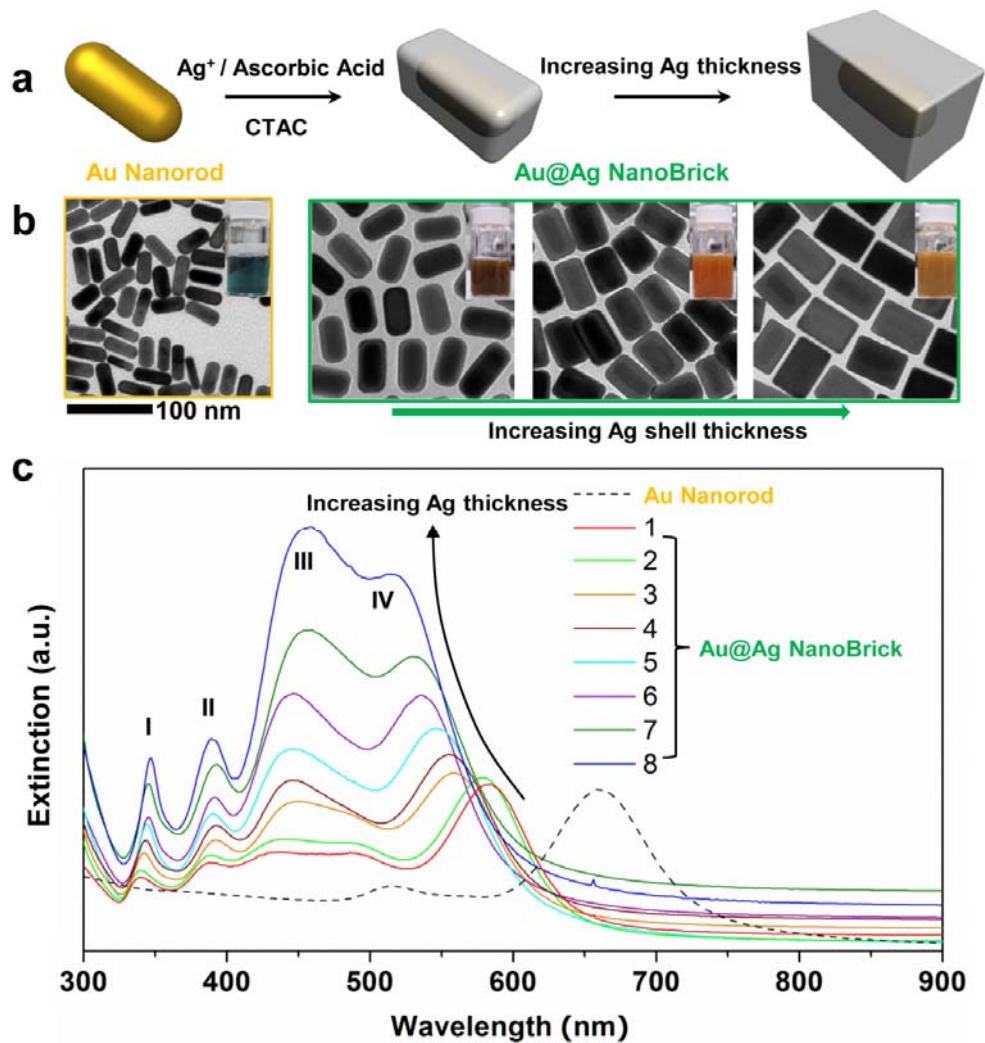


Figure 5.1 | Synthesis and characterization of monodisperse Au@Ag NBs with finely-tunable thickness. (a) Schematic illustration of growth process from Au nanorods to Au@Ag NBs. (b) TEM images of Au nanorods, and Au@Ag NBs with increasing Ag thickness. The inset shows the photographs of solution products with distinct colors. (c) Extinction spectral development of Au@Ag NBs as Ag shell thickness increased.

The starting point of fabricating a free-standing giant superlattice sheet was the synthesis of monodisperse ensembles of bimetallic Au@Ag nanobrick (NB)—which

was performed with minor modifications to a recently developed method[19, 24] In brief, $47 \text{ nm} \times 20 \text{ nm}$ gold nanorods were synthesized and used as cores, then coated by a uniform layer of silver. The presence of CTAC during the coating process was proved to be crucial for uniform coating.[25] The silver coating thickness could be tuned simply by adjusting the amount of Ag^+ and ascorbic acid. The as-prepared core-shell NBs were highly monodispersed and their coating thicknesses were precisely tunable (**Figure 5.1**).

Such NBs possessed well-pronounced dipolar, quadrupolar and octopolar localized surface plasmon resonance (LSPR) bands that were critically influenced by the silver coating thickness (**Figure 5.1c**). There were four characteristic plasmonic peaks for Au@Ag NBs. The peaks I and II shifted slightly to red as the silver coating thickness increased. The peak III first blue-shifted and then red-shifted with simultaneous increase in intensity. The peak IV kept blue-shifting but the intensity increase was slower than that for the peak III and finally the peak IV intensity was lower than that for the peak III although it was higher in the beginning.[26]

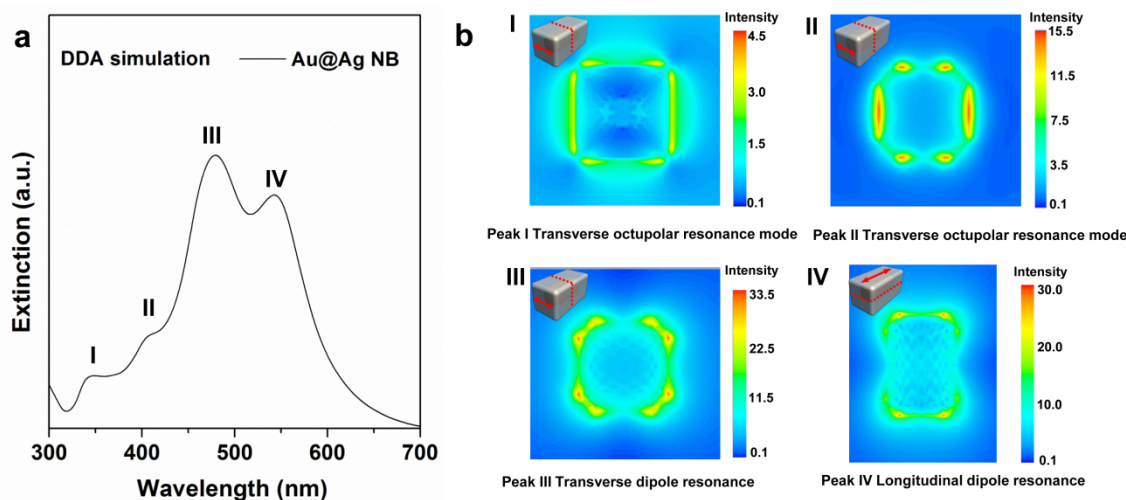


Figure 5.2 | (a) Calculated extinction spectrum of Au@Ag NB. (b) Calculation of near-field intensity distribution to evaluate electric field distribution of a single NB, when incident light is polarized along the transverse edge (TE) and longitudinal edge (LE) (as shown in inset schemes). The peaks I, II, III are excited under the TE polarization, and the peak IV is excited along the LE polarization. E-field distribution contours of Au@Ag NBs show the origin of the four plasmon resonance peaks. Moreover, the intensity of electric field in each case also predicts the relative strengths of the peaks in the extinction spectrum.

5.2.2 Plasmon modes of NBs

To further identify the nature of the four characteristic peaks and relevant plasmon modes in a single Au@Ag NB, near-field calculation of electric field intensity was performed using DDSCAT to evaluate E-field distribution in and around the nanoparticle[27]. Bulk permittivity values of gold and silver in Au@Ag NBs were obtained from the literature[28]. As shown in **Figure 5.2**, The peak I and II are assigned to octupolar plasmon modes, the peak III can be ascribed to transverse dipolar plasmon mode, and the peak IV is identified as longitudinal dipolar plasmon mode [26].

5.2.3 Synthesis of polystyrene-capped Au@Ag NBs by ligand exchange

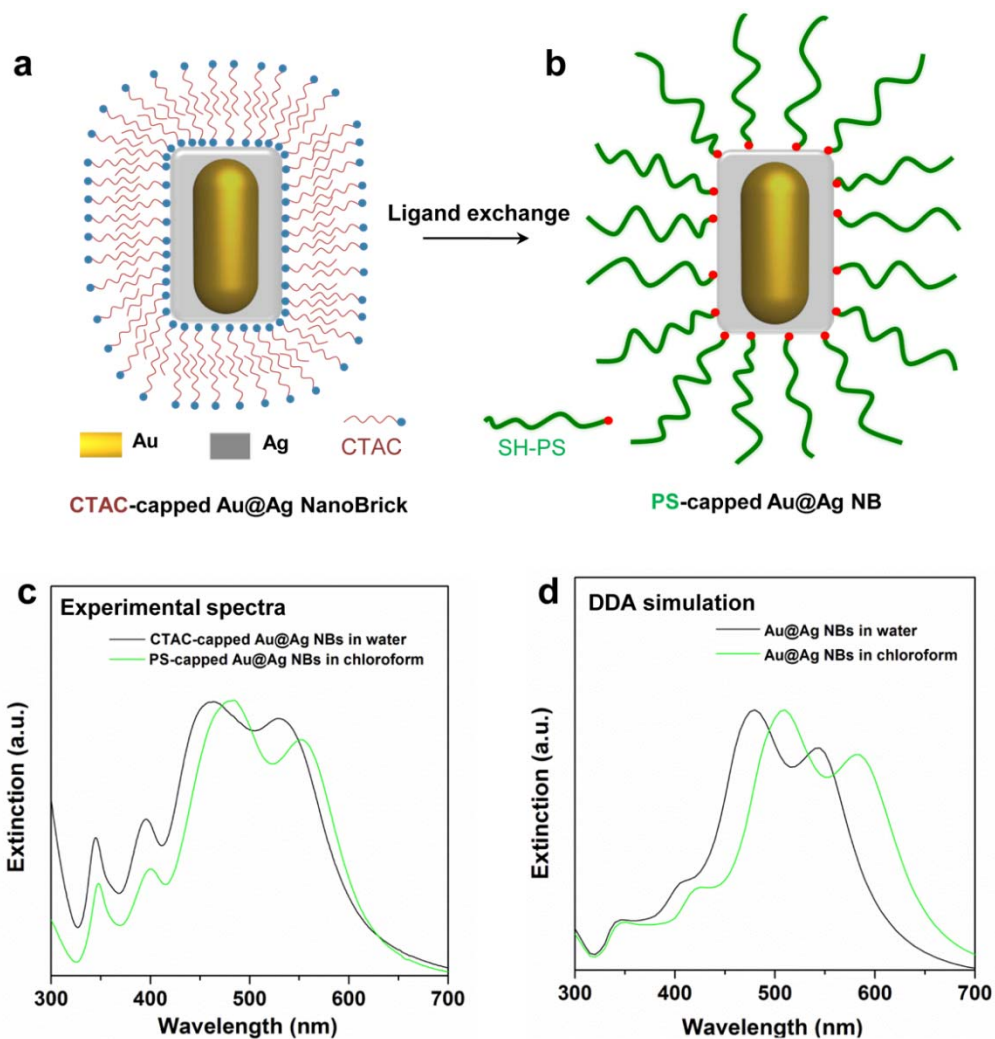


Figure 5.3 | (a, b) Schematic of fabrication process of PS-capped NB by ligand exchange (c) The experimental extinction spectra of CTAC-capped NBs in water and PS-capped NBs in chloroform; (d) Calculated extinction spectra of NBs dispersed in water ($n=1.33$) and chloroform ($n=1.45$) using DDA method; All the calculated spectra are normalized by their peak values. The capping ligands were not included in the simulation model since they had negligible influences on the overall extinction spectra.

Notably, pristine NBs were stabilized by hexadecyltrimethylammonium chloride (CTAC) – a weak-binding ligand insufficient for protection against random nanoparticle aggregation (**Figure 5.3a**). Therefore, a two-step ligand exchange procedure[20, 21] was applied to replace CTAC by a much stronger binding ligand – thiolated-polystyrene (PS) ($M_n = 50,000 \text{ g mol}^{-1}$). (**Figure 5.3b**)

The plasmonic spectra changes during the ligand exchange process were measured experimentally and computed theoretically by discrete dipole approximation (DDA) simulation. Experimentally, the PS-capped Au@Ag NBs in chloroform exhibited strong characteristic LSPR bands, indicating the absence of aggregation (**Figure 5.3c**). The lineshapes of these LSPR bands in chloroform resembled the corresponding ones in water but showed some shifts in position. Both lineshapes and spectral changes could be reproduced by DDA simulation, which is a computationally efficient approach to calculating optical responses of complex nanostructures[29] (**Figure 5.3d**). In particular, a slight discrepancy of simulation results with the experimental spectra was noted, which may be due to the fact that the numerical model did not take into account the capping of NBs with ligands. The ligand binding is known to dampen resonances[30].

5.2.4 Fabrication of NB superlattice sheets

To grow NB superlattice sheet, a droplet of concentrated chloroform solution of PS-capped NBs was spread onto a sessile water drop on a holey copper grid (2000 mesh with hole-size of $7 \mu\text{m} \times 7 \mu\text{m}$, **Figure 5.4a-c**). Rapid chloroform evaporation confined the self-assembly of PS-capped NBs at the air/water interface forming monolayered sheet patches. Subsequent slow water evaporation reduced the interface area by about 50% from hemisphere-like surface to pancake-like surface. This process gradually led to fusion of the patchy nanosheets into giant sheets covering the entire holey substrate (**Figure 5.4c**).

5.2.5 Morphological characterization of NB superlattice sheets

5.2.5.1 Giant superlattice sheets at different magnifications

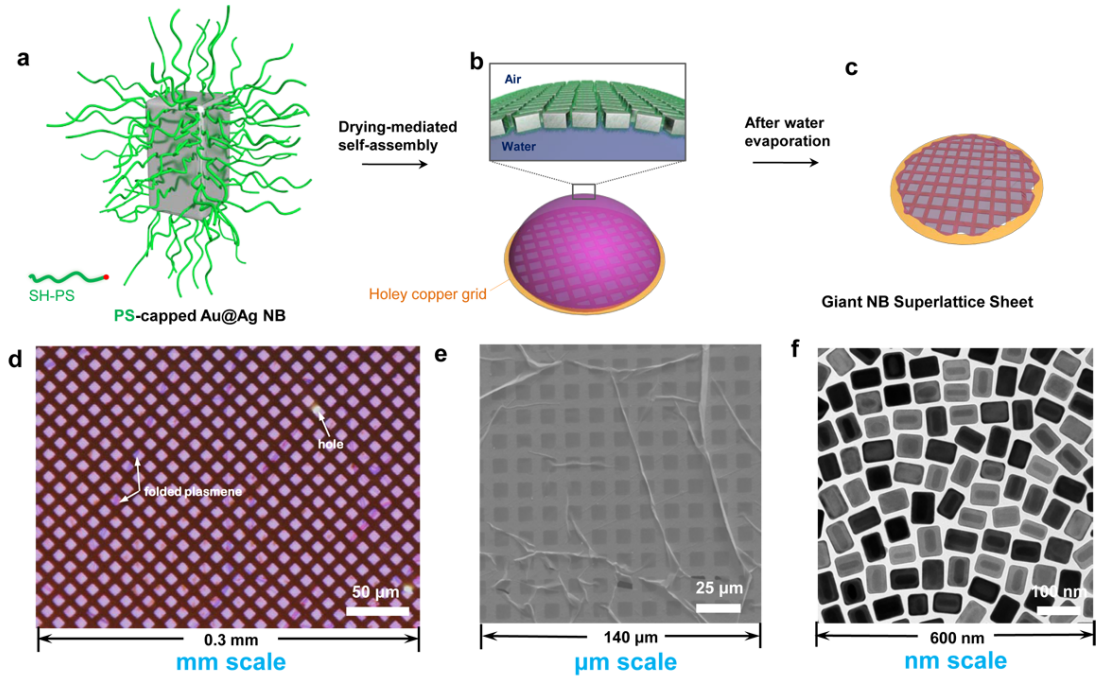


Figure 5.4 | Fabrication of giant NB superlattice sheet. (a-c), Schematic of fabrication process in conjunction with drying-mediated self-assembly. (d-f), Characterization of giant NB superlattice sheet at the macro-, micro- and nano-scale by optical microscope, SEM and TEM, respectively.

At the macroscopic scale, the superlattice sheets were readily observable under an optical microscope with distinct colors for NBs (**Figure 5.4d**); at the microscopic scale, the superlattice sheets were monolayered yet flexible (**Figure 5.4e**); at the nanoscopic scale, NBs were horizontally aligned with ordered packing (**Figure 5.4f**). Such-formed superlattice sheets could have a lateral dimension of 3 mm (**Figure 5.5**) but with a thickness of 40 nm, corresponding to an aspect ratio of about 75,000.

5.2.5.2 Ordering parameter of NB superlattice sheet

NBs were packed in a more complex way due to their anisotropy. To quantify the degree of order, 2D orientational order parameter (S_{2D}) was calculated using Hore's method[31] from TEM images as we did previously for gold nanorods[21].

$$S_{2D} = \frac{1}{N_{NBs}} \sum_{i=1}^{N_{NBs}} \cos 2\theta_i \quad \text{Equation (5.1)}$$

where θ_i is the angle between the NB i and the average orientation of Au@Ag NBs in a region of radius r around it, and N_{NBs} is the total number of Au@Ag NBs in that analyzing region.

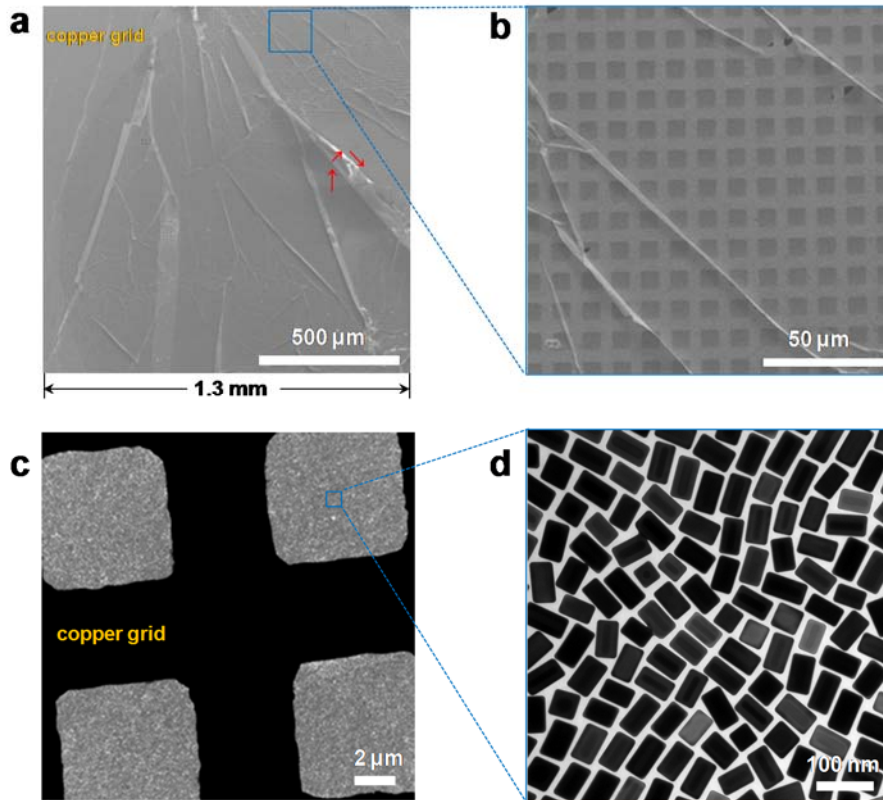


Figure 5.5 | SEM and TEM images of a typical millimeter-scale giant superlattice sheet at various magnifications. (a) SEM image showed the giant superlattice sheet covering almost the entire copper grid. The red arrows indicate the crumpled sheet with ridge-like morphology, demonstrating the high flexibility and robustness. (b) Higher-magnification SEM image of the region in (a). (c), (d) TEM images of the NB superlattice sheet show the high homogeneity in surface structures and ordered packing.

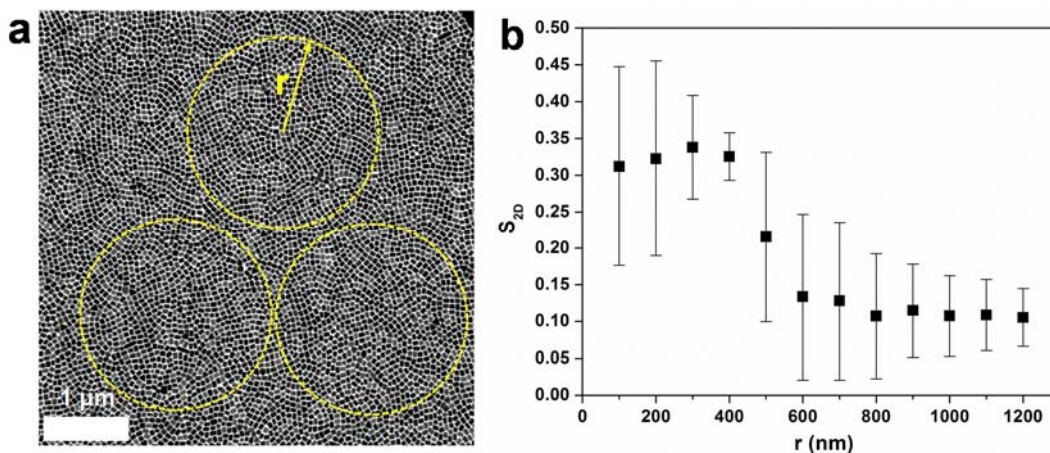


Figure 5.6 | (a) TEM image of NB superlattice sheet. (b) 2D orientational-order parameter S_{2D} plotted as a function of the radius (r) of the analyzed region, which is marked as yellow dashed circles in panels (a). The representative three circles have a radius of 1,200 nm which were selected for calculating the S_{2D} .

In the TEM image of a superlattice sheet, three circular regions were randomly selected for analysis, as shown in **Figure 5.6**. For each region, the each S_{2D} are calculated with r

= 100, 200, ... , 1200 nm and plotted in **Figure 5.6b**. The value of S_{2D} ranges from 0 for isotropic distributions to 1 for perfectly aligned Au@Ag NBs.

Note that the ordering parameter S_{2D} is about 0.3 when the chosen radius is less than ~ 400 nm. When the radii are above ~ 600 nm, the S_{2D} reached a plateau of about 0.10. This value represented the degree of ordering of giant NB superlattice sheets. It indicates an increasing localized ordering at small region, and then decreasing after a threshold, suggesting that the packing order is close to isotropic at large dimensions.[31, 32]

5.2.5.3 Parameters in affecting growth of giant superlattice sheets

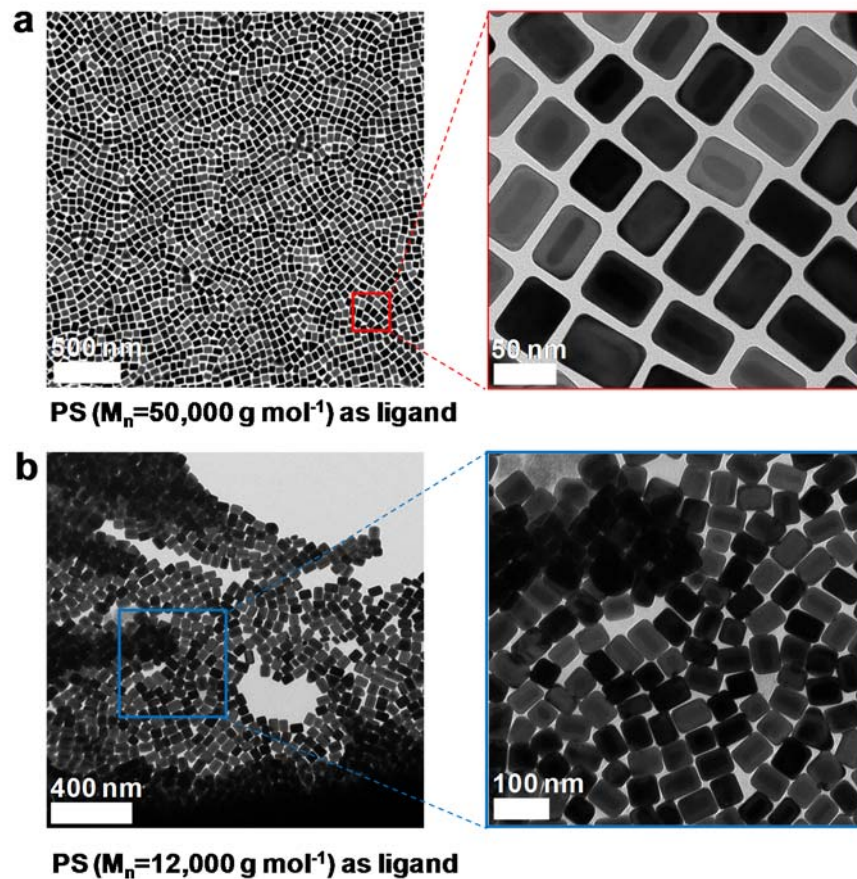


Figure 5.7 | TEM images of self-assembled Au@Ag NBs with long and short PS ligands. (a) TEM images show that the superlattice sheet is continuous in structures with uniform interparticle separations by using long PS ligand ($M_n = 50,000$ g mol⁻¹). (b) Disordered, multi-stacked and closely-packed assembly structures by using shorter PS ligand ($M_n = 12,000$ g mol⁻¹).

The quality of giant superlattice sheets was critically dependent on the length of the

polymer ligands (**Figure 5.7**) but weakly dependent on the type of substrates (**Figure 5.8**). The long PS chains successfully balanced core-core Van der Waals attraction and capillary forces during the assembly by experiencing great compression in the lateral directions,[33, 34] leading to well-defined separation and spatial distribution of NBs. Different from the previous successful example of assembling nanocrystals with small sizes, the large dimension of NBs in this system need longer molecular ligands, which was consistent with the particle softness argument – a larger particle required longer ligands to stabilize against aggregation.[35] In addition, concentrations of nanoparticle solution have a weak effect on the formation of superlattice sheets but affected their lateral dimensions. Monolayer superlattice sheets were obtained within concentrations of ~ 27 nM. The higher concentration favored the formation of giant sheets with crumpling upon water evaporation.

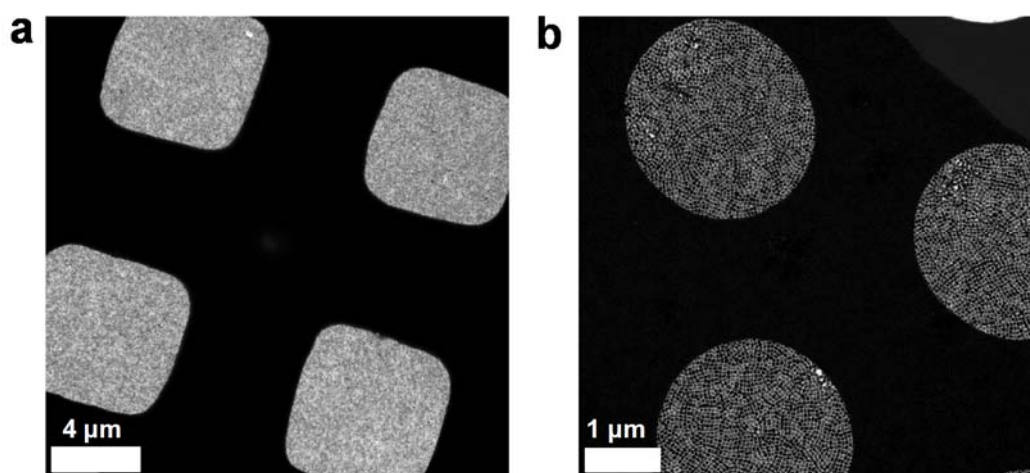


Figure 5.8 | TEM images of the giant NB superlattice sheet formed on (a) copper grid with square holes ($7 \mu\text{m} \times 7 \mu\text{m}$) and (b) holey silicon nitride substrate with $2 \mu\text{m}$ -diameter holes. In both cases, the superlattice sheets were stretched themselves across over the substrate with the holes without deterioration. The sheet in (b) was further indented by AFM for characterization of mechanical properties.

5.2.5.4 Transferability and 2D patterning of giant superlattice sheets

Strikingly, giant superlattice sheets could be transferred onto a variety of substrates including plastics, paper, silicon wafer, glass slides, and could be even shaped into desired shapes and patterned into regular arrays. **Figure 5.9a** illustrates a typical transferring process of the giant sheets to PDMS elastomer followed by peeling off from copper grid. This led to simultaneous patterning of square sheets which were

complementary replica of holey copper grid. Notably, these square sheets could be further stamped onto other substrates, such as silicon wafers.

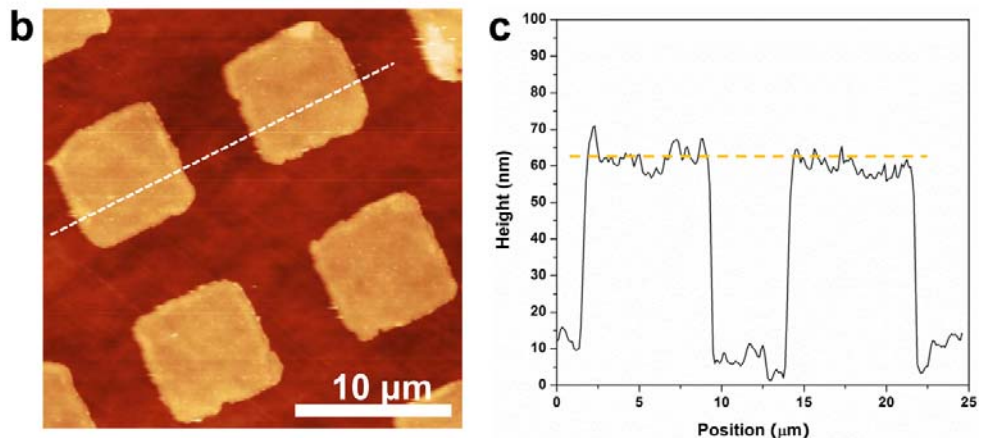
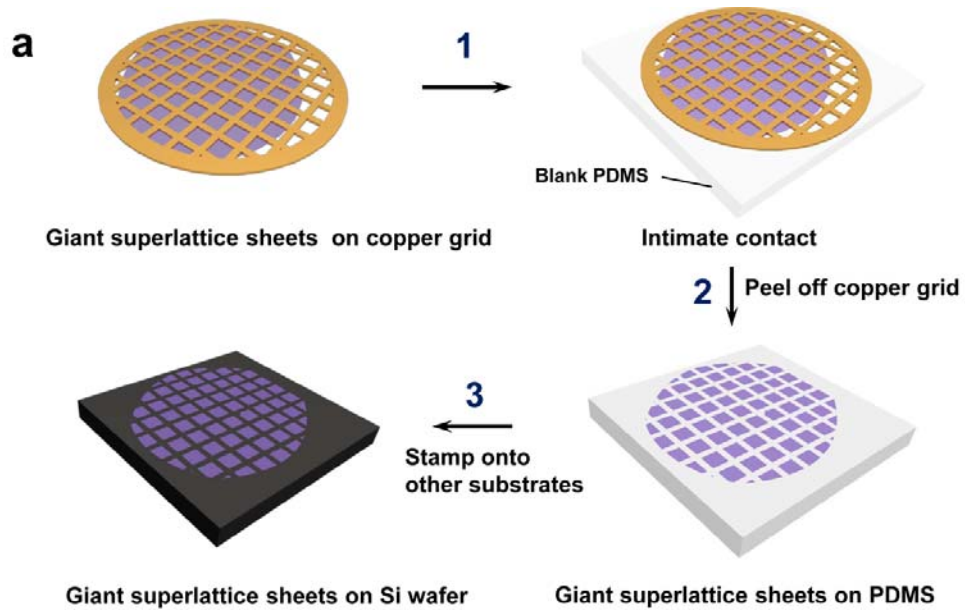


Figure 5.9 | (a) Schematic illustration of PDMS-assisted transfer process. The back side of a holey copper grid with a giant superlattice sheet on the front side was brought into contact with a PDMS elastomer with a moderate pressure applied to ensure the intimate contact (step 1). After peeling off the copper grid, the superlattice sheets were transferred onto PDMS with square-shaped patterns (step 2). The square superlattice sheets could be further stamped onto other substrates such as silicon (step 3). (b) AFM height image of NB superlattice sheets transferred to Si wafer. (c) AFM cross-sectional height plot corresponding to the dashed line in (b), showing an average thickness of 56 ± 2 nm.

Typically, a PDMS elastomer was prepared by mixing Sylgard 184 with a mass ratio of 10:1 for prepolymer to curing agent. The mixture was stirred and poured into a flat Petri dish. After annealing at 80 °C for 5 h, the cross-linked PDMS was cut into 10 mm × 10 mm stripes. The back side of a holey copper grid covered by giant superlattice

sheets in the front side was brought into contact with a fresh-made PDMS with a moderate pressure applied to ensure the intimate contact between two substrates. Then, the copper grid was slowly removed, leaving discrete square-shaped sheet arrays on PDMS. The superlattice sheets could be further tamped onto a variety of other solid substrates.

The entire transfer and patterning process has high-fidelity transfer efficiency with little cracking and deterioration. The thickness and surface morphology of superlattice sheets were further characterized after transferring onto silicon wafer by using an atomic force microscope (AFM). The sheets are uniformly continuous in square shape with little defects, which is in good agreement with the TEM imaging (**Figure 5.8a**). Further AFM line scanning gave an average thickness of 56 ± 2 nm for a typical NB superlattice sheet, indicating the monolayer structure comparable to the height of constituent nanoparticle building blocks. The line scanning profile outlined the uniform height of superlattice sheets with regular lateral dimensions, demonstrating the preserved monolayer structure without crumpling after transfer. After subtracting the height of nanoparticles, the compressed polystyrene thickness can be estimated to be ~ 5 nm. This height of PS in vertical direction indicated a collapsed brush conformation, similar to previously presented case of superlattices composed of nanospheres (Chapter 3).

5.2.6 Mechanical properties of giant superlattice sheets

Despite being extremely thin with nanoscale single-particle thickness, the sheets were mechanically strong. AFM nanoindentation was used to determine Young's modulus of superlattice sheets, following the approach described in Chapter 4. Superlattice sheets were directly fabricated on a holey silicon nitride substrate with regularly spaced $2\mu\text{m}$ -diameter holes. TEM was first used to find the specific monolayered sheets followed by AFM imaging by addressing the same circular sheets. Then nanoindentation was performed at the center of these sheets with a typical AFM tip (cantilever spring constant is 40 N m^{-1} , Bruker silicon probes, MPP-11120-10).

The typical indentation force curve plotting the applied force versus indentation depth, δ (black line) is shown in **Figure 5.11**. Numerical fitting (red line) derives a typical Young's modulus of $\sim 1.0 \pm 0.3$ GPa.

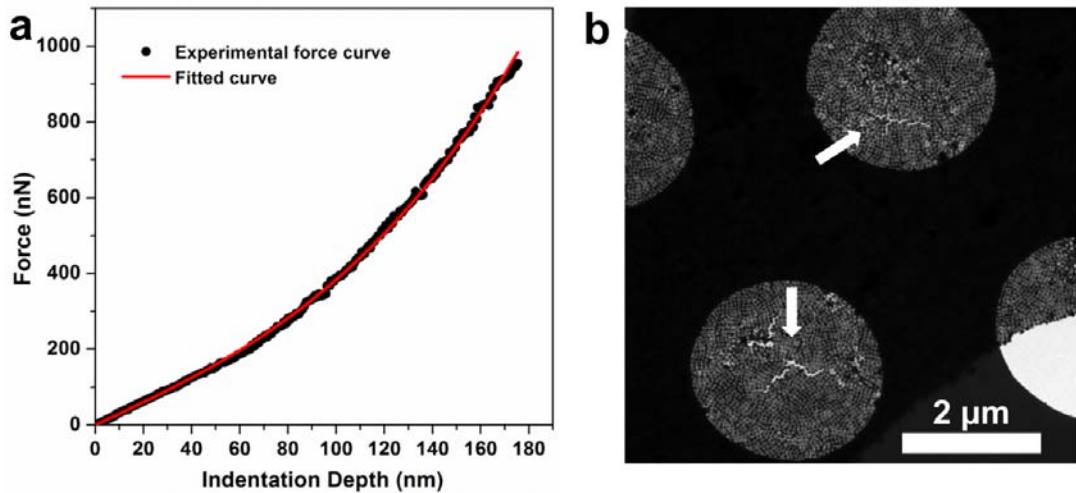


Figure 5.10 | (a) A typical force-displacement curve from AFM indentation (black) and from theoretical fitting (red) for NB superlattice sheet. (b) TEM image of superlattice sheet cover over a 2- μm -diameter microhole in the silicon nitride substrate after indentation. The inset arrows show the local rips of ruptured sheets.

5.2.7 Customizing plasmonics of superlattice sheet and theoretical modeling

5.2.7.1 Dimensions of three different plasmonic building blocks

To illustrate customizability of NB superlattice sheets, three ensembles of different NBs were synthesized with three specific Ag shell thicknesses — small-NB (s-NB), medium-NB (m-NB), large-NB (l-NB) (**Figure 5.12**). Detailed statistical dimensions of the three building blocks are shown in **Table 5.1**.



Figure 5.11 | Schematic illustration of three building blocks.

Table 5.1 | Dimension of synthesized Au@Ag NBs

Entry ^a	Length ^b (<i>l</i> , nm)	Diameter ^b (<i>d</i> , nm)	Aspect ratio	-	-
Au nanorod (core)	47 ± 3	20 ± 2	2.4	-	-
Entry ^a	Length ^b (<i>l</i> , nm)	Width ^b (<i>w</i> , nm)	Aspect ratio	End thickness (<i>l_e</i> , nm)	Side thickness (<i>l_s</i> , nm)
s-NB	59 ± 3	30 ± 1	2.0	6	5
m-NB	62 ± 3	38 ± 2	1.6	7.5	9
l-NB	63 ± 2	45 ± 2	1.4	8	12.5

a: The ligands for all the nanoparticles were thiol-functionalized polystyrene ($M_n=50,000$, $M_w/M_n = 1.06$); *b*: Obtained from TEM images of Au@Ag NBs, and statistical analysis through the free software ImageJ.

5.2.7.2 Measurement of interparticle spacing of three NB superlattice sheets

The chosen three building blocks were used to fabricate giant superlattice sheets following the procedure described in **Figure 5.4**. Their structures were characterized using TEM. The representative images were used to measure interparticle spacings. The side-by-side (l_{ss}) and end-to-end (l_{ee}) for superlattice sheets from s-NB, m-NB and l-NB were measured and fitted by Gaussian approach (**Figure 5.13**).

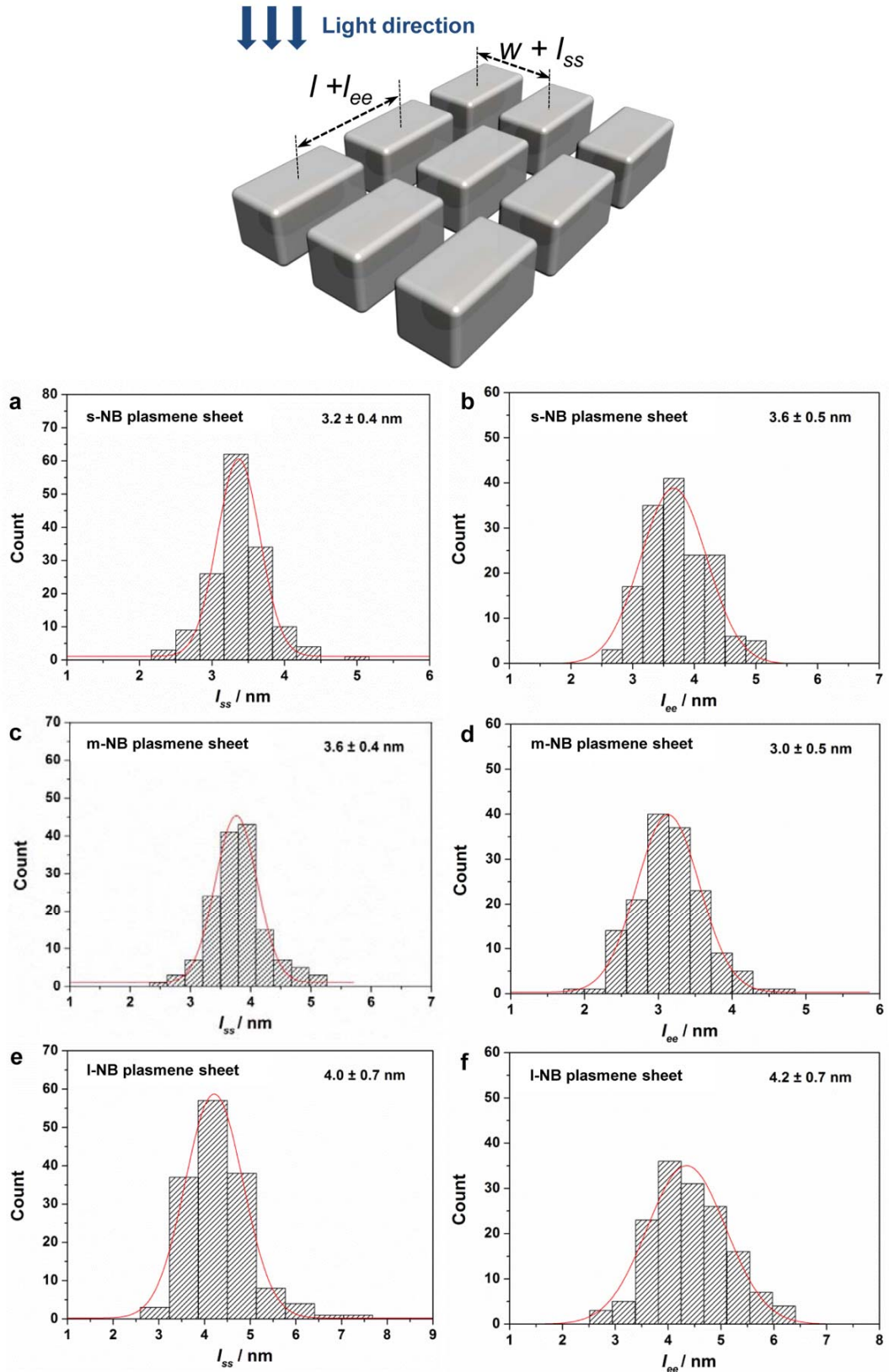


Figure 5.12 | Statistical analysis showing distribution of side-by-side (l_{ss}) and end-to-end (l_{ee}) spacing in NB superlattice sheets measured from TEM images. Red curves represent the Gaussian fits to the distributions.

5.2.7.3 Extinction spectra of three NB superlattice sheets

The extinction spectra of superlattice sheets feature distinct resonances shown in **Figure 5.14**. The positions of resonances can be varied over a wide range *via* adjusting the dimensions, geometry, and composition of its building blocks. Following the above-described procedure, s-NB, m-NB and l-NB were assembled into three giant superlattice sheets. Each sheet had its own color due to the unique spectral position of the extinction resonance, which is the function of size and shape of the nanoparticles. The major contribution to the extinction spectra of the sheets was found to stem from the dipole–dipole coupling between the plasmonic nanoparticles. The resonant peak in the spectrum of NB superlattice exhibited a significant blue shift (from 635 to 560 nm) with the thickness of silver coating (from 5 nm in s-NBs, through 9 nm in m-NBs, to 12.5 nm in l-NBs).

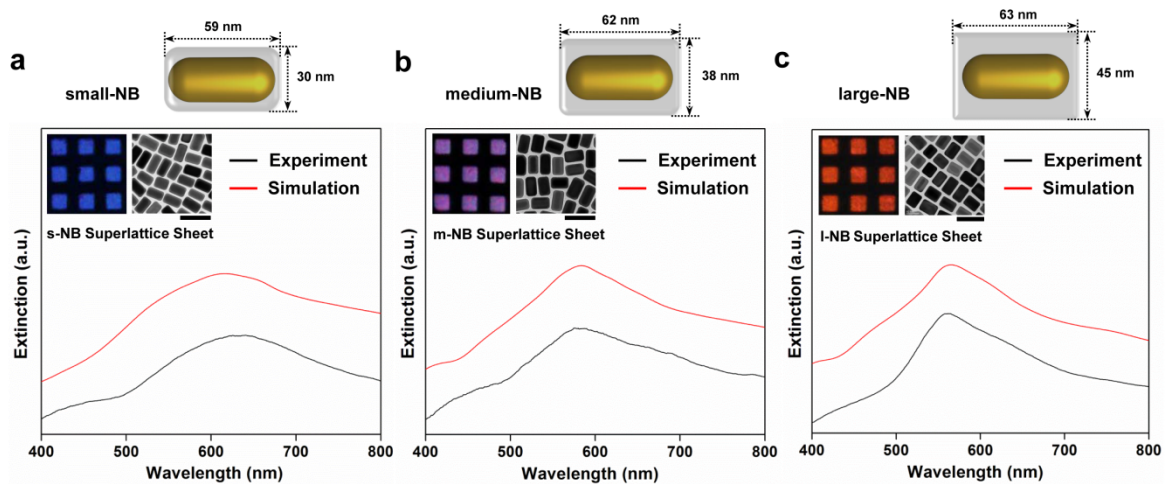


Figure 5.13 | Superlattice sheets from three different building blocks. (a-c), Experimental and simulated extinction spectra of NB-superlattice sheets. Insets are the optical microscope images and TEM images of individual sheets. Scale bar is 100 nm for all TEM images.

The observed spectral shifts have two major contributions stemming from the modification of scattering properties of individual nanoparticles with thickening of silver coating and the enhancement of interparticle interaction with nanoparticle size for a fixed edge-to-edge separation (determined by the length of the capping ligands). On one hand, the experiments with individual nanoparticles dispersed in water revealed that the increase in silver coating induced a blueshift of about 66 nm for dipolar

resonance peaks of NBs. On the other hand, both experiment and DDA simulations showed that the stronger interparticle interaction in superlattice sheets made of larger nanoparticles manifests itself through the sharpening of extinction resonances.

5.2.7.4 SERS efficiency and near-field distribution for NB superlattice sheets

Programming the sizes and shapes of nanoparticles constituting superlattice changes the strength of their near-field confinement and the efficiency of SERS on superlattice surface [since SERS enhancement factor (EF) is proportional to the fourth power of the confinement strength, $EF \propto (|E|/|E_0|)^4$]. To estimate the strength of E-field distribution, 4-aminothiophenol (4-ATP) was used as a SERS probe to measure SERS EFs for the three superlattice sheets at laser wavelengths of 514, 633, and 782 nm. The strongest EFs of the NB-superlattice sheets were observed at 633-nm wavelength, regardless of the size of the constituent nanoparticles (**Figure 5.15**).

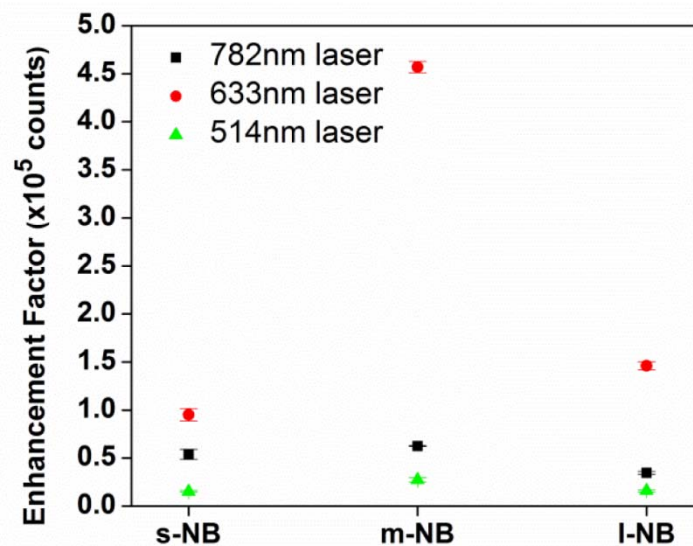


Figure 5.14 | SERS enhancement factors obtained on NB-superlattice sheets under various excitation wavelengths.

The interesting shape-discrimination phenomena could be understood from thorough DDA simulation of extinction spectra and near-field distribution. The dimensions of the nanoparticles and their spacing in the array were chosen equal to the mean dimensions of s-NB, m-NB, and l-NB (**Tables 5.1**) and the mean distances between their edges in the side-by-side (l_{ss}) and end-to-end (l_{ee}) orientations (**Figure 5.13**). The spectra for all combinations of l_{ee} and l_{ss} are obtained, which were then averaged based on the weights

assigned from their frequency of occurrence of periodicity parameters (l_{ee} and l_{ss}) given in **Figure 5.13**.

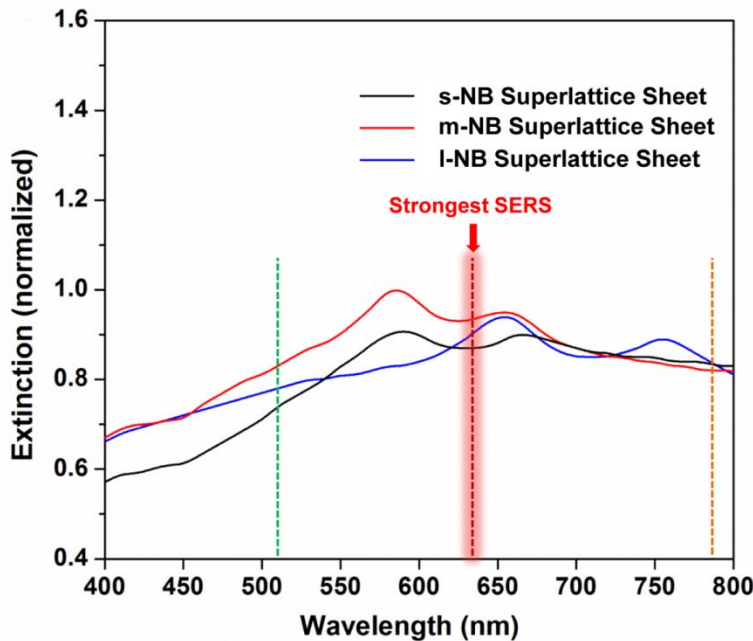


Figure 5.15 | Extinction spectra of NB superlattice sheets simulated based on DDA method. The spectra were calculated using mean values of the interparticle spacing parameters (l_{ee} and l_{ss}) shows in Fig. 5.13. The dashed vertical lines show the wavelengths of excitation laser used in Raman spectroscopy, *i.e.*, 514, 633, and 782 nm.

Comparison of the extinction efficiencies of m-NB-superlattice sheets at the three wavelengths showed that the strongest EF corresponded to the highest extinction near the LSPR band (**Figure 5.16**). Correspondingly, the near-field intensity is strongest for NB-superlattice sheets at 633 nm (**Figure 5.17**). The above simulation results were from a small area of a 2D-periodic array of 25 identical nanoparticles but these results were truly scalable independent on superlattice sizes.

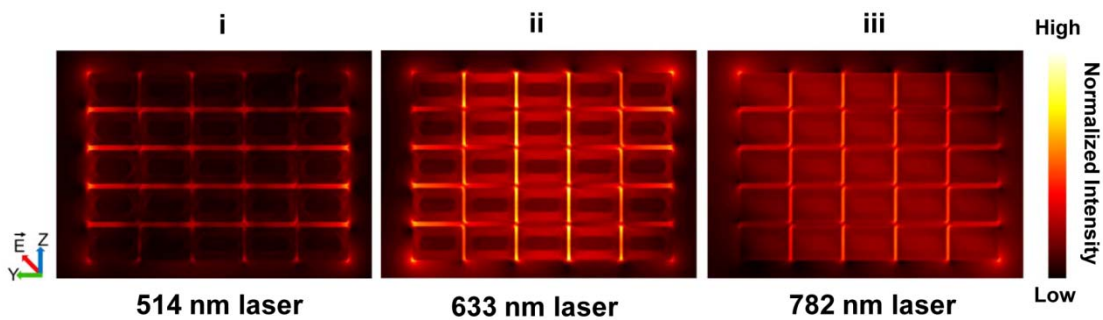


Figure 5.16 | Calculated near-field distributions on m-NB-superlattice sheet ($l_{ee} = 3$ nm, $l_{ss} = 4$ nm) under three excitation wavelengths of 514 nm, 633 nm, and 782 nm. The distribution was calculated across the plane passing through nanoparticle centres.

To compare the SERS intensity of three different NB superlattice sheets, Raman signal was probed using the fixed laser wavelength (633 nm). Based on recorded SERS intensity and simulated E-field intensity, it reveals that m-NB-superlattice sheets shows highest confinement (**Figure 5.18**). This implies that the laser (633 nm for m-NB superlattice sheet) for which the maximum amount of light gets extinct correlates fairly well with the highest confinement of E-field, which eventually leads to the maximum enhancement in Raman scattering intensity.

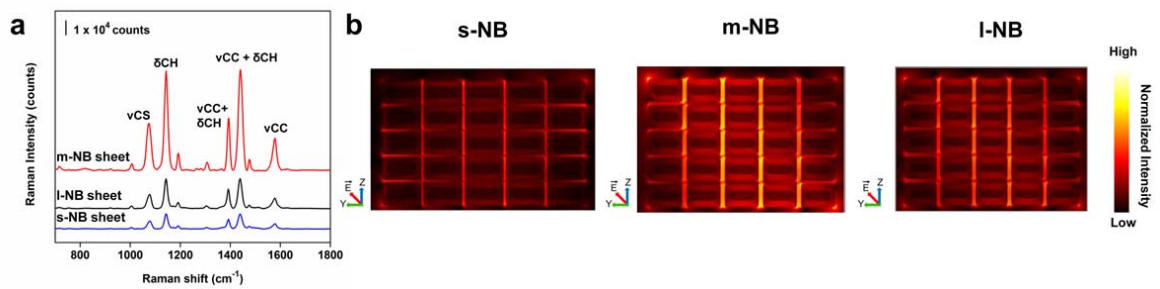


Figure 5.17 | (a) SERS spectra for NB superlattice sheet with incident laser wavelength of 633 nm. (b) Simulated E-field intensity distribution on for s-NB, m-NB, l-NB superlattice sheets at 633 nm. The simulated E-field distribution in (b) show relevant intensities of hotspots generated in NB superlattice sheets, which is consistent with the Raman scattering intensities shown in (a).

5.2.8 Giant superlattice sheets as universal and unique SERS substrates

5.2.8.1 SERS spectra from patterned square sheets

PDMS-transferring approach was used to shape the giant superlattice sheets into multiple square sheets onto silicon wafers, and then probed SERS enhancement at specific square sheets using 4-ATP as a Raman probe (**Figure 5.19**). 4-ATP has characteristic vibration bands in the region between 800 and 1800 cm^{-1} . These peaks are mainly assigned to either the a_1 or b_2 vibrational modes[36] (**Table 5.2**). The strong vibrational band at 1078 cm^{-1} was used to calculate SERS enhancement factor (EF) which was determined by the following Equation (5.2):

$$EF = \frac{I_{SERS} / N_{SERS}}{I_{BULK} / N_{BULK}} \quad \text{Equation(5.2)}$$

where I_{SERS} and I_{BULK} are the peak intensity at 1078 cm^{-1} in the SERS spectrum of 4-ATP and bulk 4-ATP, respectively; N_{SERS} is the number of adsorbed 4-ATP molecules on substrate within the laser spot; N_{BULK} is the number of 4-ATP molecules within the illumination volume of laser in a bulk sample. N_{SERS} can be further calculated by:

$$N_{SERS} = N_d A_{laser} A_N / \sigma \quad \text{Equation (5.3)}$$

where N_d is the number density of particles per unit area, A_{laser} is the area of the focal laser spot, A_N is the nanoparticle surface area determined by TEM measurements and σ is the footprint size of 4-ATP molecule ($\sim 0.20\text{ nm}^2$)[37].

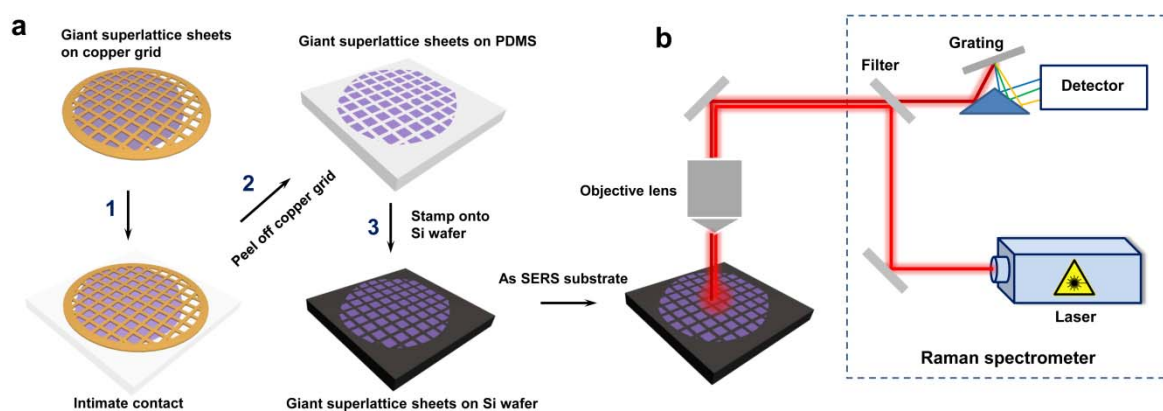


Figure 5.18 | (a) Schematic illustration of transferring superlattice sheets onto Si wafer, which can be readily used as SERS substrate. (b) Scheme shows the setup of Raman spectrometer.

Table 5.2 | Raman spectral peak assignment for 4-ATP adsorbed on superlattice sheet

4-ATP Raman (cm^{-1})	Vibrational assignment ^a
1078	νCS , 7a (a1)
1141	δCH , 9b(b2)
1392	$\nu\text{CC}+\delta\text{CH}$, 3(b2)
1438	$\nu\text{CC}+\delta\text{CH}$, 19b(b2)
1578	νCC , 8a(a1)

a: ν and δ denotes stretching and bending respectively.

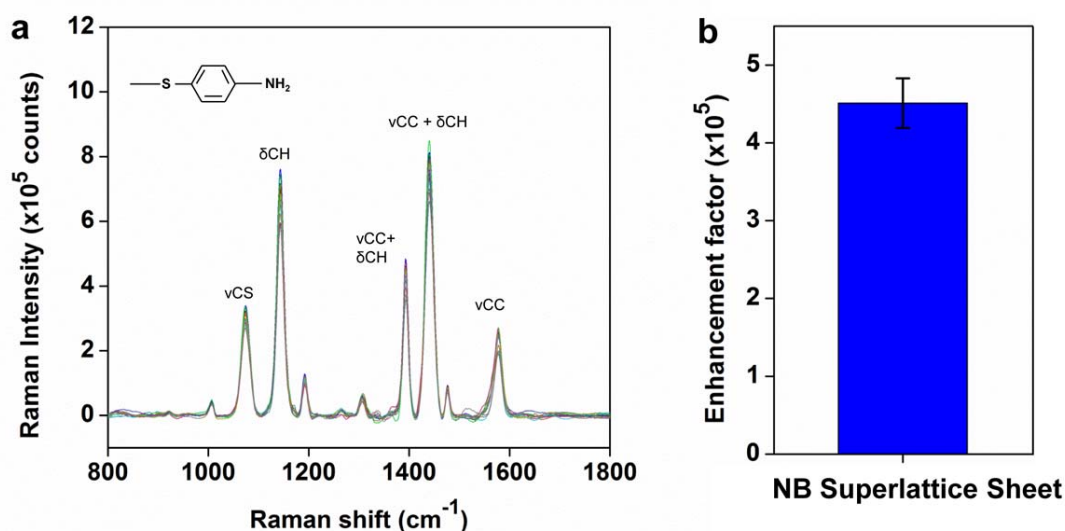


Figure 5.19 | (a) Superimposed SERS spectra obtained from 20 different spots on NB-superlattice sheets under the laser excitation wavelength of 633 nm. (b) Histogram of SERS enhancement factors on NB-superlattice sheets.

A unique feature of NB superlattice sheets is their high structural homogeneity and the resulting uniformity of SERS EFs across the surface. It was demonstrated by recording SERS spectra of 4-ATP from 20 different spots (of about $0.8\text{-}\mu\text{m}^2$ each) on the surface of superlattice sheets (**Figure 5.20a**). The almost perfect overlap of the 20 spectra indicates an exceptional uniformity of SERS from superlattice surface. In particular, the EFs variances for 1078-cm^{-1} peak were 5.6% for NB-superlattice sheets. (**Figure 5.20b**). These variances are well below those reported for nanosphere arrays,[38] dry plasma-fabricated irregular particle arrays,[39] and patterned nanoclusters.[22]

5.2.8.2 Liquid and vapor detection using free-standing superlattice sheets

Beyond signal uniformity, superlattice sheets are mechanical flexible and vapor-permeable, enabling their uses as a universal and unique SERS platform for ultrasensitive chemical identification of analyt in liquid, air. Typically, superlattice sheets enabled detection of 4-ATP dissolved in ethanol at concentrations as low as of about 100 pM (**Figure 5.21a**).

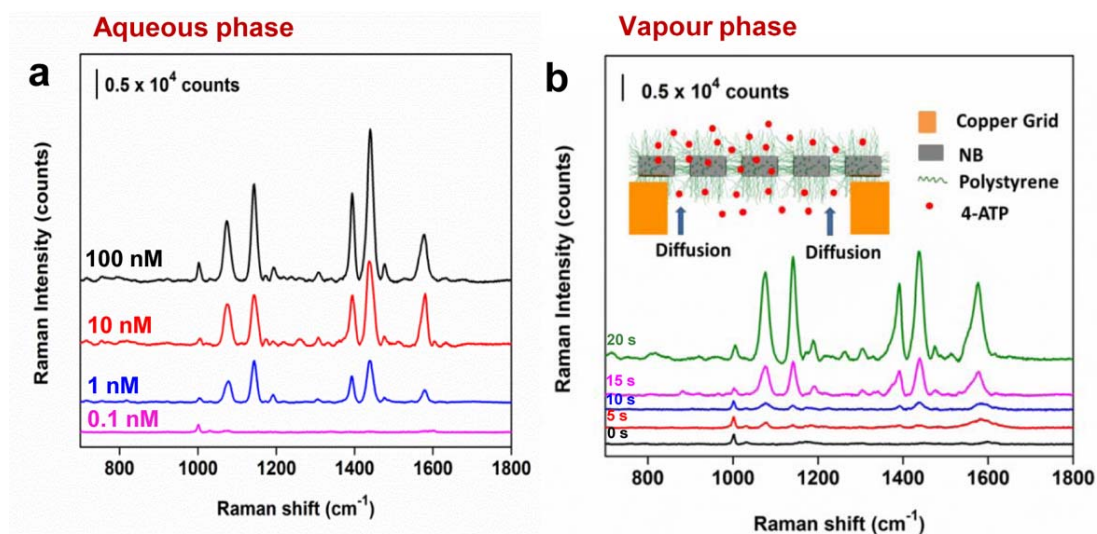


Figure 5.20 | NB superlattice sheets as universal SERS substrates for chemical identification of analytes in liquid, in air. (a) SERS spectra acquired from 4-ATP ethanol solutions. (b) SERS spectra from airborne 4-ATP at different exposure times. Inset illustrates permeation of 4-ATP molecules through and their binding onto suspended superlattice sheets.

In addition, superlattice sheets were vapor-permeable and could be suspended due to their mechanical robustness, which allowed for monitoring airborne analytes in *real-time* and *in-situ* (**Figure 5.21b**). This capability is demonstrated by measuring the SERS spectrum of the NB-superlattice sheet sealed in a plastic container together with 5 mg of 4-ATP powder. As the powder sublimated and the molecules of 4-ATP gradually diffused towards, and got attached to the superlattice surface (see inset in **Figure 5.21b**), the Raman spectrum of superlattice started featuring the SERS signature of 4-ATP. Remarkably, the characteristic Raman peak at 1078 cm^{-1} was readily seen within the first five seconds of exposure of superlattice to the 4-ATP vapor. The first 20 seconds of exposure were accompanied by a steep growth of the peak's intensity, which slowed down and got saturated in the following 40 seconds (**Figure 5.22**).

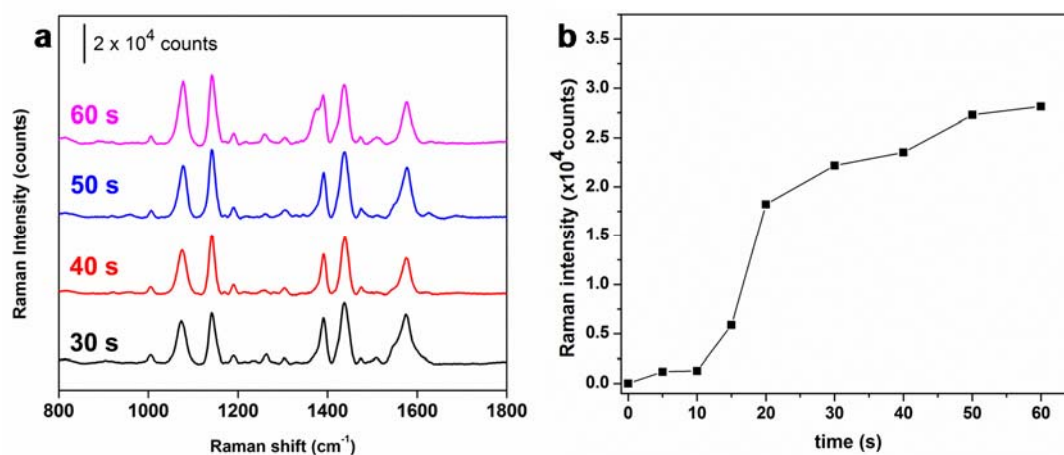


Figure 5.21 | (a) Raman spectra for airborne detection of 4-ATP at various exposure times. (b) The peak intensity at 1078 cm⁻¹ of vibrational band was plotted as a function of exposure time of free-standing superlattice sheets to the 4-ATP vapor.

5.3 Conclusion

In summary, this chapter developed a general self-assembly method to fabricate giant superlattice sheets for the first time. Plasmon modes and near-field distributions in giant superlattice sheets could be precisely customized simply by adjusting sizes and shapes of constituent Au@Ag NBs. Consequently, Raman hot spots could be generated at specific excitation wavelength in a highly predictable way. Beyond structural and functional programmability, superlattice sheets are homogeneous in structure, vapor-permeable and mechanically flexible, which enabled their uses as universal and unique SERS substrates with highly uniform Raman hotspot distributions across large area, for rapid and sensitive multi-phase detection of chemical species in air, liquid. The ease of self-assembly manufacture, highly customizable plasmonics and superior SERS enhancements in multiphase detection, as well as the potential integration with other 2D materials such as graphene, makes this giant superlattice sheet a unique material base for the next-generation of nanophotonic devices and smart sensors.

5.4 References

1. Tan, S.J., Campolongo, M.J., Luo, D. and Cheng, W.L. Building plasmonic nanostructures with DNA. *Nature Nanotech.* **6**, 268-276 (2011).

2. Bigioni, T.P., Lin, X.M., Nguyen, T.T., Corwin, E.I., Witten, T.A. and Jaeger, H.M. Kinetically driven self assembly of highly ordered nanoparticle monolayers. *Nature Mater.* **5**, 265-270 (2006).
3. Whetten, R.L., Houry, J.T., Alvarez, M.M., Murthy, S., Vezmar, I. *et al.* Nanocrystal gold molecules. *Adv. Mater.* **8**, 428-433 (1996).
4. Collier, C.P., Saykally, R.J., Shiang, J.J., Henrichs, S.E. and Heath, J.R. Reversible tuning of silver quantum dot monolayers through the metal-insulator transition. *Science* **277**, 1978-1981 (1997).
5. Kiely, C.J., Fink, J., Brust, M., Bethell, D. and Schiffrin, D.J. Spontaneous ordering of bimodal ensembles of nanoscopic gold clusters. *Nature* **396**, 444-446 (1998).
6. Courty, A., Mermet, A., Albouy, P.A., Duval, E. and Pileni, M.P. Vibrational coherence of self-organized silver nanocrystals in f.c.c. supra-crystals. *Nature Mater.* **4**, 395-398 (2005).
7. Tao, A., Sinsermsuksakul, P. and Yang, P. Tunable plasmonic lattices of silver nanocrystals. *Nature Nanotech.* **2**, 435-440 (2007).
8. Tang, Z., Zhang, Z., Wang, Y., Glotzer, S.C. and Kotov, N.A. Self-Assembly of CdTe Nanocrystals into Free-Floating Sheets. *Science* **314**, 274-278 (2006).
9. Park, S.Y., Lytton-Jean, A.K.R., Lee, B., Weigand, S., Schatz, G.C. and Mirkin, C.A. DNA-programmable nanoparticle crystallization. *Nature* **451**, 553-556 (2008).
10. Nykypanchuk, D., Maye, M.M., van der Lelie, D. and Gang, O. DNA-guided crystallization of colloidal nanoparticles. *Nature* **451**, 549-552 (2008).
11. Cheng, W.L., Campolongo, M.J., Cha, J.J., Tan, S.J., Umbach, C.C., Muller, D.A. and Luo, D. Free-standing nanoparticle superlattice sheets controlled by DNA. *Nature Mater.* **8**, 519-525 (2009).
12. Mueggenburg, K.E., Lin, X.M., Goldsmith, R.H. and Jaeger, H.M. Elastic membranes of close-packed nanoparticle arrays. *Nature Mater.* **6**, 656-660 (2007).
13. Dong, A.G., Chen, J., Vora, P.M., Kikkawa, J.M. and Murray, C.B. Binary nanocrystal superlattice membranes self-assembled at the liquid-air interface. *Nature* **466**, 474-477 (2010).
14. Korgel, B.A. Nanocrystal Superlattices Assembly at Liquid Interfaces. *Nature Mater.* **9**, 701-703 (2010).
15. Talapin, D.V., Lee, J.-S., Kovalenko, M.V. and Shevchenko, E.V. Prospects of Colloidal Nanocrystals for Electronic and Optoelectronic Applications. *Chem. Rev.* **110**, 389-458 (2009).
16. Jana, N.R., Gearheart, L. and Murphy, C.J. Seed-Mediated Growth Approach for Shape-Controlled Synthesis of Spheroidal and Rod-like Gold Nanoparticles Using a Surfactant Template. *Adv. Mater.* **13**, 1389-1393 (2001).
17. Nikoobakht, B. and El-Sayed, M.A. Preparation and Growth Mechanism of Gold Nanorods (NRs) Using Seed-Mediated Growth Method. *Chem. Mater.* **15**, 1957-1962 (2003).
18. Ng, K.C. and Cheng, W.L. Fine-tuning longitudinal plasmon resonances of nanorods by thermal reshaping in aqueous media. *Nanotechnology* **23**, 105602 (2012).
19. Okuno, Y., Nishioka, K., Kiya, A., Nakashima, N., Ishibashi, A. and Niidome, Y. Uniform and controllable preparation of Au-Ag core-shell nanorods using anisotropic silver shell formation on gold nanorods. *Nanoscale* **2**, 1489-1493 (2010).

20. Chen, Y., Fu, J., Ng, K.C., Tang, Y. and Cheng, W.L. Free-Standing Polymer-Nanoparticle Superlattice Sheets Self-Assembled at the Air Liquid Interface. *Crystal Growth & Design* **11**, 4742-4746 (2011).
21. Ng, K.C., Udagedara, I.B., Rukhlenko, I.D., Chen, Y., Tang, Y., Premaratne, M. and Cheng, W.L. Free-Standing Plasmonic-Nanorod Superlattice Sheets. *ACS Nano* **6**, 925-934 (2011).
22. Yan, B., Thubagere, A., Premasiri, W.R., Ziegler, L.D., Dal Negro, L. and Reinhard, B.r.M. Engineered SERS Substrates with Multiscale Signal Enhancement: Nanoparticle Cluster Arrays. *ACS Nano* **3**, 1190-1202 (2009).
23. Draine, B.T. and Flatau, P.J. Discrete-dipole approximation for periodic targets: theory and tests. *J. Opt. Soc. Am. A* **25**, 2693-2703 (2008).
24. Li, W., Camargo, P.H.C., Au, L., Zhang, Q., Rycenga, M. and Xia, Y. Etching and Dimerization: A Simple and Versatile Route to Dimers of Silver Nanospheres with a Range of Sizes. *Angew. Chem. Int. Ed.* **49**, 164-168 (2010).
25. Park, K., Drummy, L.F. and Vaia, R.A. Ag shell morphology on Au nanorod core: role of Ag precursor complex. *J. Mater. Chem.* **21**, 15608-15618 (2011).
26. Yu, K., You, G., Polavarapu, L. and Xu, Q.-H. Bimetallic Au/Ag Core-Shell Nanorods Studied by Ultrafast Transient Absorption Spectroscopy under Selective Excitation. *J. Phys. Chem. C* **115**, 14000-14005 (2011).
27. Jiang, R., Chen, H., Shao, L., Li, Q. and Wang, J. Unraveling the Evolution and Nature of the Plasmons in (Au Core)-(Ag Shell) Nanorods. *Adv. Mater.* **24**, OP200-OP207 (2012).
28. Palik, E.D. Handbook of Optical Constants of Solids, Vol. 3. (Elsevier, 1998).
29. Kim, S., Jung, Y., Gu, G.H., Suh, J.S., Park, S.M. and Ryu, S. Discrete Dipole Approximation Calculations of Optical Properties of Silver Nanorod Arrays in Porous Anodic Alumina. *J. Phys. Chem. C* **113**, 16321-16328 (2009).
30. Karg, M., Jaber, S., Hellweg, T. and Mulvaney, P. Surface Plasmon Spectroscopy of Gold-Poly-N-isopropylacrylamide Core-Shell Particles. *Langmuir* **27**, 820-827 (2010).
31. Hore, M.J.A. and Composto, R.J. Nanorod Self-Assembly for Tuning Optical Absorption. *ACS Nano* **4**, 6941-6949 (2010).
32. Triplett, D.A. and Fichthorn, K.A. Monte Carlo simulation of two-dimensional hard rectangles: Confinement effects. *Phys. Rev. E* **77**, 011707 (2008).
33. Denkov, N.D., Velev, O.D., Kralchevsky, P.A., Ivanov, I.B., Yoshimura, H. and Nagayama, K. Two-dimensional crystallization. *Nature* **361**, 26-26 (1993).
34. Yockell-Lelièvre, H., Desbiens, J. and Ritcey, A.M. Two-Dimensional Self-Organization of Polystyrene-Capped Gold Nanoparticles. *Langmuir* **23**, 2843-2850 (2007).
35. Cheng, W.L., Hartman, M.R., Smilgies, D.-M., Long, R., Campolongo, M.J., Li, R., Sekar, K., Hui, C.-Y. and Luo, D. Probing in Real Time the Soft Crystallization of DNA-Capped Nanoparticles. *Angew. Chem. Int. Ed.* **49**, 380-384 (2010).
36. Uetsuki, K., Verma, P., Yano, T.-a., Saito, Y., Ichimura, T. and Kawata, S. Experimental Identification of Chemical Effects in Surface Enhanced Raman Scattering of 4-Aminothiophenol[†]. *J. Phys. Chem. C* **114**, 7515-7520 (2010).
37. Kim, K. and Yoon, J.K. Raman Scattering of 4-Aminobenzenethiol Sandwiched between Ag/Au Nanoparticle and Macroscopically Smooth Au Substrate. *J. Phys. Chem. B* **109**, 20731-20736 (2005).

38. Lee, W., Lee, S.Y., Briber, R.M. and Rabin, O. Self-Assembled SERS Substrates with Tunable Surface Plasmon Resonances. *Adv. Funct. Mater.* **21**, 3424-3429 (2011).
39. Bianco, G.V., Giangregorio, M.M., Losurdo, M., Capezzuto, P. and Bruno, G. Supported Faceted Gold Nanoparticles with Tunable Surface Plasmon Resonance for NIR-SERS. *Adv. Funct. Mater.* **22**, 5081-5088 (2012).

Chapter 6

Conclusions and Outlook

This page is intentionally blank

The modular self-assembly of plasmonic superlattice nanomembranes enables new-generation of thinnest possible 2D metamaterials with programmable properties. However, it is nontrivial to grow superlattice nanomembranes, which requires high monodispersity of constituent nanoparticles, effective soft ligand capping against random nanoparticle aggregation, strict 1D confined growth, and free-standing transferability. Essential to tackle this challenge is precisely controlling over nanoparticle interactions by ligand engineering, optimizing assembly techniques for well-defined ordering, and unraveling lattice-property relationships for predictable plasmonic properties.

This thesis addresses the above challenges by presenting preparation and characterization of three superlattice nanomembranes: free-standing superlattice sheets formed by polymer-capped nanospheres, giant metallic superlattice nanomembranes from ultrathin gold nanowires, and giant superlattice sheets using bimetallic Au@Ag nanobricks (NBs). For the first time, it proposes a general polymer-ligand-based approach in conjunction with drying-mediated self-assembly at air-water interface to fabricate giant superlattice nanomembranes (e.g., the giant NB superlattice membrane is as thin as ~40 nm but as wide as ~3 mm, corresponding to an aspect ratio of ~75,000). This polymer-ligand-based assembly extends previous success with alkyl- and bio-ligands for preparing superlattice membranes. Using polystyrene-capped nanocrystal as a model system, it enables wider tuning of interparticle spacing especially for large nanoparticles which are important for plasmonic applications. With this approach, superlattice nanospheres nanomembrane reaches lateral dimensions of ~15 micrometers with a thickness of ~13 nm, corresponding to an aspect ratio (lateral size/thickness) of >1000. Both internal structures (particle size and interparticle spacing) and collective properties (plasmonic coupling) are tunable. The monolayered polymer-nanoparticle sheets are highly stable under various conditions, transferable to any arbitrary substrates, and can be manufactured with focused ion beams.

This thesis has presented the thinnest version of metallic membranes known to date, which is formed by soft 1D building blocks – ultrathin single-crystalline gold

nanowires (AuNWs) *via* Langmuir-Blodgett (LB) techniques. Such giant metallic superlattice nanomembrane has a thickness about 2.5 nm thick but with macroscopic lateral dimensions of $\sim 35 \text{ cm}^2$. Remarkably, the ultrathin superlattice nanomembranes are mechanically strong, optically transparent and electrically conductive. Notably, both synthesis of gold nanowires and fabrication process of superlattice nanomembranes are scalable, which render this methodology promising for practical applications in future lightweight foldable optoelectronics sensors. Also, this methodology can potentially be extended to fabricate nanomembranes from other types of nanowires or multiple components, therefore, it may become a general modular approach to integrate optoelectronic properties with mechanical robustness into a single lightweight, foldable 2D materials systems for promising applications in future foldable electronics.

In particular, for superlattice membranes, the hybridized plasmon modes and near-field distributions can be strictly controlled in a 2D plane, which can be in principle programmed by adjusting sizes, shapes of constituent nanoparticles and controlling interparticle spacing. As the final part of this thesis, it demonstrates both experimentally and theoretically that hybridized plasmon modes and near-field distributions of giant superlattice sheets can be customized arbitrarily. Beyond structural and functional programmability, superlattice sheets are homogeneous in structure, vapor-permeable, enabling their uses as universal and unique SERS substrates with highly uniform Raman hotspot distributions across large area, for rapid and sensitive detection of chemical species in both air and liquid. Due to its proved mechanically flexible, the detection region can be extend to topologically complex solid surfaces in the future work.

Based on the advances presented in this thesis, it is clear that undeveloped issues and more exciting works remain ahead. The major future work is recommended as the following aspects:

- ❖ Large-scale synthesis of high-quality plasmonic nanocrystals with well-defined morphology, diameters, geometry is still demanded. Once novel nanocrystals have

been synthesized, the polymer-based assembly approach can be readily used to those building blocks to create superlattice nanomembranes with unprecedented plasmonic properties.

- ❖ Binary or ternary superlattice nanomembranes constructed from different plasmonic nanocrystals extends the possibility of rational control and generating unprecedented plasmonic properties, which is rarely unexploited. In future work, it is recommended to construct such multi-component superlattice nanomembranes by precisely control over nanoscale interactions.
- ❖ By developing efficient surface modification method for nanocrystals and controllable parameters of interfacial properties, superlattice membrane with larger macroscopic dimension can be achieved. Also, by employing interfacial polymerization, it is desired to fix superlattice structure by polymer matrix or crosslinked ligands. In this way, large-scale superlattice membrane can achieve sufficient dimension for real-world optoelectronic devices and sensors
- ❖ Such plasmonic nanomembranes will definitely trigger applications such as high-performance SERS substrates. In this thesis, accumulating evidence has highlighted the enhancement of the Raman signal induced by the localized surface plasmons within metallic nanoparticles and multiple hotspots being generated through largely enhanced electromagnetic field in the interstitial spaces. It is still highly desirable to optimizing the electromagnetic field enhancement by adjusting the plasmonic properties, minimizing sophisticated process involved in nanofabrication, and maximizing uniformity applicable for reproducible and strong signal, thus achieve multiple-analyte detection and ultrasensitive universal sensors.

This page is intentionally blank

Appendix

First-Authored Papers Relevant to This Thesis

This page is intentionally blank

Mechanically Strong, Optically Transparent, Giant Metal Superlattice Nanomembranes From Ultrathin Gold Nanowires

Yi Chen, Zi Ouyang, Min Gu, and Wenlong Cheng*

Lipids and polymers are classic materials to be used in natural and artificial membrane systems, respectively. In contrast, recently there is burgeoning interest in constructing new class of membranes from nanoscale optoelectronic building blocks.^[1–11] In particular, it is possible to fabricate free-standing periodic nanoparticle arrays (superlattices) which behave as mechanically strong nanomembranes with Young's moduli of several GPa.^[3,6,11] Such superlattice nanomembranes differ from solid-supported superlattice films^[12–15] in that they exist as free-standing, isolated forms in their final stage of growth or processing. Remarkably, both optoelectronic and mechanical properties of such superlattice membranes are tunable by varying materials types, adjusting ligand length, and regulating lattice structures, etc. Hence, engineering superlattice nanomembranes constitutes an exciting route to integrate unique properties of optoelectronic nanomaterials with striking mechanical robustness and flexibility into one tailorable multifunctional system, leading to lightweight metamaterials and devices with new functions for novel applications in optoelectronics,^[9,16,17] electrocatalysis,^[18] and ultrafiltration.^[19]

Despite the exciting progress in the fabrication of free-standing metallic superlattice nanomembranes, their practical applications are often hampered by the difficulty in fabricating defect-free superlattice membranes at large area. In particular, it is highly desirable to develop the ability to fabricate giant metal superlattice nanomembranes (two-dimensional, ordered metallic nanoparticle arrays forming ultrathin membrane of a few nanometers thick but with macroscopic lateral dimensions). This is because nanoscale thickness and macroscopic lateral dimensions are apparently conflicting characteristics difficult to achieve simultaneously.^[2] Previous attempts with sphere-like hard building blocks only led to superlattice membranes restricted to small lateral dimensions.^[3–6,9,10]

Here, we report on the fabrication of giant superlattice nanomembranes from soft 1D building blocks—ultrathin single-crystalline gold nanowires (AuNWs)—via Langmuir–Blodgett (LB) techniques. Although LB techniques have been widely used for the assembly of nanowires,^[20–25] the ability to form mechanically-robust free-standing nanomembranes has not yet been reported, to the best of our knowledge. This could be due to the fact that our gold nanowires are thinner and more flexible, contributing to maintaining the integrity of the nanomembranes at large area. Specifically, we show a single-layer AuNWs superlattice nanomembrane is transparent, conductive and mechanically robust, with an optical transmittance of 90–97% over a wide spectral window of 300–1100 nm, an electrical resistance of $\sim 1142 \text{ k}\Omega \text{ sq}^{-1}$, and a breaking strength of $\sim 14 \text{ N m}^{-1}$ with a typical atomic force microscope probe. Such single-layer nanowire membranes are transferable to any arbitrary substrates, facile to be integrated into lightweight, foldable optoelectronic devices with low consumption of materials and energy. Our methodology may serve as a model system, extendable to superlattice nanomembranes from other materials for a myriad of applications in construction of new classes of two-dimensional metamaterials and devices.

We began with the large-scale synthesis of high-quality single crystalline ultrathin AuNWs by adopting the recently reported approaches.^[26–28] In brief, gold precursor (HAuCl_4) was gradually reduced by triisopropylsilane (TIPS) in the presence of oleylamine (OA). After aging the solution at room temperature for 2 days, the solution turned from yellow to dark red (Figure 1a,b), indicating complete reduction of Au^+ -amine complex into OA-capped AuNWs dispersible in hexane^[27] (Figure 1c). The nanowires were precipitated out by adding ethanol and centrifugation, and then washed twice with ethanol and re-dispersed in chloroform as concentrated stock solution for further use.

In the purified nanowires, the OA molecules contribute to 18% of the total weight as demonstrated by thermogravimetric analysis (Supporting Information, Figure S1). Thus, the OA capping effectively stabilizes nanowires and prevents them from deterioration in various characterization and processing in the fabrication of nanomembranes. Electron microscopy studies show each nanowire is single crystalline growing along the [111] direction (Figure 1d) with an interfringe distances of $\sim 0.23 \text{ nm}$ and ultrathin with a width of $\sim 2.5 \text{ nm}$. The nanowires have enormous aspect ratios, extending to tens of micrometers in length. These structural characteristics give nanowires high mechanical robustness and flexibility, leading to hairy morphology (Figure 1e). Due to strong hydrophobic interactions

Y. Chen, Prof. W. L. Cheng
Department of Chemical Engineering
Monash University
Clayton, Victoria 3800, Australia
The Melbourne Centre for Nanofabrication
Clayton, Victoria 3800, Australia



Dr. Z. Ouyang, Prof. M. Gu
Centre for Micro-Photonics
Faculty of Engineering and Industrial Sciences
Swinburne University of Technology
Hawthorn, Victoria 3122, Australia

DOI: 10.1002/adma.201202241

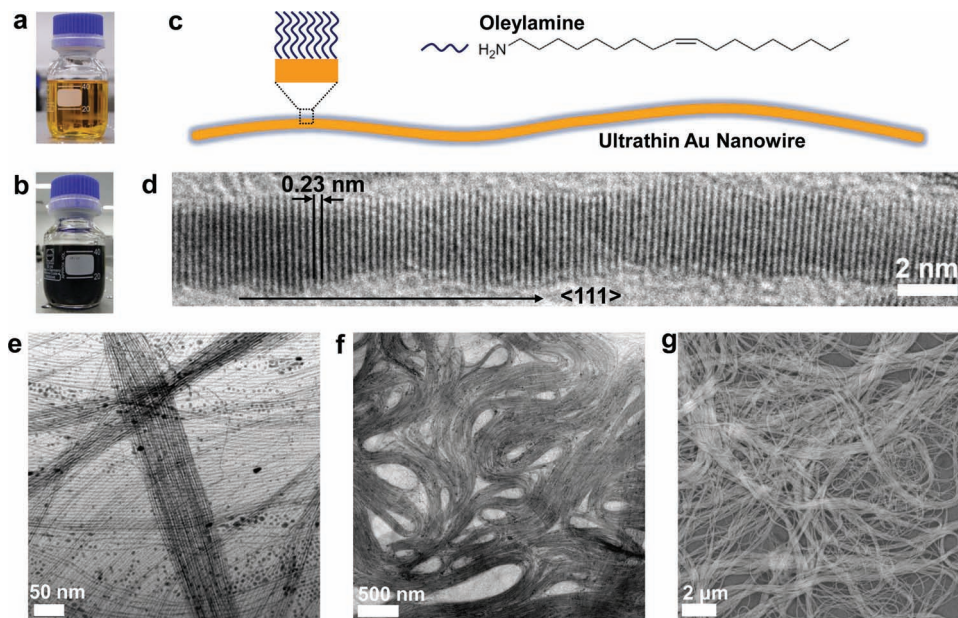


Figure 1. Large-scale synthesis of ultrathin single crystalline AuNWs with high-aspect ratio. a,b) Photographs of the synthesis of ultrathin AuNWs at the initial and final stage of reaction. c) Schematic illustration for the oleylamine-capped AuNWs. d) High-resolution TEM image of an individual single crystalline ultrathin AuNW shows [111] lattice planes. e) TEM image of aligned AuNWs assemblies. f) TEM image of AuNWs bundles. g) SEM image of AuNWs bundles.

between OA ligands, the nanowires tended to form parallel bundle-like strands (Figure 1f,g).

Furthermore, we applied the as-synthesized AuNWs to fabricate giant superlattice nanomembranes by LB techniques. Typically, one droplet (~4–6 μL) of nanowires dispersed chloroform solution was carefully spread onto the water surface in a LB trough. The droplet quickly spread and evaporated in less than 1 s, distributing the nanowires uniformly on the water surface. By moving LB baffle, the free-floating nanowires were forced to approach each other with gradual phase transitions (Supporting Information, Figure S2). In particular, a Mott-insulator-to-metal transition was noted at the surface pressure of ~13 mN m⁻¹. This transition was indicated by the appearance of red-colored metallic sheen, and further demonstrated by turning the slope in the typical π -A isotherm.^[22] A further compression led to rapid pressure buildup from 13 mN m⁻¹ to 38 mN m⁻¹ until collapse, and in this process a condensed nanowire membrane formed on the water surface. **Figure 2a** shows a giant nanowire superlattice membrane covering an entire trough area of ~35 cm². The membranes were mechanically strong yet flexible, transferable to a variety of substrates (including silicon, glass slides, paper, plastics, TEM copper grids, and PDMS, *etc*) without cracking or rupturing (Figure 2b and Supporting Information, Section 2). The coating could substantially alter the wetting properties. For example, the contact angle of a glass slide increased from ~26° to ~103° after nanomembrane covering (Figure 2c).

Remarkably, the nanomembranes consisted of dominantly monolayered nanowires aligned in parallel. Figure 2d shows a typical atomic force microscopy (AFM) image of AuNWs

nanomembranes transferred onto a silicon wafer. The membrane is uniformly continuous extending to centimeter-scale with little defects. Further AFM line scanning gave an average thickness of 2.2 ± 0.1 nm (Figure 2e). We found that monolayered superlattice nanomembranes could withstand large lateral compression forces up to ~38 mN m⁻¹. We transferred the membranes to lacey/carbon copper grid at specific surface pressures of 20 mN m⁻¹ and 30 mN m⁻¹, and characterized their morphologies (Figure 2f,g). Both images indicated predominantly the monolayered AuNWs, in agreement with the above AFM characterizations. Nevertheless, under high compression forces, the membranes tended to be crumpled by piling (Figure 2g) or bending (Supporting Information, Figure S5). Nevertheless, the membranes remain intact without any cracking or rupturing during the LB compression process.

To quantitatively determine the mechanical strength of free-standing superlattice nanomembranes, we performed AFM nanoindentation experiments. Firstly, the superlattice membranes were transferred onto holey silicon nitride substrate patterned with periodic 2 μm-diameter holes. The superlattice membranes could span over the holes. Majority of membranes (~80%) remained intact after transfer and survived from vacuum drying (Supporting Information, Figure S6). By high-resolution imaging, we located specific intact membranes (**Figure 3d**) and then indented at the center of microholes. Force-displacement curves were recorded with stepwise increase of force until rupturing the membrane (Figure 3a). Notably, the ruptured holes were V-shaped memorizing the shapes of pyramid AFM probes (Figure 3e,f), and the adjacent holes didn't coalesce

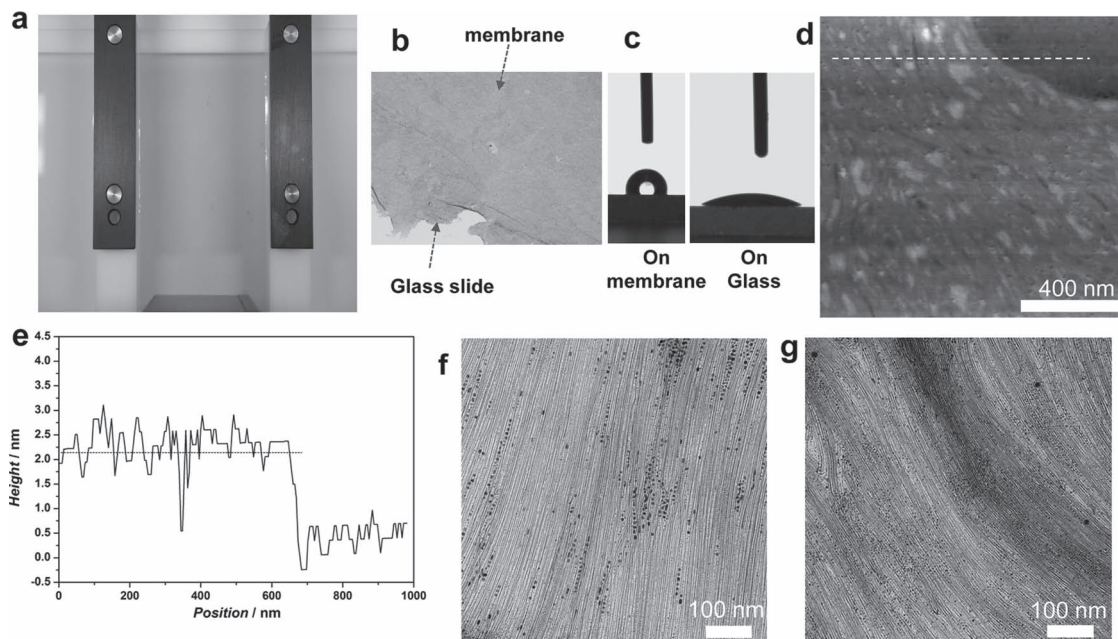


Figure 2. Fabrication of monolayered AuNWs superlattice nanomembrane. a) Photograph of a homogeneous nanomembrane with an area of 35 cm² on the LB trough. b) Photograph of a membrane transferred onto a glass slide. c) Photographs of sessile water droplets on glass and on membrane. d) AFM height image of the superlattice nanomembrane transferred onto silicon wafer. e) AFM cross-sectional height plot corresponding to the dashed line in d). f) and g) TEM images of monolayer superlattice nanomembranes collected at surface pressure of 20 mN m⁻¹ and 30 mN m⁻¹, respectively.

(Supporting Information, Figure S9), indicating paper-like mechanical properties. We observed consistent force curves for both multiple indents within a specific holey region, as well as other holey areas. Fitting of the force curves allowed us to

derive a Young's modulus of $\sim 5.2 \pm 0.4$ GPa using the similar model reported earlier^[3] (Supporting Information, Section 4). This value is comparable to those for DNA-nanoparticle membrane^[3] and alkyl-nanoparticle membrane.^[6,11]

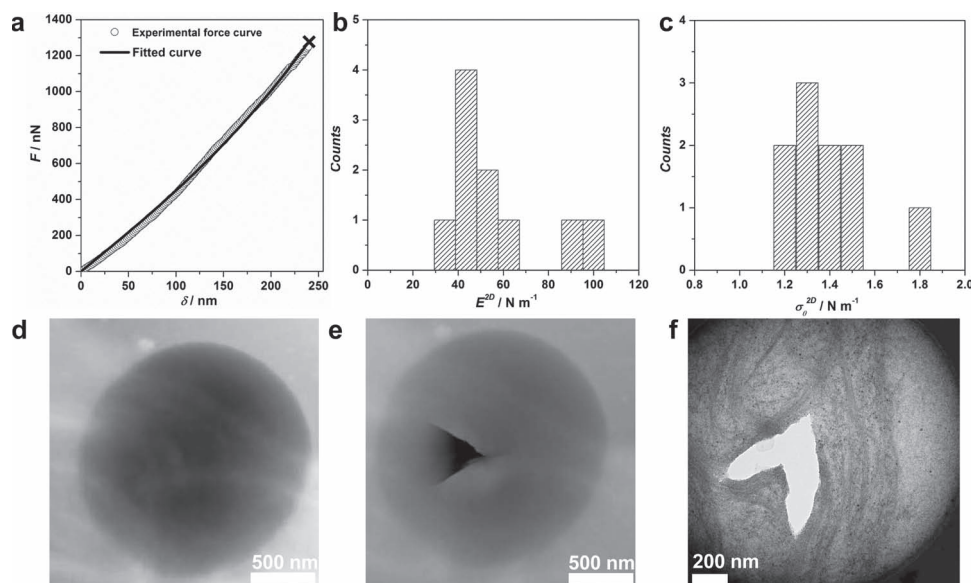


Figure 3. Mechanical properties of monolayered superlattice nanomembranes. a) Force-displacement curves from AFM indentation (circle) and from theoretical fitting (line). Fracture load is indicated by a \times mark. b) Histogram of 2D elastic modulus, E^{2D} . c) Histogram of membrane pretention, σ^{2D} . d) AFM height image of superlattice nanomembrane cover over a 2- μ m-diameter microhole in the silicon nitride substrate before indentation. e) AFM height image of a ruptured nanomembrane. f) corresponding TEM image of the same ruptured nanomembrane in e). Note that triangle hole in (e) becomes v-shaped hole in (f), which indicates that the “triangular tongue-like membrane” yielded in AFM imaging but recovered back in TEM imaging. This result echoes the strong mechanical properties as revealed in (a).

We further estimated the breaking strength when using a typical AFM probe. Based on the models used for monolayer graphene,^[29] we assume our nanowire superlattice nanomembrane as a true 2D material given the ultrathin nature and large aspect ratio of our nanomembrane. Thus, the strain energy density can be normalized by the area rather than the volume of the nanomembrane. Hence, its mechanical behavior under AFM probe indentation is properly described by a 2D stress, σ^{2D} and 2D modulus, E^{2D} . Both have units of force/length rather than force/area for normal 3D material systems. The force-displacement behavior for a clamped circular membrane under central point loading can then be approximated as:

$$F = \sigma_0^{2D} (\pi R) \left(\frac{\delta}{R}\right) + E^{2D} (q^3 R) \left(\frac{\delta}{R}\right)^3$$

where F is the applied force, σ_0^{2D} is the pre-tension in the membrane, R is the radius of circular membrane, δ is the deflection at the center, E^{2D} is the 2D modulus, and q is a constant depending on poisson's ratio, ν , by the equation, $q = 1/(1.05 - 0.15\nu - 0.16\nu^2)$. Numerical fitting of 10 sets of force curves from different locations under different loads gave σ_0^{2D} and E^{2D} of 1.4 ± 0.1 N/m and 52 ± 23 N/m, respectively (Figure 3b and c). With these values on the basis of the continuum model used for 2D material,^[29] we could then estimate the breaking strength of 14.3 ± 1.4 N/m with a typical AFM probe with a tip radius of 24 nm. Following the identical treatment, we also estimated our previous nanoparticle membranes from DNA of 30 and 50 bases long, giving breaking strengths of 4.5 N/m and 1.8 N/m, respectively. Considering the fact that 100 nm-radius probe was used in DNA-based nanomembranes, the above results show that the nanowire superlattice membrane is much stronger than DNA-nanoparticle membrane. This may originate from the 1D nanowire building blocks used in this study. It is harder to break gold nanowires than tangled DNA strands.

The monolayer AuNWs nanomembrane exhibited exceptionally high optical transmittance of 90–97% with an almost flat line over a fairly wide spectral range of 300–1100 nm (Figure 2b, and Figure 4). The observed high optical transparency is due to the ultrathin nature of our superlattice nanomembranes, which is in agreement with the theoretical prediction. We estimated the theoretical transmittances of nanomembranes with different wire diameters by calculating the decay of an electromagnetic wave after propagating through a medium (Supporting Information, Section 5). The results showed an evident decreasing trend of the transmittance with increasing diameters (Supporting Information, Figure S10). Note that the calculated theoretical transmittance of 2.5 nm AuNWs monolayer nanomembrane provides a reasonable fit of our measured profile, which further proved the monolayer structure of our nanomembrane. The slight decrease in the region of 500–550 nm is due to the surface plasmon resonance of spherical

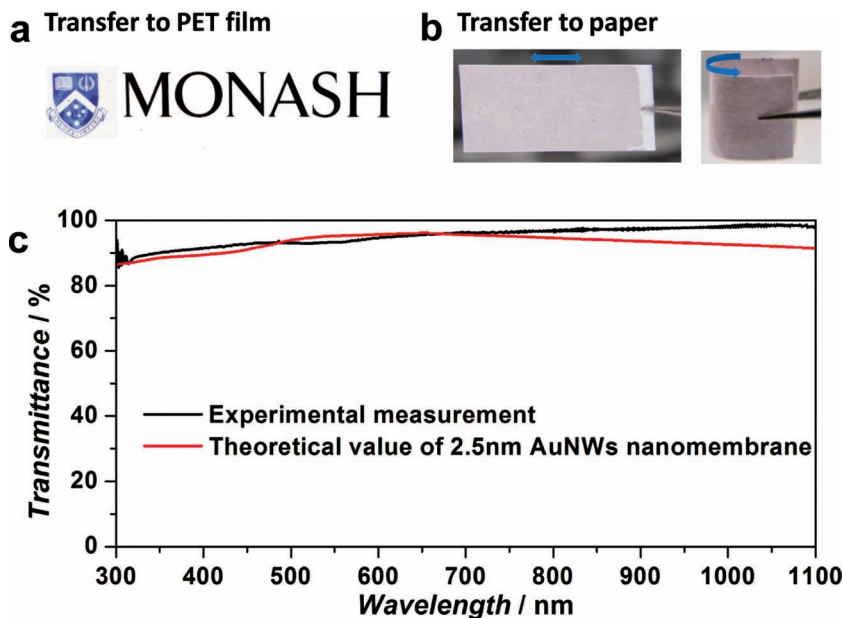


Figure 4. High optical transparency of monolayered AuNWs superlattice nanomembrane. a) photograph of a PET plastic sheet partially covered with superlattice nanomembrane. b) a paper sheet coated with nanomembrane on both sides. c) experimental (black) and theoretical (red) transmittance spectra of monolayered superlattice nanomembrane on a glass slide. Approximate agreement in experiment and theoretical calculation proves that nanomembranes are composed of predominantly a single nanowire layer.

nanoparticles existing as impurity in the nanomembrane as seen in Figure 1e.^[30]

In addition, monolayered AuNWs superlattice membranes are conductive. The square resistances of a set of superlattice membranes from 15 batches of stock nanowire solutions were measured by a four-point probe station, giving a value of 1142 ± 16 k Ω sq⁻¹. This value is substantially higher than that given by a theoretical modeling, in which nanowires are assumed to be infinitely long and ideally aligned to the device scale. This model predicted a sheet resistance of 15–200 Ω sq⁻¹ (Supporting Information, Section 6) along the direction of the AuNWs. The discrepancy may be due to the fact that AuNWs have finite length and the alignment is limited to micrometer-scale, and there may exist a large contact resistance at the joint of two nanowires.^[31] We further investigated relationship between optical transmittance and electrical conductivity by multilayer coating. As the coating layer of nanomembrane increased, both the transmittance and sheet resistance decreased (Supporting Information, Figure S11). Similar to transparent electrode from other materials,^[31,32] the relationship between the transmittance and sheet resistance can be described by Equation S4 in supporting information. However, the square resistance for multilayered nanomembrane remains very high. We applied the normal pressing forces to the multilayered membranes and observed improvement in conductivity (15–19%), which may be due to the decrease of wire-to-wire spacing during mechanical compression.^[33] Nevertheless, the conductivity remains far from theoretical prediction, indicating that the densely-packed capping oleylamine molecules surrounding AuNWs may substantially prevent electron-hopping from wire to wire.

Despite high sheet resistance, superlattice nanomembrane could withstand mechanical bending for hundreds of cycles. We monitored the sheet resistance of superlattice nanomembranes (Supporting Information, Figure S12). In particular, the sheet resistance for monolayer nanomembrane only increased by about 14% after 400 bending cycles.

In summary, this paper presents a simple yet efficient method to fabricate giant metallic superlattice nanomembrane of about 2.5 nm thick but with macroscopic lateral dimensions. To the best of our knowledge, such superlattice nanomembrane represents the thinnest version of metallic membranes known to date.^[3,6,11] Remarkably, the ultrathin superlattice nanomembranes are mechanically strong, optically transparent and electrically conductive. Notably, both synthesis of gold nanowires and fabrication process of superlattice nanomembranes are scalable, which render our methodology promising for practical applications in future lightweight foldable optoelectronics, such as touch-screen devices.^[33,34] Our methodology can potentially be extended to fabricate nanomembranes from other types of nanowires or multiple components, therefore, it may become a general modular approach to integrate optoelectronic properties with mechanical robustness into a single lightweight, foldable 2D materials systems for promising applications in future foldable electronics.

Experimental Section

Materials: Gold (III) chloride trihydrate ($\text{HAuCl}_4 \cdot 3\text{H}_2\text{O}$, $\geq 99.9\%$), Triisopropylsilane (99%) and Oleylamine were purchased from Sigma Aldrich. Hexane and chloroform were obtained from Merck KGaA. All chemicals were used as received unless otherwise indicated. All aqueous solutions were made using demineralized water, which was further purified with a Milli-Q system (Millipore). All glassware used in the following procedures was cleaned in a bath of freshly prepared aqua regia and rinsed thoroughly in H_2O prior to use.

Holey Lacey Formvar/Carbon films (300 mesh and irregular pores with sizes varying from less than a quarter of 1 μm to more than 10 μm) were purchased from Ted Pella. Quantifoil holey carbon films (2 μm -diameter hole, 2 μm in space) were purchased from Electron Microscopy Sciences. Holey silicon nitride support films (2- μm -diameter hole, 4 μm pitch) were purchased from SPI supplies.

Characterization: Morphology characterization was carried out using a Philips CM20 TEM at a 200 kV accelerating voltage, Hitachi H-7500 field emission TEM operating at 80 kV, and JEOL JSM-7001F FEG SEM. High-resolution TEM images were performed on a JEOL JEM 2011 TEM operated at an acceleration voltage of 200 kV. Stepwise focusing with low beam currents helped to avoid distortion of AuNWs by the electron beam. The transmittance of superlattice nanomembrane is measured with Agilent 8453 UV-vis spectrophotometer, and the transparent images were recorded by a CCD camera on the J&M MSP210 Microscope Spectrometry System, while the membrane was transferred onto glass slide and illuminated by a high-intensity fiber light source under a 40 \times objective. Thermogravimetric analysis (TGA) was carried out using a Mettler Toledo TGA-SDTA851 analyzer in the temperature range from 25 to 700 $^\circ\text{C}$ at a heating rate of 10 $^\circ\text{C}/\text{min}$. The runs were performed under N_2 gas, and the gas was switched to air for 10 min at the end of the run at 700 $^\circ\text{C}$ to ensure complete combustion of the organic material. N_2 and air gases were used at a rate of 50 mL/min.

Force-displacement curves from nanoindentation and topography images were obtained with a Veeco Dimension Icon AFM in tapping mode using Bruker silicon probes (MPP-21100-10). The spring constant for cantilever was 3 N m^{-1} . The typical tip speed for the indentation was 500 nm s^{-1} . Each membrane was first imaged by AFM, then gradually increased the applied force and performed multiple indentations with

the AuNWs superlattice membrane to collect the force-indentation curve, and finally imaged again to check for rupture of membrane. See Supporting Information Section 4 for a detailed analysis.

Synthesis of Ultrathin AuNWs: Large-scale synthesis of ultrathin AuNWs was performed according to the literature.^[26] $\text{HAuCl}_4 \cdot 3\text{H}_2\text{O}$ (53 mg) and hexane (50 mL) were added into a 100 mL Schott/Duran bottle, followed by addition of Oleylamine (OA, 1.8 mL) as both stabilizer and growth template. After completely dissolving of gold precursor, Triisopropylsilane (TIPS, 2.5 mL) was added into above auric solution and allowed to stand for 2 days without disturbing at room temperature. Finally, the solution turned into dark-red, indicating the formation of AuNWs (0.58 mg mL^{-1}). The residue chemicals were removed by repeated centrifuging and thorough washing by ethanol/hexane (1/3, v/v) and finally concentrated into 5 mL that dispersed in chloroform (5.82 mg mL^{-1}). Statistical evaluation from TEM images of as-prepared AuNWs shows an estimated yield of $\sim 90\%$. The surfaces of the as-made AuNWs were capped by oleylamine and indicated as hydrophobic property.

Fabrication and Transfer of AuNW Superlattice Nanomembrane: AuNWs superlattice membrane was prepared using a Langmuir-Blodgett trough (Nima Technology) at 25 $^\circ\text{C}$. The Teflon-coated trough and barrier were wiped with CHCl_3 and then purged with ethanol to remove any dust or organic contaminants. In a typical experiment, 10 mL purified AuNWs (0.58 mg mL^{-1}) was centrifuged and redispersed in 1 mL CHCl_3 (5.82 mg mL^{-1}). Then the concentrated AuNWs solution was added dropwise to the air-water interface of the LB trough. The droplet quickly spread over the water surface in less than 1 s and evaporated to leave an isotropically distributed AuNWs floating on the water surface. The trough was then covered to prevent fluid flows and solvent fluctuations, and allowed to equilibrate for 30 min. The AuNWs were then isothermally compressed by moving the two opposing barriers towards each other while the surface pressure was monitored with a Wilhelmy plate. At a target surface pressure (e.g., 20 mN m^{-1} for monolayered AuNWs superlattice membrane), the pressure was kept constant at least 1 h. After the equilibration, the AuNWs superlattice membrane was transferred onto hydrophilic substrates by slowly pulling the substrate out of the aqueous subphase with a vertical dipping speed of 5 mm min^{-1} , and transferred to hydrophobic substrates by horizontal deposition through Langmuir-Schaefer technique. Also, transfer of multilayer AuNWs nanomembrane could be realized by using layer-by-layer transfer method. See Supporting Information Section 2 for a detailed description.

Supporting Information

Supporting Information is available from the Wiley Online Library or from the author.

Acknowledgements

This work is financially supported by the New Staff Member Research Fund awarded by the Faculty of Engineering, Monash University and ARC discovery project DP120100170. The authors also acknowledge the use of facilities in the Monash Centre for Nanofabrication by the program of MCN technology fellows. Y.C. acknowledges the graduate student scholarship (MGS & IPRS) from Monash University. Z.O. and M.G. acknowledge the support from the Victoria-Suntech Advanced Solar Facility (VSASF) funded under the Victoria Science Agenda (VSA) scheme.

Received: June 4, 2012

Revised: July 24, 2012

Published online: September 18, 2012

- [1] W. L. Cheng, M. J. Campolongo, S. J. Tan, D. Luo, *Nano Today* **2009**, 4, 482.
- [2] A. G. Dong, J. Chen, P. M. Vora, J. M. Kikkawa, C. B. Murray, *Nature* **2010**, 466, 474.

- [3] W. L. Cheng, M. J. Campolongo, J. J. Cha, S. J. Tan, C. C. Umbach, D. A. Muller, D. Luo, *Nat. Mater.* **2009**, *8*, 519.
- [4] Y. Chen, J. Fu, K. C. Ng, Y. Tang, W. L. Cheng, *Cryst. Growth Des.* **2011**, *11*, 4742.
- [5] K. C. Ng, I. B. Udagedara, I. D. Rukhlenko, Y. Chen, Y. Tang, M. Premaratne, W. L. Cheng, *ACS Nano* **2011**, *6*, 925.
- [6] K. E. Mueggenburg, X. M. Lin, R. H. Goldsmith, H. M. Jaeger, *Nat. Mater.* **2007**, *6*, 656.
- [7] R. Vendamme, S.-Y. Onoue, A. Nakao, T. Kunitake, *Nat. Mater.* **2006**, *5*, 494.
- [8] Z. Tang, Z. Zhang, Y. Wang, S. C. Glotzer, N. A. Kotov, *Science* **2006**, *314*, 274.
- [9] J. Liao, Y. Zhou, C. Huang, Y. Wang, L. Peng, *Small* **2011**, *7*, 583.
- [10] J. Pang, S. Xiong, F. Jaeckel, Z. Sun, D. Dunphy, C. J. Brinker, *J. Am. Chem. Soc.* **2008**, *130*, 3284.
- [11] J. He, P. Kanjanaboos, N. L. Frazer, A. Weis, X.-M. Lin, H. M. Jaeger, *Small* **2010**, *6*, 1449.
- [12] W. L. Cheng, N. Park, M. T. Walter, M. R. Hartman, D. Luo, *Nat. Nanotechnol.* **2008**, *3*, 682.
- [13] A. Courty, A. Mermet, P. A. Albouy, E. Duval, M. P. Pileni, *Nat. Mater.* **2005**, *4*, 395.
- [14] A. M. Kalsin, M. Fialkowski, M. Paszewski, S. K. Smoukov, K. J. M. Bishop, B. A. Grzybowski, *Science* **2006**, *312*, 420.
- [15] B. A. Korgel, S. Fullam, S. Connolly, D. Fitzmaurice, *J. Phys. Chem. B* **1998**, *102*, 8379.
- [16] A. G. Dong, X. C. Ye, J. Chen, C. B. Murray, *Nano Lett.* **2011**, *11*, 1804.
- [17] A. Tao, P. Sinsersuksakul, P. Yang, *Nat. Nanotechnol.* **2007**, *2*, 435.
- [18] H.-W. Liang, X. Cao, F. Zhou, C.-H. Cui, W.-J. Zhang, S.-H. Yu, *Adv. Mater.* **2011**, *23*, 1467.
- [19] J. He, X.-M. Lin, H. Chan, L. Vuković, P. Král, H. M. Jaeger, *Nano Lett.* **2011**, *11*, 2430.
- [20] P. Yang, F. Kim, *ChemPhysChem* **2002**, *3*, 503.
- [21] A. R. Tao, J. Huang, P. Yang, *Acc. Chem. Res.* **2008**, *41*, 1662.
- [22] A. Tao, F. Kim, C. Hess, J. Goldberger, R. He, Y. Sun, Y. Xia, P. Yang, *Nano Lett.* **2003**, *3*, 1229.
- [23] D. Whang, S. Jin, Y. Wu, C. M. Lieber, *Nano Lett.* **2003**, *3*, 1255.
- [24] L. Mai, Y. Gu, C. Han, B. Hu, W. Chen, P. Zhang, L. Xu, W. Guo, Y. Dai, *Nano Lett.* **2009**, *9*, 826.
- [25] J.-W. Liu, J.-H. Zhu, C.-L. Zhang, H.-W. Liang, S.-H. Yu, *J. Am. Chem. Soc.* **2010**, *132*, 8945.
- [26] H. Feng, Y. Yang, Y. You, G. Li, J. Guo, T. Yu, Z. Shen, T. Wu, B. Xing, *Chem. Commun.* **2009**, 1984.
- [27] Z. Huo, C.-k. Tsung, W. Huang, X. Zhang, P. Yang, *Nano Lett.* **2008**, *8*, 2041.
- [28] X. Lu, M. S. Yavuz, H.-Y. Tuan, B. A. Korgel, Y. Xia, *J. Am. Chem. Soc.* **2008**, *130*, 8900.
- [29] C. Lee, X. Wei, J. W. Kysar, J. Hone, *Science* **2008**, *321*, 385.
- [30] N. Pazos-Pérez, D. Baranov, S. Irsen, M. Hilgendorff, L. M. Liz-Marzán, M. Giersig, *Langmuir* **2008**, *24*, 9855.
- [31] D. S. Hecht, L. Hu, G. Irvin, *Adv. Mater.* **2011**, *23*, 1482.
- [32] S. De, T. M. Higgins, P. E. Lyons, E. M. Doherty, P. N. Nirmalraj, W. J. Blau, J. J. Boland, J. N. Coleman, *ACS Nano* **2009**, *3*, 1767.
- [33] L. Hu, H. S. Kim, J.-Y. Lee, P. Peumans, Y. Cui, *ACS Nano* **2010**, *4*, 2955.
- [34] A. R. Rathmell, B. J. Wiley, *Adv. Mater.* **2011**, 4798.

Free-Standing Polymer–Nanoparticle Superlattice Sheets Self-Assembled at the Air–Liquid Interface

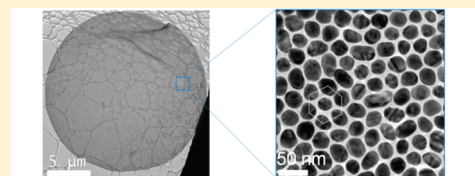
Yi Chen,[†] Jing Fu,[‡] Khee Chaw Ng,[†] Yue Tang,[†] and Wenlong Cheng^{*,†}

[†]Department of Chemical Engineering, Monash University, Clayton, Victoria 3800, Australia

[‡]Department of Mechanical and Aerospace Engineering, Room 120, Building 31, Monash University, Clayton, Victoria 3800, Australia

S Supporting Information

ABSTRACT: We report on a generic approach to use polymers as ligands to fabricate the free-standing, monolayered nanoparticle superlattice sheets based on drying-mediated, entropy-driven self-assembly at the air–liquid interface. Such superlattice nanosheets are the thinnest possible two-dimensional crystals whose structural features and functional properties can be adjusted by tailoring the sizes of their nanoparticle constituents. The monolayered superlattice nanosheets are highly stable under various conditions, transferable to any arbitrary substrates, and can be manufactured with focused ion beams. This demonstrates the potential to integrate the superlattice nanosheets into miniaturized optical and electronic devices.



Free-standing 2D Nanoparticle Crystal Sheet

The ability to produce nanoparticles (or “artificial atoms”) constitutes an exciting route to engineer structures with nanoscopic dimensions with high accuracy and to create novel properties that differ from those of their bulk counterparts. Substantial progress has been made in the past 20 years in the wet chemical synthesis of nanoparticles (particularly quantum dots and plasmonic and magnetic nanoparticles), which has led to a wide spectrum of applications, including electronics, diagnosis, drug delivery, *etc.* It is expected that the ability to assemble these elementary nanoparticles into well-defined assemblies (“artificial molecules”,^{1,2} “artificial polymers”,^{3,4} “supracrystals”^{5–10}) will further impact the way materials are synthesized and devices are fabricated. This has been supported by theoretical predictions, such as plasmon hybridization theory,¹¹ which testifies to the significance of grouping nanoparticles into well-defined architectures.

Recently, there has been emerging interest in building ultra-thin, free-standing nanoparticle sheets for a plethora of potential applications, including ultrafiltration¹² and optoelectronic devices.^{13–15} If the thickness of the nanoparticle sheets is at the single particle level and the packing order is hexagonal close-packed, then such nanosheets are the thinnest possible 2D nanoparticle crystals (or monolayered nanoparticle superlattice sheets)—the nanoscopic analogues of “graphene”. Representative success in constructing such superlattice nanosheets has been realized *via* the alkyl molecular ligands.^{13,14,16–20} The drying-mediated, entropy-driven self-assembly at air–liquid interfaces has been demonstrated to be a general approach to fabricate defect-free superlattice sheets with superior mechanical strength.¹⁹ In addition, multiple binary and ternary superlattice membranes have also been demonstrated recently by Murray and co-workers.^{13,14} Nevertheless, a potential drawback in alkyl-nanoparticle superlattice membranes is the limited molecular length that restricts the range for tailoring interparticle electro-magnetic coupling.

We recently successfully utilized DNA as a “dry ligand” under unusually low ionic strength and successfully obtained free-standing, monolayered DNA–nanoparticle superlattice sheets in a microhole-confined self-assembly process.^{21–23} The highly controllable molecular lengths of DNA ligands enable tailoring of both structural (interparticle spacings) and functional properties (plasmonic and mechanical) over a wide window. In particular, the edge-to-edge interparticle spacing for DNA-based monolayer superlattice sheets can be adjusted up to 20 nm—a greater size range than has been achieved with alkyl molecular ligands.²⁴

In this work, we extend previous success with alkyl- and bioligands to more general polymer ligands for the fabrication of free-standing superlattice sheets. Using polystyrene (PS)-capped nanoparticles as a model system, we demonstrate a generic methodology to assemble the monolayered polymer–nanoparticle superlattice sheets at the air–liquid interface. The self-assembly process is similar to the case of alkyl-capped nanoparticles, but longer polymer ligands enable wider tuning of interparticle spacing especially for large nanoparticles, which are important for plasmonic applications. Previously, polymers have been successfully used as ligands to stabilize nanoparticles either by direct synthesis^{25,26} or by a ligand-exchange procedure.²⁷ Such successes have led to ordered nanoparticle arrays self-assembled at solid substrates.^{26,28} In addition, polymers have also been used to template the assembly of nanoparticles into various structures;^{29–33} however, to the best of our knowledge, the use of generic polymers as ligands in drying-mediated assembly at the air–liquid interface has not been reported. With our approach, we obtained superlattice nanosheets as large as $\sim 15 \mu\text{m}$ in lateral dimensions with a thickness of $\sim 13 \text{ nm}$, corresponding to an

Received: July 9, 2011

Revised: September 26, 2011

Published: September 28, 2011

Table 1. Analytical Characteristics of PS-Capped AuNPs and Superlattice Sheets

entry ^a	PS-capped AuNPs					superlattice sheets		
	d_{core}^b (nm)	PS/Au % (wt %) ^c	grafting density ^c (chains/nm ²)	diameter of PS footprint ^c (nm)	calcd corona height ^d (nm)	softness ^e (χ)	edge-to-edge spacing ^b (nm)	deformation parameter ^e (λ)
13 nm PS-AuNPs	13.1 ± 1.9	26.6/73.4	0.77	1.29	18.4	2.8	2.5	0.7
26 nm PS-AuNPs	26.0 ± 4.5	19.8/80.2	1.03	1.11	20.4	1.6	2.1	0.6

^aThe ligands for all the nanoparticles were thiol-functionalized polystyrene ($M_n = 12,000$, $M_w/M_n = 1.09$, degree of polymerization = 115).

^bDetermined by TEM and statistical analysis through the free software ImageJ. ^cEstimated from data of TEM and TGA. ^dCalculated by using de Gennes's model, which assumes a polymer brush constrained inside a cylindrical tube of diameter d (footprint of PS chain) reported in ref 33.

^eThe dimensionless quantity χ and deformation parameter λ were calculated by applying the entropic spring model reported in ref 10.

aspect ratio (lateral size/thickness) of >1000. Both internal structures (particle size and interparticle spacing) and collective properties (plasmonic coupling) are tunable. The monolayered polymer–nanoparticle sheets are highly stable under various conditions, transferable to any arbitrary substrates, and can be manufactured with focused ion beams. This demonstrates the potential to integrate the superlattice nanosheets into miniaturized optical and electronic devices.

We began with the synthesis of high-quality polystyrene-capped gold nanoparticles (PS-AuNPs) with two distinct sizes: 13.1 ± 1.9 nm and 26.0 ± 4.5 nm (Figure S1, Supporting Information), based on a modified grafting approach reported by others.²⁸ In a typical procedure, the “bare” aqueous gold nanoparticles (citrate-capped AuNPs) were synthesized via Frens' approach. Then, thiolated polystyrene with a molecular weight of 12 kDa in chloroform was added to a nanoparticle solution with vigorous agitation. Thiolated polystyrene acts as both a phase-transfer reagent and capping agent *via* a robust covalent linkage between the polymer and the gold surface.²⁶

Stabilization of nanoparticles by thiolated polystyrene was confirmed by measurements of localized surface plasmon resonance (LSPR) and FT-IR. In a control experiment, 13-nm citrate-stabilized AuNPs aggregated in THF, as evidenced by a color change from ruby red to dark purple-blue and an apparent coupling LSPR peak at ~ 610 nm (Figure S2, Supporting Information). Consistent phenomena were observed for 26-nm AuNPs. In contrast, in the presence of thiolated polystyrene, the 13- and 26-nm AuNPs exhibit single LSPR bands at 525 and 533 nm, respectively, indicating no aggregation. We further used transmission FT-IR spectroscopy to characterize polystyrene-capped AuNPs (Figure S3, Supporting Information). The C=O carbonyl group valence vibrational band of citrate at 1645 cm^{-1} disappeared after the PS capping. In addition, characteristic C–C stretching vibrations bands (1492 and 1452 cm^{-1}) and C–H stretching vibrations bands (2849 , 2922 , and 3025 cm^{-1}) were observed even after washing samples multiple times to completely remove nonbonded ligands. Thus, the above results demonstrate the effective stabilization of nanoparticles by thiolated PS.

We further measured the grafting number densities of polystyrene ligands via thermogravimetric analysis (TGA). The typical TGA curve is shown in Figure S4. The weight fraction analysis led to a high grafting density of approximately 1 ligand/nm² (Table 1), which is comparable with the grafting densities reported by A. M. Ritcey et al.²⁸

To fabricate free-standing monolayered superlattice nanosheets, polystyrene-capped AuNPs with diameters of 26 nm were concentrated and finally dispersed in 0.5 mL of chloroform (80 nM , 8.5 mg mL^{-1}); then one drop ($\sim 4\text{--}6\ \mu\text{L}$) of the

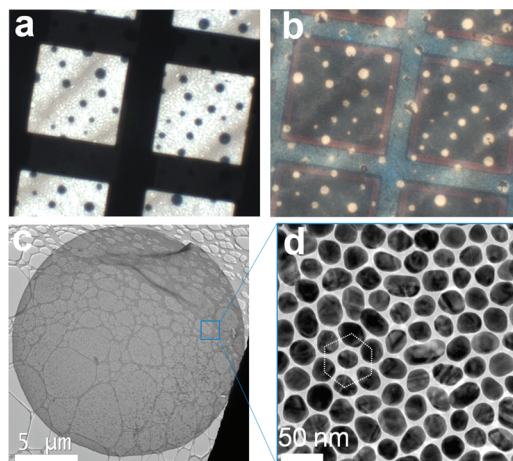


Figure 1. Low-magnification images of free-standing superlattice sheets formed using 26.0 nm PS-AuNPs in $50 \times 50\ \mu\text{m}$ grids, which were acquired under (a) transmission and (b) reflection mode by microscope. (c) TEM image of a monolayer sheet self-assembled from 26.0 nm PS-AuNPs with a diameter of $\sim 15\ \mu\text{m}$; the crumpled area indicates the flexibility of the sheet. (d) Higher-magnification TEM image of part c, showing that nanoparticles are hexagonally packed yet well spaced.

solution was carefully spread onto the surface of Milli-Q water in a plastic Petri dish. The droplet quickly spread over the water surface in less than 1 s. The dish was then covered to prevent fluid flows and solvent fluctuations. The evaporation-mediated assembly of hydrophobic PS-AuNPs led to the formation of thin particle sheets floating at the water surface. After 5 min, a gold-colored reflection was observed on the water surface, which indicated complete solidification. These sheets were circular-shaped and readily observable under an optical microscope in both transmission and reflection modes (Figure 1a and b). Similar to the kinetically driven interfacial self-assembly of AuNPs reported earlier,¹⁶ we also observed polymer-AuNP nanosheets were facilitated by the rapid evaporation, followed by nucleation and growth into 2D crystals at the monolayer level (Figure 1c and d).

2D PS-AuNP nanosheets are robust and flexible and are transferable to a variety of substrates without deterioration. The transfer can typically be achieved by either Langmuir–Blodgett or Langmuir–Schaeffer techniques. Notably, neither transfer process caused any rupturing or deterioration of the nanosheets (Figure 1c and Figure S5 of the Supporting Information). High magnification TEM micrographs show that the superlattice sheets consisted of monolayered AuNPs with hexagonal packing symmetry (Figure 1d). Unlike most previously reported

superlattices which usually formed from NPs with small diameters,^{24,29–32} our technique achieved superlattice sheets with much larger particle size. Although polymer-stabilized AuNPs with comparable sizes have been previously used to form arrays on a solid support,^{26,34–36} the success in forming large-scale, free-standing superlattice sheets has not yet been reported. We believe that it is possible to use even bigger particles when higher molecular weight polystyrene is used. When particle sizes were changed, the structural features, including monolayer and hexagonally ordered packing, were maintained (Figure 2).

We investigated the influence of particle size on the PS ligand compression during the self-assembly process. With the same ligands capping two different particles (13 and 26 nm), we fabricated two superlattice nanosheets and measured the edge-to-edge interparticle spacing (Figure 2 and Figure S1 of the Supporting Information). The former gave a spacing of ~ 2.5 nm, whereas the latter gave a spacing of ~ 2.1 nm. This indicates that the polystyrene ligands experienced greater compression in the lateral directions for larger nanoparticles. Notably, compared to those 2D particle arrays formed on a solid support,²⁸ the spacing in our system is much smaller. This may be due to the absence of particle–substrate interactions at the air–water interface, whereas the strong

particle–substrate interaction in Ritcey's report may prevent lateral particle collision. Similar small spacing was also found in the corresponding three-dimensional arrays (Supporting Information, section S3)

We also measured the vertical compression by measuring the thickness of the superlattice nanosheets with an atomic force microscope (AFM) after transferring the sheets onto a silicon wafer. A typical AFM image and the corresponding line scan are shown in Figure 3. Evidently, the monolayered structure is in agreement with the TEM imaging. After subtracting the nanoparticle diameters, the compressed polystyrene thickness in

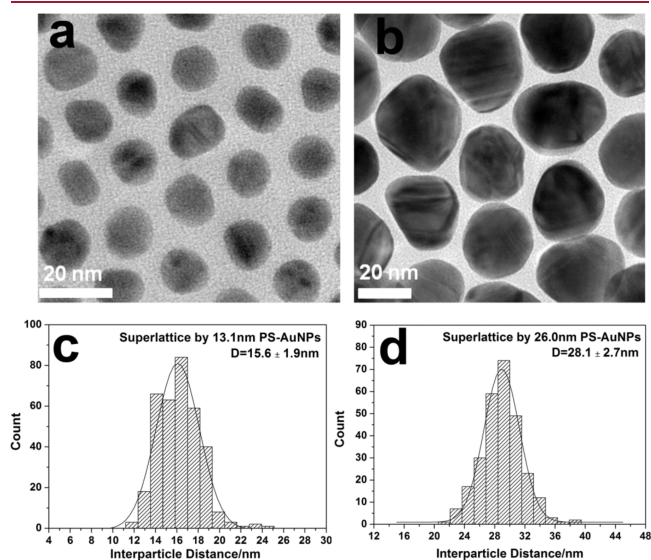


Figure 2. TEM characterization of different superlattice sheets formed using (a) 13.1 nm and (b) 26.0 nm PS-AuNPs; parts c and d are the corresponding histograms of interparticle distance analyzed from the TEM images. Curves in both plots represent Gaussian fits.

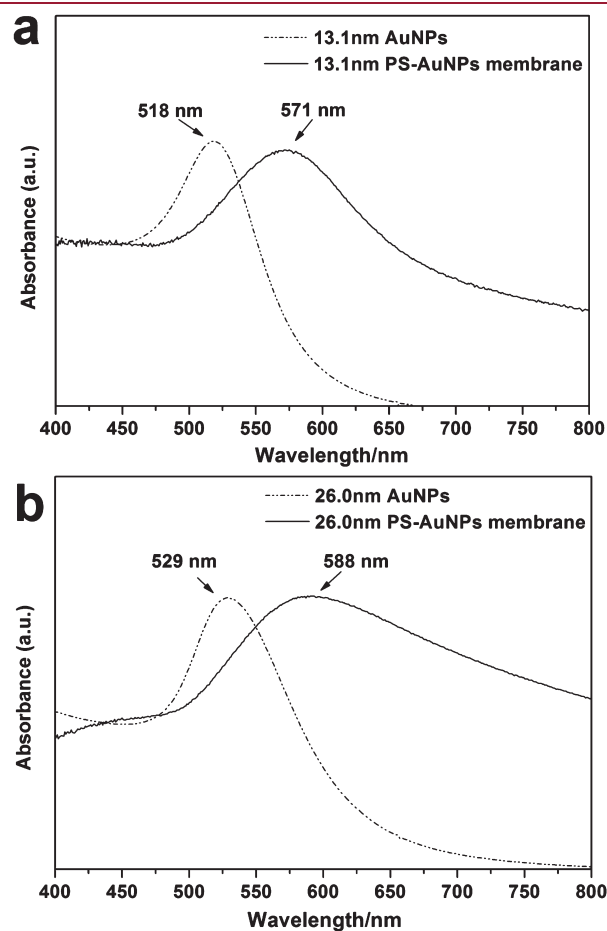


Figure 4. UV–vis spectra of AuNPs dispersed in water and superlattice sheets constructed from (a) 13.1 nm PS-AuNPs and (b) 26.0 nm PS-AuNPs.

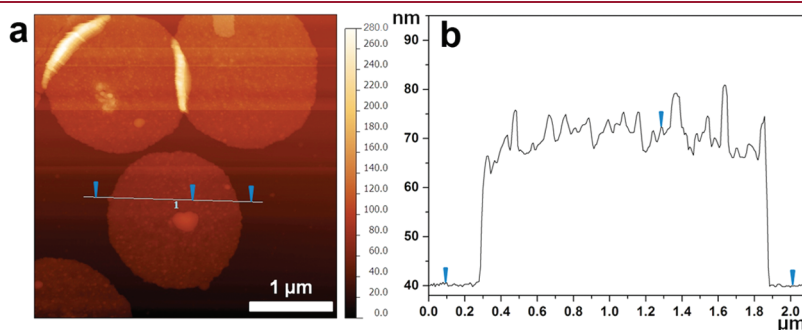


Figure 3. Representative AFM height image and the corresponding cross-sectional profile for monolayer superlattice sheets constructed from 26 nm PS-AuNPs. The measurements were repeated ten times, and the average height is 32.1 ± 2.3 nm.

vertical directions can be estimated to be 3.5 and 3.1 nm for 13 and 26 nm AuNPs, respectively.

The above experiments show that the vertical polystyrene thickness in the superlattice sheet is about 3-fold greater than the lateral thickness. Two reasons could account for this: (1) nanoparticles are trapped at the air–water interface to form monolayers, and the core–core van der Waals attraction in the late stage of solvent drying leads to the strong lateral compression;¹² (2) PS ligands may be pushed above and below the monolayers during the drying-mediated self-assembly.

We further investigated plasmonic properties of PS-AuNPs superlattice nanosheets using a microscope UV–visible spectrometer in transmission mode (Figure 4). The superlattice sheets could be clearly observed under a microscope with both transmission and reflection modes (Figure 1a and b), exhibiting blue and yellow colors, respectively. This is due to the unique absorption and scattering effects of the superlattice nanosheets due to the localized surface plasmon resonance (LSPR). Compared with the LSPR bands of dispersed AuNPs (Figure 4), the LSPR bands for the nanosheets shift significantly to red, suggesting strong interparticle coupling for both 13 and 26 nm AuNPs. The detailed coupling mechanism remains unclear and is currently under investigation. But the LSPR studies demonstrate that the plasmonic properties of superlattice nanosheets are customizable simply by adjusting particle size.³⁷

The PS-AuNP superlattice sheets are highly stable under electron irradiation and highly processable by focused ion beam (FIB) lithography. Particularly, we have transferred the superlattice onto silicon wafer and cut the sheets into rectangular shapes (Figure S7, Supporting Information), which suggested a facile way to manufacture the superlattice sheets into arbitrary shapes for optoelectronic applications. In conjunction with programmable plasmonic coupling, our methodology is potentially enabling in the integration of free-standing, monolayered sheets into future optoelectronic devices.

In summary, we report a general and facile method to construct free-standing nanoparticle superlattice sheets using generic polymers as ligands through drying-mediated self-assembly at the air–liquid interface. The sheet thicknesses are at monolayer level, yet they are mechanically robust and can be highly stable under various conditions, transferable to any arbitrary substrates, and processable with FIB cutting. The sheets also exhibit strong plasmonic coupling resonances which are adjustable simply by varying particle sizes. We believe this approach offers great modularity and versatility, and can potentially be extended to polymer-magnetic or quantum dot nanosheets. Thus, this methodology may lead to applications in substrate-free optoelectronic devices, high-density data storage, new classes of biosensors, and smart ultrafiltration membranes.

■ ASSOCIATED CONTENT

S Supporting Information. Additional details regarding the experimental and characterization methods. This material is available free of charge via the Internet at <http://pubs.acs.org>.

■ AUTHOR INFORMATION

Corresponding Author

[REDACTED]. Website: <http://users.monash.edu.au/~wenlong/>.

■ ACKNOWLEDGMENT

This work is financially supported by the New Staff Member Research Fund (2437404). The authors also acknowledge the use of facilities in the Monash Centre for Nanofabrication by the program of MCN technology fellows, and the use of the SAXS/WAXS beamline at the Australian Synchrotron. Y.C. acknowledges the graduate student scholarship (MGS & IPRS) from Monash University. We also acknowledge Mr. Michael J. Campolongo for editing the English of this manuscript.

■ REFERENCES

- Alivisatos, A. P.; Johnsson, K. P.; Peng, X.; Wilson, T. E.; Loweth, C. J.; Bruchez, M. P., Jr.; Schultz, P. G. *Nature* **1996**, *382*, 609–611.
- Maye, M. M.; Kumara, M. T.; Nykypanchuk, D.; Sherman, W. B.; Gang, O. *Nat. Nanotechnol.* **2010**, *5*, 116–120.
- Nie, Z.; Fava, D.; Kumacheva, E.; Zou, S.; Walker, G. C.; Rubinstein, M. *Nat. Mater.* **2007**, *6*, 609–14.
- Liu, K.; Nie, Z.; Zhao, N.; Li, W.; Rubinstein, M.; Kumacheva, E. *Science* **2010**, *329*, 197–200.
- Pileni, M.-P. *Acc. Chem. Res.* **2007**, *40*, 685–693.
- Heitsch, A. T.; Patel, R. N.; Goodfellow, B. W.; Smilgies, D.-M.; Korgel, B. A. *J. Phys. Chem. C* **2010**, *114*, 14427–14432.
- Jones, M. R.; Macfarlane, R. J.; Lee, B.; Zhang, J.; Young, K. L.; Senesi, A. J.; Mirkin, C. A. *Nat. Mater.* **2010**, *9*, 913–917.
- Park, S. Y.; Lytton-Jean, A. K. R.; Lee, B.; Weigand, S.; Schatz, G. C.; Mirkin, C. A. *Nature* **2008**, *451*, 553–556.
- Nykypanchuk, D.; Maye, M. M.; van der Lelie, D.; Gang, O. *Nature* **2008**, *451*, 549–552.
- Cheng, W. L.; Hartman, M. R.; Smilgies, D.-M.; Long, R.; Campolongo, M. J.; Li, R.; Sekar, K.; Hui, C.-Y.; Luo, D. *Angew. Chem., Int. Ed.* **2010**, *49*, 380–384.
- Prodan, E.; Radloff, C.; Halas, N. J.; Nordlander, P. *Science* **2003**, *302*, 419–22.
- He, J.; Lin, X.-M.; Chan, H.; Vuković, L.; Král, P.; Jaeger, H. M. *Nano Lett.* **2011**, *11*, 2430–2435.
- Dong, A. G.; Chen, J.; Vora, P. M.; Kikkawa, J. M.; Murray, C. B. *Nature* **2010**, *466*, 474–477.
- Dong, A. G.; Ye, X. C.; Chen, J.; Murray, C. B. *Nano Lett.* **2011**, *11*, 1804–1809.
- Liao, J.; Zhou, Y.; Huang, C.; Wang, Y.; Peng, L. *Small* **2011**, *7*, 583–587.
- Bigioni, T. P.; Lin, X. M.; Nguyen, T. T.; Corwin, E. L.; Witten, T. A.; Jaeger, H. M. *Nat. Mater.* **2006**, *5*, 265–270.
- Cheng, W. L.; Dong, S.; Wang, E. *Langmuir* **2003**, *19*, 9434–9439.
- Collier, C. P.; Saykally, R. J.; Shiang, J. J.; Henrichs, S. E.; Heath, J. R. *Science* **1997**, *277*, 1978–1981.
- Mueggenburg, K. E.; Lin, X. M.; Goldsmith, R. H.; Jaeger, H. M. *Nat. Mater.* **2007**, *6*, 656–60.
- Tan, S. J.; Campolongo, M. J.; Luo, D.; Cheng, W. L. *Nat. Nanotechnol.* **2011**, *6*, 268–276.
- Cheng, W. L.; Campolongo, M. J.; Cha, J. J.; Tan, S. J.; Umbach, C. C.; Muller, D. A.; Luo, D. *Nat. Mater.* **2009**, *8*, 519–525.
- Cheng, W. L.; Campolongo, M. J.; Tan, S. J.; Luo, D. *Nano Today* **2009**, *4*, 482–493.
- Long, R.; Hui, C. Y.; Cheng, W. L.; Campolongo, M. J.; Luo, D. *Nanoscale Res. Lett.* **2010**, *5*, 1236–1239.
- Martin, J. E.; Wilcoxon, J. P.; Odinek, J.; Provencio, P. J. *Phys. Chem. B* **2000**, *104*, 9475–9486.
- Corbierre, M. K.; Cameron, N. S.; Sutton, M.; Mochrie, S. G. J.; Lurio, L. B.; Rühm, A.; Lennox, R. B. *J. Am. Chem. Soc.* **2001**, *123*, 10411–10412.
- Corbierre, M. K.; Cameron, N. S.; Lennox, R. B. *Langmuir* **2004**, *20*, 2867–2873.
- Rucareanu, S.; Maccarini, M.; Shepherd, J. L.; Lennox, R. B. *J. Mater. Chem.* **2008**, *18*, 5830.

- (28) Yockell-Lelièvre, H.; Desbiens, J.; Ritcey, A. M. *Langmuir* **2007**, *23*, 2843–2850.
- (29) Balazs, A. C.; Emrick, T.; Russell, T. P. *Science* **2006**, *314*, 1107–10.
- (30) Böker, A.; He, J.; Emrick, T.; Russell, T. P. *Soft Matter* **2007**, *3*, 1231.
- (31) Genson, K. L.; Holzmueller, J.; Jiang, C.; Xu, J.; Gibson, J. D.; Zubarev, E. R.; Tsukruk, V. V. *Langmuir* **2006**, *22*, 7011–7015.
- (32) Jiang, C.; Markutsya, S.; Pikus, Y.; Tsukruk, V. V. *Nat. Mater.* **2004**, *3*, 721–728.
- (33) Lopes, W. A.; Jaeger, H. M. *Nature* **2001**, *414*, 735–738.
- (34) Gandubert, V. J.; Lennox, R. B. *Langmuir* **2005**, *21*, 6532–6539.
- (35) Dorris, A.; Rucareanu, S.; Reven, L.; Barrett, C. J.; Lennox, R. B. *Langmuir* **2008**, *24*, 2532–2538.
- (36) Milette, J.; Toader, V.; Reven, L.; Lennox, R. B. *J. Mater. Chem.* **2011**, *21*, 9043–9050.
- (37) Yockell-Lelievre, H.; Gingras, D.; Vallee, R.; Ritcey, A. M. *J. Phys. Chem. C* **2009**, *113*, 21293–21302.



DNA-based plasmonic nanoarchitectures: from structural design to emerging applications

Yi Chen^{1,2} and Wenlong Cheng^{1,2*}

Plasmonic nanoarchitectures refer to the well-defined groupings of elementary metallic nanoparticle building blocks. Such nanostructures have a plethora of technical applications in diagnostics, energy-harvesting, and nanophotonic circuits, to name a few. Nevertheless, it remains challenging to construct plasmonic nanoarchitectures at will inexpensively. Bottom-up self-assembly is promising to overcome these limitations, but such methods often produce defects and low-yields. For these purposes, DNA has emerged as a powerful nanomaterial beyond its genetic function in biology to either program or template synthesis of plasmonic nanostructures, or act as a ligand to mediate large-area self-assembly. In conjunction with top-down lithography, DNA-based strategies can afford excellent control over internal and overall structures of plasmonic nanoarchitectures. In this review, we outline the representative methodologies for building various well-defined plasmonic nanoarchitectures and cover their recent exciting applications.

© 2012 Wiley Periodicals, Inc.

How to cite this article:

WIREs Nanomed Nanobiotechnol 2012, 4:587–604. doi: 10.1002/wnan.1184

INTRODUCTION

It is an essential task in modern nanoscience and nanotechnology to understand light–matter interactions at the nanoscale as well as to develop the capability to precisely manipulate light by nanomaterials. Construction of well-defined plasmonic nanoarchitectures from elementary metallic nanoparticle building blocks constitutes an exciting route to control light propagation below the diffraction limit. Such plasmonic structures can precisely concentrate, guide and switch light at the nanoscale,^{1,2} which is leading to the development of next-generation technologies for a broad spectrum of applications, such as in miniaturized optical² and electronic devices,^{3,4} sensors⁵ and photonic circuits,⁶ and medical diagnostics and therapeutics^{7,8}

Thanks to the worldwide efforts in developing synthetic approaches with wet chemical techniques,

a wide range of recipes are available to control the key morphological parameters of metallic nanoparticles.^{9–14} In general, a particle's specific size and shape produces a unique optical signature, allowing it to serve as 'artificial plasmonic atom'.¹⁵ The following task, then, is to find an efficient way to group these artificial atoms into well-defined plasmonic architectures including vectorial (or directional) grouping of finite numbers of nanoparticle,^{16,17} one-dimensional regularly-spaced nanoparticle chains,^{18,19} two-dimensional ordered arrays^{20–22} and three-dimensional ordered nanoparticle assemblies,^{23–28} which we term in this review 'plasmonic molecules', 'plasmonic polymers', 'plasmonic sheets', and 'plasmonic crystals', respectively. The recently developed plasmon hybridization theory²⁹ justifies the need to construct plasmonic nanoarchitectures to substantially expand the scope of plasmonics to spur various technical applications.³⁰

Nevertheless, it is nontrivial to rationally group nanoparticles together due to complex nanoscale forces at different spatial and temporal scales. Unless precise control can be exercised over these forces, particularly to achieve high fidelity of vectorial

*Correspondence to: [REDACTED]

¹Department of Chemical Engineering, Monash University, Clayton, Victoria, Australia

²The Melbourne Centre for Nanofabrication, Clayton, Victoria, Australia

bonding interactions among particles, a vast variety of plasmonic nanoarchitectures with arbitrary design will never be realized. Numerous attempts have been made by using physical methods (optical, electrical, magnetic, mechanical), chemical methods (small molecule, polymer), and biological approaches (peptide, protein, DNA).³¹ Among all these strategies, DNA turns out to be the most promising candidate to manipulate nanoparticles at will due to its many inherent advantages, such as (1) the unique Watson–Crick base-pairing forces between complementary strands that allow for adjusting interparticle potentials with high accuracy; (2) DNA length that is finely and widely tunable from nanoscale to microscale with available chemical and biological toolkits; (3) emerging structural DNA nanotechnologies that allow for facile control over topology and mechanics of DNA motifs, enabling superior accuracy in templated assembly of plasmonic nanoparticles. These unique characteristics enable DNA to be engineered either into various topological structures (structural engineering) or with desired sequences to optimize hybridization forces (sequence engineering), allowing for facile programmed, templated, or ligand-based assembly of plasmonic nanoparticles into well-defined nanoarchitectures. To date, a number of novel plasmonic nanostructures, including ‘plasmonic molecules’, ‘plasmonic polymers’, ‘plasmonic sheets’, and ‘plasmonic crystals’ have been developed.¹⁵ In this sense, DNA has gone beyond its traditional role as genetic information carrier, and has become a powerful nanomaterial to manipulate materials synthesis at the nanoscale with high accuracy.

A few excellent reviews have discussed this exciting topic from different perspectives. In this article, we review from a methodological perspective the various viable approaches for building structurally well-defined plasmonic nanoarchitectures and discuss their pros and cons. In addition, we cover some emerging applications of these plasmonic nanoarchitectures as well as discuss opportunities and challenges.

METHODOLOGIES

We thoroughly summarize viable strategies developed for building DNA-based plasmonic nanoarchitectures (Table 1). These methods and techniques can be categorized in three types, namely DNA-programmed self-assembly, DNA-templated self-assembly, and unconventional DNA technologies and nanopatterning.

DNA-PROGRAMMED SELF-ASSEMBLY

One of the unique features of DNA molecules is the specific Watson–Crick base pairing interactions between complementary sequences. These forces can be used to regulate interparticle potentials (enthalpic interactions) between adjacent nanoparticles and, therefore, program assembly of pre-synthesized nanoparticles. In two seminal papers, Alivisatos and Mirkin reported their initial results in 1996: the former focused on grouping finite-number nanoparticles together,¹⁶ whereas, the later focused on constructing three-dimensional arrays.⁴³ The initial reports outlined the concepts of DNA-programmed materials synthesis in which multicomponent assemblies could be arranged in space on the basis of rational design of DNA linkers and conjugates. Numerous techniques and methods, inspired by these pioneering approaches, have since been developed.

Plasmonic Structures Derived from Mono-DNA Conjugates

To precisely define the spatial positions of nanoparticles in plasmonic architectures, it is often necessary to obtain high-purity mono-DNA conjugates (i.e., one oligonucleotide per particle).¹⁶ In the initial paper, Alivisatos et al. obtained mono-DNA conjugates which led to the assembly of homodimeric and homotrimeric nanostructures that are not attainable with multi-DNA conjugates (i.e., multiple oligonucleotides per particle). However, this strategy has been limited to small nanoparticles (< 10 nm) and typically leads to mixtures that need separation by electrophoretic methods. In their subsequent work, they improved the design and obtained hetero-dimeric/trimeric plasmonic nanostructures³² (Figure 1(a)). Briefly, gold nanoparticles (AuNPs) with two different diameters (5 and 10 nm) were used as building blocks and three different strategies were tested. The first involved the use of two complementary strands; the second involved the use of three DNA strands in which one of them act as a linker; the third involved multiple DNA strands and post-hybridization attachment of nanoparticles. All the desired products were purified by gel electrophoresis on 3–4% agarose gel. Dimer and trimer plasmonic molecules were formed by all three strategies as confirmed by transmission electron microscope (TEM). However, the resulting assemblies were not structurally rigid, with deviations in the interparticle spacings and orientations because of the flexibility of DNA molecules. This flexibility resulted in different spatial arrangements of the AuNPs ranging from collinear to triangular distributions. The relative

TABLE 1 | Summary on Methodologies for Constructing DNA-Based Plasmonic Nanoarchitectures

Methodologies	Category of Architectures	Building Blocks	Conjugation Method	Specific Structures	References		
DNA-Programmed Self-Assembly	'Plasmonic Molecules'	AuNPs (5/10nm)	Mono-DNA Conjugation	Dimer/Trimer	16,32		
		AuNPs (5–20 nm)	Mono-DNA Conjugation	Pyramids	33		
		AuNPs (13/30/60 nm)	Site-Specific DNA Conjugation	Cat Paw/Satellite /Dendrimer	34		
		Au/Ag core-shell (20 nm)	Site-Specific DNA Conjugation	Nanodumbbells	35		
		AuNP/AgNP & nanoshell (11–75 nm)	Site-Specific DNA Conjugation	Heteropentamer/Janus Nanoclusters	17,36,37		
		Au Nanorods and Spheres	Site-Specific DNA Conjugation	Heteromers	38		
		AuNPs (5–18 nm)	PCR/RCA	Dimer to multimer	39–41		
		AuNP (4.4 nm)	Nonspecific Electrostatic forces	Linear Chains	42		
		AuNP (11–15 nm)	Multi-DNA conjugation	BCC/FCC superlattices	17,26–28,43		
		Anisotropic NPs (14–140 nm)	Multi-DNA conjugation	superlattices	25		
DNA-templated Self-Assembly	'Plasmonic Molecules'	AuNPs (5–20 nm)	Multi-DNA conjugation	Multiple Lattice Structures	44,45		
		AuNPs (5/15 nm)	Cyclic DNA frames	Triangles/squares	46		
		Au/AgNPs (5–20 nm)	DNA Origami	Dimers/Trimers	47,48		
		AuNPs & AuNRs	DNA Origami	Heter-dimers	49		
		AuNPs (10/15 nm)	DNA Nanotube	Nanopeapod	50		
		AuNPs (5–15 nm)	DNA tile/origami	Stacked Rings/Spirals	51–53		
		AuNPs (6.2 nm)	DNA tiles	2D superlattices	54–56		
		AuNPs (5 nm)	Origami/ lithography	2D arrays	57		
		Unconventional DNA Technologies and Nanopatterning	'Plasmonic Polymers'	AuNPs (40 nm)	Printing	Plasmonic Chains	58
				AuNPs (13 nm)	Dry-ligand combined with top-down	Large-area free-standing superlattices	20,59
AuNPs (13 nm)	Dry-ligand /lithography			Chains/corrals/ sheets/crystals	60		

AuNPs, Au nanoparticles; AuNRs, Au nanorods; ss/ds-DNA, single strand/double strand-DNA; BCC, body-centered cubic; FCC, face-centered cubic; PCR, polymerase chain reaction; RCA, rolling circle amplification.

spatial distances between AuNPs was controllable by adjusting the lengths of double-stranded DNA, and the interparticle spacings of 1.2, 1.5, and 5.8 nm were reported for the sequences with 18, 28, and 38 bp, respectively. The yields of designed plasmonic nanostructures are highly dependent on the quality of plasmonic nanoparticle mono-DNA conjugates which requires purification by gel electrophoresis and anion-exchange high-performance liquid chromatography (HPLC) purification methods.^{61,62}

Vectorial control over nanoparticle placement by DNA programming is possible. In one excellent demonstration, nanoparticles could be grouped with high spatial control, leading to the formation of plasmonic tetrahedral molecules.³³ In this work, dsDNA was used as a scaffold to control the placement of 5-nm-diameter AuNPs. Four different types of AuNPs could be precisely positioned to each tip of the DNA tetrahedron. Gel electrophoresis was used to purify the tetrahedral assemblies which were further confirmed by both TEM and small-angle X-ray scattering (SAXS) characterization. Remarkably, this method could be used to produce chiral plasmonic structures with two different configurations of the constituent particles (Figure 1(b)). The authors argued that their system could potentially act as a more sensitive plasmon ruler than simple dimeric

structures because the conformation changes in such a multiparticle assembly could create a symmetry breaking that is apparent in the optical spectral measurements.

Plasmonic Structures Derived from Site-Specific DNA Conjugates

Site-specific DNA conjugates refer to DNA-nanoparticle conjugates with multiple DNA strands attached to only specific sites on nanoparticle surfaces. Such conjugates can lead to the formation of anisotropic plasmonic assemblies. The asymmetric DNA-functionalization of AuNPs could be achieved by using magnetic microparticles as geometric restriction templates.³⁴ With this strategy, AuNPs could be anisotropically functionalized with two different oligonucleotide sequences. This offers the divalent linking capability of the resulting AuNPs, allowing for the design and programmable assembly of discrete nanoparticle heterostructures, such as satellite, cat paw, and dendrimer-like assemblies (Figure 1(c)). Nam et al. used the similar method to synthesize SERS-active Au–Ag core-shell nanodumbbells.³⁵ By virtue of magnetic particle-assisted separation, a high yield of anisotropically functionalized nanoparticle conjugate was achieved, consequently, led to large

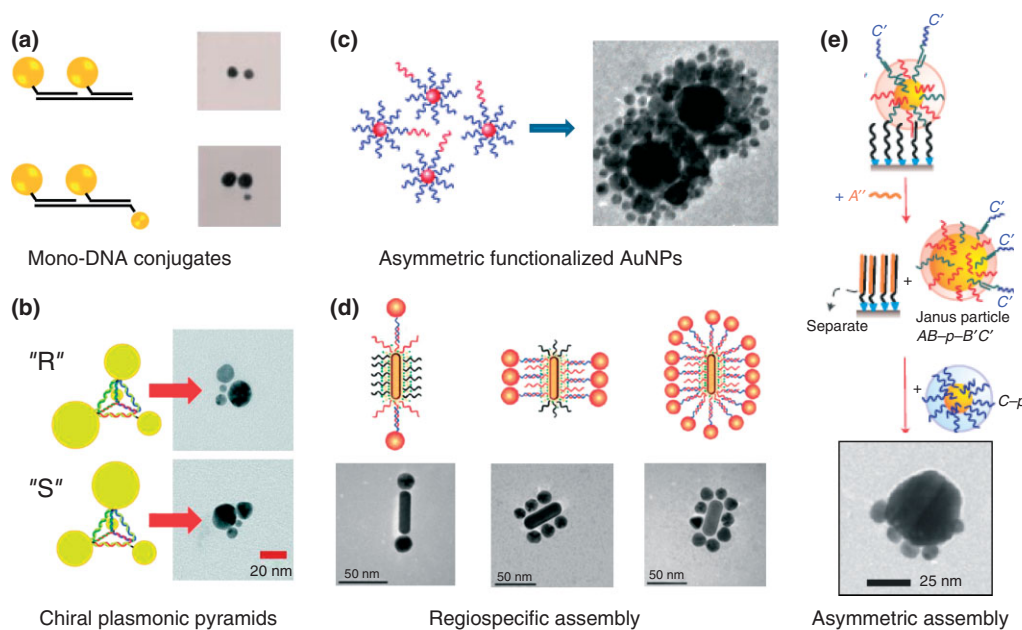


FIGURE 1 | Plasmonic nanostructures derived from mono-DNA and site-specific DNA conjugates. (a) Schematic and TEM images for 10 nm AuNPs homodimer and 5/10/10 nm AuNPs heterotrimer constructed from mono-DNA conjugates. (b) Chiral nanostructures built by using DNA-AuNPs monoconjugates with four different sizes at DNA pyramids tips. (c) Dendrimer-like nanostructures formed by asymmetric functionalized AuNPs. (d) End, side, and satellite nanostructures formed by AuNPs and Au nanorods after selective modification using DNA. (e) Stepwise surface modification of AuNPs and formation of two-faced cluster with anisotropic nanostructures.

quantities of dimeric AuNPs upon DNA hybridization. Furthermore, silver shells could be specifically deposited onto AuNP cores, forming Au–Ag core–shell nanodumbbells. The interparticle spacing could be controlled by adjusting Ag shell thickness. By fine-tuning this spacing, a detection limit of single molecule could be achieved.

In a different approach, Kotov et al. reported complex assemblies from nanoparticles and nanorods based on selective modification of gold nanorods (AuNRs) with DNA. Three types of regiospecific assemblies denoted as *End*, *Side*, and *Satellite* isomers were achieved with a yield of exceeding 85%³⁸ (Figure 1(d)). All three types of nanostructures had an AuNR in the center and AuNPs sentinels at different positions that were controlled by regiospecific modification of AuNRs. Multiple experimental techniques were used to verify the various structural features, uniformity, and stability of the designed plasmonic assemblies. These plasmonic structures could serve as label-free intracellular probes to acquire local organelle environment information within live cells.

Alternatively, Gang et al. reported a stepwise assembly approach to synthesize AuNP dimers from anisotropically functionalized AuNPs.³⁶ In this approach, DNA-encoded nanoparticles were assembled onto a solid support in a stepwise manner. The steps of repeated assembly and disassembly at a surface imparted AuNPs with anisotropy, consequently generating remarkably high yields of well-defined dimer clusters and Janus (two-faced) nanoparticles (Figure 1(e)). The authors claimed that the stepwise approach could give higher yield of dimers than the conventional solution-based strategies.

Plasmonic Structures Derived from Multi-DNA Conjugates

Multi-DNA conjugates refer to DNA-nanoparticle conjugates with multiple DNA strands associated with one particle. Programming self-assembly of multi-DNA conjugates often leads to three-dimensional assemblies, which, however, requires careful control over DNA sequences, number density, ionic strength, and hybridization temperatures. Initial attempts only led to aggregates with limited order,⁴³ with observable red–blue color changes due to plasmonic coupling. Interestingly, the formation of particles aggregates were reversible, which could be controlled by DNA sequence and length, solvent, and temperature along with supporting electrolyte concentration. This finding was rapidly developed into a powerful

diagnostic tool for detections of DNA, RNA, and protein. Furthermore, the success in single-component systems could be extended to binary nanoparticle systems.⁶³

More recently, the quality of 3D crystals from multi-DNA conjugates was significantly improved. In the same issue of Nature journal, two independent groups reported their 3D nanoparticle crystals from multi-DNA conjugates by programmed temperature control.^{26,27} Both groups characterized the formation of nanoparticle crystals by synchrotron-based small-angle X-ray scattering (SAXS) and revealed the crystallization mechanism during each heating and cooling cycle. The results show that it is possible to achieve two distinct crystalline states [i.e., face-centered-cubic (FCC) or body-centered-cubic lattices (BCC)] by choosing different DNA sequences even with the same type of nanoparticle²⁶ (Figure 2(a)). Nanoparticles could be assembled through a single DNA linker that gave rise to equal binding affinities between particles, resulting in a close-packed FCC structure; alternatively, nanoparticles could be assembled through two different DNA linkers, leading to a binary system which favored the less close-packed BCC structure. These results demonstrated the power of DNA in regulating lattice structures of nanoparticle crystals.

The concept of optimizing crystallization of multi-DNA conjugates by precise temperature control could also be extended to anisotropic building blocks such as gold nanorods, rhombic dodecahedra and octahedral nanoparticles. It was found that particle shape had a strong influence on the superlattice dimensionality, crystallographic symmetry and phase of DNA-functionalized nanoparticles.²⁵ One-, two- and three-dimensional structures were observed from anisotropic particles but the similar structures could not be made through the assembly of spherical particles. For example, AuNRs formed predominantly into 2D sheets with hexagonal symmetry in most samples investigated (Figure 2(b)). They argued that this was due to the preferred base-pairing interactions perpendicular to their long axis to maximize the hybridization events.

Furthermore, a diverse array of 3D nanoparticle superlattices were thoroughly investigated from different DNA linkers and particles with various sizes.⁴⁴ Six basic design rules were formulated for regulating crystal structures, including crystallographic symmetry, and interparticle distances. In a recent work, the library of achievable DNA-programmed 3D superlattices was extended to new lattice structures by using hollow DNA nanostructures as 3D spacers⁴⁵ (Figure 2(c)). The unique hollow DNA structures

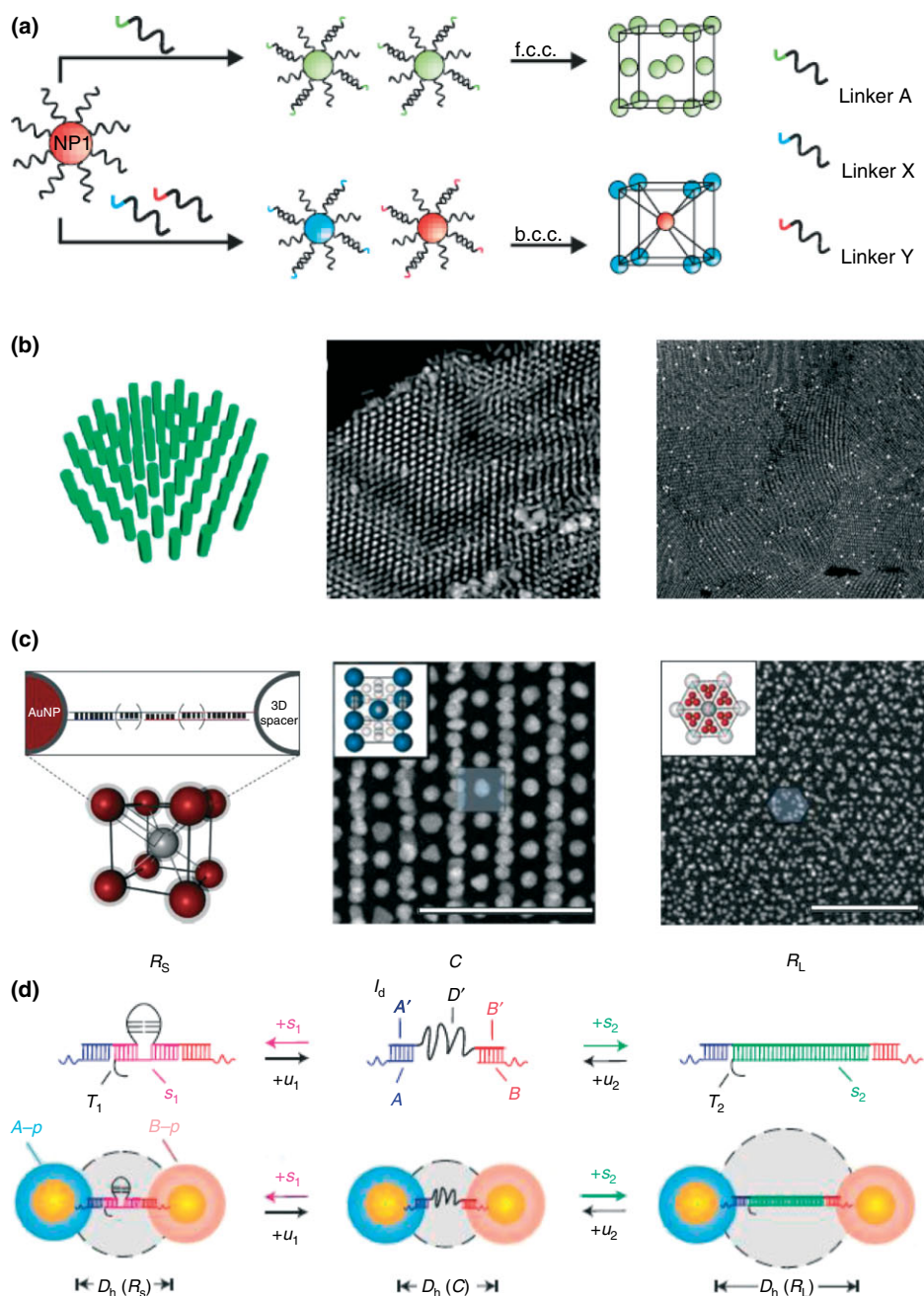


FIGURE 2 | (a) DNA-functionalized AuNPs can be assembled into different crystallographic lattice structures programmed by the sequence of the DNA linkers. (b) Schematic of hexagonal superlattice of standing AuNRs with corresponding TEM images. (c) Scheme illustration of using 3D hollow DNA spacers in AuNP crystallization. TEM images of a bcc lattice (left) formed from AuNPs (20 nm) and DNA spacer (10 nm), and 'Lattice X' (right) structure formed from AuNPs (10 nm) and DNA spacer (20 nm). (d) Controllable switching of interparticle distances by using a reconfigurable DNA device (I_d) that acts as an interparticle linkage. After addition of set DNA strands (s_1, s_2), I_d structure can be reversibly transformed from a flexible C configuration to stem loop R_S and linear R_L morphologies.

served as voids that could be selectively placed into a lattice structure of AuNPs, leading to several distinct lattice structures that were difficult to obtain by conventional strategies (e.g., AB_2 type, simple hexagonal, graphite type, AB_6 type, 'lattice X').

This hollow DNA spacer-based method opens a new route to design crystals with novel lattice structures that are not naturally occurring.

The structural flexibility of DNA and the reversibility of DNA hybridization events make

it possible to obtain dynamic, reconfigurable and responsive nanostructures.^{64,65} In one example, 3D superlattices and dimer clusters could be constructed with controllable switching of interparticle distances (in the range of 15–25%) by using a reconfigurable DNA structure that acted as an interparticle linkage.¹⁷ By adding the specific DNA strands, the interparticle distances in the superlattices and clusters can be modified even in their post-assembly states (Figure 2(d)). The transition states and local rearrangements were probed by SAXS which revealed the structural integrity of the systems during the reconfiguration process.

DNA-programmed pathways could be combined with other methods, such as capillary force-assisted self-assembly. In one example, AuNPs and nanoshells could be grouped into structurally well-defined heteropentamer clusters (pentamers), consisting of a 74 nm-diameter AuNP surrounded by four nanoshells.³⁷ To obtain this structure, the pentamers were first synthesized by DNA hybridization but the structures were ‘loose’ due to the soft nature of DNA. In a following step, the ‘loose’ pentamers in solution could be ‘compressed’ into a 2D plane by capillary forces during drying process (Figure 3(a)). To optimize the pentamer formation, a 75 bases ds-DNA spacer was used. Interestingly, this heteropentamer nanostructure showed specific magnetic and Fano-like resonances characterized by a broad electric dipole resonance spanning the entire range of the spectra.

Plasmonic Structures from DNA Polymerization

DNA-programmed materials synthesis can be combined with polymerase chain reaction (PCR) or rolling circle amplification (RCA) to form various superstructures. DNA primers could be attached to nanoparticle surfaces and then followed by PCR reactions.³⁹ By changing the density of the primer on the surface of AuNPs and controlling the number of PCR cycles, a number of plasmonic nanostructures were generated ranging from a mixture of dimers, trimers, tetramers, to chiral spatial organizations of AuNPs. The improvement of this method would rely on the development of separation methods for different oligomers. High yield of different generations of products will also be highly desirable for systematic studies of their chiral properties.

Another DNA polymerization-based method to fabricate plasmonic nanostructures is by RCA which can produce long and linear single DNA strands from a short (< 100 bases), circular DNA template. The first RCA-based method to plasmonic structures was reported by Mao et al. They first synthesized monofunctionalized DNA-AuNPs (5 nm) and then mixed them with RCA products (namely, long DNA strands with repeating sequences complementary to DNA sequence on AuNPs). This process led to the formation of micrometer-long 1D chains of AuNPs.⁴⁰ In a different approach, Li et al. fabricate satellite-like plasmonic nanostructures by RCA.⁴¹ In this report,

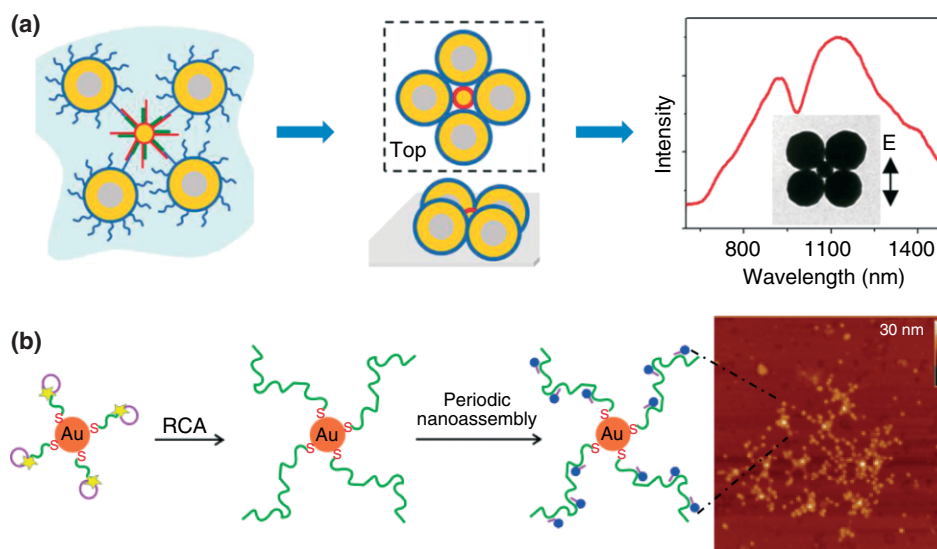


FIGURE 3 | (a) DNA-functionalized nanoparticles/nanoshells into heteropentamer clusters (pentamers), which consist of a smaller gold nanosphere (74 nm) surrounded by a ring of four larger nanoshells ($[r_1, r_2] = [62.5, 92.5]$ nm). (b) Schematic illustration of RCA on DNA-AuNPs that served as a scaffold for the formation of satellite 3D nanostructures. AFM image (right) showed superstructures constructed from 5 and 15 nm AuNPs (large bright spots).

DNA oligonucleotides were tethered to AuNPs as the primer and a single-stranded circular DNA was used as a template. In the presence of ϕ 29 DNA polymerase, RCA reactions led to extension of nanoparticle-tethered DNA with repeats complementary to circular DNA templates (Figure 3(b)). Furthermore, AuNPs were attached to these repeats, forming satellite 3D nanoassemblies.

DNA-TEMPLATED SELF-ASSEMBLY

Simple ds DNA Templates

Murray et al. described the assembly of 1D linear chains of AuNPs (4.4 nm) coated by cationic trimethyl (mercaptoundecyl) ammonium (TMA) monolayers.^{42,66} The DNA acted as a template for cationic AuNPs by electrostatic interactions. The morphology of nanostructures varied from chains to complex bundles, which was controlled by controlling relative ratios of nanoparticles versus DNA base pairs. The edge-to-edge distance was estimated to 2.9 ± 0.9 nm, consistent with the predicted thickness corresponding to twice the TMA monolayer thickness. However, some precipitation would occur if the ratio of DNA to monolayer-protected cluster increased. This was likely due to the large binding constant provided by individual cation–anion electrostatic interactions.

Templates Based on DNA Tiles, Frames, and Origami

Both DNA-programmed and dsDNA-templated nanostructures suffer from weak mechanical strength. Dehydration often leads to the structural collapse or shrinkage. Recently developed structural DNA nanotechnology can overcome this challenge by sophisticated design of rigid DNA tiles, frames, and origami.

DNA can be interweaved to form rigid double-crossover (DX) tiles which can be further interlinked to form 2D DNA grids. Kiehl et al. utilized four different DX tiles to assemble 2D DNA grids on a solid substrate.^{54,67} Then DNA-modified AuNPs were positioned onto the grids with precisely defined regular inter-row spacing, via Watson-Crick base-pairing forces (Figure 4(a)). Seeman et al. used a similar method but with different DNA scaffolds and reported the formation of two-component (5 and 10 nm AuNPs) 2D periodic patterns.⁵⁵ By using 3D DX triangles, a rhombic lattice arrangement tailed with different sticky ends enabled the formation of the two-component template which then guided formation of 2D nanoparticle assemblies.

DNA-tile-based method can also lead to 3D plasmonic nanostructures. Yan et al. reported the formation of 3D plasmonic tubular nanostructures (stacked rings, single spirals, double spirals, and nested spiral tubes) of AuNPs by using DNA tile-mediated self-assembly⁵¹ (Figure 4b). The different conformations of tubular structure and chiralities could be controlled by size-dependent steric repulsions among AuNPs. With two different AuNPs (5 and 10 nm), complex 3D patterns, such as double helix and quadruplex structures, were obtained. These AuNPs were wrapped parallel to the DNA tubular axis. By further engineering the DX-DNA tiles structures, it should be possible to place AuNPs of different sizes in or outside of the DNA tubes. This work extended DNA-templated nanostructures to 3D complex architectures similar to some naturally existing patterns.

With the aid of synthetic chemistry techniques, Sleiman et al. developed a different route to fabricate rigid DNA frames. They reported the creation of dynamic DNA templates which were fully functional in their single-stranded and cyclic forms. This template guided the selective attachment of AuNPs with different diameters on the complementary arms. Different nanostructures have been established by using the same square DNA template, such as square, trapezoidal, and rectangular clusters. Interestingly, post-assembly ‘write/erase’ methods were demonstrated by selectively removing one particle from triangles of three AuNPs, followed by positioning another AuNP onto the specific site.⁴⁶

Linear chain structures of AuNPs could also be produced from rigid DNA frames. In particular, AuNPs could be positioned inside DNA nanotubes fabricated from rigid DNA triangles to form ‘nanopeapod’⁵⁰ (Figure 4c). The advantages of using the DNA nanotubes are that conjugation with AuNPs (10 and 15 nm) was size-specific, and the core-to-core distances of AuNPs could be precisely controlled. Notably, the encapsulated AuNPs could be spontaneously released from the nanotubes by simply adding specific DNA replacement strands. The external strands could selectively open the DNA nanotube structure and break the chain-like structures, which could potentially be applied in gene-triggered delivery of drugs and cell-specific therapies.

Structurally more complex plasmonic nanoarchitectures could be produced from DNA origami templates. DNA origami has attracted much attention to the field of DNA nanotechnology since the landmark paper reported by Rothemund.⁶⁸ In contrast to the conventional crossover strategy that uses single building block to construct larger structures in a

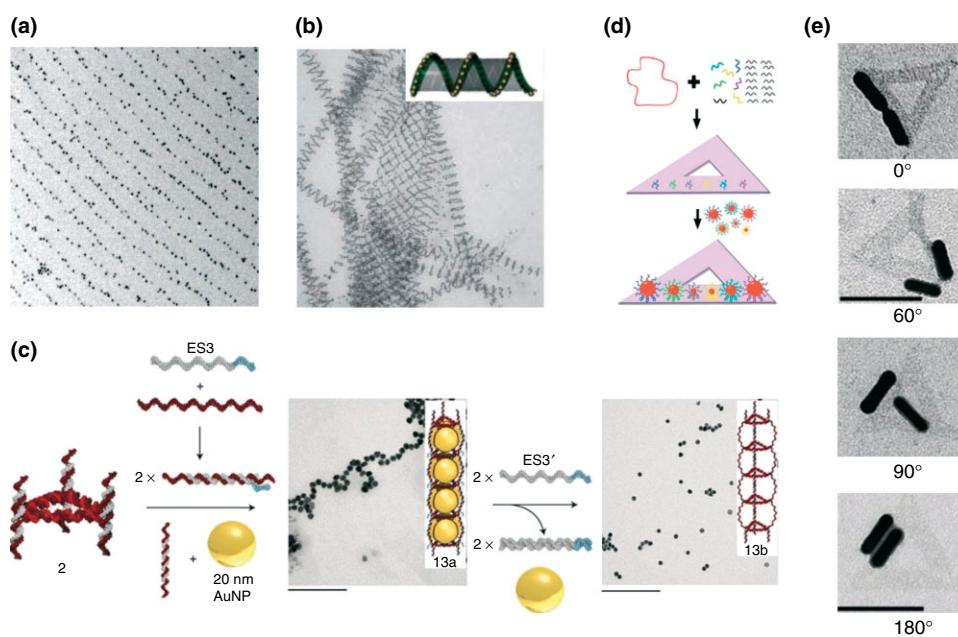


FIGURE 4 | DNA-templated self-assembly constructed by using DNA tiles and DNA origami. (a) DNA-functionalized AuNPs were organized into closely packed rows with precisely defined regular inter-row spacings templated by the DNA scaffolding. (b) Three-dimensional plasmonic tubular spirals of AuNPs using DNA tile-mediated self-assembly. (c) Encapsulated ‘nanopeapod’ AuNPs 1D chains using triangular DNA nanotubes with longitudinal variation as host. TEM image (right side) shows that encapsulated AuNPs could be spontaneously released from the nanotubes by simple addition of specific DNA strands. (d) Six-nanoparticle self-similar chain nanostructures using triangular DNA-origami templates. (e) DNA origami-templated AuNRs dimer that form with various predetermined inter-rod angles.

‘two-step’ process, DNA origami provides a versatile and simple ‘one-pot’ method to create addressable DNA nanopatterns by using various short staple DNA strands to fold genomic DNA into geometrically desired nanopatterns.⁴⁷

Liu et al. reported a bottom-up assembly method to synthesize monomeric, dimeric, and trimeric AgNPs (20 nm) cluster, and AgNP–AuNP heterodimer nanostructures templated by triangular-shaped DNA origami with a side length of 114 ± 2 nm.⁴⁷ The synthesis involved two steps: (1) preparation of triangular-shaped DNA origami with high quality and desired capture strands at predetermined locations on the structure; (2) hybridization of phosphorothioated chimeric DNA conjugated AgNPs on the DNA origami template. They demonstrated that the core-to-core distance between each AgNPs can be precisely controlled from 29 to 94 nm. The yield of dimer could reach 81%, and the yield of trimer could reach 62.5%.

In addition, Bokor et al. developed the six-nanoparticle self-similar chain structures by using DNA origami templates.⁴⁸ The long scaffold strand hybridized with designed staple strands, forming the triangular DNA origami with specific binding sites on one side of the origami surface (Figure 4(d)). These binding sites guided the different AuNPs

(5, 10, 15 nm) to the desired locations through complementary base-pairing forces. A plasmonic resonance band shift from 521 to 526 nm was observed, indicating strong local electromagnetic field enhancements in the interstices between nanoparticles.

The anisotropic building blocks could also be assembled into nanoarchitectures by DNA-origami templates. AuNRs have been successfully assembled into discrete, well-ordered AuNR and AuNR–AuNP hybrid nanoarchitectures.⁴⁹ The DNA origami-templated AuNRs dimer could form various predetermined inter-rod angles (0° , 60° , 90° , 180°) (Figure 4(e)). This opens a new route to coordinate the spatial orientations of anisotropic nanoparticle building blocks.

With DNA origami methods, it is possible to design more complex plasmonic nanostructures^{69,70} for various applications in nanodevices.⁷¹ For example, Ding et al. reported the construction of 3D AuNP helices by rolling and stapling 2D rectangular DNA origami.⁵² The geometric dimension of stapling positions on DNA origami could be rationally controlled, tailoring the structural parameters of AuNPs helices. Similar nanohelices with left- and right-handed morphologies were reported by Kuzyk et al. using a different DNA origami-template

method.⁵³ For each plasmonic helix, nine AuNPs were specifically conjugated to the site of DNA origami 24-helix bundles consisting of complementary staple DNA extensions. The nanohelices exhibited both circular dichroism and optical rotatory dispersion effects due to plasmonic coupling in chiral structures. These plasmonic helices resembled natural chiral molecules, opening a new route to manipulate light by programming chirality.

UNCONVENTIONAL DNA TECHNOLOGIES AND NANOPATTERNING

As Entropic Ligands in Drying-Mediated Self-Assembly

The programmed pathway and template strategies have led to a diverse range of plasmonic nanostructures. In a different route, Cheng et al. successfully put DNA to an unconventional use as an entropic ‘dry ligand’ in a drying-mediated self-assembly process.⁷² Under low ionic strength, this method led to large-area highly-ordered nanoparticle superlattices without, in some circumstances, the requirement of specific Watson–Crick base-pairing (Figure 5(a)). Cheng et al. systematically investigated

the mechanism of dry-DNA-ligand-mediated self-assembly on solid support, holey substrate, and at the air/water interface. In particular, drying-mediated self-assembly of DNA-capped nanoparticles has been systematically investigated by synchrotron-based small-angle X-ray scattering (SAXS).²⁸ This represented a hybrid strategy of drying-mediated self-assembly and programmable crystal formation, and the studies on such dynamic crystallization demonstrated that DNA-mediated nanoparticle crystals were soft with continuously scalable lattice constants (Figure 5(b)). Furthermore, this result showed that crystallization time in the soft-crystallization process can be tuned by programming base-pairing forces. It also revealed that DNA behaved as a molecular spring in the drying-mediated self-assembly process, from which a simple entropic spring argument could be applied to generic soft-corona hard-sphere interactions at the nanoscale (such as alkyl-molecule-mediated self-assembly of nanoparticles).

Furthermore, DNA-mediated self-assembly of AuNPs has been investigated at the air/water interface by Synchrotron-based Grazing-incidence Small-Angle X-ray Scattering (GISAXS).⁵⁹ Specifically, an X-ray beam was positioned parallel to a silicon support, raster-scanning a droplet containing DNA-capped nanoparticles. This allows for mapping spatial

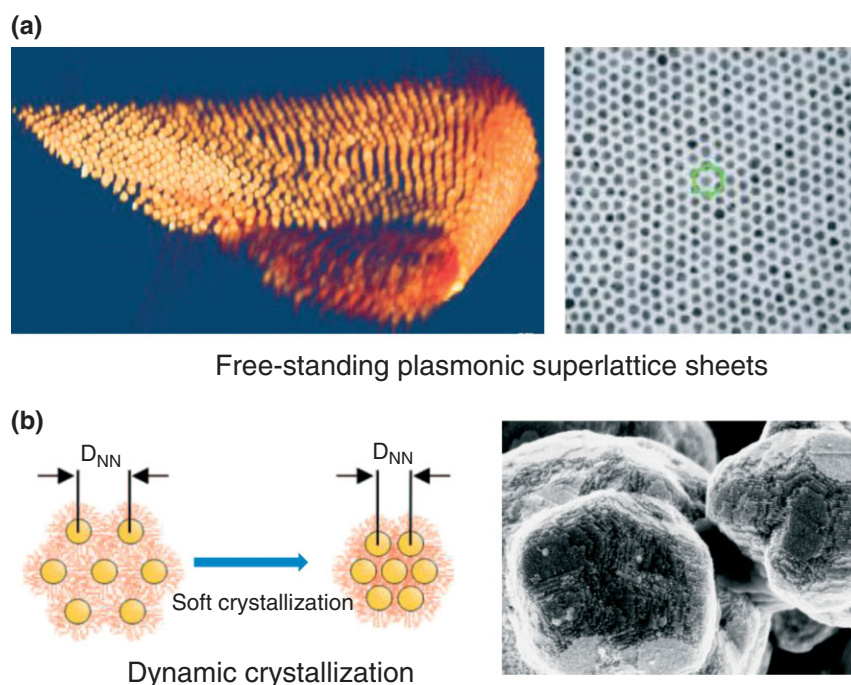


FIGURE 5 | DNA as entropic ligands in drying-mediated self-assembly. (a) Free-standing monolayered DNA-AuNPs superlattice sheets. Three-dimensional STEM tomography reconstruction of a folded sheet (left) and TEM image (right) showing hexagonal ordering. (b) Drying-mediated deformation of DNA corona in 3D supercrystals.

crystallization events across the entire droplet. The experimental results showed that DNA could direct self-assembly of the nanoparticles into Gibbs monolayers at the air/water interface, and that the spacing within the monolayer was highly dependent on ionic strength. These synchrotron-based studies on DNA-ligand-mediated self-assembly showed that DNA can manipulate nanoparticle crystallization both temporally and spatially. This may substantially extend the scope of application of DNA in materials and interfaces.

DNA ligands offer superior advantages to alkyl molecule ligands. The highly controllable molecular lengths of DNA ligands enable tailoring of both structural (inter-particle spacings) and functional properties (plasmonic and mechanical) over a wide window. In particular, the edge-to-edge inter-particle spacing in DNA-based nanoparticle superlattices can be adjusted up to 20 nm in dehydrated state,²⁰ which is a significantly wider range than that has been achieved with alkyl molecular ligands. Such control allows for tuning plasmonic colors without changing chemical compositions and shows potential applications in future plasmonic circuits. Compared to DNA-programmed and DNA-templated strategies, DNA-ligand-based method provides a simple yet efficient route to fabricate large-area nanoparticle superlattices stable in dehydrated state with low cost. However, the drawback of ligand-based approach is to lose the specificity in constructing more complex lattice structures other than FCC or hexagonally close packed (HCP) packing geometries.

In Conjunction with Top-Down Lithography

DNA-based bottom-up self-assembly can be combined with top-down lithography. In particular, DNA-dry-ligand-based strategy exhibited excellent compatibility with top-down lithography. This combination may be a critical step for future integration of DNA-derived plasmonic nanostructures into nanophotonic circuits.

By virtue of lithographically-fabricated micro-moulds, DNA-mediated nanoparticle crystallization events could be localized, leading to patterned superlattices.⁶⁰ This strategy was able to rationally control the local crystallization events of the nanoparticles superlattices, which resulted in versatile structures with high degrees of internal order, such as single particle-width corrals, single particle-thickness microdiscs and submicrometre-sized 'super-crystals'⁶⁰ (Figure 6(a) and (b)). These nanoscale features were produced from micrometer-sized moulds, corresponding to a few hundreds times of size reduction. Notably,

these patterned superlattices could be addressed by micropatterned electrode arrays, suggesting compatibility with current solid-state devices.

Furthermore, by virtue of lithographically fabricated microholes, the crystallization of DNA-capped nanoparticles can be confined to 2D planes.²⁰ This process led to free-standing monolayered DNA-nanoparticle superlattice membranes (Figure 5(a)). Both internal and overall structures of sheets could be controlled. For examples, circular and square sheets were obtained conforming to the hole geometries defined by top-down lithography; the edge-to-edge interparticle spacing could be precisely tuned from ~1 to ~20 nm. The spacing control influenced the plasmonic coupling, leading to plasmonic nanosheets with different colors. This method opens a simple yet efficient avenue toward the assembly of plasmonic nanoparticle sheets in their ultimate thickness limit—a promising step that may enable their integration into solid-state nanodevices.

DNA origami-templated plasmonic nanostructures could also be combined with top-down lithography. Cha et al. reported the repeated patterning of large-area arrays of 10 nm ssDNA-functionalized AuNPs by a soft-lithographic subtraction printing process.⁷³ In this method, ssDNA were first adsorbed on PDMS substrates, followed by subtraction printing using a lithographically templated silicon master. The patterned ssDNA domains were then transferred to silicon substrates. Furthermore, DNA hybridization was applied to induce assembly of ssDNA-functionalized AuNPs. Finally, patterned and crossed lines were achieved. Furthermore, they achieved the large-area patterning of AuNPs (5 nm) into spatially ordered, 2D arrays through the site-selective deposition of triangular DNA origami onto lithographically patterned substrates⁵⁷ (Figure 6(c)). Precise binding of AuNPs to each DNA structure was achieved and formed macroscopic arrays with characteristic length scales ranging from a few to several hundreds of nanometers. Different patterns, such as multiple triangles with alternating left and right orientations, were also formed, providing a new way to rationally generate complex patterned networks.⁷⁴

In addition, there were reports of using printing methods with photolithographically fabricated stamps to pattern DNA-capped nanoparticles. Stellacci et al. reported the applicability of supramolecular nanostamping for replicating DNA arrays by using 9 nm AuNPs with high fidelity.⁷⁵ Udo et al. reported a Gutenberg-type method with electron beam-fabricated stamps to replicate lithographically defined nanostructures.⁷⁶ Dense nanoparticle loading

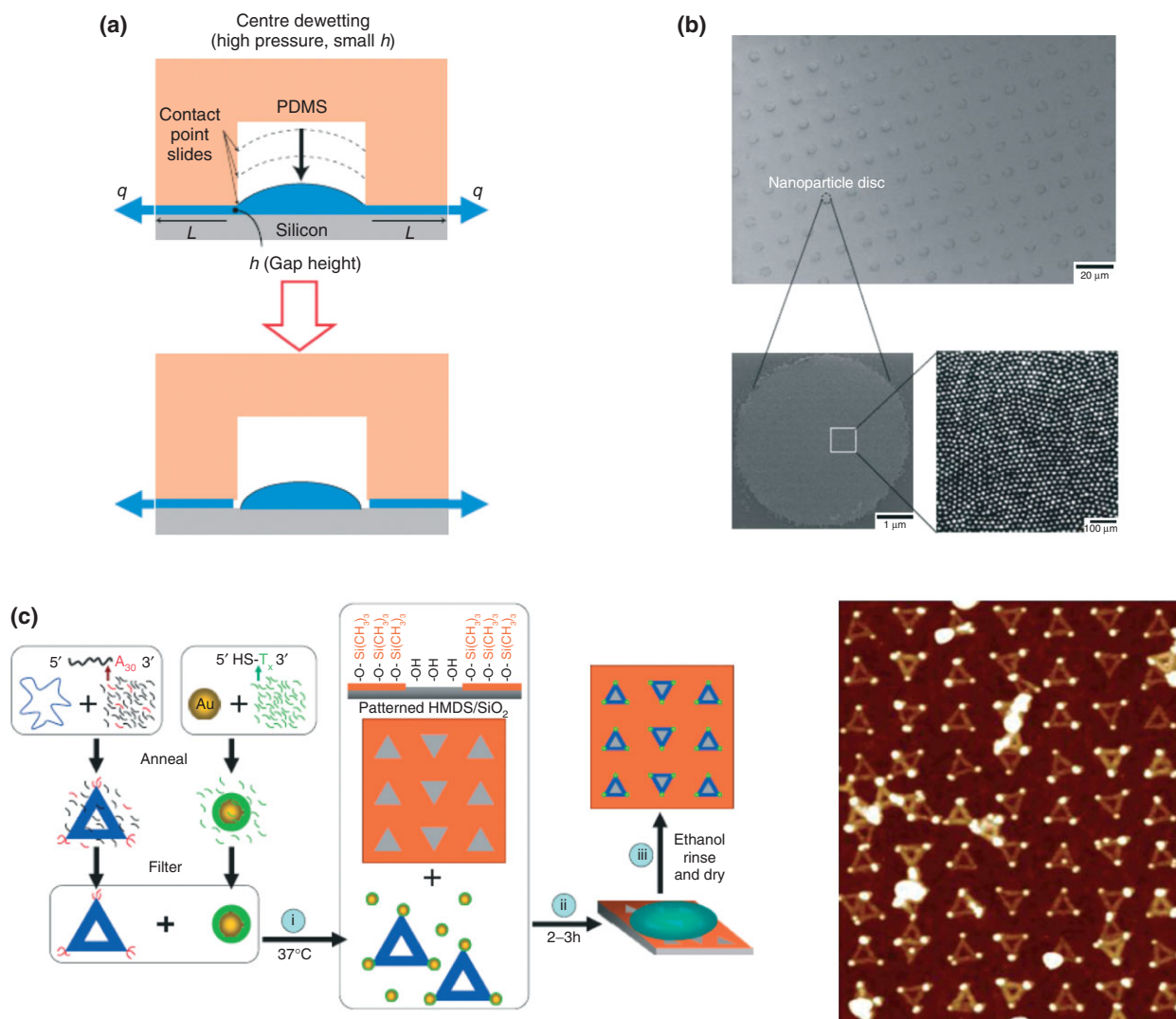


FIGURE 6 | Top-down lithography integrates with bottom-up DNA-programmed self-assembly. (a) Cross-sectional scheme of a microdroplet confined in a micromould showing center dewetting. Localized assembly of the AuNPs microdiscs was then achieved by DNA-programmed crystallization. (b) SEM image of nanoparticle disks pattern with highly ordered internal structures. (c) Large-area patterning of AuNPs (5 nm) onto spatially ordered, 2D arrays through the site-selective deposition of triangular DNA origami onto lithographically patterned substrates.

and high transfer yields were achieved over three consecutive printing cycles.

APPLICATIONS

A fascinating aspect of plasmonic nanoparticles is that their optical properties are strongly affected by structural parameters such as size and shape, as well as material composition and the surrounding dielectric environment.^{77–81} This originates from so-called localized surface plasmon resonance (LSPR)—the coherent oscillation of conduction band electrons at a certain frequency of light. By virtue of the powerful LSPR of plasmonic nanoparticles, one can design

superior sensing/diagnostic devices,^{82,83} and high-efficiency energy-harvesting systems.⁸⁴

Since their advent, DNA-based strategies to form 3D plasmonic aggregates have become powerful diagnostic tools for detection of DNA, RNA, and proteins.^{58,85} Such colorimetric DNA detection methods utilize DNA-functionalized particles as probes and the complementary DNA strands as target molecules. In the presence of complementary target DNA, large plasmonic aggregates formed, leading to a red shift of the plasmonic resonance band with a concomitant red-to-purple color change (Figure 7(a)). A striking feature of this method is the sharpness and clarity of the transition simply on the basis of color

change. In addition, the optical properties⁸⁶ and specific melting characteristics⁸⁷ of macroscopic DNA-functionalized plasmonic structures can be controlled through the choice of DNA as well as size and shape of nanoparticles.^{88,89}

Taking advantage of extreme sensitivity of plasmonic coupling in response to interparticle spacing, researchers have developed an AuNP/AgNP-based heterodimeric plasmonic biosensor for detecting DNA sequences.⁶⁵ In the presence of target DNA molecules, the hybridization events induced dimer formation, which led to a spectral shift of 102 nm for AgNPs and 23 nm for AuNPs (Figure 7(b)). The sensing was based on the sensitivity of LSPR to interparticle spacing, bringing the concept of plasmonic dimeric ruler which could be used to ‘measure’ a sensing distance

up to 70 nm. Unlike fluorescence-based methods that often suffer from issues of bleaching or blinking, plasmonic ruler sensor can be used to monitor biological binding events in *real-time* for virtually unlimited length of time. The results from real-time imaging studies revealed the binding and cleavage events of restriction enzymes,⁹⁰ providing physical insights on the potential energy change between the straight and bent/break DNA states.

Impressively, sensors based on plasmonic nanostructures could reach single-molecule detection accuracy by surface-enhanced Raman scattering (SERS). One such example is the Au–Ag core–shell nanodumbbells,³⁵ in which a Raman-active Cy3 dye molecule was located between dimeric particles. In this approach, the Raman dye position could be

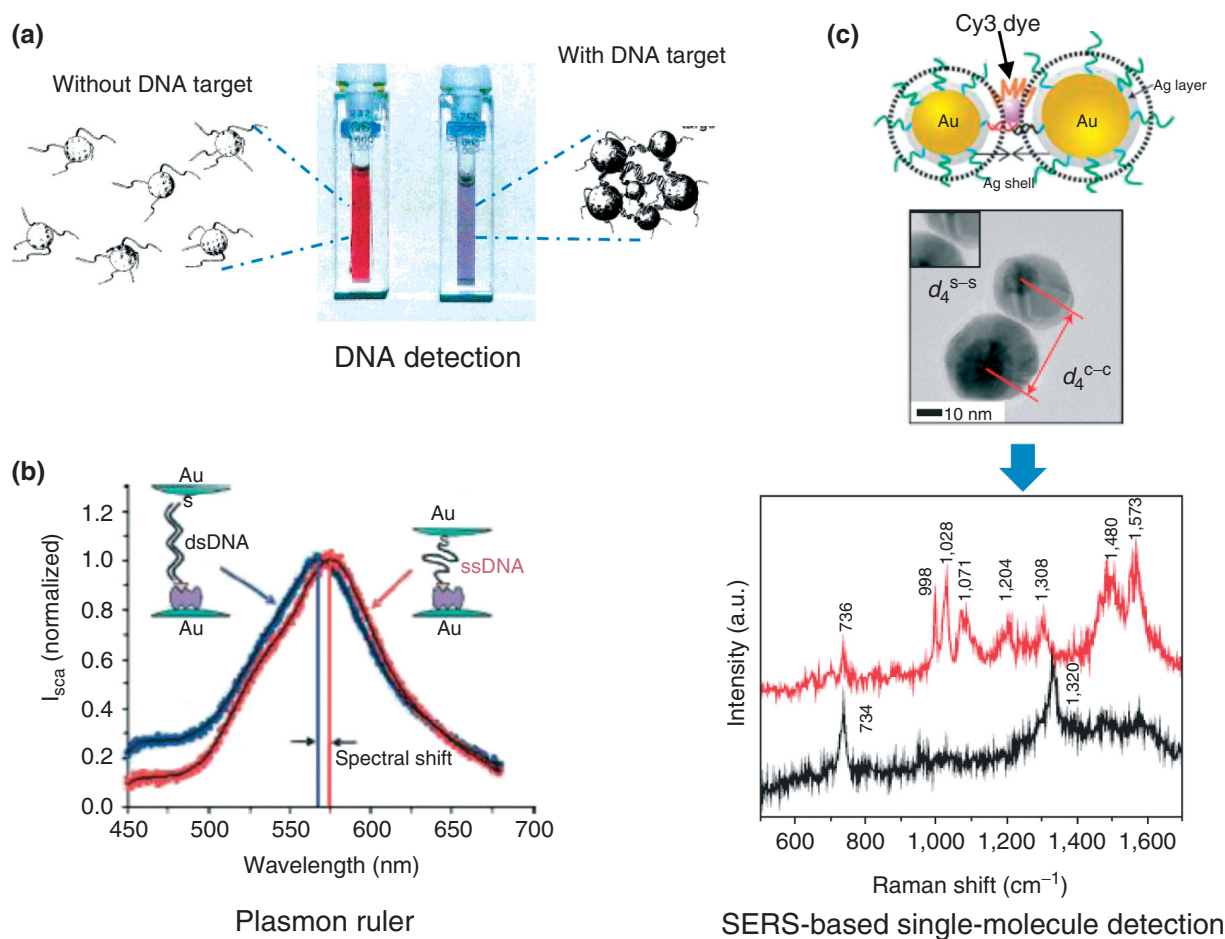


FIGURE 7 | Applications of DNA-based plasmonic nanostructures. (a) Colorimetric DNA detection method using DNA-functionalized particles as probes and the complementary DNA strands as target molecules. (b) Plasmon ruler used in the detection of the hybridization of complementary DNA to the ssDNA linkers. After hybridization, the particles were pushed apart due to the more rigid nature of dsDNA than ssDNA, which resulted in a blue-shift of ~2.1 nm measured by monitoring the spectrum of single AuNPs dimer. (c) SERS-active Au–Ag core–shell nanodumbbells assembled by DNA hybridization. In this nanostructure, a single Raman-active Cy3 dye molecule is located in the gap of this heterodimer, followed by Ag shells deposition on the surface of the dimeric nanodumbbell. Left figure shows Raman spectra taken from Cy3-modified oligonucleotides (red line) and Cy3-free oligonucleotides (black line) in NaCl-aggregated silver colloids.

precisely defined by synthetic chemistry techniques and the gap between particles could be controlled by Ag shell thickness (Figure 7(c)). The characteristic Raman peaks for Cy3 dye were observed with a laser of 514.5 nm. Quantitative analysis of these peaks revealed an enhancement factor (G) of 2.7×10^{12} , which is large enough for single-molecule detection.

Owing to the great enhancement of electrical fields in region-specific isomers,^{91,92} plasmonic nanostructures could be used as a platform for nanoscale sensors in living cells. Three types of isomers of AuNPs and AuNRs were incubated with HeLa cells,³⁸ which exhibited sufficient field enhancement to detect structural changes in lipids of mitochondria and small metabolites. The satellite isomer was able to penetrate through the cellular membrane entering the cytoplasm directly. The structural control over the position of plasmonic nanoparticles by DNA opens a new route to real-time probing of the local organelle environment in live cells.

CONCLUSIONS AND OUTLOOK

In this review, we present various viable methodologies for the DNA-based design of plasmonic nanoarchitectures, including DNA-programmed structures (Homo/Heterodimer, multimers, tetrahedrons, 1D chains, 2D superlattices, and 3D supercrystals), rigid DNA scaffold-templated assembly, and unconventional use of DNA ligands in combination with top-down lithography. DNA has proven by far the most successful molecule for programmable assembly of plasmonic nanoparticles into an assortment of functional nanostructures. These well-defined nanostructures have a broad spectrum of applications, especially in high-sensitivity biological diagnosis, based on their localized surface plasmon resonance and SERS effects.

Moreover, it is important to note that all the DNA-based strategies covered in this review are in principle extendable to other materials systems,⁶¹ such as quantum dots, magnetic nanoparticles, etc. An existing example is the self-assembly of quantum dot complexes using DNA-functionalized cadmium telluride nanocrystals.⁹³ Cross-shaped complexes containing three different types of dots can be achieved, providing a potential application in nanoscale optoelectronic devices. Another example is the fabrication of quantum dot arrays with programmable periodicity by DNA origami nanotube-guided assembly.⁹⁴ Accordingly, DNA plays multiple roles, not only in templating of plasmonic nanostructures, but also

in tailoring the coupling of heterogeneous material systems.

Despite the potentiality, modularity and generality of DNA-based strategies in directing the synthesis of well-defined materials at the nanoscale, it is still in its embryonic stage of development. Many challenges need to be overcome before real-world applications can be realized. For example, it remains a grand challenge to use DNA to manipulate nanoparticle at will. As seen in Table 1, most of successful examples are based on isotropic spherical building blocks. DNA conjugation with structurally more complex plasmonic nanoparticles⁹⁵ and assembly of high-quality multi-component assemblies,⁴⁹ remain material challenges. For example, current mono-DNA conjugation approaches are based on controlling DNA/NP ratios in initial reactions followed by purification. Such a method is tedious with low yields. Systematic evolution of ligands by exponential enrichment (SELEX) is a new combinatorial chemistry technique in molecular biology for producing oligonucleotide sequence that can bind specifically to proteins or even entire cells. The SELEX technologies may be extended to produce highly specific DNA to bind nanoparticles forming high-yield monoconjugates. In addition, to date DNA-based strategies often lead to plasmonic nanoarchitectures with limited local order and limited stability in the dehydrated state, potentially hampering real-world applications. This may call for a multidisciplinary collaboration among chemistry, physics, biology and materials science to find a route to achieve control of the DNA-based assemblies at multiple scales ranging from nanoscale all the way to macroscale.^{56,96} For example, the DNA design rules for 3D nanoparticle crystals have been formulated recently,⁹⁷ which outlines the versatility of controlling internal structures including lattice structures and inter-particle spacing. As a further step to apply these elegant nanoparticle crystals to real-world energy and sensing devices, a critical step may be needed to control their overall structure by other means (such as microshaping and nanopatterning) or to grow device-scale large crystals by preventing kinetically trapped structures.

In conclusion, given the versatility of DNA as a designer nanomaterial as continuously improved methodologies are developed, substantially more sophisticated plasmonic structures will be successfully produced in the near future. Hence, we believe that DNA-based nanoarchitectures will soon be seen in real-world intelligent optoelectronic devices and smart diagnostic systems.

ACKNOWLEDGMENTS

This work is supported by Australian Research Council (DP120100170). Y.C. acknowledges the graduate student scholarship (MGS & IPRS) from Monash University. We also acknowledge Dr. Michael Campolongo for proofreading and correcting English.

REFERENCES

1. Polman A. Plasmonics applied. *Science* 2008, 322: 868–869.
2. Schuller JA, Barnard ES, Cai W, Jun YC, White JS, Brongersma ML. Plasmonics for extreme light concentration and manipulation. *Nature Mater* 2010, 9:193–204.
3. Shipway AN, Katz E, Willner I. Nanoparticle arrays on surfaces for electronic, optical, and sensor applications. *ChemPhysChem* 2000, 1:18–52.
4. Ozbay E. Plasmonics: merging photonics and electronics at nanoscale dimensions. *Science* 2006, 311: 189–193.
5. Anker JN, Hall WP, Lyandres O, Shah NC, Zhao J, Van Duyne RP. Biosensing with plasmonic nanosensors. *Nature Mater* 2008, 7:442–453.
6. Maier SA, Kik PG, Atwater HA, Meltzer S, Harel E, Koel BE, Requicha AAG. Local detection of electromagnetic energy transport below the diffraction limit in metal nanoparticle plasmon waveguides. *Nature Mater* 2003, 2:229–232.
7. Lal S, Clare SE, Halas NJ. Nanoshell-enabled photothermal cancer therapy: impending clinical impact. *Acc Chem Res* 2008, 41:1842–1851.
8. Yavuz MS, Cheng Y, Chen J, Cobley CM, Zhang Q, Rycenga M, Xie J, Kim C, Song KH, Schwartz AG, et al. Gold nanocages covered by smart polymers for controlled release with near-infrared light. *Nature Mater* 2009, 8:935–939.
9. Frens G. Controlled nucleation for the regulation of the particle size in monodisperse gold suspensions. *Nature, Phys Sci* 1973, 241:20.
10. Jana NR, Gearheart L, Murphy CJ. Seeding growth for size control of 5–40 nm diameter gold nanoparticles. *Langmuir* 2001, 17:6782–6786.
11. Millstone JE, Park S, Shuford KL, Qin L, Schatz GC, Mirkin CA. Observation of a quadrupole plasmon mode for a colloidal solution of gold nanoprisms. *J Am Chem Soc* 2005, 127:5312–5313.
12. Nikoobakht B, El-Sayed MA. Preparation and growth mechanism of gold nanorods (NRs) using seed-mediated growth method. *Chem Mater* 2003, 15:1957–1962.
13. Perrault SD, Chan WCW. Synthesis and surface modification of highly monodispersed, spherical gold nanoparticles of 50–200 nm. *J Am Chem Soc* 2009, 131: 17042–17043.
14. Xia Y, Xiong Y, Lim B, Skrabalak SE. Shape-controlled synthesis of metal nanocrystals: simple chemistry meets complex physics? *Angew Chem Int Ed* 2009, 48:60–103.
15. Tan SJ, Campolongo MJ, Luo D, Cheng WL. Building plasmonic nanostructures with DNA. *Nature Nanotech* 2011, 6:268–276.
16. Alivisatos AP, Johnsson KP, Peng X, Wilson TE, Loweth CJ, Bruchez MP, Schultz PG. Organization of 'nanocrystal molecules' using DNA. *Nature* 1996, 382:609–611.
17. Maye MM, Kumara MT, Nykypanchuk D, Sherman WB, Gang O. Switching binary states of nanoparticle superlattices and dimer clusters by DNA strands. *Nature Nanotech* 2010, 5:116–120.
18. Nie Z, Fava D, Kumacheva E, Zou S, Walker GC, Rubinstein M. Self-assembly of metal-polymer analogues of amphiphilic triblock copolymers. *Nature Mater* 2007, 6:609–614.
19. Liu K, Nie Z, Zhao N, Li W, Rubinstein M, Kumacheva E. Step-growth polymerization of inorganic nanoparticles. *Science* 2010, 329:197–200.
20. Cheng WL, Campolongo MJ, Cha JJ, Tan SJ, Umbach CC, Muller DA, Luo D. Free-standing nanoparticle superlattice sheets controlled by DNA. *Nature Mater* 2009, 8:519–525.
21. Dong A, Chen J, Vora PM, Kikkawa JM, Murray CB. Binary nanocrystal superlattice membranes self-assembled at the liquid-air interface. *Nature* 2010, 466: 474–477.
22. Mueggenburg KE, Lin X-M, Goldsmith RH, Jaeger HM. Elastic membranes of close-packed nanoparticle arrays. *Nature Mater* 2007, 6:656–660.
23. Pileni M-P. Self-assembly of inorganic nanocrystals: fabrication and collective intrinsic properties. *Acc Chem Res* 2007, 40:685–693.
24. Heitsch AT, Patel RN, Goodfellow BW, Smilgies D-M, Korgel BA. GISAXS characterization of order in hexagonal monolayers of FePt nanocrystals. *J Phys Chem C* 2010, 114:14427–14432.
25. Jones MR, Macfarlane RJ, Lee B, Zhang J, Young KL, Senesi AJ, Mirkin CA. DNA-nanoparticle superlattices formed from anisotropic building blocks. *Nature Mater* 2010, 9:913–917.
26. Park SY, Lytton-Jean AKR, Lee B, Weigand S, Schatz GC, Mirkin CA. DNA-programmable nanoparticle crystallization. *Nature* 2008, 451:553–556.

27. Nykypanchuk D, Maye MM, van der Lelie D, Gang O. DNA-guided crystallization of colloidal nanoparticles. *Nature* 2008, 451:549–552.
28. Cheng WL, Hartman MR, Smilgies D-M, Long R, Campolongo MJ, Li R, Sekar K, Hui C-Y, Luo D. Probing in real time the soft crystallization of DNA-capped nanoparticles. *Angew Chem Int Ed* 2010, 49:380–384.
29. Prodan E, Radloff C, Halas NJ, Nordlander P. A hybridization model for the plasmon response of complex nanostructures. *Science* 2003, 302:419–422.
30. Halas NJ, Lal S, Chang W-S, Link S, Nordlander P. Plasmons in strongly coupled metallic nanostructures. *Chem Rev* 2011, 111:3913–3961.
31. Jones MR, Osberg KD, Macfarlane RJ, Langille MR, Mirkin CA. Templated techniques for the synthesis and assembly of plasmonic nanostructures. *Chem Rev* 2011, 111:3736–3827.
32. Loweth CJ, Caldwell WB, Peng X, Alivisatos AP, Schultz PG. DNA-based assembly of gold nanocrystals. *Angew Chem Int Ed* 1999, 38:1808–1812.
33. Mastroianni AJ, Claridge SA, Alivisatos AP. Pyramidal and chiral groupings of gold nanocrystals assembled using dna scaffolds. *J Am Chem Soc* 2009, 131:8455–8459.
34. Xu X, Rosi NL, Wang Y, Huo F, Mirkin CA. Asymmetric functionalization of gold nanoparticles with oligonucleotides. *J Am Chem Soc* 2006, 128:9286–9287.
35. Lim D-K, Jeon K-S, Kim HM, Nam J-M, Suh YD. Nanogap-engineerable Raman-active nanodumbbells for single-molecule detection. *Nature Mater* 2010, 9:60–67.
36. Maye MM, Nykypanchuk D, Cuisinier M, van der Lelie D, Gang O. Stepwise surface encoding for high-throughput assembly of nanoclusters. *Nature Mater* 2009, 8:388–391.
37. Fan JA, He Y, Bao K, Wu C, Bao J, Schade NB, Manoharan VN, Shvets G, Nordlander P, Liu DR, et al. DNA-enabled self-assembly of plasmonic nanoclusters. *Nano Lett* 2011, 11:4859–4864.
38. Xu L, Kuang H, Xu C, Ma W, Wang L, Kotov NA. Regiospecific plasmonic assemblies for in situ raman spectroscopy in live cells. *J Am Chem Soc* 2011, 134:1699–1709.
39. Chen W, Bian A, Agarwal A, Liu L, Shen H, Wang L, Xu C, Kotov NA. Nanoparticle superstructures made by polymerase chain reaction: collective interactions of nanoparticles and a new principle for chiral materials. *Nano Lett* 2009, 9:2153–2159.
40. Deng Z, Tian Y, Lee S-H, Ribbe AE, Mao C. DNA-encoded self-assembly of gold nanoparticles into one-dimensional arrays. *Angew Chem Int Ed* 2005, 44:3582–3585.
41. Zhao W, Gao Y, Kandadai SA, Brook MA, Li Y. DNA polymerization on gold nanoparticles through rolling circle amplification: towards novel scaffolds for three-dimensional periodic nanoassemblies. *Angew Chem Int Ed* 2006, 45:2409–2413.
42. Wang G, Murray RW. Controlled assembly of monolayer-protected gold clusters by dissolved DNA. *Nano Lett* 2003, 4:95–101.
43. Mirkin CA, Letsinger RL, Mucic RC, Storhoff JJ. A DNA-based method for rationally assembling nanoparticles into macroscopic materials. *Nature* 1996, 382:607–609.
44. Macfarlane RJ, Lee B, Jones MR, Harris N, Schatz GC, Mirkin CA. Nanoparticle superlattice engineering with DNA. *Science* 2011, 334:204–208.
45. Auyeung E, Cutler JI, Macfarlane RJ, Jones MR, Wu J, Liu G, Zhang K, Osberg KD, Mirkin CA. Synthetically programmable nanoparticle superlattices using a hollow three-dimensional spacer approach. *Nature Nanotech* 2012, 7:24–28.
46. Aldaye FA, Sleiman HF. Dynamic DNA templates for discrete gold nanoparticle assemblies: control of geometry, modularity, write/erase and structural switching. *J Am Chem Soc* 2007, 129:4130–4131.
47. Pal S, Deng Z, Ding B, Yan H, Liu Y. DNA-origami-directed self-assembly of discrete silver-nanoparticle architectures. *Angew Chem Int Ed* 2010, 49:2700–2704.
48. Ding B, Deng Z, Yan H, Cabrini S, Zuckermann RN, Bokor J. Gold nanoparticle self-similar chain structure organized by DNA Origami. *J Am Chem Soc* 2010, 132:3248–3249.
49. Pal S, Deng Z, Wang H, Zou S, Liu Y, Yan H. DNA directed self-assembly of anisotropic plasmonic nanostructures. *J Am Chem Soc* 2011, 133:17606–17609.
50. Lo PK, Karam P, Aldaye FA, McLaughlin CK, Hamblin GD, Cosa G, Sleiman HF. Loading and selective release of cargo in DNA nanotubes with longitudinal variation. *Nature Chem* 2010, 2:319–328.
51. Sharma J, Chhabra R, Cheng A, Brownell J, Liu Y, Yan H. Control of self-assembly of DNA tubules through integration of gold nanoparticles. *Science* 2009, 323:112–116.
52. Shen X, Song C, Wang J, Shi D, Wang Z, Liu N, Ding B. Rolling up gold nanoparticle-dressed DNA origami into three-dimensional plasmonic chiral nanostructures. *J Am Chem Soc* 2011, 134:146–149.
53. Kuzyk A, Schreiber R, Fan Z, Pardatscher G, Roller E-M, Hogele A, Simmel FC, Govorov AO, Liedl T. DNA-based self-assembly of chiral plasmonic nanostructures with tailored optical response. *Nature* 2012, 483:311–314.
54. Le JD, Pinto Y, Seeman NC, Musier-Forsyth K, Taton TA, Kiehl RA. DNA-templated self-assembly of metallic nanocomponent arrays on a surface. *Nano Lett* 2004, 4:2343–2347.
55. Zheng J, Constantinou PE, Micheel C, Alivisatos AP, Kiehl RA, Seeman NC. Two-dimensional nanoparticle

- arrays show the organizational power of robust DNA motifs. *Nano Lett* 2006, 6:1502–1504.
56. Michelotti N, Johnson-Buck A, Mazon AJ, Walter NG. Beyond DNA origami: the unfolding prospects of nucleic acid nanotechnology. *WIREs Nanomed Nanobiotechnol* 2012, 4:139–152.
 57. Hung AM, Micheel CM, Bozano LD, Osterbur LW, Wallraff GM, Cha JN. Large-area spatially ordered arrays of gold nanoparticles directed by lithographically confined DNA origami. *Nature Nanotech* 2010, 5:121–126.
 58. Cederquist KB, Dean SL, Keating CD. Encoded anisotropic particles for multiplexed bioanalysis. *WIREs Nanomed Nanobiotechnol* 2010, 2:578–600.
 59. Campolongo MJ, Tan SJ, Smilgies D-M, Zhao M, Chen Y, Xhangolli I, Cheng W, Luo D. Crystalline Gibbs monolayers of DNA-capped nanoparticles at the air–liquid interface. *ACS Nano* 2011, 5:7978–7985.
 60. Cheng WL, Park N, Walter MT, Hartman MR, Luo D. Nanopatterning self-assembled nanoparticle superlattices by moulding microdroplets. *Nature Nanotech* 2008, 3:682–690.
 61. Zanchet D, Micheel CM, Parak WJ, Gerion D, Williams SC, Alivisatos AP. Electrophoretic and structural studies of DNA-directed Au nanoparticle groupings. *J Phys Chem B* 2002, 106:11758–11763.
 62. Claridge SA, Liang HW, Basu SR, Fréchet JM, Alivisatos AP. Isolation of discrete nanoparticle-DNA conjugates for plasmonic applications. *Nano Lett* 2008, 8:1202–1206.
 63. Mucic RC, Storhoff JJ, Mirkin CA, Letsinger RL. DNA-directed synthesis of binary nanoparticle network materials. *J Am Chem Soc* 1998, 120:12674–12675.
 64. Sebba D, LaBean T, Lazarides A. Plasmon coupling in binary metal core–satellite assemblies. *Appl Phys B* 2008, 93:69–78.
 65. Sonnichsen C, Reinhard BM, Liphardt J, Alivisatos AP. A molecular ruler based on plasmon coupling of single gold and silver nanoparticles. *Nat Biotechnol* 2005, 23:741–745.
 66. Wolfe RL, Balasubramanian R, Tracy JB, Murray RW. Fully ferrocenated hexanethiolate monolayer-protected gold clusters. *Langmuir* 2006, 23:2247–2254.
 67. Pinto YY, Le JD, Seeman NC, Musier-Forsyth K, Taton TA, Kiehl RA. Sequence-encoded self-assembly of multiple-nanocomponent arrays by 2D DNA scaffolding. *Nano Lett* 2005, 5:2399–2402.
 68. Rothmund PWK. Folding DNA to create nanoscale shapes and patterns. *Nature* 2006, 440:297–302.
 69. Han D, Pal S, Nangreave J, Deng Z, Liu Y, Yan H. DNA origami with complex curvatures in three-dimensional space. *Science* 2011, 332:342–346.
 70. Pinheiro AV, Han D, Shih WM, Yan H. Challenges and opportunities for structural DNA nanotechnology. *Nature Nanotech* 2011, 6:763–772.
 71. Endo M, Yang Y, Emura T, Hidaka K, Sugiyama H. Programmed placement of gold nanoparticles onto a slit-type DNA origami scaffold. *Chem Commun* 2011, 47.
 72. Unconventional DNA-based route to self-assembled superlattices. *Nano Today* 2009, 4:287.
 73. Noh H, Hung AM, Choi C, Lee JH, Kim J-Y, Jin S, Cha JN. 50 nm DNA nanoarrays generated from uniform oligonucleotide films. *ACS Nano* 2009, 3:2376–2382.
 74. Kershner RJ, Bozano LD, Micheel CM, Hung AM, Fornof AR, Cha JN, Rettner CT, Bersani M, Frommer J, Rothmund PWK, et al. Placement and orientation of individual DNA shapes on lithographically patterned surfaces. *Nature Nanotech* 2009, 4:557–561.
 75. Akbulut O, Jung J-M, Bennett RD, Hu Y, Jung H-T, Cohen RE, Mayes AM, Stellacci F. Application of supramolecular nanostamping to the replication of DNA nanoarrays. *Nano Lett* 2007, 7:3493–3498.
 76. Zheng Y, Lalander CH, Thai T, Dhuey S, Cabrini S, Bach U. Gutenberg-style printing of self-assembled nanoparticle arrays: electrostatic nanoparticle immobilization and DNA-mediated transfer. *Angew Chem Int Ed* 2011, 50:4398–4402.
 77. Liz-Marzán LM. Tailoring surface plasmons through the morphology and assembly of metal nanoparticles. *Langmuir* 2005, 22:32–41.
 78. Kelly KL, Coronado E, Zhao LL, Schatz GC. The optical properties of metal nanoparticles: the influence of size, shape, and dielectric environment. *J Phys Chem B* 2002, 107:668–677.
 79. Mie G. Beiträge zur Optik trüber Medien, speziell kolloidaler Metallösungen. *Ann Phys* 1908, 330:377–445.
 80. Raschke G, Kowarik S, Franzl T, Sönnichsen C, Klar TA, Feldmann J, Nichtl A, Kürzinger K. Biomolecular recognition based on single gold nanoparticle light scattering. *Nano Lett* 2003, 3:935–938.
 81. Mulvaney P. Surface plasmon spectroscopy of nano-sized metal particles. *Langmuir* 1996, 12:788–800.
 82. Katz E, Willner I. Integrated nanoparticle–biomolecule hybrid systems: synthesis, properties, and applications. *Angew Chem Int Ed* 2004, 43:6042–6108.
 83. Ofir Y, Samanta B, Rotello VM. Polymer and biopolymer mediated self-assembly of gold nanoparticles. *Chem Soc Rev* 2008, 37.
 84. Rycenga M, Cobley CM, Zeng J, Li W, Moran CH, Zhang Q, Qin D, Xia Y. Controlling the synthesis and assembly of silver nanostructures for plasmonic applications. *Chem Rev* 2011, 111:3669–3712.
 85. Elghanian R, Storhoff JJ, Mucic RC, Letsinger RL, Mirkin CA. Selective colorimetric detection of polynucleotides based on the distance-dependent optical properties of gold nanoparticles. *Science* 1997, 277:1078–1081.
 86. Storhoff JJ, Lazarides AA, Mucic RC, Mirkin CA, Letsinger RL, Schatz GC. What controls the optical

- properties of DNA-linked gold nanoparticle assemblies? *J Am Chem Soc* 2000, 122:4640–4650.
87. Jin R, Wu G, Li Z, Mirkin CA, Schatz GC. What controls the melting properties of DNA-linked gold nanoparticle assemblies? *J Am Chem Soc* 2003, 125:1643–1654.
88. Rosi NL, Mirkin CA. Nanostructures in biodiagnostics. *Chem Rev* 2005, 105:1547–1562.
89. Storhoff JJ, Mirkin CA. Programmed materials synthesis with DNA. *Chem Rev* 1999, 99:1849–1862.
90. Reinhard BM, Sheikholeslami S, Mastroianni A, Alivisatos AP, Liphardt J. Use of plasmon coupling to reveal the dynamics of DNA bending and cleavage by single EcoRV restriction enzymes. *Proc Natl Acad Sci USA* 2007, 104:2667–2672.
91. Cao YC, Jin R, Mirkin CA. Nanoparticles with Raman spectroscopic fingerprints for DNA and RNA detection. *Science* 2002, 297:1536–1540.
92. Wustholz KL, Henry A-I, McMahon JM, Freeman RG, Valley N, Piotti ME, Natan MJ, Schatz GC, Duyn RPV. Structure-activity relationships in gold nanoparticle dimers and trimers for surface-enhanced Raman spectroscopy. *J Am Chem Soc* 2010, 132:10903–10910.
93. Tikhomirov G, Hoogland S, Lee PE, Fischer A, Sargent EH, Kelley SO. DNA-based programming of quantum dot valency, self-assembly and luminescence. *Nature Nanotech* 2011, 6:485–490.
94. Bui H, Onodera C, Kidwell C, Tan Y, Graugnard E, Kuang W, Lee J, Knowlton WB, Yurke B, Hughes WL. Programmable periodicity of quantum dot arrays with DNA origami nanotubes. *Nano Lett* 2010, 10:3367–3372.
95. Ng KC, Qi A, Yeo LY, Friend J, Cheng WL. Evaporative self-assembly of gold nanorings via a surface acoustic wave atomization. *Proc SPIE* 2011, 8204:820434–820439.
96. Morrow TJ, Li MW, Kim J, Mayer TS, Keating CD. Programmed assembly of DNA-coated nanowire devices. *Science* 2009, 323:352.
97. Macfarlane RJ, Jones MR, Senesi AJ, Young KL, Lee B, Wu JS, Mirkin CA. Establishing the design rules for DNA-mediated colloidal crystallization. *Angew Chem Int Ed* 2010, 49:4589–4592.